

SiD Letter of Intent

v0.94 25 February 2009

Editors: H. Aihara, P. Burrows, M. Oreglia

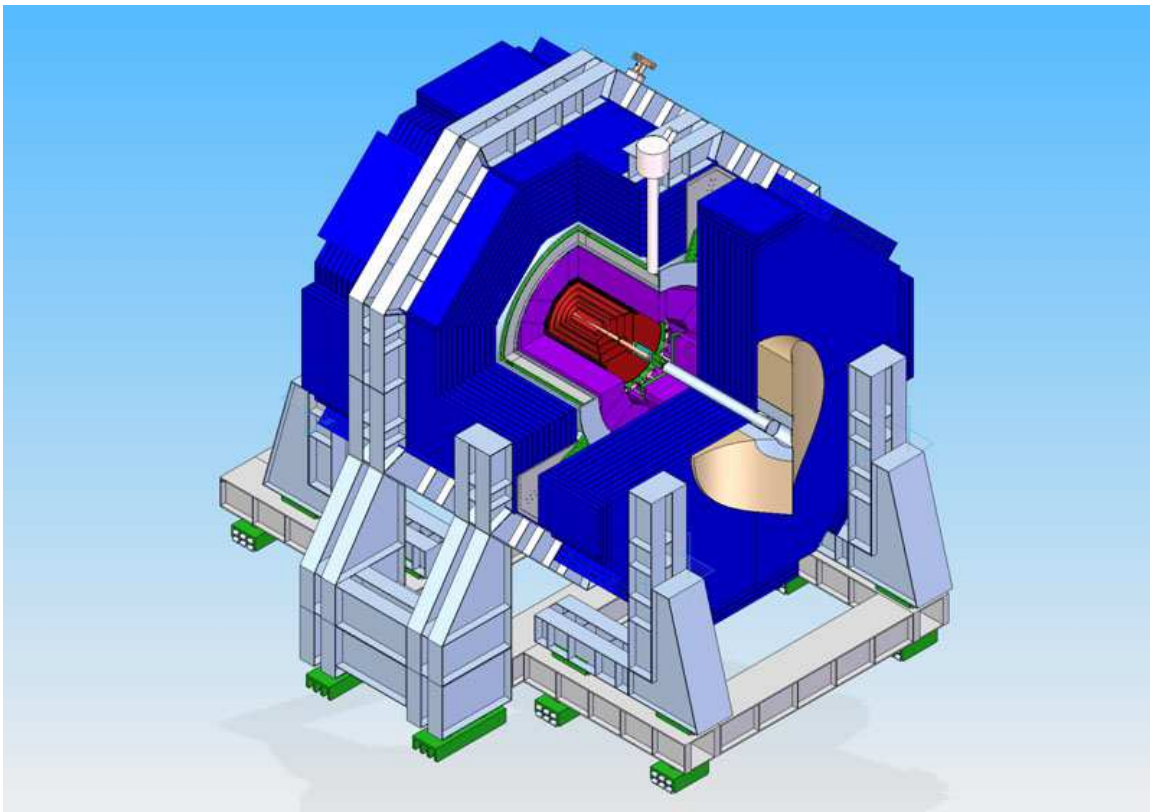


Figure 1: The SiD detector concept.

Contents

1	Introduction	3
1.1	The ILC Physics Menu	3
1.2	Detector Overview	4
1.3	Polarimeters and Energy Spectrometers	7
1.4	SiD Detector Optimization	8
1.5	ILC Environmental Concerns	10
1.5.1	Expected Backgrounds at the ILC	12
1.5.2	Vertex Detector	13
1.5.3	Forward Tracker	14
1.5.4	Barrel Tracker	16
1.5.5	Electromagnetic Calorimeter	16
1.5.6	Beamcal and Lumcal.	16
	References	19
2	Subsystems	21
2.1	Vertex and Tracking System	22
2.1.1	Introduction	22
2.1.2	Beam Environment	23
2.1.3	Vertex Detector Design	25
2.1.4	Tracker Design	31

CONTENTS

2.1.5	Tracker Module Design	33
2.1.6	Simulation Infrastructure	36
2.1.7	Vertex Detector Hit Digitization	37
2.1.8	Tracker Hit Digitization	39
2.1.9	Track Reconstruction	39
2.1.10	Tracking Performance	42
2.1.11	Tracker Alignment	43
	References	44
2.2	Calorimeters	55
2.2.1	Introduction to Calorimeters	55
2.2.2	Electromagnetic Calorimeter	55
2.2.3	Hadronic Calorimeter	65
2.3	Homogeneous Dual Readout Option	80
2.3.1	Principles of Operation: Energy Resolution	80
2.3.2	Enabling Technological Developments	84
2.3.3	Conceptual Design of High Resolution Calorimeter (HRC)	84
2.3.4	Principal Challenges of the HRC	85
2.3.5	R&D Program	85
	References	88
2.4	SiD MAGNET SUBSYSTEM	89
2.4.1	Superconducting Solenoid	89
2.4.2	Cryostat and Magnet Iron	94
2.4.3	Detector Integrated Dipole (DID)	95
2.5	Muon System	97
2.5.1	Overview	97
2.5.2	Design	97
2.5.3	Function	97

2.5.4	Requirements	98
2.5.5	Detector Design	98
2.5.6	Backgrounds	98
2.5.7	Resistive Plate Chambers	99
2.5.8	R&D	100
2.5.9	Milestones	106
	References	108
2.6	Forward Detector	109
2.6.1	Design criteria	109
2.6.2	Baseline Design	112
2.6.3	Expected Performance	114
2.6.4	High energy electron detection in BeamCal	117
2.6.5	R&D	119
	References	121
3	Machine-Detector Interface and Global Issues	123
3.1	SiD Assembly	123
3.2	Push Pull	124
4	Physics Performance and Benchmarking	129
4.1	Simulation of SiD.	129
4.1.1	Beampipe:	131
4.1.2	Vertex Detector:	131
4.1.3	Tracker:	132
4.1.4	Calorimeters:	133
4.1.5	Solenoid:	134
4.1.6	Muon System:	134
4.1.7	Masks and Far Forward Detectors	135

CONTENTS

4.2	Benchmark Reactions	135
4.2.1	$e^+e^- \rightarrow e^+e^-H, \mu^+\mu^-H, \sqrt{s}=250 \text{ GeV}$	136
4.2.2	$e^+e^- \rightarrow ZH, H \rightarrow c\bar{c}, Z \rightarrow \nu\bar{\nu}, q\bar{q}, \sqrt{s}=250 \text{ GeV}$	136
4.2.3	$e^+e^- \rightarrow ZH, H \rightarrow \mu^+\mu^-, Z \rightarrow \nu\bar{\nu}, q\bar{q}, \sqrt{s}=250 \text{ GeV}$	144
4.2.4	$e^+e^- \rightarrow \tau^+\tau^-, \sqrt{s}=500 \text{ GeV}$	147
4.2.5	$e^+e^- \rightarrow t\bar{t}, t \rightarrow bW^+, W^+ \rightarrow q\bar{q}', \sqrt{s}=500 \text{ GeV}$	150
4.2.6	$e^+e^- \rightarrow \tilde{\chi}_1^+\tilde{\chi}_1^-/\tilde{\chi}_2^0\tilde{\chi}_2^0, \sqrt{s}=500 \text{ GeV}$	153
4.2.7	$e^+e^- \rightarrow ZHH, H \rightarrow b\bar{b}, \sqrt{s}=500 \text{ GeV}$	156
4.2.8	Sbottom Quark Production: $e^+e^- \rightarrow \tilde{b}\tilde{b}, \tilde{b} \rightarrow b\tilde{\chi}_1^0$	159
4.2.9	$e^+e^- \rightarrow e^+e^-(\gamma), \mu^+\mu^-(\gamma), \sqrt{s}=500 \text{ GeV}$	163
	References	165
5	Cost Estimate	167
6	Research and Development Issues	175

List of Figures

1	The SiD detector concept.	1
1.1	Illustration of a quadrant of SiD.	5
1.2	Fractional error in the triple Higgs coupling, g_{hhh} , as a function of the jet energy resolution, $\Delta E/E$ [%], from the measurement of the cross section for $e^+e^- \rightarrow ZHH$ at 500 GeV with an integrated luminosity of 2000 fb^{-1}	10
1.3	Physics backgrounds from $\gamma\gamma$ produced e^+e^- pairs, muon pairs, and hadronic events integrated over 150 bunch crossings (left) and a single bunch crossing (right).	11
1.4	VXD Hits/mm ² /train for Barrel Layer 1 for the various ILC beam parameter sets.	15
1.5	The number of charged particles / BX which reach a maximum radius between R and R + 2 cm, as a function of radius R, for nominal 500 GeV beam parameters. The e^+e^- pairs are shown in red; hadrons and muon pairs in green.	15
1.6	The density of electron and positron tracks / cm ² / BX in Layer #1 of the forward tracker, as a function of the radius of the hit.	17
2.1	Maximum envelope of the e^+e^- -pair backgrounds in a 5 Tesla field. Indicated is the 12 mm radius beampipe.	24
2.2	R-z view of the vertex detector and its support structure.	25
2.3	Barrel end view of the vertex detector (left) and layer arrangement of the silicon sensors only (right).	27
2.4	Tracker in the open position for servicing of the vertex detector.	31
2.5	Hit pattern and material summary of the vertex detector as function of polar angle.	45
2.6	R-z view of the whole tracking system.	46

LIST OF FIGURES

2.7	Detail of the sensor overlap in the barrel region in the z and $R\varphi$ projection.	46
2.8	$R\varphi$ projection view of the tracker barrels and disks.	47
2.9	Detail of the sensor overlap and cable routing for the tracker disks.	48
2.10	Material budget of the tracking system.	49
2.11	Photograph of a prototype SiD tracker sensor.	49
2.12	Detail of the double-metal routing of the traces to the readout chip and the connections to the readout cable, visible to the right of the bump-bond array.	50
2.13	Sketch of a module to the tracker barrel. This figure should be replaced.	50
2.14	R - z view of the simplified tracking system as implemented in sid02.	51
2.15	The central vertex detector showing the layout of the silicon pixel sensor modules.	51
2.16	The central tracker showing support barrels tiled with overlapping readout modules.	52
2.17	Track finding efficiency as function of $\cos\vartheta$.	52
2.18	Track finding efficiency as function of p_T .	53
2.19	Number of mis-assigned hits on a track.	53
2.20	Resolution in momentum (right) and DCA (left) as function of momentum for tracks at various angles.	54
2.21	Sketch of the IR alignment method.	54
2.22	Simulated $\rho^+ \rightarrow \pi^+\pi^0$ in SiD.	56
2.23	Energy resolution for two longitudinal configurations.	58
2.24	Overall mechanical layout of the ECAL.	59
2.25	Drawing of a silicon sensor for the ECAL.	61
2.26	Readout gap in the vicinity of the KPjX readout chip.	62
2.27	Paul's Digital ECAL plot and a nice MAPS Shower picture	62
2.28	Drawing of initial ECAL test module.	63
2.29	Cross-section of the HCAL barrel.	65
2.30	Face and top views of the forward HCAL.	66

2.31 Schematic of the RPC design with two glass plates.	67
2.32 Schematic of the RPC design with one glass plate.	67
2.33 MIP detection efficiency	68
2.34 Longitudinal shower shape	69
2.35 MIP detection efficiency as function of time	69
2.36 Schematic layout of GEM-based DHCAL	71
2.37 GEM results from FNAL beam test.	71
2.38 Signal from KP1X chip - anode pad under source	72
2.39 MicroMegas 12x32 cm ² prototype.	74
2.40 MicroMegas analog response to a ⁵⁵ Fe X-ray source.	74
2.41 Example of a prototype mapping with analog readout.	75
2.42 Prototype of the MicroMegas with DIRAC digital readout.	76
2.43 Prototype mapping of the MicroMegas with DIRAC digital readout.	76
2.44 Prototype of the MicroMegas with 4 HARDROCs digital readout.	77
2.45 Design of the 1 m ² MicroMegas Prototype.	77
2.46 CALICE test beam setup at CERN.	78
2.47 Response of charged pions in the scintillator-SiPM HCAL.	79
2.48 Barrel wedge instrumented with IRL planes.	79
2.49 Response uniformity of a directly coupled tile.	80
2.50 Scintillator and Cherenkov signals and their correlation	81
2.51 Dual readout response	82
2.52 Response linearity, energy resolution, and scaled energy resolution for hadronic jets.	83
2.53 SiD Superconducting Magnet: Solenoid with Winding/Quench Back Cylinder/LHe Cooling Tubes, Cryostat, Thermal Shields, and Detector Integrated Dipole.	91
2.54 SiD central field contours in B , fields in the iron shown by intensity scale. The iron Pac Man is included and shown in the rectangle in the lower right.	92

LIST OF FIGURES

2.55	Photo CMS conductor and proposed SiD conductor.	92
2.56	Solenoid shown with valve box, current leads and attachments to barrel iron plates.	94
2.57	4.5 K Detector Integrated “anti” Dipole with magnetic field profile. Dipole field is horizontal. Gaps in dipole winding are connection points to current leads.	96
2.58	Quarter-section of the SiD flux return(a). Sub-division of the endcap into RPC modules.	97
2.59	Fraction of pions between 1-50GeV/c that produce a hit at a depth x or greater.	99
2.60	Sum of the pulse heights in 13 RPC strips readout by KPIX. The peak position of ~ 3 pC and efficiency of $>90\%$ are consistent with previous studies of avalanche mode RPCs.	102
2.61	SIPM Hamamatsu MPPC and 2cm scale front-end electronics test setup. The output is generated with a pulsed LED providing the input light.	104
2.62	Forward region.	112
2.63	LumiCal sensor and segmentation.	114
2.64	BeamCal sensor and segmentation.	115
2.65	(a) Deposited energy in Si layers (b) Energy resolution	116
2.66	(a) Total energy distribution (b) Correlation of e^+ and e^- polar angles	117
2.67	Efficiency to reconstruct high energy electrons at three azimuthal angles	118
2.68	Energy deposition in Si layers as a function of $\cos \theta$	119
2.69	Number of photons penetrating the tungsten mask as a function of the mask thickness	120
3.1	WBS for SiD installation.	127
4.1	Higgs recoil mass spectra for several values of parameters characterizing the tracker momentum resolution.	137
4.2	SM Higgs production cross-section.	138
4.3	Visible energy (a) and the number of leptons per event (b). The distributions are used for channel classification	139
4.4	kinematic variables: (a) Higgs (dashed) and SM di-jet mass, (b) angle between jets and (c) c quark nn output versus b quark nn output for jet 1	140

4.5	Neural Network Selection	141
4.6	Kinematic variables: (a) Higgs (dashed) and Z-boson mass, (b) angle between jets and (c) c quark nn output versus b quark nn output for jet 1	142
4.7	Neural Network Selection	143
4.8	Standard Model Higgs branching fractions	145
4.9	Higgs production in the SM	145
4.10	The invariant mass of the $\mu\mu$ system and the di-jet system in the hadronic channel	146
4.11	The invariant mass of the $\mu\mu$ system and the missing mass in the missing energy channel	147
4.12	Optimal observable ω for the decay $\rho^- \nu_\tau$	149
4.13	Tau polarization versus $\cos \Theta$	149
4.14	Btag of all jets for b quarks(red) c quarks(blue) and uds quarks(green) (a) and (b) Btag sum over all jets for all signal(full line,area) and background(dashed line) events before and after preliminary cuts.	151
4.15	Top Mass after Kinematic fitting(, black signal+ background, red background only).	152
4.16	(a) Combined charge for b and bbar quarks. (b) Events used in calculation of Afb for the b quark - black signal plus background, blue SM backgrounds, red mistagging backgroun.	153
4.17	The reconstructed boson masses from the four jets, selecting chargino events. left: pure chargino; right: pure neutralino	155
4.18	Upper: The reconstructed W energy (left) and mass (right) for chargino event selection; Lower: The reconstructed Z energy (left) and mass (right) for neutralino event selection. Blue is the true chargino events and green the neutralino events.	155
4.19	(a)Mass distribution of reconstructed bosons before (blue) and after (red) kinematic fitting; (b)Energy distribution of reconstructed bosons. Black is MC information, Green and Red lines are before and after kinematic fitting.	156
4.20	The boson energy distribution for $m_{\tilde{\chi}_1^0} = \dots$ and \dots	157
4.21	Feynman diagrams describing $e^+e^- \rightarrow ZHH$ process. Higgs self-interaction vertex contributes to the first diagram.	157

LIST OF FIGURES

4.22	(a):Neural Network output for signal (filled histogram) and background. (b): Cross section measurement statistical error as a function of a number of selected signal events.	159
4.23	Jet flavour tagging efficiency as a function of the jet momentum for b-jets. The gray line corresponds to a fitted Gompertz-like curve.	160
4.24	Selected points in SUSY model space. Color coding corresponds to an estimated difficulty of the measurement (lighter is more challenging). Full line shows a kinematic limit corresponding to $m_{\tilde{b}} > m_{\tilde{\chi}_1^0}$ while dashed line to a limit $m_{\tilde{b}} > m_{\tilde{\chi}_1^0} + \Delta M$, where $\Delta M = 5 \text{ GeV}$	161
4.25	The main selection variables, from top left: Distance of jets in $\eta - \phi$ plane, acoplanarity and maximum pseudorapidity of jets. Signal (green) is shown together with major backgrounds: two photon background (red), $e^+e^- \rightarrow b\bar{b}$ (black), $e^+e^- \rightarrow b\bar{b}\nu\nu$ (blue) and $e^+e^- \rightarrow t\bar{t}$ (yellow). Neural Network output (bottom right) is shown for events which passed the basic selection cuts (see text for details) for signal (green) and backgrounds (red). All histograms are normalised to luminosity.	162
4.26	Confidence level plotted as a function of a number of selected signal events, depending on a particular Neural Net output cut used for signal event selection. Dashed line shows a limit of four standard deviations.	163
4.27	Error in E_{cm} as a function of the parameters describing the tracker momentum resolution coming from several possible measurements.	164
5.1	Subsystem Summary of Costs	169
5.2	Subsystem M&S Costs	169
5.3	Subsystem Labor	169
5.4	SiD Base M&S Cost vs Tracker Radius	170
5.5	SiD Base M&S Cost vs Hadronic Calorimeter Thickness	170
5.6	SiD Base Cost vs B	171
5.7	SiD Base Cost vs Tracker Aspect Ratio	171
5.8	Example of WBS	173

List of Tables

1.1	Key parameters of baseline SiD detector.	5
1.2	Background sources for the nominal ILC 500 GeV beam parameters.	13
2.1	30
2.2	32
2.3	34
2.4	35
2.5	Nominal parameters of the silicon-tungsten ECal for SiD.	58
2.6	Parameters of baseline silicon-tungsten ECal.	60
2.7	Parameters of MAPS silicon-tungsten ECAL.	63
2.8	Efficiencies for the MicroMegas prototypes with analog readout	75
2.9	SiD and CMS Superconducting Solenoid Comparison.	90
2.10	Mechanical Comparison of SiD and CMS Solenoids.	93
2.11	Muon/Tail Catcher R&D Summary	105
2.12	LumiCal Parameters	113
2.13	Radial segmentation	116
2.14	Azimuthal segmentation	117
4.1	Standard Model Higgs Boson branching ratios for 120 GeV mass.	138
4.2	Standard Model Higgs Boson branching ratios for different masses calculated using HDECAY.	144

4.3	- Tau decay mode efficiencies and purities.	148
4.4	MC sample parameters.	154
4.5	Pre-selection cuts. $\theta(i, j)$ defines the angle between the i th and j th jet. The jets are ordered in energy, e.g. jet 1 is the most energetic jet.	154
4.6	- Selection cuts used to preselect events for both Neural Network training and the cross section measurement analysis.	158
4.7	Selected parameters of the EWSB SUSY model corresponding to various masses of sbottom quark \tilde{b} and neutralino $\tilde{\chi}_1^0$	160
5.1	Cost Sensitivity to selected unit costs	171

LIST OF TABLES

Chapter 1

Introduction

1.1 The ILC Physics Menu

SiD has been designed to address questions of fundamental importance to progress in particle physics:

- What is the mechanism responsible for electroweak symmetry breaking and the generation of mass?
- How do the forces unify?
- Does the structure of space-time at small distances show evidence of extra dimensions?
- What are the connections between the fundamental particles and forces and cosmology?

These are addressed through precision measurements by SiD at the International Linear Collider (ILC) of the following:

- Higgs boson properties;
- Gauge boson scattering;
- Effects resulting from the existence of extra dimensions;
- Supersymmetric particles; and
- Top quark properties.

The Higgs boson studies will measure in detail the properties of the Higgs boson in order to determine its consistency with Standard Model expectations, and the nature of any deviations. These measurements will include the mass, width, spin, branching ratios and

couplings, and the Higgs self-coupling. The precision anticipated is a function of the Higgs mass and is sufficient to discriminate between competing theories for electroweak symmetry breaking. With the decay independent detection of Higgstrahlung events by Z tagging, sensitivity to a wide range of models is possible. Such measurements would establish the role of the Higgs boson in electroweak symmetry breaking, and the generation of mass. Should Nature choose a Higgs-less scenario, it could be addressed by studying the coupling of gauge bosons.

Should additional Higgs bosons beyond the one of the Standard Model exist, SiD will be prepared to detect these up to very large masses. For example, in the MSSM, the additional four Higgs bosons can be detected if they are within the kinematic reach of the ILC. If supersymmetric particles are produced at the ILC, they will be studied by SiD, establishing an important link in the couplings of the forces at low and high energies, and experimentally testing the unification of forces. SiD has a reach up to ~ 3 TeV in Higgs-less strong coupling scenarios. Such models would include the Little-Higgs model, strongly interacting W and Z bosons, and extra dimensions models. A universe with extra dimensions of a scale within reach of the ILC can be probed, with sensitivity to the separate parameters of scale and number of dimensions. By observing masses and widths of excited graviton states, the length scale and the curvature in an additional fifth dimension of space-time can be determined.

SiD plans to study the top quark at the ILC, including the precise measurement of the top quark mass, and its Yukawa coupling. A number of connections to issues of interest in cosmology would be realized through many of the measurements described above. These focus on two fundamental issues, namely the mechanism behind the present day baryon asymmetry and the nature of the cold dark matter

1.2 Detector Overview

The Silicon Detector, SiD, is a linear collider detector concept designed to strike a optimum balance between precision measurements and searches for new phenomena at the ILC. A plan view of one quadrant of the detector is shown in Figure 1.1. tracking, silicon-tungsten electromagnetic calorimetry, highly segmented hadronic calorimetry, and a powerful silicon pixel vertex detector. SiD also incorporates a high field solenoid, iron flux return, and a muon identification system. The choice of silicon detectors for tracking and vertexing ensures that SiD is robust against unexpected beam backgrounds or beam loss, provides superior charged particle momentum resolution, and eliminates out of time tracks and backgrounds. The main tracking detector and calorimeters are “live” only during a single bunch crossing, so beam backgrounds and low mass gamma-gamma backgrounds will be reduced to the minimum possible levels. The SiD design has been cost-conscious from the beginning, and the present global design represents a careful balance between cost and physics performance. The SiD proponents are convinced that two detectors are required both sociologically and technically to fully exploit the ILC physics potential, therefore SiD is engineered to make the push pull process efficient and to minimize the time required for alignment and calibration after a move.

The key parameters of the SiD design starting point are listed in Table 1.1.



Figure 1.1: Illustration of a quadrant of SiD.

SiD BARREL	Technology	Inner radius	Outer radius	Z max
Vertex detector	Pixel	1.4	6.1	6.25
Tracker	Silicon strips	20.0	126.5	± 167.9
EM calorimeter	Silicon-W	127.0	140.0	± 180.0
Hadron calorimeter	RPCs	141.0	250.0	± 277.2
Solenoid	5 Tesla	250.0	330.0	± 277.0
Muon chambers	RPCs	333.0	645.0	± 277.0

SiD FORWARD	Technology	Inner Z	Outer Z	Outer radius
Vertex detector	Pixel	71.9	172.0	71.0
Tracker	Silicon strips	26.7	165.4	126.5
EM calorimeter	Silicon-W	168.0	182.0	127.0
Hadron calorimeter	RPCs	182.0	277.0	140.7
Muon chambers	RPCs	277.5	589.5	645.0
LumCal	Silicon-W	170.0	183.0	19.0
GamCal				
BeamCal	Silicon-W	321.0	334.0	18.0

Table 1.1: Key parameters of baseline SiD detector. (All dimension are given in cm.)

INTRODUCTION

SiD tracking begins with 5 cylinders and 4 sets of endcap pixilated sensors closely surrounding the beampipe for the Vertex Detector (VXD); the impact parameter resolution will surpass $\sigma_{r\phi} = \sigma_{rz} = 5 \oplus 10/(\beta \sin^{3/2}\theta)$ [μm]. SiD has chosen a 5 T solenoidal field in part to control the e^+e^- pair background, and the cylinder and disk geometry is chosen to minimize scattering and ensure high performance in the forward direction. The VXD sensor technology is not yet chosen because the relatively high luminosity per train at the ILC makes integration through the train undesirable, and optimal technologies for separating the train into small temporal segments, preferably bunches, have not been determined. This is not a problem, since this choice will have almost no effect on the rest of the SiD design, and the VXD can be installed late or even exchanged.

SiD has chosen Si strip technology, arrayed in 5 cylinders and 4 endcaps for precision tracking and momentum measurement. Particular attention has been given to supporting the cylinders with minimal material on the ends to enhance forward tracking. The sensors are single sided Si, approximately 15 cm square, with a pitch of 25 μm . With an outer cylinder radius of 1.25 m and a 5 T field, the charged track momentum resolution will be better than $\sigma(1/p_T) = 5 \times 10^{-5}$ for high momentum tracks. The sensors are read by two 1024 channel KPjX chips, which are directly bump bonded to the double metal sensors to eliminate the material of a hybrid connection. The endcaps utilize two sensors bonded together for small angle stereo measurements. Highly efficient track finding has been demonstrated in simulation, either with the tracker alone or in combination with the VXD.

SiD calorimetry is optimized for jet measurement, and is based on a Particle Flow strategy, in which charged particle momenta are measured in the tracker; neutrals are measured in the calorimeter, and then the charged and neutral components are added. Of course, the challenge is removing charged particle contributions from the calorimeters. SiD calorimetry begins with an exceptionally dense, highly pixilated Silicon – Tungsten electromagnetic section. The EMCal has 20 layers of 2.5 mm W and 1.25 mm gaps, followed by 10 layers of 5 mm W and the same gaps. This results in a Moliere radius for the thin section 13.5 mm. The sensors are hexagonal, approximately 15 cm across flats. The sensor is divided into 1024 hexagonal pixels and is read out by a bump bonded KPjX chip, forming an imaging calorimeter with a track resolution of ~ 1 mm. The EMCal has a total of 28.5 X_0 . The same technology is used in the endcaps. The consistent Si technology from the VXD through the EMCal is chosen to be both robust against machine backgrounds and to have sufficiently high performance that additional detector subsystems are avoided. While this is most critical for limiting material that degrades measurement performance, it also limits costs.

The Hadronic Calorimeter (HCal) is made from 4.5 λ of Stainless Steel, divided into 40 layers of steel and detector. The baseline detector is an RPC with 1 cm square pixels read out by KPjX chips, inserted into 8 mm gaps between the steel layers. The same technology is used for endcaps. The PFA performance has been studied with Pandora and also with an SiD-specific program, resulting in a jet energy resolution $\Delta E/E = 4\%$. Further improvement is expected as the algorithm matures. Having such superb jet energy resolution will allow, for the first time, the invariant masses of W's, Z's, and tops to be reconstructed with resolutions approaching the natural widths of these particles.

The calorimetric coverage is completed in the forward direction by a Lumcal and a Beamcal. The Lumcal overlaps the endcap EMCal, and is designed for a $\Delta L/L$ precision

of 1×10^{-3} . The Lumcal is Si-W, with the pixilation designed to optimize the luminosity measurement precision. The Beamcal is the smallest angle calorimeter and is mounted to the inboard side of QD0. The Beamcal sensor technology may be diamond or low resistivity Si. Both calorimeters are designed for a 14 mrad crossing angle and an anti-DID correction winding on the main solenoid.

The SiD 5 T superconducting solenoid is based on the CMS solenoid, but has 6 layers of conductor. The stored energy is ~ 1.6 GJ. The critical cold mass parameters, such as stored energy/Kg, are similar to CMS. The CMS conductor is the baseline choice, but SiD is developing an advanced conductor that would eliminate the e-beam welding of structural alloy and be easier to wind. SiD will carry all the solenoid utilities (power supply, quench protection, etc) except for the He liquefier, which will be connected by a vacuum insulated flex line. The flux is returned by an iron structure of a barrel and end doors with a field leakage criterion of < 100 G at 1 m. The flux return is 11 layers of 20 cm iron. The flux return also is the absorber for the muon identifier and is an important component of SiD self shielding. The barrel is composed of full length modules to help keep the structure stable during push pull and to enable full length muon detectors. The doors supports the QD0's at all positions of the doors, with provision for transverse alignment of the quads and vibration isolation. A platform fixed to the barrel supports the 2K cryogenic system for the QD0's. SiD is designed for rapid push pull and rapid recovery after such motion. Precision alignment will be by a geodetic network of frequency scanning interferometers.

1.3 Polarimeters and Energy Spectrometers

The ILC physics program demands precise polarization and beam energy measurements [1], and SiD will have major responsibilities for these. The ILC baseline configuration is defined in the RDR [2] and specifies many key features of the machine that impact these measurements and the related physics program. These features are summarized in Reference [3] and include:

- a highly polarized electron beam with $P > 80\%$
- a polarized positron beam with an initial polarization of $\sim 30 - 45\%$
- spin rotator systems for both electron and positron beams to achieve longitudinal polarization at the collider IP
- polarimeters and energy spectrometers upstream and downstream of the IP for both beams. The polarimeters utilize Compton scattering and aim to measure the polarization with an accuracy of $\Delta P/P = 0.25\%$. The energy spectrometers aim to achieve an accuracy of 100-200 parts per million (ppm).
- capability to rapidly flip the electron helicity at the injector using the source laser. (The possibility of fast positron helicity flipping is not included in the baseline configuration, but a scheme for fast positron helicity flipping has been proposed.)

The baseline ILC features described above achieve the requirements described in the Linear Collider parameters document [4]. Reference [4] does not require polarized positrons,

but this capability is provided in the RDR and has the potential to add significant physics reach. SiD endorses realizing the capability for longitudinally polarized positrons at the IP if a helical undulator is used for the positron source. SiD also endorses implementing capability for fast positron helicity flipping, which is needed to minimize systematic errors for some of the precision measurements planned.

SiD endorses the goals stated in References [3] and [5] for the polarimeters to achieve a systematic error of 0.25% and for the energy spectrometers to achieve an accuracy of 100-200 ppm. SiD also endorses implementing both upstream and downstream polarimeters and energy spectrometers to achieve and demonstrate these goals. Two recommendations were made in Reference [3] to modify the RDR design to improve the polarimeter capabilities. SiD endorses these recommendations to i) provide a dedicated upstream polarimeter chicane and to ii) modify the extraction line polarimeter chicane from a 4-magnet chicane to a 6-magnet chicane to allow the Compton electrons to be deflected further from the disrupted beam line.

The baseline ILC provides beam energies in the range 100-250 GeV with precise polarization and energy measurements required for this full range. The baseline also provides for detector calibration at the Z-pole with 45.6 GeV beam energies, but does not require accurate polarimetry or energy spectrometer measurements at the Z-pole. As discussed in References [3] and [5] there is strong motivation to require accurate polarization and energy measurements at the Z-pole to calibrate the polarimeters and energy spectrometers and to enhance the physics program. A modest amount of running using calibration runtime and perhaps some dedicated runtime could significantly improve many of the Z-pole measurements made at LEP and SLC. SiD endorses the proposal for this made in Reference [5].

The polarimeter and energy spectrometer systems need to be a joint effort of the ILC BDS team and the Detector collaborations as summarized in Reference [3]. SiD intends to take significant responsibility for the design, development, operation and performance of these systems. SiD participants are already active in making significant contributions to their design and development. Data from the polarimeters and spectrometers must be delivered to the SiD DAQ in real time to be logged and permit fast online analysis. Fast online analysis results must also be provided to the ILC controls system for beam tuning and diagnostics. Details for integrating the polarimeter and energy spectrometer data with the SiD DAQ remain to be worked out, but SiD DAQ experts will assume responsibility for integrating the polarimeter and spectrometer data streams with the SiD DAQ.

1.4 SiD Detector Optimization

It is the design of the calorimeters, more than other subsystems, which determines the global parameter choices for the whole detector. The calorimeters are costly, and their performance and costs depend critically on how far from the interaction point they are placed and how thick they must be to contain most of the energy of jets, and therefore how big and costly the detector must be. The problem of optimizing the global detector design simplifies, at least in broad brush, to optimizing the parameters of the calorimeters and solenoid. Bigger is more performant, but bigger is also more costly. A balance must be struck.

Optimizing SiD’s global parameters required three tools. First, a parametric cost model was developed which could calculate the total cost based on the choice of global parameters, assumptions about what materials and detectors comprised each detector element, and per unit cost assumptions appropriate for the materials and detectors chosen.

Second, algorithms to estimate the jet energy resolution of the detector or the momentum resolution and impact parameter resolution of the tracker were needed to evaluate the subsystem performance as a function of the global parameters. The key parameters include the outer radius of the tracker, R , the tracker’s length, Z , the magnetic field, B , and the thickness of the hadronic calorimeter absorber λ . SiD utilized its own algorithms to estimate the tracking and vertexing performance, and employed parameterizations of the PFA performance derived by Mark Thomson from his Pandora PFA studies, to estimate the jet energy resolution as a function of the key parameters. Pandora was chosen, because at the time this exercise was conducted, the SiD PFA code was still under development. Since most of Thomson’s studies were appropriate to the (then) LDC detector, a special SiD-like variant, “SiDish”, was created for detailed study. Cross-checks showed that Thomson’s parameterization of the jet energy resolution agreed with results from SiDish. Additional studies were undertaken with SiDish to explore jet energy resolution as a function of the number of layers and thickness in the hcal, and in the forward direction as Z was changed.

Third, we studied how changing the subdetector performance, e.g. the jet energy resolution, would result in changing the ultimate physics performance of SiD, where the chosen metrics were the accuracy with which the triple Higgs coupling, or the chargino mass, could be determined. Fast Monte Carlo studies of these and other important physics measurements were conducted for a full range of possible jet energy resolutions, and the resulting measurement accuracy determined as a function of input jet energy resolution.

Figure 1.2 shows an example. These studies confirmed the results of earlier studies that showed slow improvements in physics measurement capability as jet energy resolution is improved; for several possible measurements, improving the jet energy resolution (i.e. $\Delta E/E$) by a factor of two, from $60\%/\sqrt{E}$ to $30\%/\sqrt{E}$, reduced the error in the measurement by about 30%, equivalent to roughly 60% more luminosity. This is a significant improvement, but not enough to make night and day differences in measurement capability.

The final step is to use the cost vs jet energy resolution and the physics performance vs jet energy resolution inputs, to see how errors in a measured physics quantity change as the cost of the detector is varied. What performance is good enough? Obviously, the detector performance must be adequate for making measurements to the accuracy motivated by the physics. Once that is satisfied, it is desirable to pay as little for such performance as possible. Ideally, the chosen design should sit near the “knee” of the performance vs cost plot, the point of optimal bang for the buck. The optimisation procedure is described in much greater detail in Chapter 5.

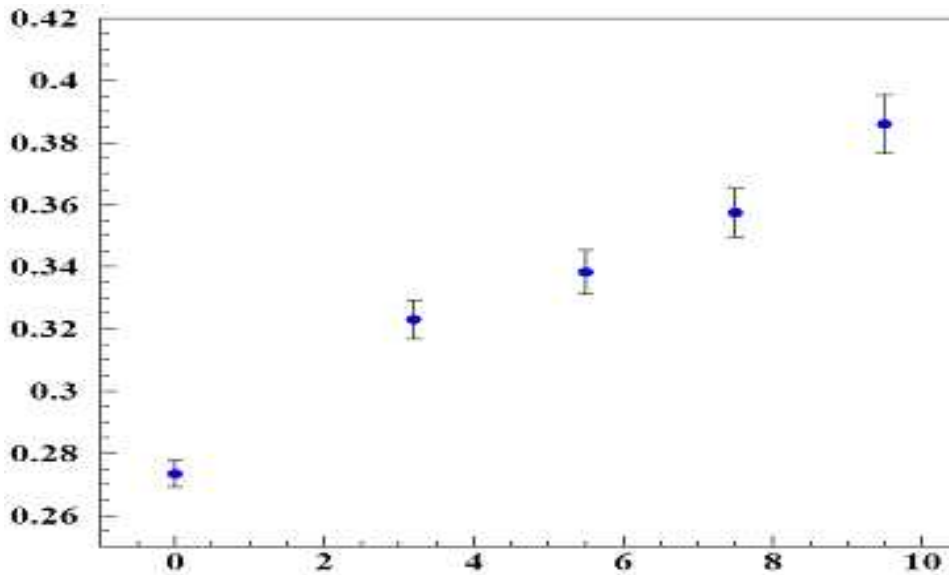


Figure 1.2: Fractional error in the triple Higgs coupling, g_{hhh} , as a function of the jet energy resolution, $\Delta E/E$ [%], from the measurement of the cross section for $e^+e^- \rightarrow ZHH$ at 500 GeV with an integrated luminosity of 2000 fb^{-1} .

1.5 ILC Environmental Concerns

The ILC time structure results in collisions of bunches at the interaction point every 308 nsec. Bunch trains consisting of 2820 bunches in each beam pass through the IP five times per second. Consequently, the bunch trains are about one millisecond long, separated by 199 milliseconds. The design luminosity is $2 \times 10^{34} \text{ cm}^{-2} \text{ sec}^{-1}$. Backgrounds generated by stray beam particles upstream, and collisions of the bunches themselves (beamstrahlung and beam-beam interactions), consist of large numbers of low energy ($\sim \text{MeV}$) photons, and electron-positron pairs. Furthermore, the hadronic collision rate itself, including the two-photon events, is about 200 events per bunch train. Other than the two-photon events, high energy interactions comprise only one event in about every ten bunch trains. Therefore, the pile up of the two-photon events could significantly confuse detection of the principal signal of interest unless the detector can cleanly select single bunch crossings, which SiD is designed to do. For example, only a few Higgstrahlung events per hour, or less, might be produced, motivating clean separation of the overriding two-photon events, and the lower energy backgrounds. The electron-positron pairs, largely produced in beam-beam interactions, while soft, are a particular problem for the inner-most layers of the detector. SiD's high solenoidal field is an effective protection from the bulk of these pairs, and allows the smallest possible beam pipe radius, optimizing vertexing resolution.

A further complication comes from lessons learned at the first linear collider, the SLC. There, bunch-to-bunch variations in the beam parameters were large, and hard to predict, model, and control. Individual bunches with anomalous backgrounds were problematic to operation of the SLD detector. Significant precautions are being taken at ILC to deal with this, but experience suggests the need for robust detectors. SiD's reliance on silicon sensors

for vertexing, tracking, and electromagnetic calorimetry promises the needed robustness.

While these constraints are mild compared to those imposed on LHC detectors, the high flux of photons concomitant with the collisions, from virtual sources and beamstrahlung, results in the copious production of e^+e^- pairs as well as the frequent production of muon pairs and hadronic interactions. The e^+e^- pairs account for most of the background in the inner detectors, directly as charged tracks with low transverse momentum. They also cause a general flux of $\sim\text{MeV}$ photons which result when they shower in the beam calorimeters on the front face of the final quadrupoles. These photons, and the higher transverse momentum muons and charged and neutral hadrons which also result from photon-photon interactions, spray the entire detector with charged particles and photons.

SiD is largely immune to these backgrounds because the detector as a whole is only sensitive to backgrounds associated with a single bunch crossing. The silicon microstrip and pixel detectors used in the vertexing, tracking, and electromagnetic calorimetry can be made sensitive to ionization which is deposited within just $1\ \mu\text{s}$ of the interaction time, and the resultant hits can be uniquely associated with a single bunch crossing. A channel-by-channel buffer, which is 4 deep in current designs, will store hits over the course of the entire bunch train, and record each responsible bunch crossing. Consequently, SiD is sensitive only to the physics and backgrounds of a single bunch crossing, in contrast to detectors with longer inherent livetimes, which can be sensitive to ~ 150 bunch crossings or more. Figure 1.3 contrasts the $\gamma\gamma$ backgrounds when the detector livetime is short or long. Pattern recognition benefits tremendously from this cleanest possible environment, and physics ambiguities are minimized. Channel-by-channel deadtime inefficiencies are minimal, and the event buffering insures that essentially no physics data is lost because of noise hits.

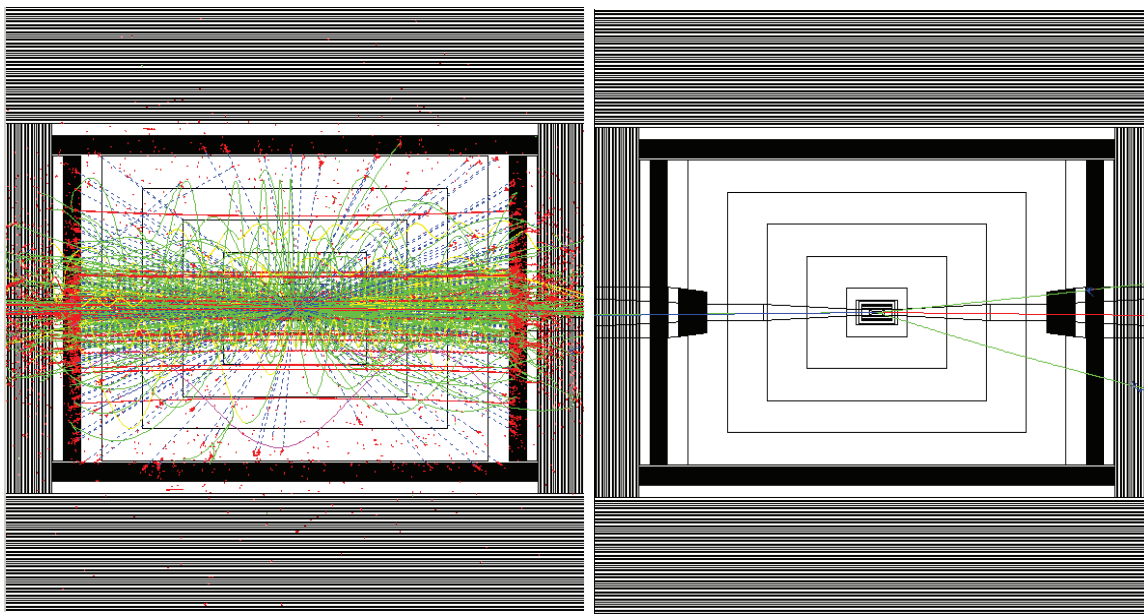


Figure 1.3: Physics backgrounds from $\gamma\gamma$ produced e^+e^- pairs, muon pairs, and hadronic events integrated over 150 bunch crossings (left) and a single bunch crossing (right).

Background hits do remain in SiD, of course, which could complicate pattern recog-

INTRODUCTION

dition in the vertex detector, tracker, and calorimeter. In fact, as we show in detail below, pattern recognition in SiD is uncompromised by these backgrounds, even allowing for considerable margin, because the material budget is kept to a minimum, and because the detector is only sensitive to a single bunch crossing's worth of background. This is not to say that these background levels are inconsequential. In fact, they will dictate how rapidly the vertex detector must be read out, impact the design of the forward tracking sensors, and determine the depth of buffering required for those sensors at small radii, where rates are high.

Experience at the first linear collider, the SLC, taught that bunch-to-bunch parameter variations are to be expected, that populations in the tails of the beam phase space were hard to predict and control, and that, in general, backgrounds beside those intimately related to the production of luminosity, like the $\gamma\gamma$ induced backgrounds discussed above, are to be expected and will likely be unpredictable, at least in the beginning. At the SLC, synchrotron radiation backgrounds were far beyond naïve expectation, leading to low energy photons backscattering into the detector, and occasionally off-energy electrons showered in the interaction region. The net radiation dose from these backgrounds was not a problem, but the high instantaneous dose was often enough to trip-off gas chambers at the SLC. Silicon sensors in the SLC experiments registered very large occupancies in these background events, but kept on running, with no ill effect. SiD, relying on silicon sensors, is especially robust against such backgrounds at the ILC.

In the following, we discuss the ILC backgrounds and their evaluation in more detail and quantify occupancies for each of the SiD detector subsystems, for the range of machine parameters under consideration.

1.5.1 Expected Backgrounds at the ILC

Detector backgrounds are expected to come from the following sources:

- IP Backgrounds Machine Backgrounds
- Disrupted primary beam Direct beam loss
- Beamstrahlung photons beam-gas scattering
- e^+e^- pairs from beam-beam interactions collimator edge scattering
- Radiative Bhabhas Synchrotron radiation
- Hadrons/muons from $\gamma\gamma$ interactions, muon production
- Neutron back-shine from dump
- Extraction line loss

Each of these sources has been studied. Among these sources the most dominant source is e^+e^- pairs from beam-beam interactions. The pairs are produced at the IP, interact with the beam pipe, inner vertex detector layers, mask and beamline magnets, and produce a large

number of secondary e^+e^- , photons and neutrons which in turn contribute background in the vertex detector and in the Si tracker and calorimeter at large radius.

Guinea-Pig is used to simulate the beam-beam interaction and to generate pairs, radiative Bhabhas, disrupted beams and beamstrahlung photons. The ILC beam parameters are used for the simulation. Table 2 summarizes the number of particles per bunch and average energy for the nominal ILC 500 GeV beam parameters. $\gamma\gamma$ interactions are included without a transverse momentum cut, to be sensitive to the entire cross sections for these processes. The $\gamma\gamma$ hadronic cross section is approximated in the scheme of Peskin and Barklow (ref).

Table 1.2: Background sources for the nominal ILC 500 GeV beam parameters.

Source	#particles/bunch	$\langle E \rangle$ (GeV)
Disrupted primary beam	2×10^{10}	244
Beamstrahlung photons	2.5×10^{10}	4.4
e^+e^- pairs from beam-beam interactions	75K	2.5
Radiative Bhabhas	320K	195
$\gamma\gamma \rightarrow$ hadrons/muons	0.5 events/1.3 events	-

Detector backgrounds are calculated in the SiD detector and IR layout with parameters described in <http://www.lcsim.org/detectors/#sidmay05>. The beamline magnets up to about 20 m from the IP are included, and the three crossing angle options, 20 mrad, 14 mrad and 2 mrad, are considered. The nearest quadrupole magnet of the final doublet ends at 3.51 m for all three options. The BeamCal has two holes (1 cm radius for incoming beam and 1.5 cm radius for outgoing beam) for the 20 mrad and 14 mrad options, while there is only one 1.5 cm radius hole for the 2 mrad option. The detector solenoid field is 5 Tesla, and the field map instead of a constant field is used for the calculations. GEANT 3 is used to calculate e^+/e^- and photon background. Since GEANT 3 does not simulate photo-nuclear interactions, FLUKA is used to calculate neutron background.

1.5.2 Vertex Detector

The background hits in the vertex detector come predominantly from the e^+e^- pairs. The number of VXD hits / mm^2 / train in the first barrel layer of the vertex detector, is shown in Figure 1.3 for the various beam parameters considered for the ILC. The backgrounds fall off rapidly with the radius of the sensor layer, so this represents the worst case. For the nominal ILC beam parameters, nearly 80 hits / mm^2 are expected over the full train for 500 GeV operations; at 1 TeV, in the high luminosity option, this number rises to about 400 hits / mm^2 .

Pattern recognition studies (Ref. Sinev, LCWS05 and Snowmass05) have demonstrated fully efficient pattern recognition in a five layer pixel vertex detector with $20 \times 20 \mu\text{m}^2$ pixels, even with backgrounds accumulated over >150 beam crossings. Taking this level of background as a conservative pattern recognition tolerance limit imposes a constraint on the vertex detector readout. The readout must limit the vertex detector sensitive time to ≤ 150

INTRODUCTION

BX (beam crossings), which corresponds to a maximum of about 6 hits / mm^2 . To handle higher energies, or more aggressive collision parameters, the readout must limit sensitive time to 30 BXs. This constraint has been long appreciated, and is motivating the development of several new technologies for pixilated vertex detectors, including those being considered for SiD.

The hit densities from pairs in the forward vertex disks at their innermost radii match the densities in the barrel section of the detector, and the densities fall off with increasing radius. So the limits determined above for the barrel detector should apply also to the forward disks. In general, the radiation damage to detectors at the ILC is very modest compared to detectors at the LHC. For the vertex detector, the radiation dose arising from the pairs on layer 1 is about 10 kRADs/ year. Neutrons are especially damaging to silicon sensors. They are produced both in the beam dump, which is more than 400m distant, and in the beamcal, where roughly 100MRADs / year is deposited by the e^+e^- pairs, and which is only a few meters distant from the vertex detector. Neutrons produced in the EM showers at the beamcal produce the dominant flux at the VXD, integrating to about 5×10^8 n's / cm^2 / year. So it is essential that the vertex detector sensors not significantly degrade with a few 10's of kRADs of EM radiation, or neutron fluences near 10^9 / cm^2 / year. They must also endure exposure to sporadic doses of radiation, coming from errant beam particles showering in the IR.

Finally, the possibility has been raised that the high frequency RF pulse which accompanies passage of each beam could leak beyond the beampipe to produce electromagnetic interference (EMI) in the vertex detector readout, and limit data transmission to the times between trains. This would impose severe constraints on local data storage and the vertex detector readout. Hopefully tests now in the planning stages will determine if this problem is real or imagined.

1.5.3 Forward Tracker

Figure 1.4 shows the number of charged particles / BX which reach a maximum radius between R and $R + 2$ cm, as a function of radius R . It clearly shows that the charged backgrounds are appreciable only at the very small radii affecting the vertex detector and inner most sections of the forward tracking system. The SiD forward tracking is naturally divided into disks extending beyond 20 cm in radius, which are mostly immune from these high rates, and disks extending from small radii out to about 20 cm. The innermost radii of the forward tracking system for layers 1, 2, 3, and 4 are respectively, 4 cm, 5 cm, 6 cm, and 7 cm.

Figure 1.5 shows the density of hits in the forward tracker layer #1 from e^+e^- pairs, which dominate. At a radius of 4 cm, the hit density is about 0.045 hits / cm^2 / BX. For a radial microstrip channel of length 10 cm and width 50 microns, extending from a radius of 4 cm to 14 cm, this would correspond to an occupancy of about 7×10^{-4} / BX, or about 1.9 hits/ train in each channel, for nominal beam conditions. The occupancy is safely below the maximum allowable occupancy for pattern recognition (which we assume to be an about 0.01 / BX), but is large enough to require additional buffering (beyond the presently conceived 4

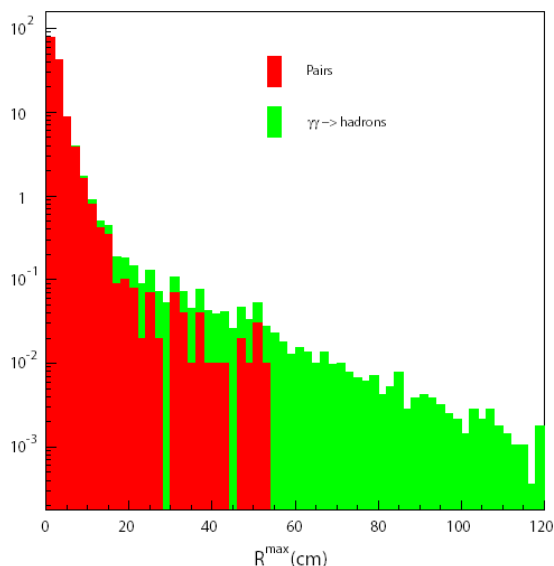


Figure 1.4: VXD Hits/mm²/train for Barrel Layer 1 for the various ILC beam parameter sets.

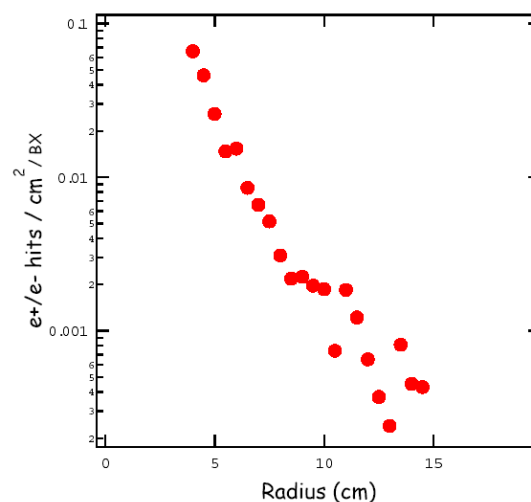


Figure 1.5: The number of charged particles / BX which reach a maximum radius between R and $R + 2$ cm, as a function of radius R , for nominal 500 GeV beam parameters. The e^+e^- pairs are shown in red; hadrons and muon pairs in green.

deep buffer) to maintain high efficiency, especially in the case of the higher energy and higher luminosity beam parameter sets. Microstrip detectors do have sufficiently low occupancies to operate in even the extreme forward tracking direction, although pixel detectors may make pattern recognition easier.

At larger radii in the forward tracker, two backgrounds are significant, charged tracks from $\gamma\gamma$ produced muon pairs and hadrons, and interactions of the ~ 1 MeV photons which were produced by pairs in the beamcal. Figure 13 shows the density of these photons hitting layer 1 of the forward tracker, which is roughly uniform over the entire layer 1 disk. Under nominal beam conditions at 500 GeV, between 0.5 and 1 photons hit / cm² / BX. Detailed Geant 3 simulations of the interactions of these photons in silicon, including the subsequent interactions of the Compton electrons produced, have shown that the total number of hits resulting in the microstrip detector is approximately 2% of the number of incident photons. Consequently, the photon flux accounts for 0.02 hits / cm² / BX in each detector layer, which corresponds to an occupancy of about 10^{-3} / BX in a radially oriented microstrip channel. The sum of the charged and neutral backgrounds in the forward tracking disks, would produce a maximum density of 0.065 hits / cm² / BX, equivalent to an occupancy of 3.3×10^{-3} / BX, still below the limit considered tolerable for pattern recognition, but without enough margin to handle the highest backgrounds expected with high luminosity running. The average number of hits per channel per train would be about 9, at least at the innermost radii. This would result in unacceptable efficiency losses unless the buffering depth were increased well beyond 4.

1.5.4 Barrel Tracker

In comparison with the forward tracker, the SiD barrel tracker background rates are benign. Even in the innermost layer, at radius 20 cm, the total rate of charged tracks from e^+e^- pairs, muon pairs, and hadrons, has dropped off to about 1.5 / BX over all of layer 1. The photon interactions dominate the background, but as Figure 1.6 shows, under nominal beam conditions, the photon density is less than 0.1 / cm^2 / BX in barrel layer 1, corresponding to 0.002 hits / cm^2 / BX (assuming microstrip channels 10 cm long and 50 microns wide), or an occupancy of 1×10^{-4} / BX. Background hits will pose no pattern recognition problem in the barrel tracker. In fact, studies of pattern recognition in the barrel tracker have shown that it is fully efficient for backgrounds that are even 200 times nominal (Ref. Sinev, Wagner). Since the average number of hits over an entire train per microstrip channel is just 0.3, a buffer depth of 4 is adequate. With other beam conditions, the photon rates could increase as much as 20 times. Pattern recognition efficiency would be unaffected, but additional buffering would be required to store the average of 6 hits / channel.

1.5.5 Electromagnetic Calorimeter

Backgrounds in the electromagnetic calorimeter arise from the $\sim\text{MeV}$ photons originating in the beamcal, and photons and occasional charged particles arising from $\gamma\gamma$ interactions. Muons produced upstream of the IP in collimators also contribute, but at an insignificant level. The electromagnetic calorimeter is highly segmented, with 30 layers of silicon pixel detectors, each with transverse pixel size about 4 mm, interspersed with tungsten absorber. Simulations have shown that the occupancy rate resulting from the sum of the backgrounds cited is at most 1×10^{-4} / BX. Noise is thus expected to be inconsequential in calorimetric pattern recognition, and the electronic buffer size is more than adequate to insure full efficiency.

1.5.6 Beamcal and Lumcal.

These calorimeters are both situated very near the beam line, in the vicinity where most of the energy of the e^+e^- pairs is intercepted. Consequently, high radiation doses must be tolerated for normal operation. Occupancies approach 100% / BX in many of the beamcal channels, and are high in the Lumcal as well. The ILC environment thus imposes severe requirements on radiation hardness and readout speed.

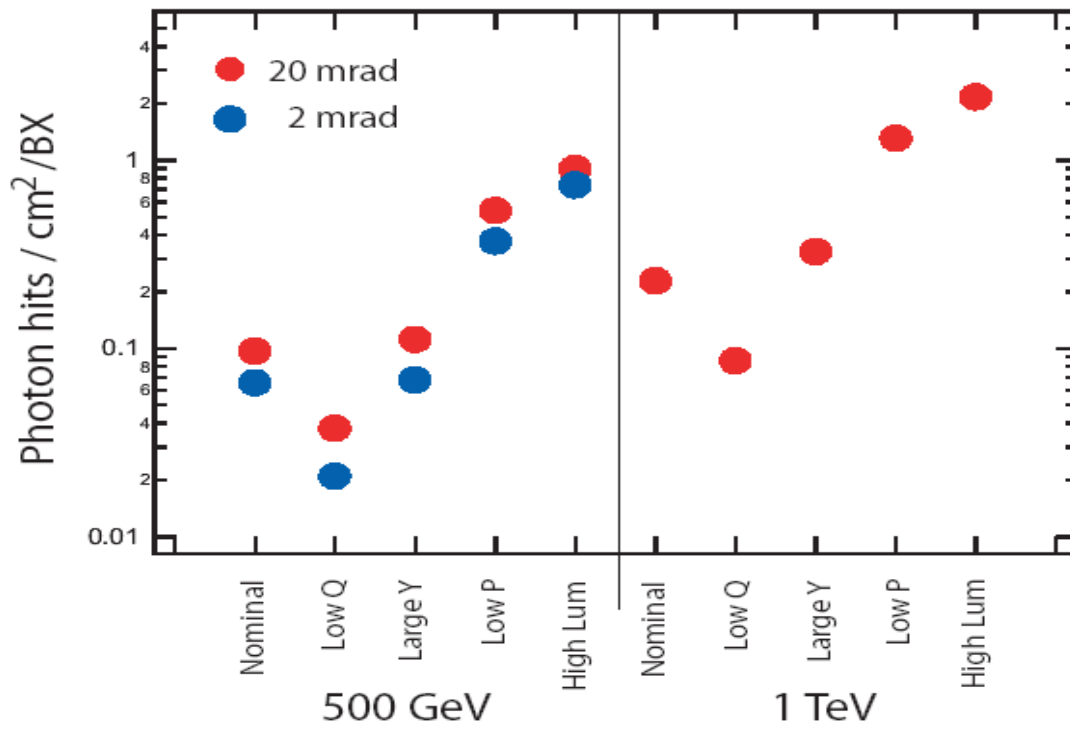


Figure 1.6: The density of electron and positron tracks / cm² / BX in Layer #1 of the forward tracker, as a function of the radius of the hit.

INTRODUCTION

References

- [1] G. Moortgat-Pick et al. The role of polarized positrons and electrons in revealing fundamental interactions at the linear collider. *Phys. Rept.*, 460:131–243, 2005.
- [2] N. Phinney, N. Toge and N. Walker Editors, *International Linear Collider Reference Design Report - Volume 3: Accelerator*, <http://www.linearcollider.org/cms/?pid=1000437> (2007).
- [3] Polarization and Energy technote 2009 for Dector LOIs, in progress.
- [4] *Parameters for the Linear Collider*, November 2006 Update.
- [5] B. Aurand et al., *Executive Summary of the Workshop on Polarisation and Beam Energy Measurement at the ILC*, DESY-08-099, ILC-NOTE-2008-047, SLAC-PUB-13296 (2008); Workshop website is <https://indico.desy.de/conferenceDisplay.py?confId=585>.

REFERENCES

Chapter 2

Subsystems

2.1 Vertex and Tracking System

2.1.1 Introduction

The tracking system of the SiD detector uses a barrel-disk layout. Five cylindrical layers of pixel detectors surround the interaction point, complemented by four disks of pixel sensors on either end. These inner layers are followed by a set of five barrels of silicon strip sensors in the central region, capped by four nested disks of silicon strip sensors at both ends. To provide uniform hit coverage, three disks with pixel sensors are provided in the transition region between the inner and outer disks in both the forward and backward region.

Within the SiD detector concept the tracking system is regarded as an integrated tracking system. Although individual detector components can be identified in the vertexing and tracking system, the overall design is driven by the combined performance of the pixel detector at small radius, the outer strip detector at large radius and the electromagnetic calorimeter for the identification of minimum ionizing track stubs. The physics at the ILC requires good track reconstruction and particle identification for a wide array of topologies. The main elements for the pattern recognition are the highly pixellated vertex detector and the low occupancy outer strip detector. Various strategies are employed to reconstruct particle tracks. One approach relies on identifying tracks in the vertex detector, where pattern recognition is simplified by the fact that precise three-dimensional information is available for each hit. Tracks found in the vertex detector are then propagated into the outer tracker, picking up additional hits and the track curvature is measured. Nevertheless, an important class of events, notably highly boosted b-quarks, will decay at radii that do not allow for pattern recognition in the vertex detector because there are either too few hits, or simply because the decay occurs outside the vertex detector. The tracks from these decays are reconstructed by a more general tracking algorithm using as seed any three hits in the tracking volume, either the outer tracker, the vertex detector or a combination of both. In a third class of events, tracks produced by the decay products of long-lived particles that decay outside the second or third layer of the outer tracker cannot possibly be reconstructed with a vertex detector-based pattern recognition or a stand-alone outer-tracker track finder. Obvious examples are long-lived particles such as K_s^0 's and Λ 's.

However, the detector should also be capable of detecting new physics signatures that would include long-lived exotic particles like those predicted by some gauge-mediated supersymmetry breaking scenarios. There are also issues of reconstructing kinked tracks produced by particles that lose a substantial portion of their energy in the tracker, as well as reconstructing backscatters from the calorimeter. The tracks from these event topologies are captured with a calorimeter-assisted tracking algorithm. This algorithm uses the electromagnetic calorimeter to provide seeds for pattern recognition in the tracker. The very fine segmentation of the EM calorimeter allows for detection of traces left by minimum ionizing particles. These can be used to determine the track entry point, direction, and sometimes curvature with a precision sufficient for extrapolating the track back into the tracker. This set of complementary algorithms provides for very robust pattern recognition and track finding and it is the performance of this integrated tracking system that determines the overall physics reach of the detector. In the next section the boundary conditions for operating an

integrated tracking system at the ILC will be presented. These will form the basis for the choice of design of the overall system, which will be discussed in the following section. The remainder will describe the details of the design, the implementation of the detector in the Monte Carlo simulations and some preliminary results. The R&D needed in the next few years will conclude this section.

2.1.2 Beam Environment

The bunch structure of the ILC, which consists of trains of 2820 bunches which are spaced 308 ns apart, repeated 5 times per second, and the physics and machine backgrounds resulting from bunch-bunch collisions, impose many constraints on ILC detector technologies and on the readout electronics. The two main backgrounds are backgrounds from the interaction point and machine backgrounds. Events contributing to the first category are

- disrupted primary beam
- beamstrahlung photons
- e^+e^- -pairs from beam-beam interactions
- radiative Bhabha events
- hadrons or muons from $\gamma\gamma$ interactions.

The second category is populated with events from

- direct beam losses
- beam-gas interactions
- collimator edge scattering
- synchrotron radiation
- neutron back-shine from the beam dump
- extraction line losses

Although these constraints are mild compared to those imposed on LHC detectors, the high flux of photons concomitant with the collisions, from virtual sources and beamstrahlung, results in the copious production of e^+e^- -pairs as well as the frequent production of muon pairs and hadronic interactions. The e^+e^- -pairs account for most of the background in the inner detectors, directly as charged tracks with low transverse momentum. They also cause a general flux of photons in the MeV energy range, which results when they shower in the beam calorimeters on the front face of the final quadrupoles. These photons, and the higher transverse momentum muons and charged and neutral hadrons which also result from photon-photon interactions, spray the entire detector with charged particles and photons.

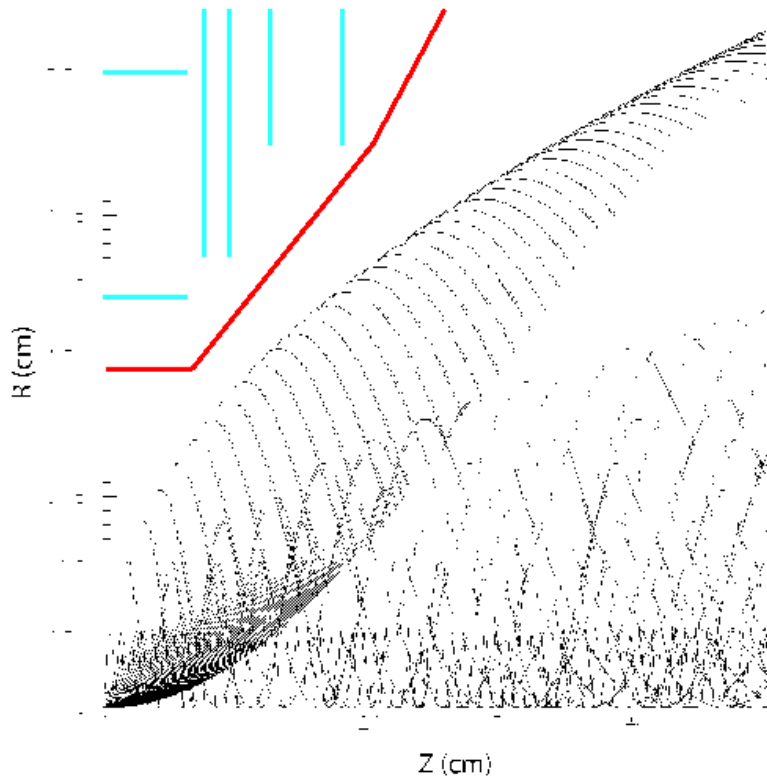


Figure 2.1: Maximum envelope of the e^+e^- -pair backgrounds in a 5 Tesla field. Indicated is the 12 mm radius beampipe.

As will be quantified in the following sections, SiD is largely immune to these backgrounds because the detector as a whole is only sensitive to backgrounds associated with a single bunch crossing. The pixel detector is assumed to have a bunch-by-bunch timestamp and a channel-by-channel buffer, which is 4 deep in the current design, will store hits over the course of the entire bunch train and record each responsible bunch crossing, for the silicon strip detector. Similarly for the electromagnetic calorimeter. Consequently, SiD is sensitive only to the physics and backgrounds of a single bunch crossing.

The effects of these backgrounds have been evaluated with the Guinea-Pig program. The nominal ILC beam parameters have been used for the simulation. The beamline magnets up to about 20 m from the interaction point have been included, using a beam crossing angle of 14 mrad . The nearest quadrupole magnet of the final doublet ends at 3.51 m. The detector solenoid field is 5 Tesla, and a field map instead of a constant field is used for the calculations of the beam backgrounds. The beam pipe through the central portion of the vertex detector has been taken to be all-beryllium. Within the barrel region of the vertex detector, the beryllium beam pipe has been taken to be a straight cylinder with inner radius of 1.2 cm and a wall thickness of 0.04 cm. At $z = \pm 6.25 \text{ cm}$, a transition is made to a conical beam pipe with a wall thickness of 0.07 cm. The half angle of the cone is 3.266° . Transitions from beryllium to stainless steel are made beyond the tracking volume, at approximately

$z = \pm 20.5$ cm. The initial stainless steel wall thickness is 0.107 cm; it increases to 0.15 cm at approximately $z = \pm 120$ cm. The half angle of the stainless steel cone is 5.329° . The inner profile of the beam pipe is dictated by the need to avoid the envelope of beam related backgrounds, as shown in Fig. 2.1. A titanium liner of thickness 0.0025 cm is included within the central beryllium portions of the beam pipe. The liner provides shielding against soft X -rays (> 10 keV). The titanium liner in the cone section of the beam pipe is expected to be a factor of 3 thicker than in the central region to take into account the incidence angle of back-scattered photons.

With these assumptions, the background in the tracking detector has been evaluated. The background hits in the vertex detector come predominantly from the e^+e^- pairs. The number of VXD hits in the first barrel layer of the vertex detector is expected to be nearly 80 hits/mm²/train over the full train for 500 GeV operations; at 1 TeV, in the high luminosity option, this number rises to about 400 hits/mm²/train. The charged backgrounds are appreciable only at the very small radii affecting the vertex detector and inner most sections of the forward tracking system. The hit densities from pairs in the forward vertex disks at their innermost radii match the densities in the barrel section of the detector, and the densities fall off with increasing radius. So the limits determined for the barrel detector should apply also to the forward disks. These boundary conditions, imposed by the machine, have led to the design described in the following section.

2.1.3 Vertex Detector Design

The vertex detector integrates with the outer tracker and remainder of the detector to provide significantly extended physics reach through superb vertex reconstruction – primary, secondary and tertiary. To date, all vertex detectors at collider experiment are silicon based, and the vertex detector for the SiD concept is no exception. The vertex detector consists of a central barrel section with five silicon pixel layers and forward and backward disk regions, each with four silicon pixel disks. Three silicon pixel disks at larger $|z|$ provide uniform coverage for the transition region between the vertex detector and the outer tracker. Barrel layers and disks are arranged to provide good hermeticity for $\cos\vartheta \leq 0.984$ and to guarantee good pattern recognition capability for charged tracking and excellent impact parameter resolution over the whole solid angle. A side-view of the vertex detector is shown in Fig. 2.2.

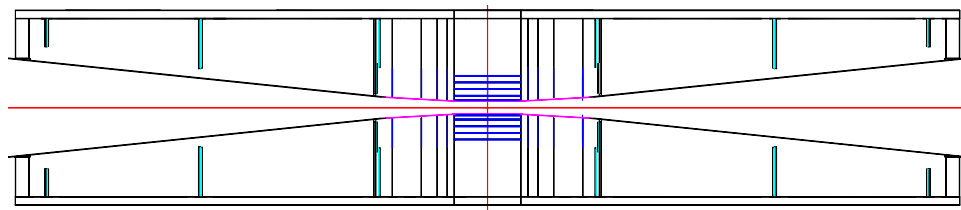


Figure 2.2: R-z view of the vertex detector and its support structure.

Vertex detectors are generally plagued by a mismatch in thermal expansion coefficients between the silicon and its support structures. Moreover, these supports in general add to the material budget in a region of physics phase space where it is least desired. To partially address those considerations, an ‘all-silicon’ structure is proposed for the vertex

detector barrel. In this context, ‘all-silicon’ means that sensors of each barrel layer are joined along their edges with adhesive to approximate an arc of a circular cylinder, and no other structural materials are present in that limited region. Thermal distortions are reduced by limiting material to that of the sensors themselves and adhesive, which has a low elastic modulus relative to silicon. Longitudinal deflection of a layer is controlled by the cylindrical shape, thereby minimizing additional material. The quasi-cylindrical shape of a layer is maintained by annular, flat rings at each end. In turn, the end rings are joined to one another and connected to an outer support cylinder via web-like support disks. Though various possibilities are still under consideration for the end ring and support disk material, we would like a material, such as carbon fiber laminate or silicon-based foam, which has a longer radiation length than that of silicon. Because other materials than silicon are used for external mechanical connections, the term ‘all-silicon’ is used with parentheses.

At this time, many sensor options remain under investigation and we have yet to choose a specific sensor technology. The candidates for sensor technology are discussed in the R&D section. The design presented here makes the assumption, independent of sensor technology, that fabrication and assembly of the detector occurs at room temperature and that the sensors are operated at a temperature > -10 °C. Because sensors are used as a structural element and other material has been minimized, our design favors relatively thick sensors. The sensor thickness has been taken to be $75\ \mu\text{m}$. Sensor cut width is 8.68 mm in the innermost layer and 12.58 mm in all other layers. The cut sensor length for all layers is 125 mm.

To allow assembly about the beam pipe and later servicing, all barrels, disks, and support elements of the vertex detector are split about approximately the horizontal plane into top and bottom sub-assemblies. Once mated, the two sub-assemblies are supported from the beam pipe and stiffen the portion of the beam pipe passing through them. Fig. 2.3 is an end view of the barrel region, showing the five silicon barrel layers and their end disk. The outer rings indicate the double-walled carbon fiber support tube. Since the silicon is very thin on the scale of this drawing, the layer arrangement of the individual sensors is shown in the right drawing in Fig. 2.3 for clarity.

The five layers are arranged at radii ranging from 14 to 60 mm. The vertex detector also has four disk layer sensors which are attached to carbon fiber support disks at z positions ranging from about 72 to 172 mm. The innermost disk covers radii from 14 mm out to 71 mm; the outermost, from 20 mm to 71 mm. Forward tracking continues beyond the vertex detector proper with three additional small pixel disks, extending in z from about 207 to 834 mm. Their inner radii range from 29 to about 117 mm, and their outer radius is about 166 mm.

To prevent bending of the small-radius portion of the beam pipe and ensure good stability of vertex detector position, the outer vertex detector support cylinder is coupled to the beam pipe at four longitudinal locations: ± 21.4 and ± 88.2 cm. Inner and outer support cylinder walls are 0.26 mm thick. They are made from four plies of high modulus carbon fiber resin pre-preg. Wall separation is 15 mm. We propose to deliver cooling air via the vertex detector outer support cylinder. To allow that, the two walls of the cylinder would be separated by radially-oriented ribs running the full cylinder length. Calculations assumed ribs at 60 azimuths. Openings, each approximately 12.2 mm x 15 mm, at 18 z -locations in the inner cylinder wall distribute flow to the various disk locations and to the barrel.

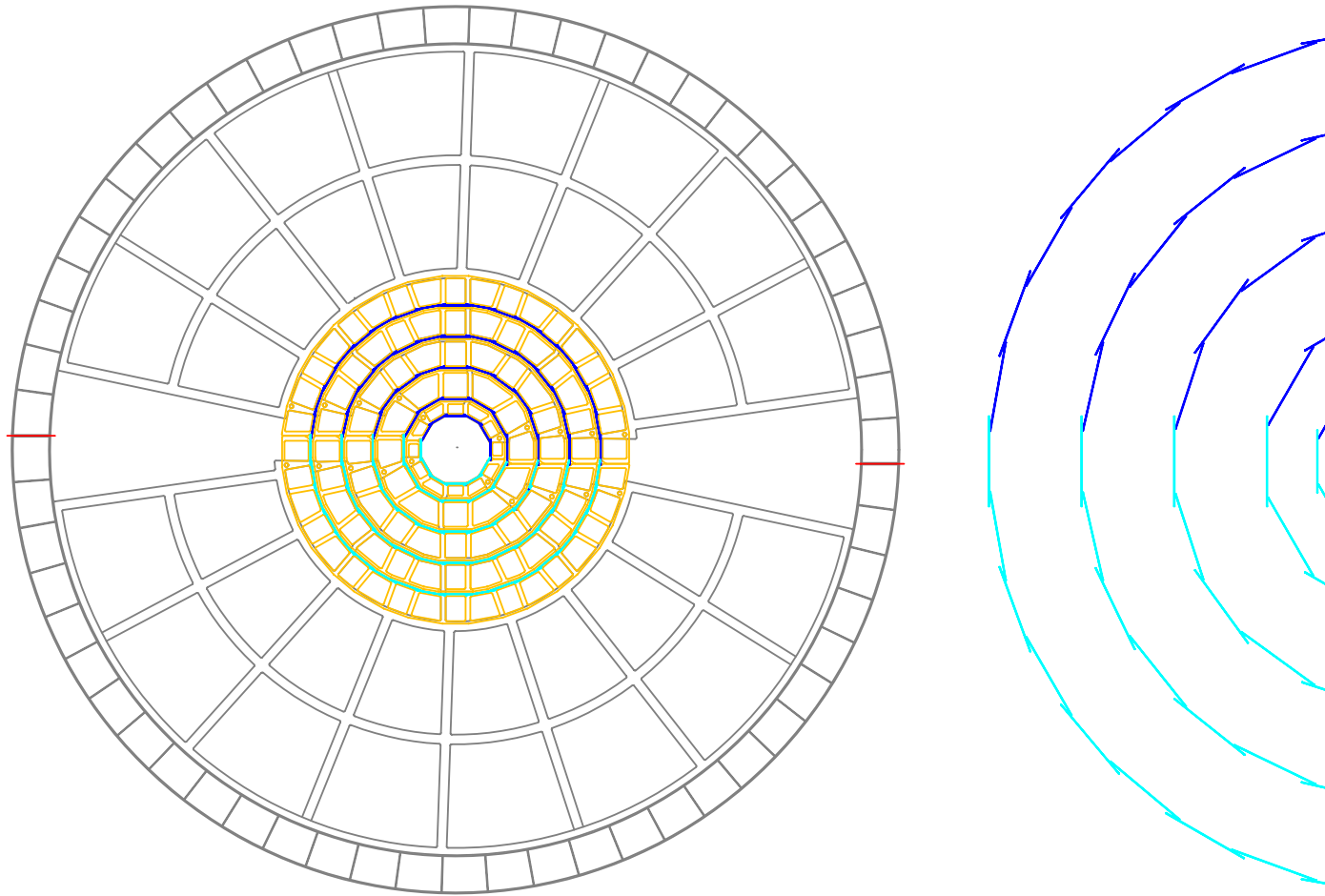


Figure 2.3: Barrel end view of the vertex detector (left) and layer arrangement of the silicon sensors only (right).

SUBSYSTEMS

For our initial investigation the flow for barrel cooling was assumed to be from one barrel end to the other. The average power dissipated in a sensor was taken to be $131 \mu\text{W}/\text{mm}^2$. That corresponds to a total power of 20 watts for the 5-layer barrel considered. These numbers presume power cycling, i.e., that most power is dissipated during the roughly 1 ms during which the beam train is present, and that power is turned off in the 199 ms between trains. We assumed that power is distributed uniformly over the sensor active surface and that both sensor surfaces participate in heat removal. Supply air temperature was taken to be -15°C . For a given sensor, power transferred inward through the carbon fiber cylinder was taken to be proportional to the surface contact between the sensor and carbon fiber. Thermal impedance through silicon, epoxy, and carbon fiber laminate has been included, but turns out not to be particularly significant. The remaining power was assumed to be transferred outward into the layer to layer gap. For flow and heat transfer calculations, the gap between barrel layers was taken to be 1 mm less than the nominal layer spacing. Laminar flow was assumed.

The cooling power was evaluated as a function of Reynold's number, which was required to be the same for all barrel gaps. To provide laminar flow and limit the likelihood of vibration, a maximum Reynold's number of 1800 was considered. Cooling with turbulent flow and acceptable stability of sensor positions may also be possible, but remains to be investigated.

As mentioned before, openings, each approximately 12.2 mm x 15 mm, are envisioned at 18 z-locations and 60 azimuths in the inner cylinder wall to distribute flow to the various disk locations and to the barrel. At each azimuth, the cell through which flow passes was approximated by a rectangle of height 15 mm and width 18.246 mm. The wall thickness was assumed to be 0.26 mm for both cylinders and for all ribs. The result was a Reynold's number of 3105 in the portion of the cell which sees full flow, which indicates flow will be turbulent. Since a portion of the flow exits the cell at each opening, the Reynold's number drops to 1725 at approximately $z = 51.9$ cm (a short distance inboard of the two outermost disks). While entrance effects may remain, flow should gradually become laminar after that point. Supply and return connections to the outside world remain to be fully evaluated.

The sensors of the outermost layer, where it is easier to provide cross-section for air flow, and sensors in the innermost layer, where we have assumed that the beam pipe includes thermal intercepts and will introduce no heat, are noticeably cooler than sensors of the three middle layers, rather independent of the flow. In the outermost layer, the cross section provided for air flow could be reduced to raise the temperature of that layer. In the gap between the innermost layer and the beam tube, flow is likely to be lower and temperature higher, once supply and return distribution patterns of air flow have been taken into account. Higher flow rate clearly improves the uniformity of sensor temperatures end to end and reduces the difference between the temperature of a sensor and the cooling air. All flow rates which have been considered, lead to temperature variations which should be acceptable for dimensional stability, which is crucial for high precision vertexing. The time-dependent effects of power cycling remain to be investigated. Those depend on the thermal mass presented by the barrels and the details of the way in which power is cycled. External heat input to the barrel has been assumed to be negligible. Satisfying that assumption will require reasonable care in designing cables, in providing heat intercepts should they be needed, and in providing an external thermal enclosure. The outer support cylinder of the vertex

detector offers a natural thermal enclosure. Details of end openings in barrel membranes remain to be included. Those openings provide a natural mechanism for adjusting relative flow between barrel layers. A membrane between the outermost barrel layer and the vertex chamber support cylinder would ensure that flow does not excessively bypass the barrel-to-barrel gaps.

Similar calculations have been made to understand disk cooling. Those calculations are based upon barrel results with a Reynold's number of 1800 (barrel flow = 20 g/s). Disk power dissipation is dependent upon the sensor technology chosen, and that choice remains to be made. At each end of the barrel region, the first four disks have been assumed to employ pixel sensors. For heat removal calculations, they have been assumed to dissipate the same power per unit area as the pixel sensors of the barrels. The result is a total power of 16.9 Watts for all eight disks and an air flow of 16.4 g/s.

For the next three disks outboard at each end the sensors were treated as silicon pixels with $\frac{1}{4}$ the power dissipation per unit area as that of barrel pixels; that assumes pixels which are twice as large. The result was a total power of 13.25 Watts for all six disks and an air flow of 12.8 g/s. The total required flow is the sum of that for the barrel, inner disks and outer disks, that is, 48.65 g/s. To take into account warming of air and to allow a small margin, flow calculations assumed an air temperature of -20°C and a flow rate of 50 g/s.

The readout scheme for the SiD vertex detector is closely coupled to the sensor technology. Any technology will be required to adequately address hit occupancies, so that pattern recognition is not overwhelmed by background. Ideally the readout will associate hits with single beam crossings. The column-parallel CCD, DEPFET, and many MAPs-based readout schemes utilize a rolling shutter during the bunch train. In this scheme the detector frame is completely read out multiple times during the bunch train, with the effective time resolution equivalent to the frame readout time. The ISIS technology and some MAPS-based designs use in-pixel storage of multiple analog samples, with full readout between trains. The Chronopixel design stores analog pulse heights and digital and/or analog time stamps in the pixel, also with readout between trains.

The vertex detector readout is illustrated using the scheme with in-pixel storage of analog information and digital time stamps used in the 3D-VIP chip. In this scheme analog and digital information is stored within a pixel during the bunch train and read out between trains. Pixel complexity is minimized by storing address information on the periphery of the chip. Table 2.1 summarizes the power consumption of this readout scheme. Electrical connections of about one meter from the ladders to optical links installed on the support tube have been assumed. Assuming 32 bits are used per hit and 100 pF interconnect capacitance at 1.5 V, the local readout consumes 0.24 Watts of average power. If each of the 108 ladders is independently driven with a 200 MHz clock speed, the inner layers would dominate the readout time at 75 ms/ladder. The peak power at the start of readout, with all layers reading at 200 MHz, is 4.8 Watts. This could be reduced to 1.3 Watts if the outer layers are clocked more slowly to match the 75 ms inner layer readout time, or to a value close to the average power if the clock rate on each layer is tuned to match the data load. The bit rate from the entire vertex detector is about 2 Gbits/sec.

The power delivery is expected to be a major source of material contribution. The

Layer	Number of ladders	hits/crossing	hits/train	bits/train	Readout time (ms)
Layer 1	12	2000	$5.6 \cdot 10^6$	$1.8 \cdot 10^8$	75
Layer 2	12	1200	$3.4 \cdot 10^6$	$1.1 \cdot 10^8$	45
Layer 3	20	800	$2.3 \cdot 10^6$	$7.2 \cdot 10^7$	18
Layer 4	28	450	$1.3 \cdot 10^6$	$4.1 \cdot 10^7$	7.3
Layer 5	36	400	$1.1 \cdot 10^6$	$3.6 \cdot 10^7$	5.0

Table 2.1: Readout rates for the vertex detector assuming 3D-VIP readout scheme.

instantaneous power of many of the sensor technologies could be 50W or more per sensor. One naive scheme is to deliver power through short copper wires with e.g. $300\mu\text{m}$ diameter to each sensor and use DC-DC conversion on the vertex detector support cylinder from a higher supply voltage. There are concerns with regard to the mechanical force on these wires with high current in the magnetic field in this naive scheme if the currents do not run parallel to the magnetic field. A low mass local DC-DC conversion near the sensors with higher incoming voltage would be more favorable in many respects if it can be realized. An extension of the radiation hard optical transmission technology used for LHC detectors could be foreseen as the means of control and data transmission. The material from the thin fibers are expected to be significantly less than the material involved in power delivery. However, the major issue for both power delivery and signal transmission is the connection to the thin sensors. The miniaturization of the connectors and the transceivers will be key R&D projects to ensure the material minimization. For simulation purposes the readout section at each end of a sensor is assumed to be a 2mm tall and 5mm long block spanning the full width of the sensors with same radiation length as G10. The number of radiation lengths represented by vertex detector structures, averaged over φ in most cases, is given in Fig. 2.10.

During silicon servicing, the vertex detector and beam pipe remain fixed while the outer silicon tracker rolls longitudinally (see Fig. 2.4). To allow that motion, to allow the outer silicon tracker elements to be at the lowest possible radius, and to leave space for any additional thermal insulation which might be needed, the outer radius of the vertex detector, including its support structures, has been limited to 18.5 cm. To maximize physics potential, the inner radius of vertex detector elements has been chosen to be as small as practical consistent with beam-related backgrounds and the beam pipe profile. In the barrel region, the minimum radius to a sensor surface is 1.4 cm, governed by the beam backgrounds as discussed earlier.

The vertex detector hit pattern and material sum as a function of polar angle is shown in Fig. 2.5. The irregular features of the readout and service contributions are due to the blocks at the end of the sensors. Most of the readout material are beyond the first few layers of the vertex detector hits so that their influence on the impact parameter resolution are limited. The fact that the effective readout and service material integrates to comparable amount as sensors or mechanical support, calls for close attention in the realization of low mass design for power delivery and signal transmission. If the readout and service material can indeed meet what is in the current model, the material balance would be more favorable for considerable

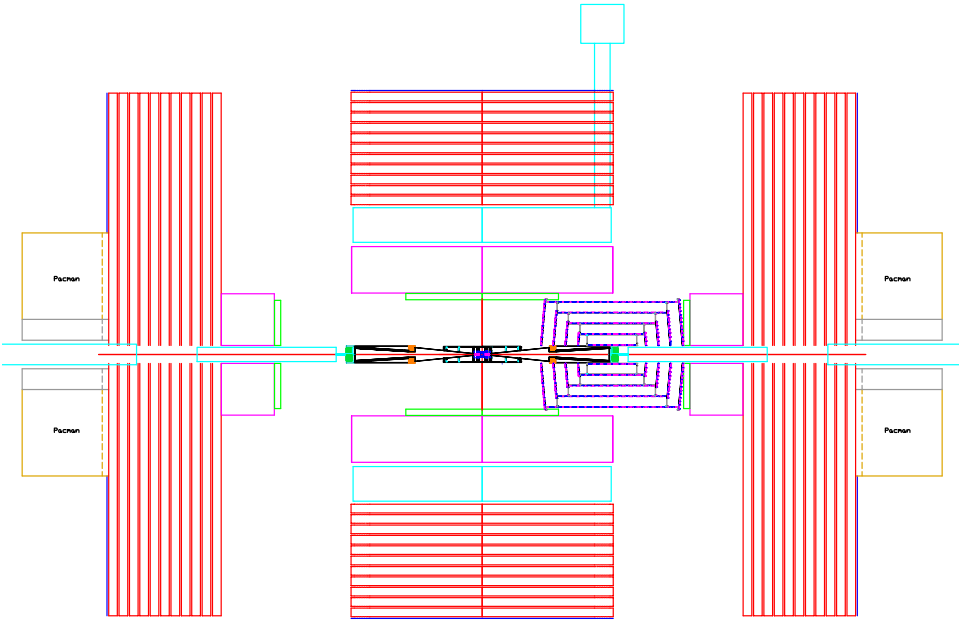


Figure 2.4: Tracker in the open position for servicing of the vertex detector.

portion of the endcap region compared to the $1/\sin\vartheta$ growth for a long barrel geometry. With this material balance, the benefit of the endcap geometry in spatial resolution with a better track entrance angle and smaller radial alignment effect, is a meaningful advantage. Table 2.2 summarizes the main parameters of the vertex detector.

2.1.4 Tracker Design

The ILC experiments demand tracking systems unlike any previously envisioned. In addition to efficient and robust track-finding, the momentum resolution required to enable precision physics at ILC energies must improve significantly upon that of previous trackers. The design must minimize material in front of the calorimeter that might endanger particle-flow jet reconstruction. Even with the largest feasible magnetic field, the tracking volume is quite large so that tracker components must be relatively inexpensive and easily mass-produced. Finally, the tracker must be robust against beam-related accidents and aging. These requirements have led to the choice of silicon microstrip detectors for the tracker. The outer silicon tracker design consists of five nested barrels in the central region and four cones in each of the end regions. The support material of disks follows a conical surface with an angle of 5-degrees with respect to the normal to the beamline. Sensors of disk modules are normal to the beam line. The barrel supports are continuous cylinders formed from a sandwich of pre-impregnated carbonfiber composite around a Rohacell core. The support cones are also double-walled carbonfiber structures around a Rohacell core. Each support cone is supported off a barrel. Spoked annular rings support the ends of each barrel cylinder from the inner surface of the next barrel out. It is expected that openings will be cut in the support structures to reduce material, once module mounting locations are known. These openings not only reduce the number of radiation lengths, but also reduce the weight to be

Barrel Region	R (mm)	Length (cm)	Number of sensors in φ
Layer 1	14	125	12
Layer 2	21	125	12
Layer 3	34	125	20
Layer 4	47	125	28
Layer 5	60	125	36
Disk	R_{inner}	R_{outer}	z_{center}
Disk 1	15	75	76
Disk 2	16	75	95
Disk 3	18	75	125
Disk 4	21	75	180
Forward Disk	R_{inner}	R_{outer}	z_{center}
Disk 1	28	166	211
Disk 2	76	166	543
Disk 3	118	166	834

Table 2.2: Parameters of the vertex detector. Units are mm.

supported. Openings may also be needed for an optical alignment system. It is envisioned that the electronics and power cables that supply entire segments of the detector are mounted on these spoked rings. The dimensions of the barrels and cones are given in Table 2.3. Fig. 2.6 shows an elevation view of the tracking system.

Because of the very low occupancies in the outer barrel, the nominal design for the outer tracker employs only axial readout in the barrel region. In the baseline design, the barrels are covered with silicon modules. Modules are comprised of a carbon fiber composite frame with rohacell/epoxy cross bracing and have one single-sided silicon sensor bonded to the outer surface. Sensors are obtained from one single 6-inch wafer and are approximately $10\text{ cm} \times 10\text{ cm}$. This size sets the longitudinal readout segmentation of the barrel detectors. The sensors are $300\mu\text{m}$ thick with a strip pitch of $50\mu\text{m}$ with intermediate strips. Full coverage is obtained by ensuring small overlap both longitudinally and azimuthally. Azimuthal overlap is obtained by slightly tilting the sensors. The angle by which the sensor is tilted partially compensates for the Lorentz angle of the collected charge in the 5T field of the solenoid. Longitudinal overlap is obtained by placing alternate sensors at slightly different radii. Fig. 2.7 shows a detail of the overlap in the z and $R\varphi$ direction, respectively.

Modules are attached to the cylinder using a PEEK mounting clip. The readout chips and cables are mounted directly to the outer surface of the silicon sensors. The cables supply power and control to the readout chip from electronics located at the ends of the barrel.

Fig. 2.8 shows an $R\varphi$ -view of the barrel region. The outermost disk is projected onto

the barrel layout in this figure. For pattern recognition, the disks will provide 3d-space points. The current design has two single-sided wedge detectors back-to-back, with strips at $\pm 6^\circ$ with respect to the long axis of the wedge for a stereo angle of 12° . Two types of sensors are needed to tile the disks, one type at the inner radii and a second sensor type to populate the area at the outer radii. Also in the forward region sensors will be $300\mu\text{m}$ thick with intermediate strips. The conical support disk design (“lampshade design”) provides an elegant way to implement module overlaps, eliminating any dead areas, and allows for easy module mounting and cable routing. Fig. 2.9 shows a side view of modules mounted on a disk. The support disks have penetrations for cable routing. In this scheme all cable are routed on the inner surface of the disks.

The inner radius of the outer tracker is set by forward, beam-monitoring calorimetry and beamline elements, over which the tracker is intended to slide. Once the tracker inner radius is set, the outer radius of vertex detector structures follows. During servicing, the vertex detector and beam pipe remain fixed while the outer silicon tracker rolls longitudinally, as shown in Figure 2.4. To allow that motion, no element from the outer tracker can be at a radius smaller than the radius of the vertex detector outer support cylinder. To allow for good acceptance and pattern recognition, the small angle region is covered by three small silicon disks at each end with radius below 20cm, which has been described in the section on the mechanical layout of the vertex detector. Figure 2.10 shows the cumulative amount of material as function of polar angle as modeled in the Monte Carlo. The lowest curve shows the contribution from the beampipe and the readout for the vertex detector. The material corresponding to the various readout elements has conservatively been assumed to be uniformly distributed in the tracker volume. The following two curves indicate the additional material due to the active vertex detector elements and the supports, respectively. The outer curve gives the amount of material of the tracker as a whole, that is, the sum of the vertex detector and the outer tracker and anticipated dead material in the tracking volume. Overall a material budget of about $0.8\% X_0$ per layer is achieved for the outer tracker. Table 2.3 lists some of the parameters of the tracker for the current design. There are 8130 modules in the barrel region and 2848 modules for the end regions combined.

2.1.5 Tracker Module Design

To build a large volume silicon tracker within an acceptable material budget is quite challenging. The scale of the project puts a premium on minimizing the number of different components and achieving a modular construction process, while at the same time limiting the mass budget of the overall system. To achieve this goal, the design of the SiD tracker employs silicon modules with novel characteristics.

A module is the most elementary working component of the SiD tracker. Each module has a single sensor; square sensors in the barrel region and wedge shaped sensors in the end regions. In the barrel region, each sensor is read out with a pair of 1024-channel readout chips, called the kPix chip. A short Kapton readout cable provides power and control signals to the readout chips and carries the signals to the edge of the module where they are transmitted to a longer bus cable which takes the signals to the end of the tracker volume. There is no hybrid circuit board in this design nor mechanical cooling path since gas flow can provide

Barrel Region	$\langle R \rangle$ (cm)	Length of sensor coverage (cm)	Number of modules in φ	Number of modules in z
Barrel 1	21.95	111.6	20	13
Barrel 2	46.95	147.3	38	17
Barrel 3	71.95	200.1	58	23
Barrel 4	96.95	251.8	80	29
Barrel 5	121.95	304.5	102	35
Disk Region	z_{inner} (cm)	R_{inner} (cm)	R_{outer} (cm)	Number of modules per end
Disk 1	78.89	20.89	49.80	96
Disk 2	107.50	20.89	75.14	238
Disk 3	135.55	20.89	100.31	428
Disk 4	164.09	20.89	125.36	662

Table 2.3: Parameters of the tracking detector.

the required cooling.

The sensors for the SiD tracker (see Fig. 2.11) are square, 9.53 cm on a side, 300 μm thick, $\langle 100 \rangle$, single-sided, double-metal, p^+ -on- n sensors with 25 μm sense pitch and 50 μm readout pitch. This floating-strip design provides the best possible single-hit resolution for a reasonable channel count as long as the signal-to-noise ratio remains large. This motivates the use of short readout strips to reduce capacitance. The sensors are AC-coupled with poly-silicon bias resistors. The two readout chips are bump-bonded directly to the face of the sensor in the barrel region and the readout strips of the sensor connect to the bonding array via double-metal traces (see Figure 6). Fig. 2.12 shows a detail of the double-metal routing of the traces for one half of the sensor to one of the two readout chips. The pads for bump-bonding to the readout chip are $70 \times 70 \mu\text{m}^2$, with a 200 by 500 μm pitch. A necessary complication of this scheme is that the power, control and readout signals of the kPix chip must also be routed to a bonding array for the readout cable on the double-metal layer. This array is visible to the right of the bump-bonding array in Fig. 2.12. A reduced set of specifications for prototype barrel sensors is given Table 2.4.

The central component of the readout architecture proposed for the SiD tracker is the 1024-channel KPiX readout chip. The KPiX chip is designed for pulsed power, starving the power-hungry front end for current between bunch trains. This reduces the power consumption to 20 mW on average for a 1024-channel KPiX chip, or 40 mW for a single-sided module. The chip has four time-stamped analog buffers per channel that store signals from the detector until the inter-train period for digitization and readout. As a result, the only digital activities on KPiX during the bunch train are a synchronous LVDS clock and individual comparators firing when a channel crosses the readout thresholds. This low-noise mode of operation during the bunch train allows KPiX to be mounted directly to the sensor without inducing large RF pickup on the strips.

Parameter	Value
Overall Dimensions	$93.531 \times 93.531 \text{ mm}^2$
Active Area	$92.031 \times 92.031 \text{ mm}^2$
Strip pitch	$25 \mu\text{m}$
Readout pitch	$50 \mu\text{m}$
Number of strips	3679
Number of readout strips	1840
Depletion voltage	$< 100\text{V}$
Biasing scheme	R_{poly}
Poly resistor value	$20\text{-}40\text{M}\Omega$
Implant strip width	$8 \text{ to } 9 \mu\text{m}$
Width of Al sense strips	$8 \text{ to } 9 \mu\text{m}$
Width of double-metal readout traces	$3 \text{ to } 4 \mu\text{m}$
Resistivity of Al sense strips	$< 25\Omega/\text{cm}$
Resistivity of double-metal readout traces	$< 60\Omega/\text{cm}$
Insulation thickness between metal layers	$0.9 \mu\text{m}$
Coupling capacitor value	$> 10 \text{ pf}/\text{cm}$
Passivation (except bonding areas)	SiO_2 , $0.5\text{-}1.0\mu\text{m}$ thick
Width of unpassivated regions on bias ring	$\geq 200\mu\text{m}$
Junction breakdown	$> 200 \text{ V}$
Micro-discharge breakdown	$> 150 \text{ V}$
Coupling capacitor breakdown	$> 100 \text{ V}$
Total detector current at 150V	$< 4\mu\text{A}$
Interstrip capacitance	$< 1.2 \text{ pf}/\text{cm}$

Table 2.4: Specifications for some of the SiD sensor parameters.

A low mass readout cable, called a “pigtail”, is glued to the module and connects the module to a two-meter long extension cable which connects to concentrator boards at the end of the barrels. The cable includes two pairs of traces each for analog and digital power, sixteen traces (eight per KPjX readout chip) for digital control and readout, along with one pair for sensor bias. The pigtail cable has a pair of tabs near the sensor edge for connection of the sensor bias as well as surface mount pads for bias and power filtering, and for LVDS signal termination resistors. Since this cable glues directly to the surface of the sensor, pickup and crosstalk on the underlying strips must be well controlled.

The low-mass readout cable connects tracker modules to a bus cable which runs along the length of the barrel and transmits the signals from all modules in one $R - \varphi$ -sector to a concentrator board mounted at the end of the barrel.

An important issue is control of the material budget for the modules. The support frame of a module is composed of a pair of thin, high-modulus carbon-fiber skins sandwiched around a Rohecell core. The frame has injection-molded carbon-filled Torlon strips on two edges into which precision silicon-nitride balls are molded, providing a kinematic, three-point mount. Mounting clips are used to place the module on the support structure. They are manufactured in the same way and include custom silicon nitride mating parts for the mounting balls of the support frame. The current barrel module design represents roughly 0.5% X_0 per unit coverage including longer readout cables needed to connect the pigtailed to the power and readout distribution boards mounted on the support rings at the ends of the barrels. Although a detailed design for the forward modules awaits further simulation study, it is presumed that forward modules will be of similar design. Fig. 2.13 shows a sketch of a barrel module.

2.1.6 Simulation Infrastructure

The vertex detector and tracker designs have been incorporated in the compact xml detector description that drives our simulation studies. This detector description serves as an input both to slic, the GEANT4-based detector simulation used by SiD, as well as the event reconstruction software.

The current detector description includes both the active sensing elements, as well as our estimates of the dead material required to provide mechanical support, beam tube, readout electronics, and required services (including power and cooling). For the tracking studies reported here, the barrel sensors have been approximated by thin cylinders, while the disk sensors have been approximated by planar disks perpendicular to the beamline. The dead material is modeled as a cylinder, planar disk, or cone as appropriate. Fig. 2.14 shows an x-y quarter view of the tracking system as implemented in this simplified geometry. Fig. 2.10 shows a plot of the material, expressed as a fraction of a radiation length (X/X_0), as a function of the polar angle. This model has been used to simulate the detector response for the large number of events generated for the physics benchmarking. Further details of the detector model are, therefore, presented in that section.

We have also developed a fully detailed tracker description that closely matches the engineering designs. It incorporates each individual sensor as a planar device with its mounting hardware. The fully segmented tracker description provides a highly realistic model of the tracker geometry, allowing us to study the effects of sensor overlaps and gaps, sensor mis-alignment, support material and more generally improve the precision of our detector modeling. Having the complete geometry fully defined and configurable at runtime (using a plain-text file), and immediately available to the reconstruction software, provides enormous flexibility to the design and optimization process.

Figs. 2.15 and 2.16 show the sensor layout for the fully segmented vertex detector and the sensor layout and support barrels for the central region of the fully segmented tracker description, respectively, as

extracted from the GEANT4 description.

We do not include the individual pixels and strips in the Geant simulation, preferring to defer this to the reconstruction stage. Instead, we store the full Monte Carlo information about the particle's interaction with the sensitive sensor material (e.g. track ID, deposited energy, time, position). Hit digitization is the process of transforming these GEANT energy deposits into strip and pixel charge depositions, and then clustering these charge depositions to form tracker hits. This allows us to study different readout configurations without the overhead of having to rerun the full simulation. A number of digitization packages have been developed and are described in the following sections.

2.1.7 Vertex Detector Hit Digitization

Although no baseline sensor technology has been established for the vertex detector, two vertex detector sensor simulation algorithms are currently implemented. The first one is based on a CCD simulation from SLD and is used in the simulation studies described here, which employs a cylindrical geometry. The second simulation package is more detailed and was developed for a more realistic planar geometry.

The main process to be simulated in a CCD is the diffusion of the charge from a charged particle track. In a CCD the larger part of the active layer is not depleted. That is, there is no electrical field in that part of the sensor and the charge collection occurs because of a slow diffusion of the charge into the CCD channel. In this case transverse diffusion has the same scale as the un-depleted layer thickness. To simulate the diffusion, a Gaussian distribution of the probability of an electron, generated at some point deep in the active layer, to reach the collection point a certain distance away from the projection of the generation point was assumed. The width of this distribution is proportional to the depth of the generation point. To be more precise, the model assumes two Gaussian distributions. The first one is for electrons that diffuse directly towards the CCD channel. The second distribution is for electrons reflected at the epitaxial layer, the substrate boundary, where there is a potential barrier. An important role in the performance of a tracking detector is played by the generation of the δ -electrons, that is, large energy transfer by the ionizing particle to a single electron. This effect has been simulated by assuming that the energy loss in the tail of the Landau distribution is due to such δ -electrons. The width of the Landau distribution is simulated according to an empirical formula, which is in good agreement with experiment to thicknesses as small as about $10\mu\text{m}$ of silicon. The simulation package also includes special functions for simulating low-energy electrons, such as Compton electrons generated by photons.

Apart from the physics effects in the silicon detector, its performance is affected by the noise level of the readout electronics and the parameters of the signal digitization. All these effects have been simulated. This package does have its limitations, however, and was not designed for detailed studies of sensor effects. For example, it does not take into account specific effects in the energy loss in very thin layers ($\approx 1\mu\text{m}$). This effect as well as full simulation of diffusion and drift of charge carriers in any configuration of electric and magnetic fields inside the sensors are taken into account in second simulation package, which is described below.

The CCD simulation package starts with an initialization procedure that defines the CCD simulation parameters and geometry. At that time lookup tables are generated for the simulation of electron diffusion. The actual movement of each electron is not simulated in this package. Rather precalculated density functions for the distribution of electrons generated at a given depth inside the active layer are used. The next step in the simulation includes processing of every hit in the CCD detector. For every such hit, first the CCD and the pixel in the CCD is found where the hit is located. The CCD active layer is then divided into thin sublayers and the energy deposition in every sublayer is simulated. If the energy deposition in any sublayer is in the tail of the Landau distribution, the generation of a δ -electron is assumed. The charge is propagated to the CCD surface according to the diffusion density functions, and charge signals in the central pixel, as well as in neighboring ones are found. The electronics noise is then added, and the ADC digitization algorithm is applied. The resulting ADC outputs for all pixels in the CCD are fed to the cluster finding routine, which finds clusters of pixels and the coordinates of their centers. Different algorithms may be used for coordinate finding. For the current studies a charge weighted average clustering algorithm is used. It should be noted that, although the name of the package implies simulation of CCDs, the package is rather versatile. By changing the parameters of the simulated sensor and by setting appropriate depletion depth and bias voltage, other types of silicon sensors can be simulated.

In a second, more detailed simulation package, the parameterization of the diffusion and the approximation of the Landau distribution has been eliminated. This package simulates every ionizing collision of a relativistic charged particle travelling through the sensitive layer of silicon. Algorithms and functions, developed by Hans Bichsel, were used to simulate interaction points and the energy losses of such collisions. If the energy loss exceeds a few keV, the generation of a δ -electron is assumed. If it is not a δ -electron, all electron-hole pairs generated in this collision are assumed to originate at the collision point. If it is a δ -electron, a random vector is generated for its direction and the path length of its trace is taken from a range table for low energy electrons in silicon. For each electron or hole, depending of the type of signal generating carriers in the given sensor, the drift and diffusion in the sensor volume is simulated. Electric and magnetic maps are used to simulate the path of each single carrier. The sensor geometry description defines the regions where carriers are collected. These simulation studies not only provide the signal amplitude in each pixel, but also the signal shape and time of the charge collection.

Detailed simulation takes a lot of computing resources. To enable physics benchmark studies, lookup tables are used, which tabulate the probability for each pixel to collect charge as function of the impact point inside the pixel under consideration or in a neighboring pixels. When using lookup tables, the timing of the charge collection is also simulated, though it is less accurate than in the case of the detailed simulation of carriers propagation. In addition to the probabilities of the carriers generated at a given space point to be collected by given pixel, the average time of such collection is also tabulated. This information can then be used at a later stage to generate the distribution of arrival time for carriers from given point inside a pixel. The shape of the distribution may change, however, depending on the electric field map and a correction may need to be applied based on the detailed simulation.

In addition to digitizing real particle hits, the simulation package also provides the possibility to generate fake hits from the electronics noise. Signal processing for different

technologies may be different and the simulation can use amplitude and time information as appropriate.

2.1.8 Tracker Hit Digitization

Missing

2.1.9 Track Reconstruction

The SiD detector concept has adopted a nested barrel-disk geometry for both the vertex and tracking detector based on silicon technology. This permits hermetic, uniform coverage with a uniform material distribution. Particles originating from the interaction point typically generate at least 10 hits in the tracker, while angular coverage for tracking extends to $|\cos\vartheta| < 0.99$. The transition from cylindrical to disk geometry was designed to provide reasonably uniform tracking performance for all incident track angles. The selection of silicon as the tracking technology optimizes the detector hit resolution, two-track separation and tags the specific beam bunch the hit is associated with. Optimizing the performance of an all-silicon tracker within the requirements placed on the material budget naturally leads to a design where charged particles leave a relatively modest number of precisely located hits. Demonstrating adequate pattern recognition in this configuration is critical.

The standard pattern recognition algorithm developed by SiD is designed to efficiently find tracks using pixel and strip hits in the tracker. The pattern recognition algorithm treats the tracker as a single integrated device that is “agnostic” as to the origin of the hits (pixel or strip, barrel or endcap). This approach provides uniform pattern recognition throughout the tracking volume, effortlessly handling transitions between the different parts of the detector. Typically, 6-7 hits are sufficient for finding a track, which allows the standard pattern recognition algorithm to efficiently track particles originating near the interaction point with $p_T > 200$ MeV.

Since pattern recognition is of utmost importance in a sparse hit environment, additional track finding algorithms are explored. Of particular note is the calorimeter assisted track finder, which uses the tracking capability of the electromagnetic calorimeter to associate hits in the outer tracker with calorimeter “track stubs”. Calorimeter assisted tracking is particularly well suited to reconstructing tracks that originate outside the vertex detector, as often occurs in K_s and Λ decays.

Both the standard pattern recognition and calorimeter assisted tracking algorithms are described below.

2.1.9.1 Standard Pattern Recognition Algorithm

The standard pattern recognition algorithm is explicitly designed for the task of optimizing the design of an all-silicon tracker. Variations in tracker geometry and layout can be easily

studied with no change to the software. Since the algorithm bases all decisions on a global χ^2 , there are no internal parameters that need to be tuned. A high level of user control over the tracking “strategies” is available if desired, but more typically a “strategy builder” tool is used to automate the process of developing an optimized set of strategies for a given detector configuration.

The first step in track finding is to convert the digitized hits into a common hit format. This format encapsulates all the information needed by the standard pattern recognition algorithm, while insulating the track finding from differences and changes in the digitization algorithms.

Three types of hits are supported: pixel hits that have two measured coordinates, axial strip hits that have one measured coordinate and one bounded coordinate, and stereo hits formed from a pair of strip hits. The pixel and stereo hits may be associated with either barrel or disk geometries, while the axial strip hits have the bounded coordinate parallel to the beam axis and are intrinsically associated with barrel geometries. One further limitation is placed on stereo hits: the two strip sensors must be parallel to each other.

Track finding is controlled by a set of strategies. A strategy consists of the list of detector layers to be used, the role of each layer (seed, confirm, or extend), kinematic constraints (p_T , impact parameters), requirements on the number of hits, and the χ^2 cut. Multiple strategies can be processed by the track finding algorithm, and the resulting tracks is the collection of all distinct tracks found. The set of strategies is contained in an *xml* file that is easily understood and can be viewed/edited with a text editor.

The track finding algorithm is exhaustive in the sense that all combinations of hits that could potentially lead to a successful track fit are considered. The algorithm proceeds in four steps:

1. The first step is to form a 3-hit track seed candidate by taking all 3-hit combinations possible among the 3 seed layers. A helix fit is performed on the seed candidate, and those seeds that fail the χ^2 cut are eliminated.
2. The second step tries to “confirm” the seed by adding additional hit(s) from the confirm layer(s). A helix fit is performed on the new seeds and those that fail the χ^2 cut are eliminated. Typically, it is found that good performance is achieved with one confirmation layer.
3. The third step seeks to “extend” a confirmed seed by trying to add additional hits from the extend layers. Each time a new hit is considered, a helix fit is performed and the hit is discarded if it fails the χ^2 cut. If no hits in a given extend layer give a satisfactory helix fit, then the original track seed is kept and the next extend layer is tried.
4. Track seeds that meet the strategy’s requirement on the minimum number of hits are merged to form a list of distinct tracks. Two track candidates are allowed to share a single hit, but if a track candidate shares more than one hit with another candidate, an arbitration scheme is used to select the better candidate. Precedence is given to the candidate with the greatest number of hits, while the candidate with smaller χ^2 is selected when the number of hits is equal.

Consistency checks and hit sorting algorithms are used to minimize the number of helix fits performed, substantially improving the performance of the algorithm. Furthermore, a “bad hit χ^2 ” cut is used to identify track candidates with an outlier hit and allows preference to be given to track candidates without the outlier hit.

A key component of the pattern recognition algorithm is a fast helix fitter. The helix fitter takes as input 3 or more tracker hits. The hits can be any combination of pixel, axial strip, or stereo hits in the barrel and/or endcap detectors. The fitter is the one place in the tracking code that distinguishes between the various types of hits. The fast fitter is used to estimate the helix parameters and helix fit χ^2 . First, a circle fit to the x,y coordinates of all hits is performed using the Karimaï algorithm to determine the helix parameters ω , ϕ_0 , and d_0 . If there are two or more pixel/stereo hits, then a line fit in the $s - z$ plane is used to determine the z_0 and $\tan \lambda$ helix parameters. In order to provide full helix fits for the case where there are fewer than two pixel/stereo hits, a new fitting algorithm was developed.

While an axial strip does not measure the z coordinate, it has well defined bounds that determine impose the constraint $z_{min} < z < z_{max}$. These bounds lead to each axial strip having an allowed band in the z_0 - $\tan \lambda$ plane. For two or more axial strips, the intersection of these bands will produce a polygonal allowed region, the centroid of which is taken to be the measured values for z_0 and $\tan \lambda$. If there is no region of intersection, the hits are inconsistent with being from a helix and the fit fails. For the case of a single pixel/stereo hit, the pixel/stereo hit is treated like a very short strip and the above algorithm is used.

For all but the highest momentum particles, the multiple scattering errors will exceed the intrinsic hit resolution. Multiple scattering errors for both the active and dead materials are estimated and included in the helix fit. Correlations in the multiple scattering errors are ignored, leading to an under-estimate of the helix parameter errors by a factor of ≈ 1.5 . For stereo hits, full account is taken for the separation between the two stereo layers in calculation of both the hit position and hit covariance matrix.

The performance of the standard pattern recognition algorithm is shown in the section on tracker performance and is also reflected in the benchmarking studies. Unless otherwise noted, the tracking strategies require 1 confirmation hit, a total of at least 7 hits (6 hits for barrel-only tracks), $p_T > 0.2$ GeV, $d_0 < 10$ mm, and $z_0 < 10$ mm.

2.1.9.2 Calorimeter-Assisted Tracking

The development of the calorimeter assisted track finding algorithm was primarily motivated by the need to reconstruct non-prompt tracks and long-lived particles in the SiD detector. As will be shown later, the standard track finding algorithm achieves excellent efficiency in reconstructing prompt tracks that originate close to the interaction point. However, using the same algorithm for finding non-prompt tracks is difficult because those tracks often do not produce enough hits in the vertex detector to seed the track finder, and creating seeds from 3-hit combinations in outer layers without limiting combinatorics by constraining the track origin to the interaction region can be problematic.

The calorimeter assisted tracking solves the problem by seeding the track finder from

traces left by charged particles in the electromagnetic calorimeter - so called MIP stubs. The standard SiD track finder is run first, and the found tracks are then propagated through the calorimeter. Clusters are created and attached to the tracks. After that, topological clustering is applied to the remaining calorimeter hits. Those of the created clusters that include hits in inner electromagnetic calorimeter layers are analyzed for consistency with being produced by minimum ionizing particles. Clusters that pass the test are converted into track seeds that contain information about the track position and direction at the calorimeter entry point. Depending on the MIP stub quality, the seed can also contain a track curvature estimate. The seeds are propagated back into the tracker, picking up hits that are not attached to any existing tracks. The search window in each tracker layer is calculated based on the trajectory parameters uncertainties, and the track parameters are re-evaluated after attaching every new hit. If more than one hit can be attached to the track in a certain layer, multiple track candidates are created. Once all seeds have been processed, the newly created tracks are rated based on quality, and duplicates are removed. This algorithm is essential for reconstructing all kinds of non-prompt tracks - K_s^0 and Λ decay products, new physics signatures that might include long-lived particles, kinked tracks, and calorimeter backscatters. It also performs high purity, topologically linked initial clustering in the calorimeter, and associates clusters with tracks. The possibility of using this algorithm as a first step in particle flow reconstruction could be investigated.

2.1.9.3 Track Fitting

A Kalman filter track fitter is under development to provide helix fitting that fully accounts for multiple scattering and energy loss. The combination of the high precision of silicon sensors, in combination with potentially large extrapolation distances, in certain cases can lead to significant numerical round-off errors in the application of the Kalman filter technique. These numerical issues have been extensively studied for the SiD geometry and work-arounds have been developed where necessary. Final development and testing of the SiD Kalman filtering code is underway and completion is expected shortly. Unless otherwise noted, track parameter measurements are based on the fast helix fitter described in the section on the standard pattern recognition algorithm.

2.1.10 Tracking Performance

In this section the performance of the vertex and tracking detector will be described, along with its associated track-parameter fitter. The goal of these studies is to evaluate the overall performance of the SiD tracking system with the most realistic simulation available. As described in the previous sections, the simulation did include the effects of material and did incorporate a full pulse-development model for the baseline vertex and tracking detector.

Figs. 2.17 and 2.18 show the efficiency of the track finder as function of $\cos\vartheta$ and p_T . The track finding efficiency for tracks with $p_T > 500$ MeV is essentially 100%, except for the transition region between the barrels and the disks where the efficiency drops by about 10%. A key indicator for the number of fake tracks is the number of mis-assigned hits on a track. More than 99% of tracks have at most one wrong hit on the track, as seen from Fig. 2.19

The momentum resolution of the tracker is shown in Fig. 2.20 as function of momentum for various track angles. Also shown in the impact parameter resolution for various track angles. An impact parameter resolution of $4 \mu\text{m}$ is obtained in the high momentum limit.

2.1.11 Tracker Alignment

The unprecedented track momentum resolution contemplated for linear collider detectors demands minimizing systematic uncertainties in sub-detector relative alignments. At the same time, there is a strong impetus to minimize the amount of material in the tracking system, which might compromise its stability. These two requirements put a premium on accurate alignment of the various elements of the tracker. The short time scales on which alignment could change (e.g., from beam-driven temperature fluctuations) may preclude reliance on traditional alignment schemes based on detected tracks, where it is assumed the alignment drifts slowly, if at all, during the time required to accumulate sufficient statistics. A system that can monitor alignment drifts in real time would be highly desirable in any precise tracker and probably essential to an aggressive, low-material silicon tracker. The tradeoff one would make in the future between low material budget and rigidity will depend critically upon what a feasible alignment system permits. The SiD tracker is considering two alignment methods, one based on Frequency Scanned Interferometry (FSI), and one based on Infrared Transparent Silicon Sensors (IRSS).

The FSI system incorporates multiple interferometers fed by optical fibers from the same laser source, where the laser frequency is scanned and fringes counted, to obtain a set of absolute lengths. With a test apparatus the state of the art in precision DC distance measurements over distance scales of a meter under laboratory-controlled conditions has been reached and even extended. Precisions better than 100 nm have been attained using a single tunable laser when environmental conditions are carefully controlled. Precisions under uncontrolled conditions (e.g., air currents, temperature fluctuations) were, however, an order of magnitude worse with the single laser measurements. Hence a dual-laser FSI system is foreseen for the tracker, that employs optical choppers to alternate the beams introduced to the interferometer by the optical fibers. By using lasers that scan over the same wavelength range but in opposite directions during the same short time interval, major systematic uncertainties can be eliminated. Bench tests have achieved a precision of 200 nm under highly unfavorable conditions using the dual-laser scanning technique.

The second method exploits the fact that silicon sensors have a weak absorption of infrared (IR) light. Consecutive layers of silicon sensors are traversed by IR laser beams which play the role of infinite momentum tracks (see Fig. 2.21). Then the same sophisticated alignment algorithms as employed for track alignment with real particles can be applied to achieve relative alignment between modules to better than a few microns. This method employs the tracking sensors themselves, with only a minor modification to make them highly transparent to infrared light. The modification to a tracking sensor is minimal. Only the aluminum metalization on the back of the sensor needs to be swept away in a circular window with a diameter of few millimeters to allow the IR beam to pass through. Since IR light produces a measurable signal in the silicon bulk, there is no need for any extra readout electronics.

SUBSYSTEMS

A key parameter to understand the ultimate resolution of this method is the transmittance of a silicon sensor and the diffraction of the light. As a first approximation a silicon sensor is viewed as a stack of perfectly homogeneous planoparallel layers, each characterized by its index of refraction and thickness. The layers are, however, not continuous but present local features, so that diffraction phenomena will appear if the size of the obstacle is comparable to the wavelength used. For instance, the strips of the detector, pitched every 10 to 50 μm are good examples of an optical diffraction grating for an incoming beam in the IR. It has been determined that a key parameter that determines the overall transmittance of a microstrip detector is the pitch to strip ratio, that is, the fraction of the strip covered by aluminum. The smaller the strip width, the more light is transmitted. It was determined that good transmittance was achieved when the strip width was set to 10% of the pitch. Tuning of sensor thickness was found to contribute up to 5% over the layout optimized value. In bench tests, based on CMS strip detectors, a relative alignment of a few microns has been achieved.

It should be noted that this alignment method has been implemented at the Alpha Magnetic Spectrometer (AMS) and has been by the tracking system of the Compact Muon Solenoid experiment. Furthermore, both methods, developed for central and forward tracker alignment, may also prove useful for the vertex detector.

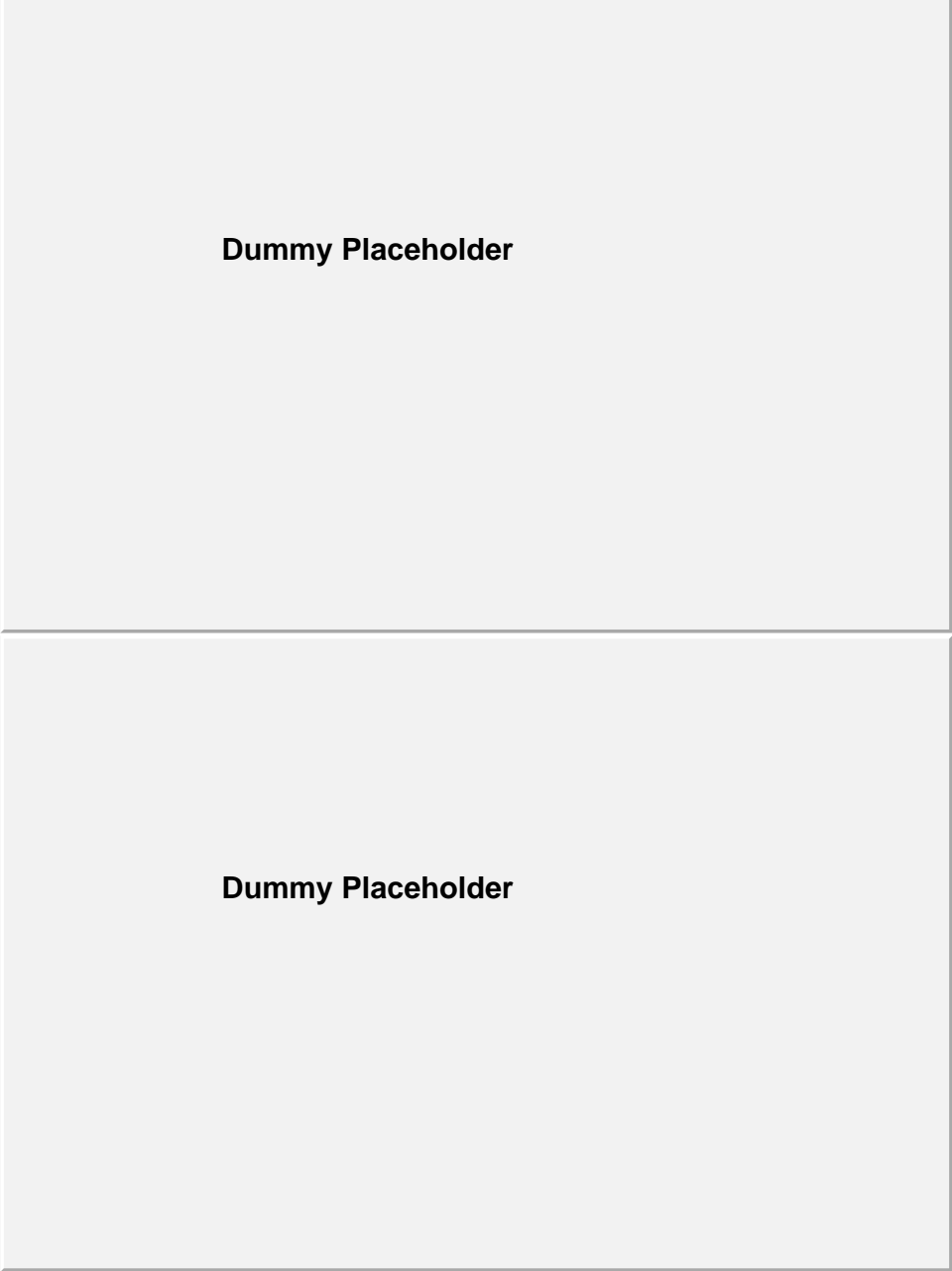


Figure 2.5: Hit pattern and material summary of the vertex detector as function of polar angle.

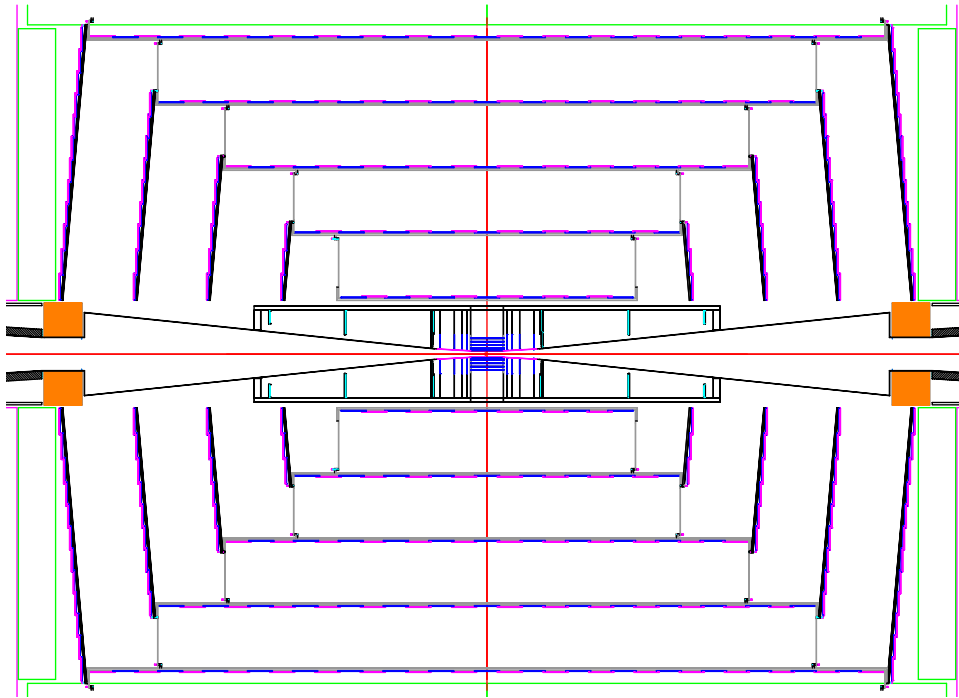


Figure 2.6: R-z view of the whole tracking system.

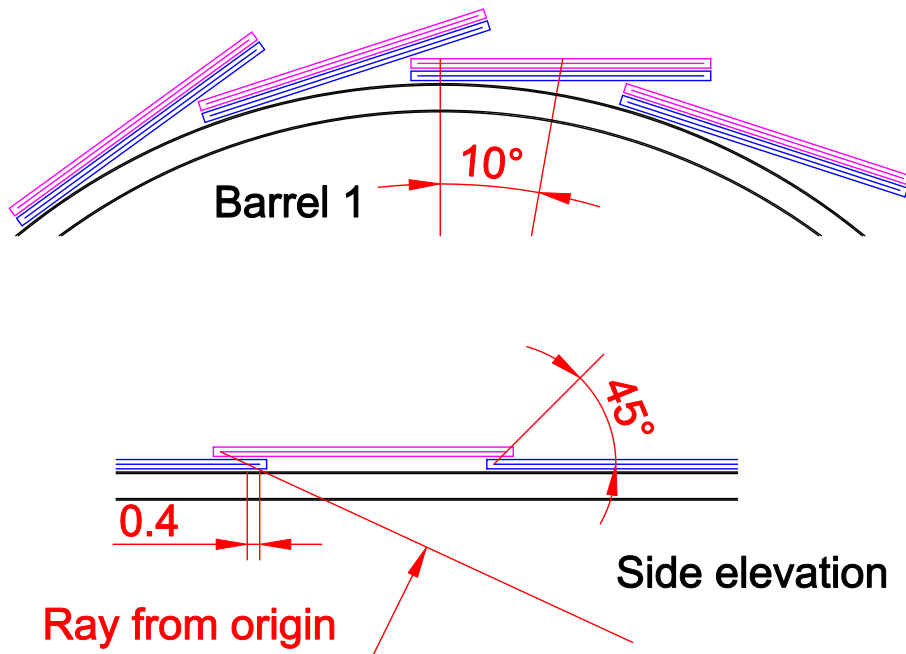


Figure 2.7: Detail of the sensor overlap in the barrel region in the z and $R\phi$ projection.

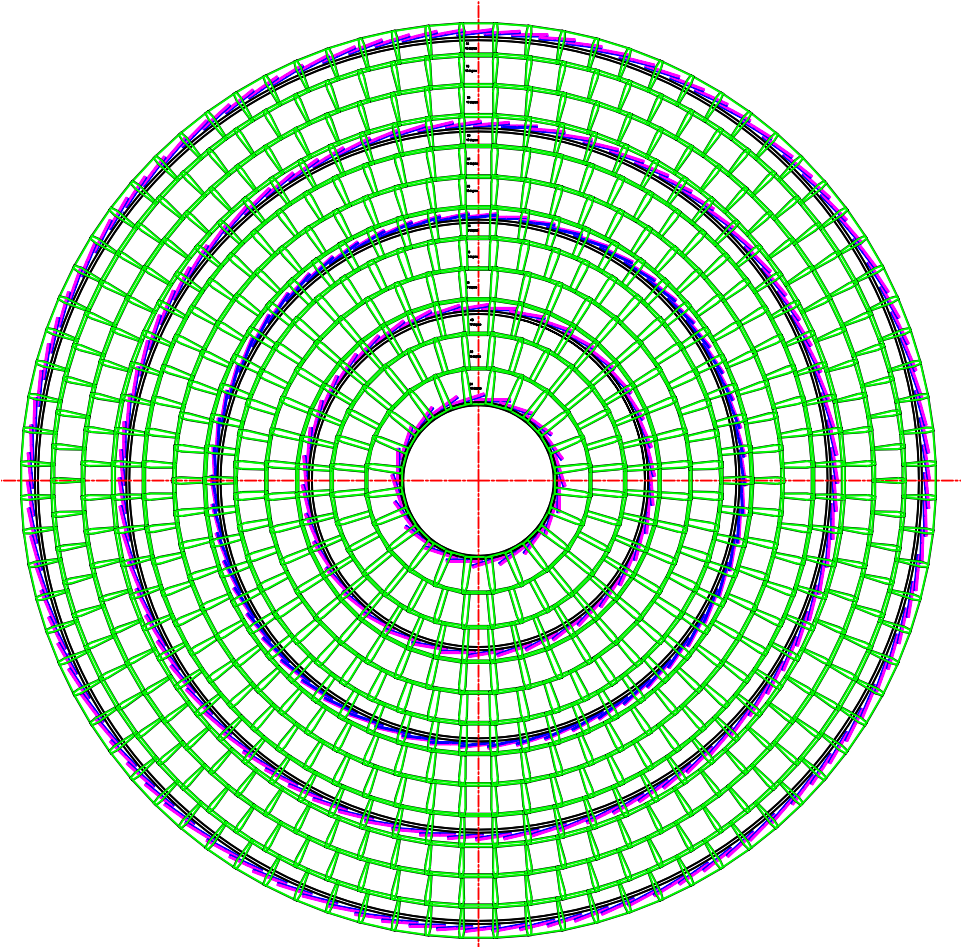
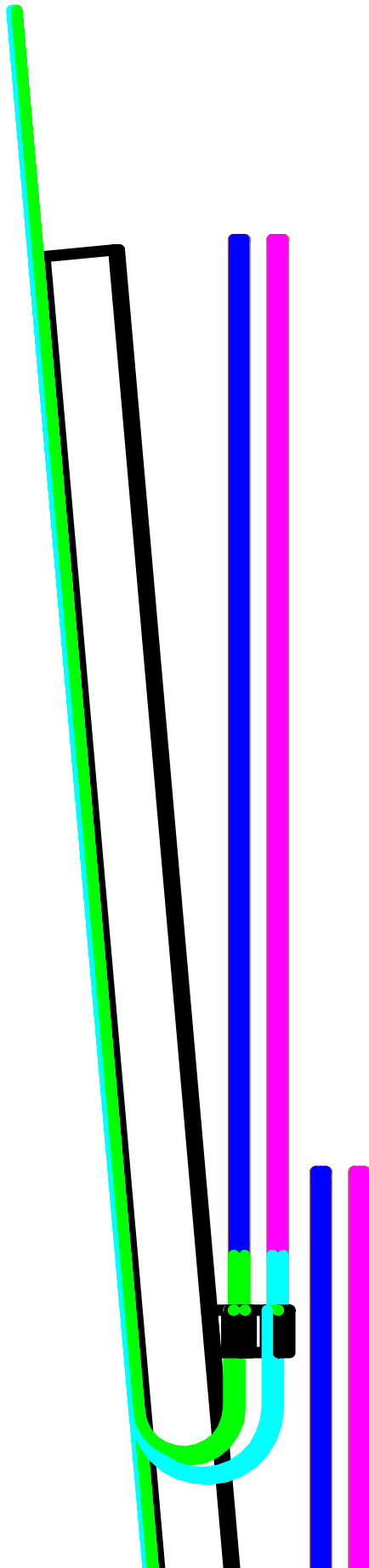


Figure 2.8: $R\phi$ projection view of the tracker barrels and disks.

SUBSYSTEMS



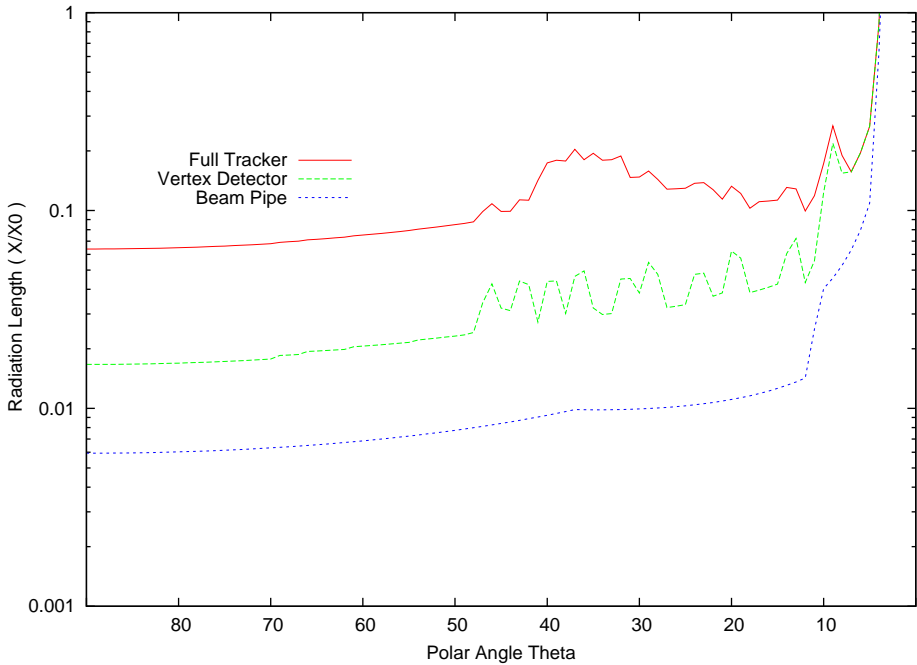


Figure 2.10: Material budget of the tracking system.

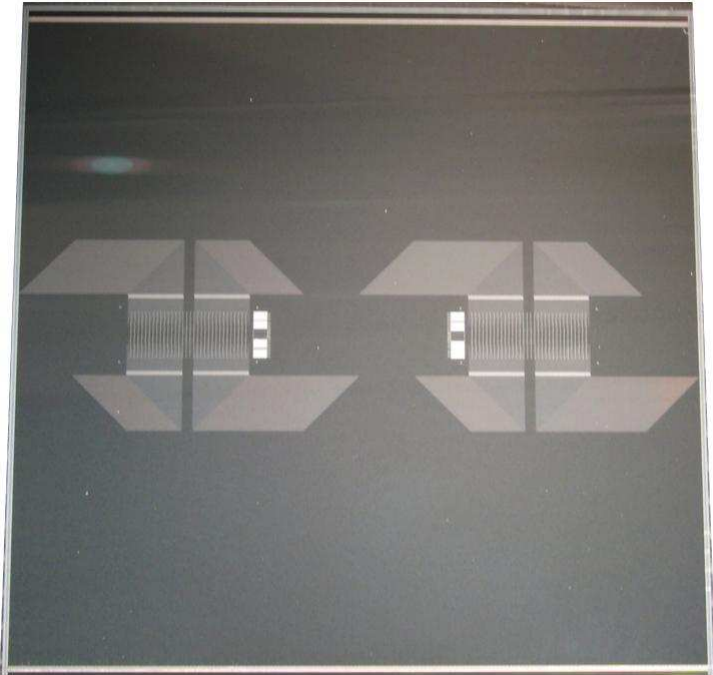


Figure 2.11: Photograph of a prototype SiD tracker sensor.

SUBSYSTEMS

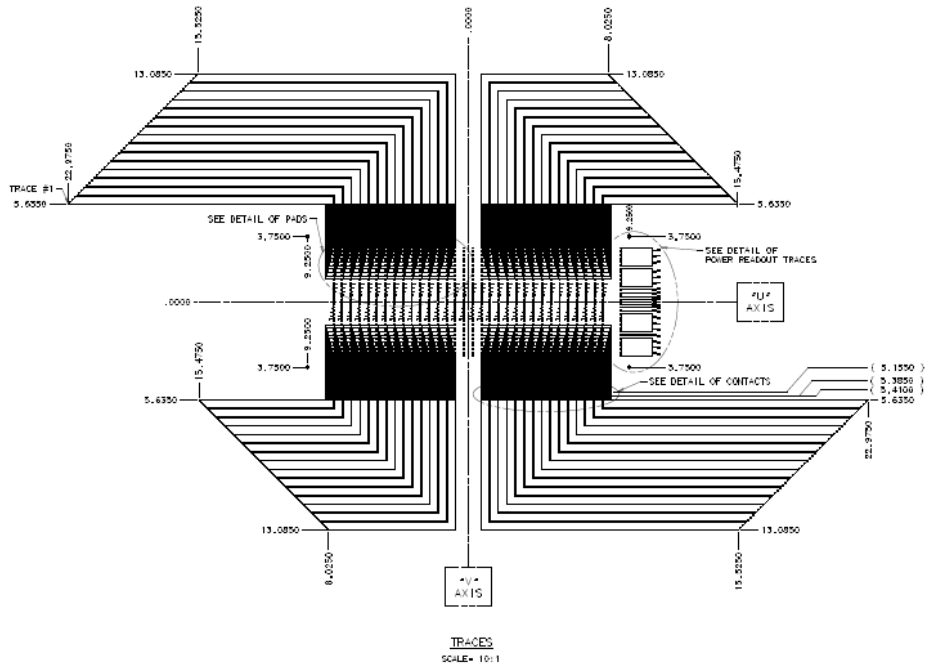


Figure 2.12: Detail of the double-metal routing of the traces to the readout chip and the connections to the readout cable, visible to the right of the bump-bond array.

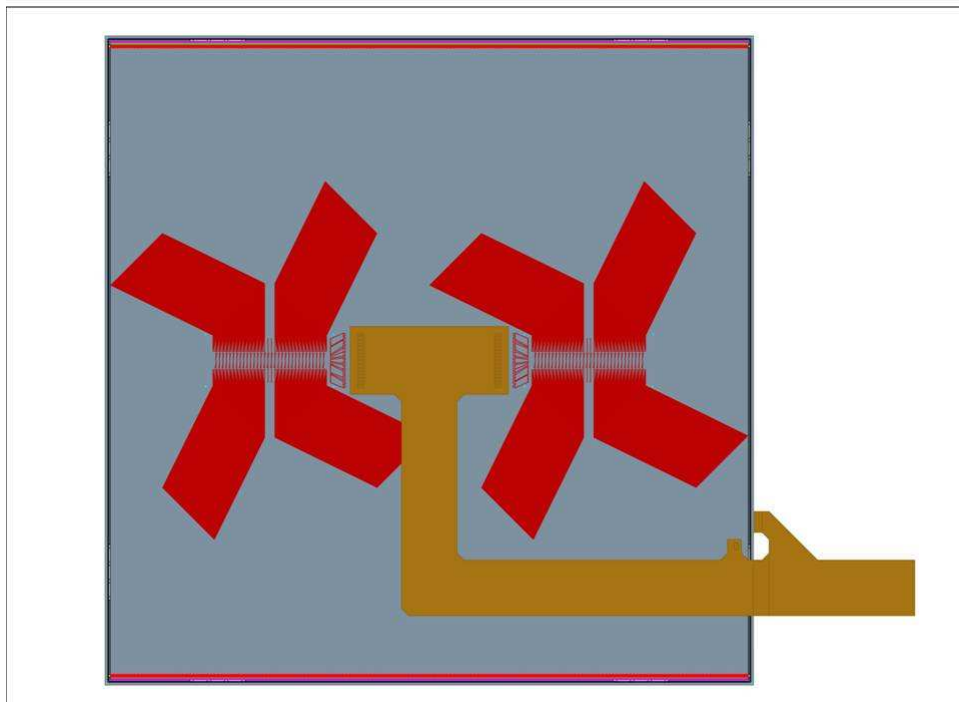


Figure 2.13: Sketch of a module to the tracker barrel. This figure should be replaced.

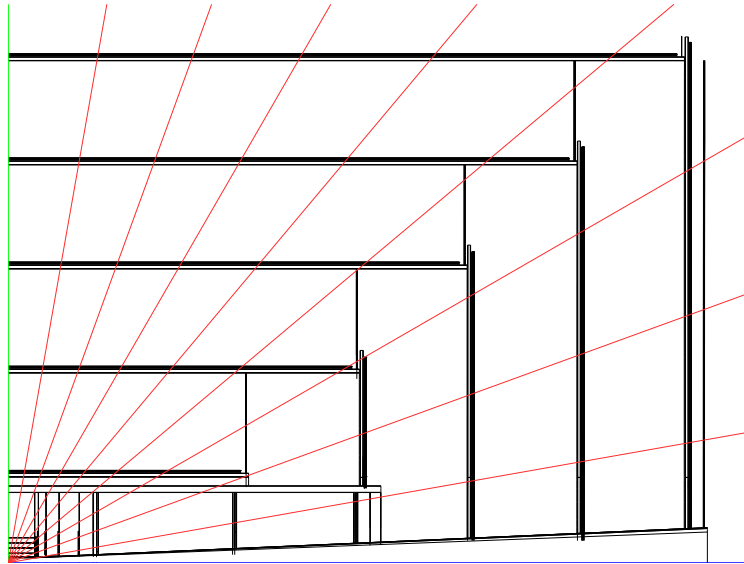


Figure 2.14: R-z view of the simplified tracking system as implemented in sid02.

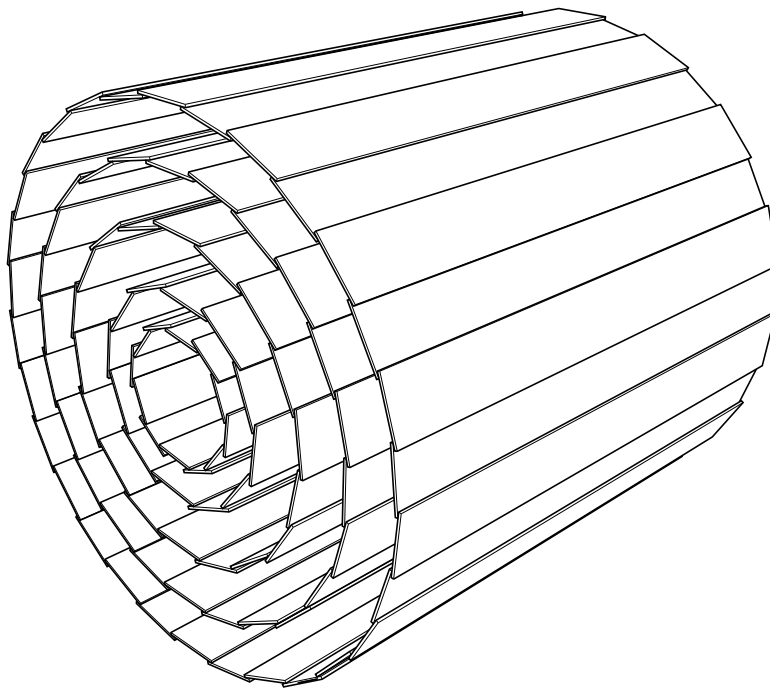


Figure 2.15: The central vertex detector showing the layout of the silicon pixel sensor modules.

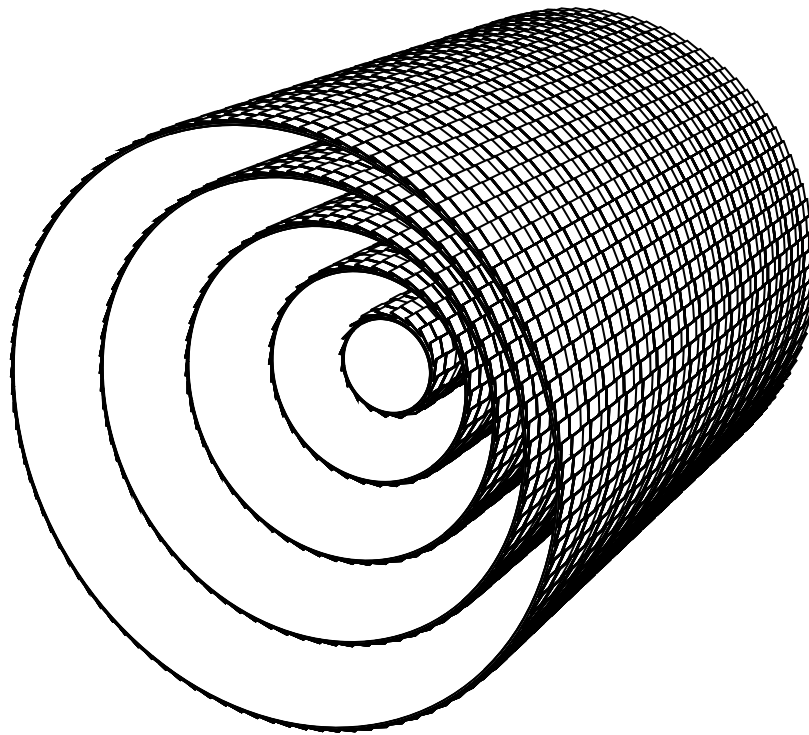


Figure 2.16: The central tracker showing support barrels tiled with overlapping readout modules.

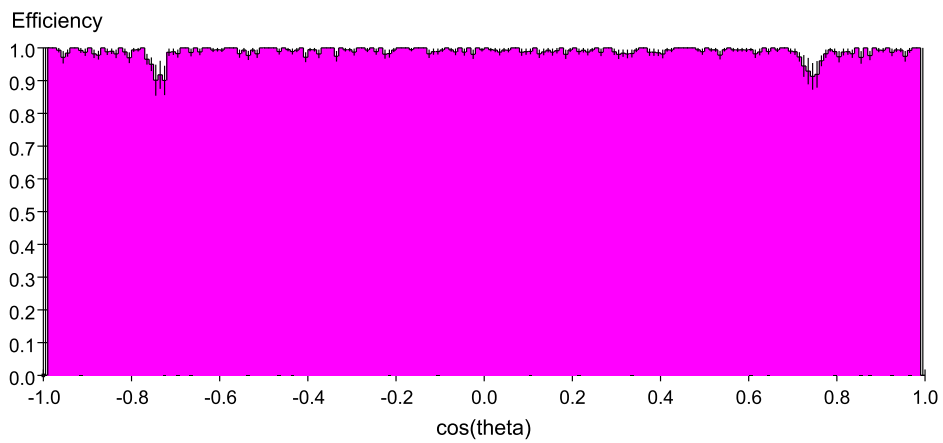


Figure 2.17: Track finding efficiency as function of $\cos \vartheta$.

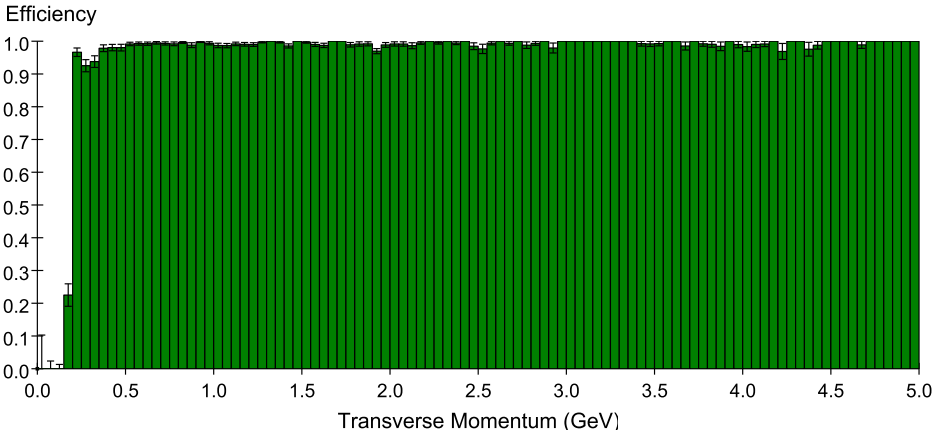


Figure 2.18: Track finding efficiency as function of p_T .

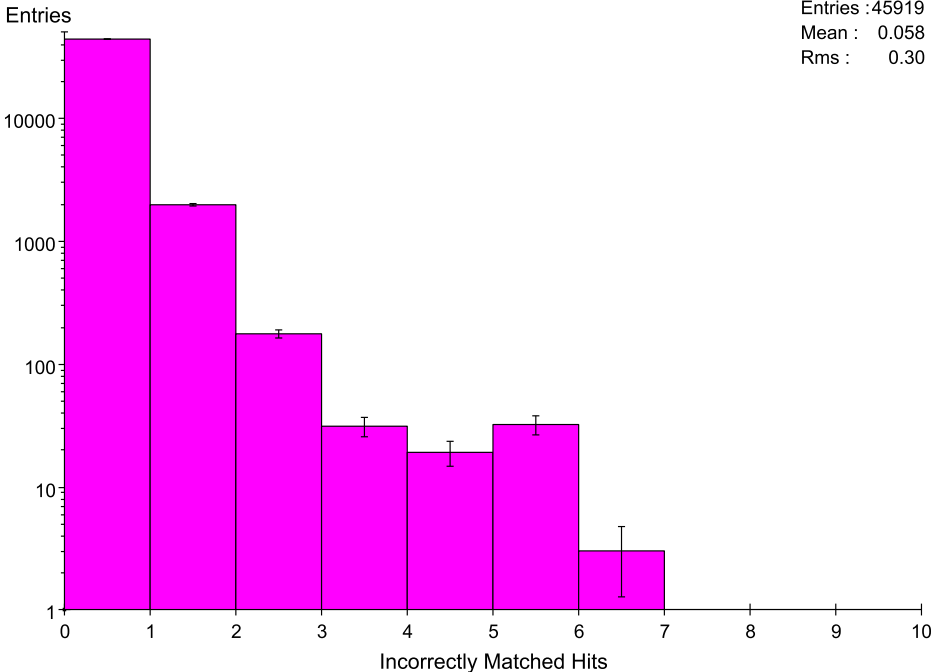


Figure 2.19: Number of mis-assigned hits on a track.

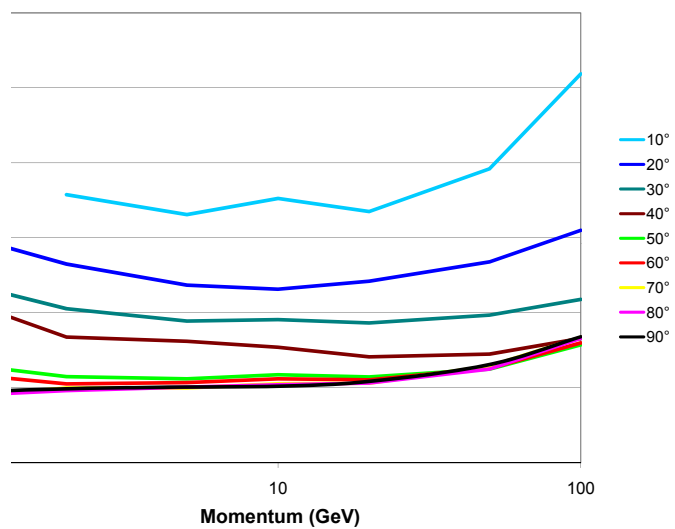


Figure 2.20: Resolution in momentum (right) and DCA (left) as function of momentum for tracks at various angles.

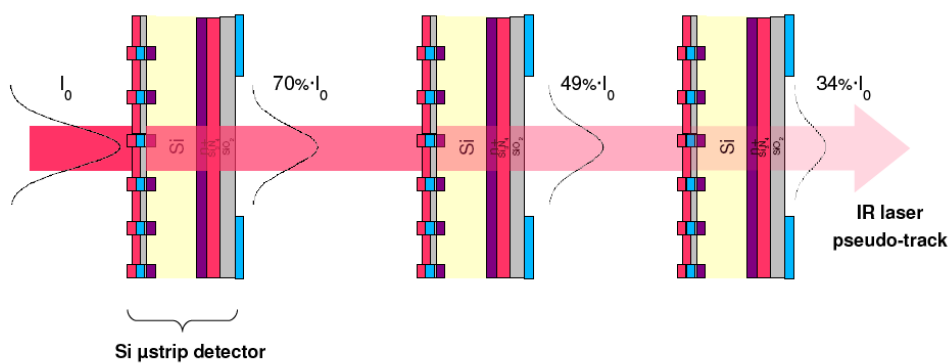


Figure 2.21: Sketch of the IR alignment method.

2.2 Calorimeters

2.2.1 Introduction to Calorimeters

To measure hadronic jets of particles produced in high-energy collisions of electrons and positrons, with sufficient precision it is widely accepted that a new approach is necessary. The most promising method, called a Particle Flow Algorithm (PFA), utilizes both the tracking information for charged particles and the calorimeter for the measurement of the energy of neutral particles. PFAs applied to existing detectors, such as CDF and ZEUS, have resulted in significant improvements of the jet energy resolution compared to methods based entirely on calorimetric measurement alone. However, these detectors were not designed with the application of PFAs in mind. The SiD concept on the other hand accepts that a PFA is necessary and is designing the detector to optimize the PFA performance with the goal of obtaining jet energy resolutions of the order of $30\%/\sqrt{E}$ or better.

The major challenge imposed on the calorimeter by the application of PFAs is the association of energy deposits with either charged or neutral particles impinging on the calorimeter. This results in several requirements on the calorimeter design:

- To minimize the lateral shower size of electromagnetic clusters the Molière radius of the ECAL needs to be minimized This promotes efficient separation of electrons and charged hadron tracks.
- Both ECAL and HCAL have to have imaging capabilities which allow assignment of energy cluster deposits to charged or neutral particles. This implies that the readout of both calorimeters needs to be finely segmented transversely and longitudinally.
- HCAL needs to be inside the solenoid to be able to do particle cluster association.
- In addition, the design of the calorimeter needs to be as uniform as possible, minimizing the use of different technologies, extendable to small angles to ensure hermeticity, and to provide enough depth for the longitudinal containment of hadronic showers. The design needs to consider the cost as an additional boundary condition.

Following is a short description of the baseline designs and options for the ECAL and the HCAL, as defined in December 2008.

An alternative approach to a PFA, based on homogenous crystal calorimetry, has recently been proposed. A description of this approach is also given later in this chapter.

2.2.2 Electromagnetic Calorimeter

2.2.2.1 Introduction

The major challenge imposed on the calorimeter by the application of PFAs is the association of individual particles with their energy depositions in the calorimeters. For the ECAL, this

implies that electromagnetic showers be confined to small volumes in order to avoid overlaps. Effective shower pattern recognition is possible if the segmentation of readout elements is small compared to the showers. This level of transverse segmentation then also facilitates the separability of the electromagnetic showers from charged particle tracks due to uninteracted charged hadrons (and muons). The longitudinal segmentation is chosen not only to achieve the required electromagnetic energy resolution, but also to provide discrimination between electromagnetic showers and those hadrons which interact (typically deeper) in the ≈ 1 interaction length of the ECAL. Finally, there should be a sufficient number of longitudinal readout layers to provide charged particle tracking in the ECAL. This is important not only for the PFA algorithms, but also to aid the tracking detectors, especially for tracks which do not originate from the IP.

An important benefit of an ECAL which meets these requirements is that it is an imaging calorimeter. This is illustrated in Fig. 2.22, which shows a simulation in SiD of $\rho^+ \rightarrow \pi^+ \pi^0$. The photons are clearly distinguished from each other and from the charged track in the ECAL.

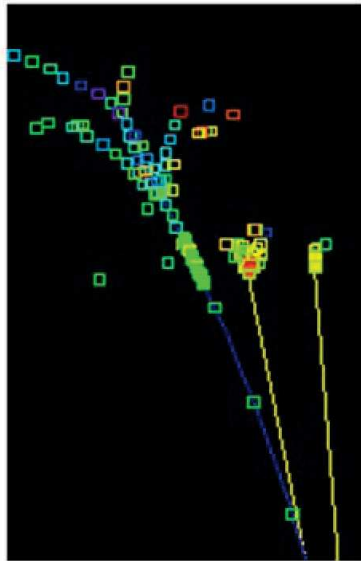


Figure 2.22: Simulated $\rho^+ \rightarrow \pi^+ \pi^0$ in SiD.

The ECAL described in this section according to the qualitative description above is expected to capabilities including:

- Measurement of beam-energy electrons and positrons (and photons) from (radiative) Bhabha scattering. This is sensitive to contact terms and the angular distribution provides important information on electroweak couplings, for example in interference terms between Z , γ , and a new Z' . Precise Bhabha acollinearity distributions provides a key piece of the measurement of the luminosity spectrum[?], which is crucial for correct measurement of sharp threshold features in the annihilation cross section.
- electrons from $Q \rightarrow Q' e \nu$
- adequate electromagnetic energy resolution; explain that $\sim 0.17/\sqrt{E}$ is OK.

The imaging ECAL can also provide these more challenging measurements abilities, most of which have not yet been fully demonstrated in simulation:

- PFA reconstruction of photons in jets with high (95%) efficiency
- PFA tracking of charged particles in jets
- ECAL-assisted tracking (especially of V0s)
- π^0 reconstruction in jets – this allows improvement of the EM component of jet energy[2]
- photon vertexing – the impact parameter resolution for photons of ~ 1 cm would be important for identifying decays where photons are the only visible decay products, such as predicted from some gauge-mediated SUSY-breaking models
- π^0 reconstruction in τ decays. This is a crucial for identification of τ final states which are important for measuring τ polarization, P_τ .

Global ECAL design

A sampling ECAL provides adequate energy resolution for the ILC physics, as discussed above. Because of its small radiation length and Molière radius, as well as its mechanical suitability, we have chosen tungsten absorber/radiator. Due to practical considerations for ease of production of large plates and machining, the tungsten will be a (non-magnetic) alloy. This currently chosen alloy includes 93% W with radiation length 3.9 mm and Molière radius 9.7 mm. An additional benefit of tungsten is that it has a relatively large interaction length, which helps to ameliorate confusion between electromagnetic and hadron showers in the ECAL.

The longitudinal structure we have chosen has 30 total layers. The first 20 layers each have 2.50 mm tungsten thickness and 1.25 mm readout gap. The last 10 layers each have 5.00 mm tungsten plus the same 1.25 mm readout gap. This configuration attempts to compromise between cost, shower radius, sampling frequency, and shower containment. The cost is roughly proportional to the silicon area, hence the total number of layers. We chose finer sampling for the first half of the total depth, where it has the most influence on electromagnetic resolution for showers of typical energy. However, as discussed below, an increase in sampling with fixed readout gaps has a detrimental effect on the shower radius. The total depth is $26X_0$, providing reasonable containment for high energy showers. Figure 2.23 shows that the energy resolution at low energy does not suffer relative to a design with 30 layers all having the thinner radiator. The resolution of the baseline design is well fit by the function $0.17/\sqrt{E}$. These simulations were made with EGS4, but have been verified by GEANT4 simulations.

Silicon detectors are readily segmented. In the baseline design we have chosen (see description below), there is little penalty for segmenting the silicon sensors much more finely than typical shower radii. (The MAPS option takes this to the extreme.) As discussed above, the scale for this is set by the shower size, which we wish to be as small as feasible. A useful figure of merit for this is the Molière radius, which is 9 mm for pure tungsten. Since showers

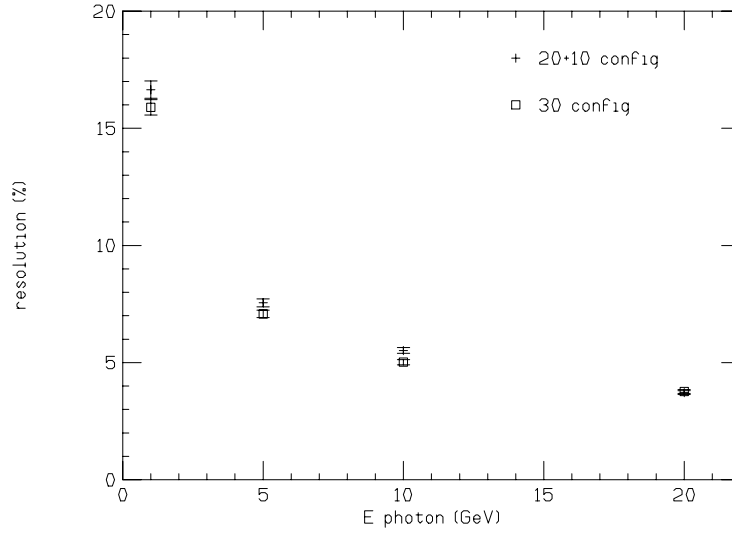


Figure 2.23: Energy resolution at low energy for two longitudinal configurations. The “20+10” configuration is our chosen design.

will spread in the material between tungsten layers, it is crucial to keep the readout gaps as small as possible. We can scale the shower radii by a simple factor to provide a figure of merit. In our case, this factor is $(2.50 + 1.25)/2.50 = 1.50$ for the crucial first 20 layers. We can then define the *effective* Molière radius, \mathcal{R} , as the Molière radius of the radiator multiplied by this factor. In our case, this is about 14 mm. A crucial driving force in our design has been to provide as small a \mathcal{R} as feasible, along with a transverse segmentation of the readout which is well below \mathcal{R} .

Table 2.2.2.1 summarizes the basic ECAL parameters. Figure 2.24 shows the overall mechanical structure of the ECAL barrel, including detectors layout (for the baseline option) and readout gap.

Table 2.5: Nominal parameters of the silicon-tungsten ECAL for SiD.

inner radius of ECAL barrel	1.27 m
maximum z of barrel	1.7 m
longitudinal profile	$(20 \text{ layers} \times 0.64X_0) + (10 \text{ layers} \times 1.3X_0)$
EM energy resolution	$0.17/\sqrt{E}$
readout gap	1.25 mm (or less)
effective Moliere radius (\mathcal{R})	14 mm

Technology choice

There are two technology options, both of which utilize silicon sensors. Silicon will provide excellent transverse segmentation, while providing readout in a thin gap, which is a crucial performance criterion, as discussed above. The baseline technology option uses silicon sensors

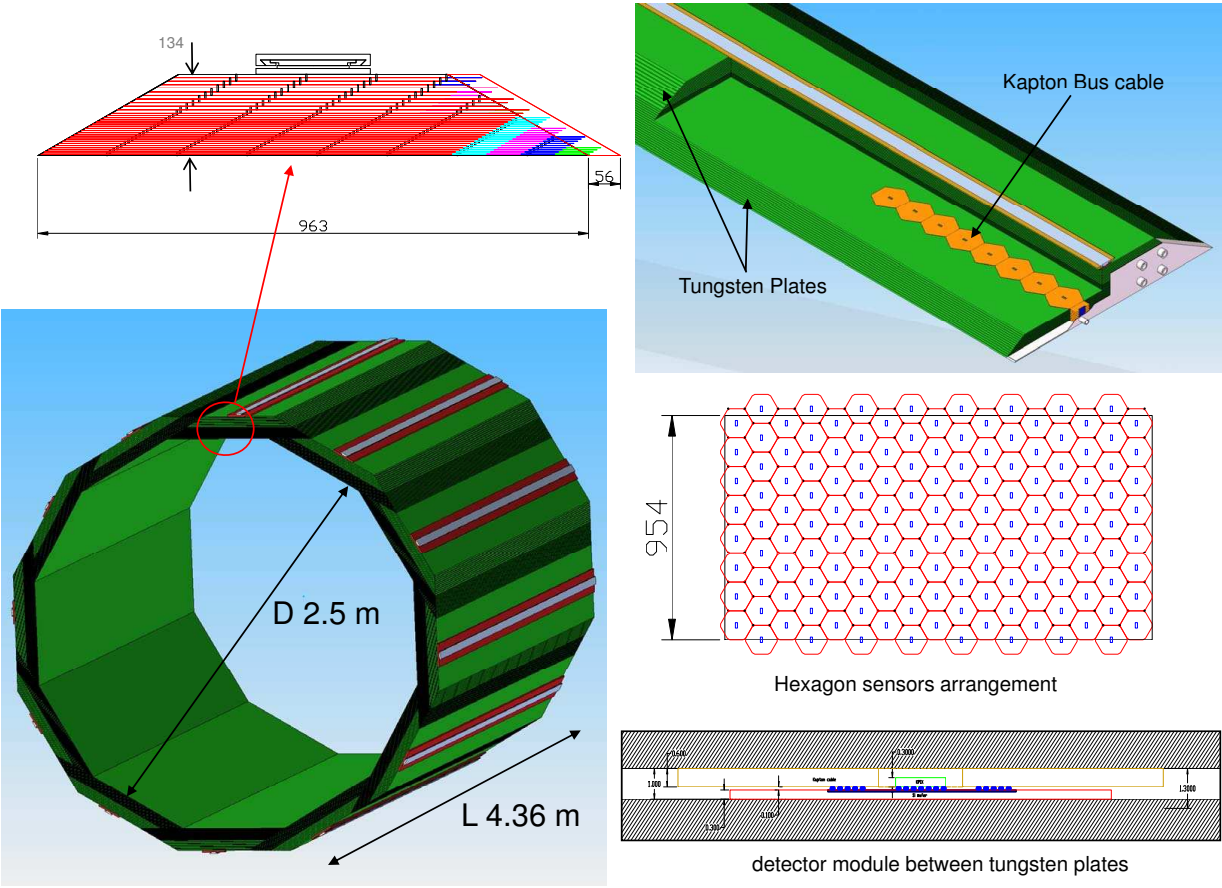


Figure 2.24: Overall mechanical layout of the ECAL.

segmented into pixels of area 13 mm^2 . The other option uses the MAPS technology. Both options are discussed below. An important feature of the SiD ECAL mechanical design is that it can accommodate either technology option without change to the basic mechanical configuration.

2.2.2.2 Baseline option

In the baseline design, the ECAL readout layers are tiled by large, commercially feasible silicon sensors (presently from 15 cm wafers). The sensors are segmented into pixels which are individually read out over the full range of charge depositions. The complete electronics for the pixels is contained in a single chip (the KPiX ASIC) which is bump bonded to the wafer. We take advantage of the low beam-crossing duty cycle (10^{-3}) to reduce the heat load using power pulsing, thus allowing passive thermal management within the ECAL modules. The realization of this technology has been the subject of an intensive, ongoing R&D program.

The main parameters associated with the baseline technology choice are given in Table 2.2.2.2. Some details of the design and R&D results are given below. Further details can be found in the references [3].

Table 2.6: Parameters of baseline silicon-tungsten ECal.

pixel size	13 mm^2
readout gap	1.25 mm (includes 0.32 mm thick Si sensors)
effective Moliere radius	14 mm
pixels per silicon sensor	1024
pixel area	13 mm^2
channels per KPiX readout chip	1024
pixel dynamic range requirement	~ 0.1 to 2500 MIPs
heat load requirement	20 mW per sensor

Figure 2.25 shows a sensor with 1024 pixels. Not shown in the drawing are the signal traces, part of the second layer metallization of the sensors, which connect the pixels to a bump-bonding pad at the center of the sensor for input to the KPiX readout chip. The pixels are DC-coupled to the KPiX, thus only two metallization layers are required for the sensors. The pixels near the bump-bonding array at the center are split to reduce capacitance from the large number of signal traces near the sensor center. The electronic noise due to the resistance and capacitance of the traces has been minimized within the allowed trace parameters. The cutouts at the corners of the sensor are to accommodate mechanical standoffs which support the gaps between the tungsten layers.

Figure 2.26 depicts a cross-sectional view of the readout gap in the vicinity of the center of the sensor. The silicon sensor is about $320 \mu\text{m}$ thick. The KPiX is bump-bonded to the silicon sensor at an array of bump pads which are part of the second metallization layer from sensor fabrication. This is a 32×32 array of bump bond pads. Polyimid (kapton) flex cables

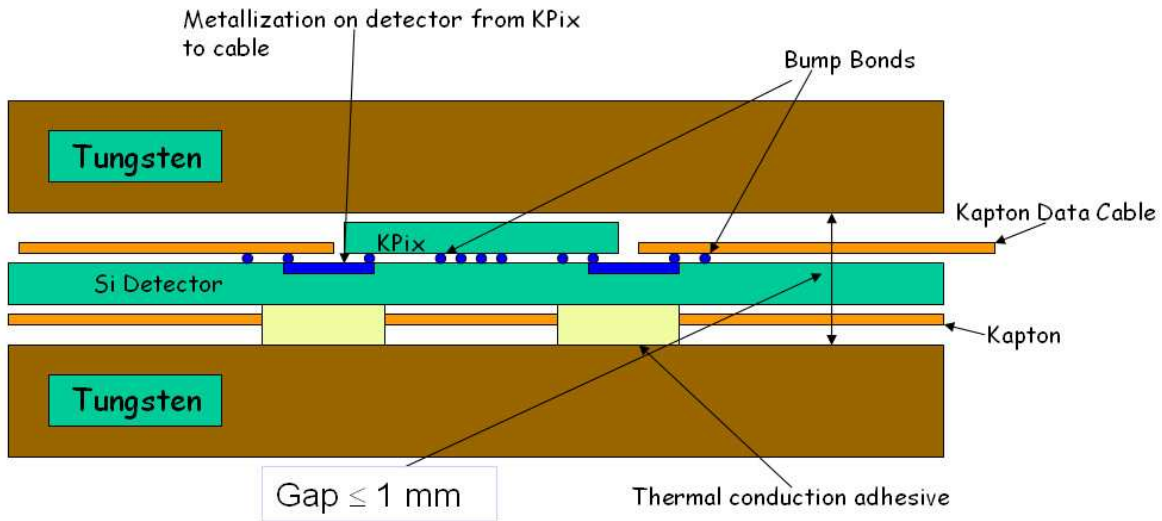


Figure 2.26: View into a readout gap in the vicinity of the KPiX readout chip. Representative bump bond connections are indicated by the small blue circles. Traces (dark blue lines) connect the KPiX serial readout stream, control signals, and power to the polyimide.

2.2.2.3 MAPS option

In the Monolithic Active Pixel Sensor (MAPS) option[4] we propose to use $50 \times 50\ \mu\text{m}$ silicon pixels as readout material. The main difference here is the usage of digital electromagnetic calorimetry where the ECAL is operated as a shower particle counter. For manufacturing these pixel we foresee the usage of MAPS manufactured in a commercial 180 nm mixed-mode CMOS process using 300 mm wafers. As this is an industrial and widely available process, we expect very competitive pricing for these wafers.

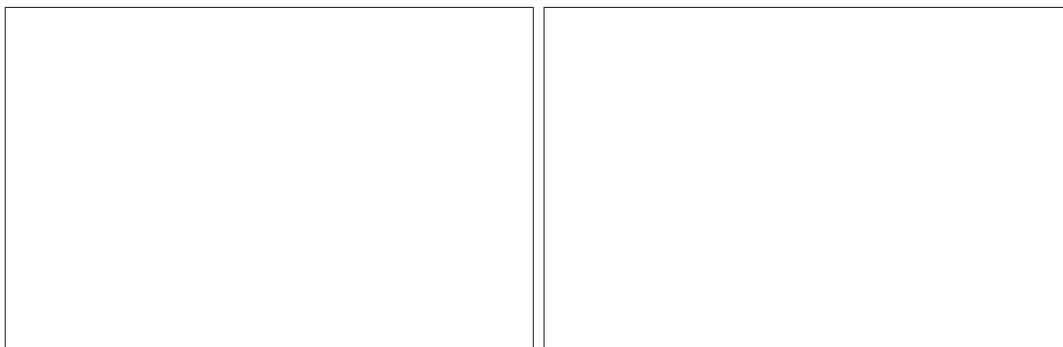


Figure 2.27: Paul’s Digital ECAL plot and a nice MAPS Shower picture

We have manufactured and tested two first-generation sensors for digital electromagnetic calorimetry, TPAC 1.0 and 1.1 which both consists of 168×168 pixels with the required size of $50 \times 50\ \mu\text{m}$. TPAC 1.0 had two different pixel architectures, while TPAC 1.1 only uses the pre-Shaper architecture which will now be described in more detail. It consists of a charge preamplifier, a CR-RC Shaper shaper which generates a shaped signal pulse proportional to the amount of charge collected and a two-stage comparator which triggers the hit-flag. The

sensor supports single-bunch time stamping with up to 13 bits. Each pixel has a 4 bit trim to compensate for pedestal variations and each pixel can be masked off individually. A bank of forty-two pixels shares nineteen memory buffers to store the hits during the bunch train. The sensor also supports power-pulsing already as is able to turn of its front-end in the quiet time between bunch trains. As the active sensor area is only about $20\ \mu\text{m}$ thick, it allows backthining of the wafers to $100\ \mu\text{m}$ or less. The MAPS option is designed to fit in the same mechanical structure as the baseline option and we foresee a sensor size of $5\ \text{x}\ 5\ \text{cm}$ (baseline) for a final system.

Table 2.7: Parameters of MAPS silicon-tungsten ECAL.

pixel size	$50\ \text{x}\ 50\ \mu\text{m}$
readout gap	1.25 mm (includes 0.32 mm thick Si sensors)
effective Moliere radius	14 mm
Channels per Sensor	1,000,000
pixel dynamic range requirement	1 MIP
readout	digital
heat load requirement	20 mW per sensor (check/update)

2.2.2.4 ECal R&D: Near term

The highest priority near-term goal is to demonstrate the baseline design. It is important to note that all of the major components of the baseline ECAL are under current development and test. The goal is to build a small test module from these components for validation in a beam test. The test module, a drawing of which is shown in Fig. 2.28, would consist of a one-sensor wide stack. In depth, the test module would be identical to the SiD ECAL modules (see Table 2.2.2.1).

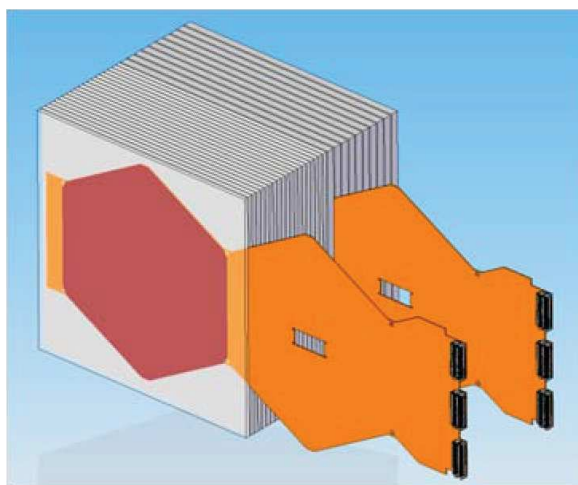


Figure 2.28: Drawing of initial ECAL test module.

The test module would consist of

- 30 silicon sensors, which are already in hand (see drawing in Fig. 2.25)
- 30 tungsten plates, which are in hand
- 30 1024-channel KPiX readout chips, to be procured
- 30 flex-cables (short), to be procured
- the KPiX-sensor and cable-sensor interconnects

The KPiX development needs to evolve from the 64-channel prototype devices to 256-channel and then 1024-channel devices. It is expected that this will occur in 2009. A nearly satisfactory version of the short flex cables have been made previously, so it is not expected that this will be a serious issue. The interconnection techniques are currently under development. For the KPiX-sensor connections, some form of bump-bonding will be used. The pitch of the bump pad array is not especially demanding (0.20 mm in x ; 0.50 mm in y). For the test module, we are performing trials of a gold-bump process. For the connections of sensors to flex-cables, we are investigating several options, including thermoplastic conductive adhesives.

It is quite realistic to assume that these steps can occur to allow fabrication of the test module for evaluation in a beam in 2010, with results well before 2012.

There are a few elements of the ECAL design which are not included in the test module. The ability to fabricate long (1.8 m) flex-cables to span the length of an ECAL module in z , as depicted in Fig. 2.24, needs to be demonstrated. We have initiated this. Finally, we would like to demonstrate the mechanical and thermal aspects of the ECAL module design. We will build a mechanical prototype consisting of a sizeable fraction of a barrel module. This will allow testing the assembly method involving the small readout gaps and a mockup of the thermal dissipation and cooling can be implemented. We expect this to be completed in 2009-10.

For the MAPS option, in the short term we would like to make a second generation chip which is sufficiently large to make a ECAL stack to study digital electromagnetic calorimetry in detail. It will also allow it to make a real system test to explore also issues like heat load, power pulsing and DAQ needs.

2.2.2.5 ECal R&D: Long term

The detector R&D will be completed in the near term, before 2012. Beyond this, we will be ready to implement the technology in building a full barrel module. We also need to finalize the design for the mechanical structure and sensor layout for the endcap modules. Since larger numbers of silicon sensors will be required, exploring various options with vendors will be important. In particular, it would be desirable for reasons of efficiency and cost to do the bump bonding of KPiX to sensors as a final step of the sensor fabrication.

A key aspect for the MAPS R&D is the capability to manufacture large sensors with sufficient yield, so the R&D will focus on stitched CMOS sensors.

2.2.3 Hadronic Calorimeter

2.2.3.1 Introduction

HCAL barrel geometry

The PFA-based HCAL is a sandwich of absorber plates and instrumented gaps with active detector elements. It is located inside the magnet and surrounds the electromagnetic calorimeter (ECAL), the latter being fixed to it. The total absorber depth amounts to 4.5λ , made of stainless steel, divided into 40 layers, separated by 8mm gaps. Thus the HCAL internal and external radii are respectively: $R_{\text{int}} = 1419 \text{ mm}$ and $R_{\text{ext}} = 2583 \text{ mm}$. The overall length is 6036mm long, centered on the interaction point.

The HCAL is divided into twelve azimuthal modules. In order to avoid cracks in the calorimeter, the module boundaries are not projective with respect to the interaction point. Consequently, in order to keep a symmetric shape two types of modules are used: 6 rectangles and 6 pseudo-trapezoids, as illustrated in Fig. 2.29.

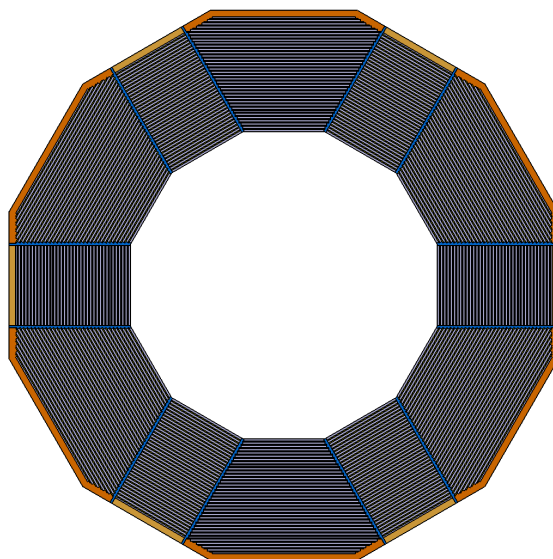


Figure 2.29: Cross-section of the HCAL barrel.

Each module covers the whole longitudinal length. Chambers are inserted in the calorimeter along the Z-direction from both ends and can eventually be removed without taking out the absorber structure from the magnet. Special care of the detector layout has to be taken into account to avoid a crack at 90 degrees.

The absorber plates are supported by several stringers fixed radially on both sides of the modules. Stringers of two consecutive modules are shifted in order to maximise the active detector area. Although the space between two consecutive modules is not instrumented, it

SUBSYSTEMS

is however filled by the absorber material. The barrel will be fixed on the magnet at 3 and 9 o'clock or 5 and 7 o'clock.

HCAL forward

Each endcap forms a plug that is inserted into an end of the barrel calorimeter. The layer structure of the end cap calorimeters is the same as for the barrel. Fig. 2.30 shows a view of one endcap.

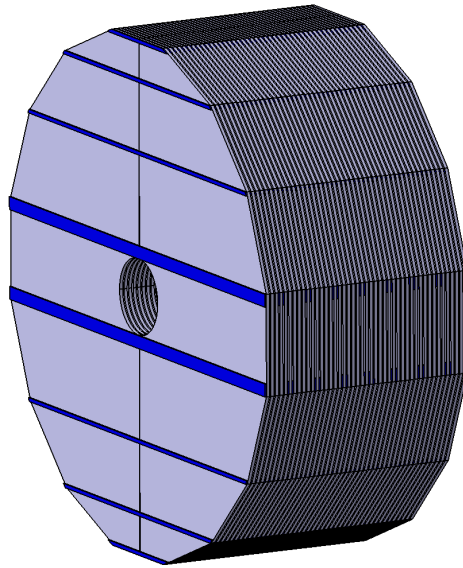


Figure 2.30: Face and top views of the forward HCAL.

2.2.3.2 Baseline option: Resistive Plate Chambers

Resistive Plate Chambers (RPCs) are gaseous (micro)-strip detectors primarily in use for the large muon systems of colliding beam detectors. The detectors feature a gas volume defined by two resistive plates, typically bakelite or glass. The outer surface of the plates is coated with a layer of resistive paint to which a high voltage is applied. Charged particles crossing the gas gap initiate a streamer or an avalanche, depending on the high voltage setting of the chamber. These in turn induce signals on the readout strips or pads located on the outside of the plates.

In recent years RPCs have seen a wide range of applications. Using glass as resistive plates, these detectors have shown excellent long-term stability and reliability. The assembly of the chambers is straightforward and does not require special skills or tools. The materials needed for their construction are readily available and cheap.

Current designs of the active layer

Various chamber designs have been investigated[5]. Of these two are considered particularly promising: a two-glass and a one-glass plate design. A schematic of the two chamber designs is shown in Figs. 2.31 and 2.32. The thickness of the glass plates is 1.1 mm and the gas gap is maintained with fishing lines with a diameter of 1.2 mm. The overall thickness of

the chambers, including layers of Mylar for high voltage protection, is approximately 3.7 mm and 2.6 mm, respectively.

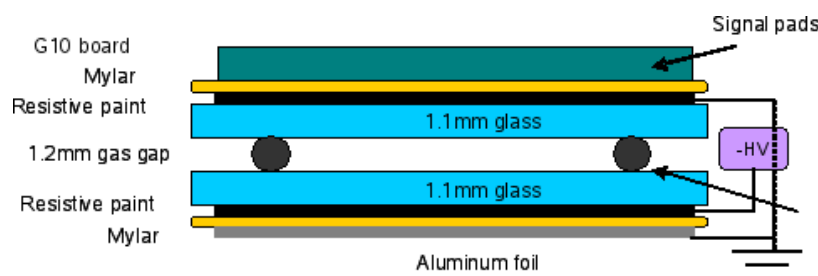


Figure 2.31: Schematic of the RPC design with two glass plates. Not to scale.

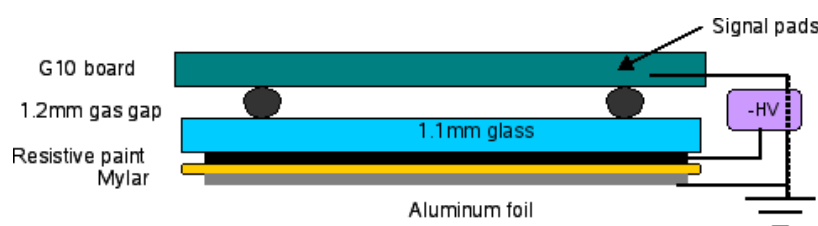


Figure 2.32: Schematic of the RPC design with one glass plate. Not to scale.

The chambers are operated in saturated avalanche mode with an average high voltage setting around 6.1 kV. The gas consists of a mixture of three components: R134A (94.5%), isobutane (5.0%) and sulfur-hexafluoride (0.5%).

The readout of the chambers consists of a pad board with $1 \times 1 \text{ cm}^2$ pads, read out individually. In order to avoid an unnecessary complexity of the readout system, the charge resolution of individual pads is reduced to a single bit (digital readout). In such a calorimeter the energy of incident particles is reconstructed as a function of the number of pads with signals above threshold.

Results from tests

As part of the program of the CALICE collaboration[6], a group consisting of members from Argonne, Boston University, Fermilab, and University of Iowa[7] built and tested of the order of 20 chambers.

The tests included extensive characterization of the chambers with a 14-bit (analog) readout system. As an example Figure 2.33 shows the MIP detection efficiency and the fraction of streamers as a function of high voltage. Additional results can be obtained from reference ??.

A small test calorimeter consisting of up to 10 chambers with an area of $20 \times 20 \text{ cm}^2$ was assembled and tested with both cosmic rays and in the Fermilab test beam. The active media were interleaved with 20 mm thick Steel plates. The results from the calibration using broad-band muons have been published in[8]. As an example of the results obtained with showering particles, Fig. ?? shows the longitudinal shower shape for 1, 2, 4, 8, and 16 GeV positrons. Additional tests with pions of various momenta were performed and showed the expected results[9].

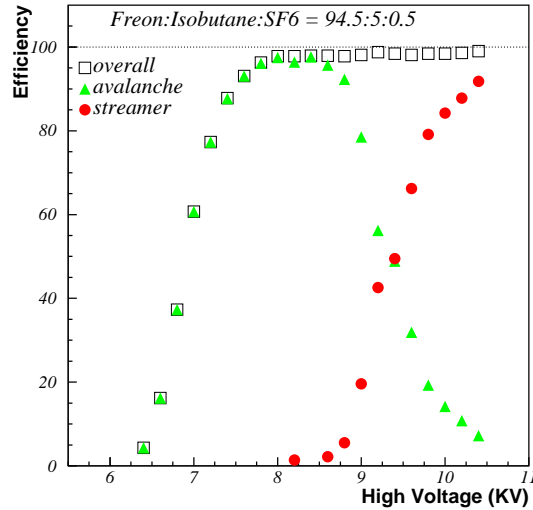


Figure 2.33: MIP detection efficiency and fraction of streamers as a function of high voltage.

The stack was also exposed to 120 GeV protons at various beam intensities to study the rate capability of RPCs. The results show no evidence of a dead time in excess of 0.3 ms. For rates in excess of 100 Hz/cm² the MIP detection efficiency drops exponentially (with a time constant depending on the beam intensity) until reaching a constant level, see Fig. 2.35 and reference[10] for more details.

Furthermore, the stack has been operated continuously for over 18 months. During this time the noise rate, MIP detection efficiency and pad multiplicity have been constantly monitored using cosmic rays. Their dependence of the RPC performance on the environment has been studied in great detail[11]. So far no long-term degradation of the response has been observed.

In summary, the tests show the viability of an RPC-based hadron calorimeter with digital readout as an integral part of a detector optimized for the application of Particle-Flow Algorithms to the measurement of hadronic jets.

Plans for further tests

The group is currently assembly a larger prototype calorimeter with 40 planes and approximately 400,000 readout channels. The completed calorimeter will be tested in the Fermilab test beam in standalone mode and also together with the CALICE Silicon-Tungsten electromagnetic calorimeter. The tests will validate the concept of a digital hadron calorimeter with RPCs as active medium and the proposed technical approach presented here. The prototype calorimeter will provide precision measurements of hadronic showers with unprecedented spatial resolution, to be confronted with various models of these showers.

HCAL module design

Several models of the HCAL barrel have been developed and are described in other parts of this document. These models require large area RPCs, provide minimal space for the readout electronic, gas and high voltage supplies and preclude easy access.

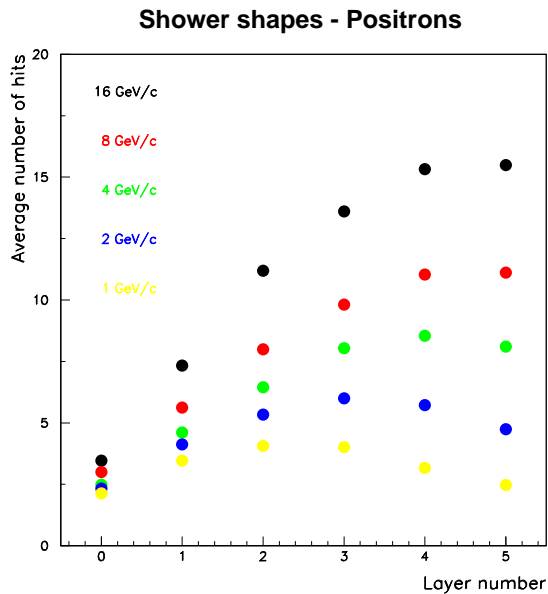


Figure 2.34: Longitudinal shower shape as measured with 1, 2, 4, 8 and 16 GeV positrons.

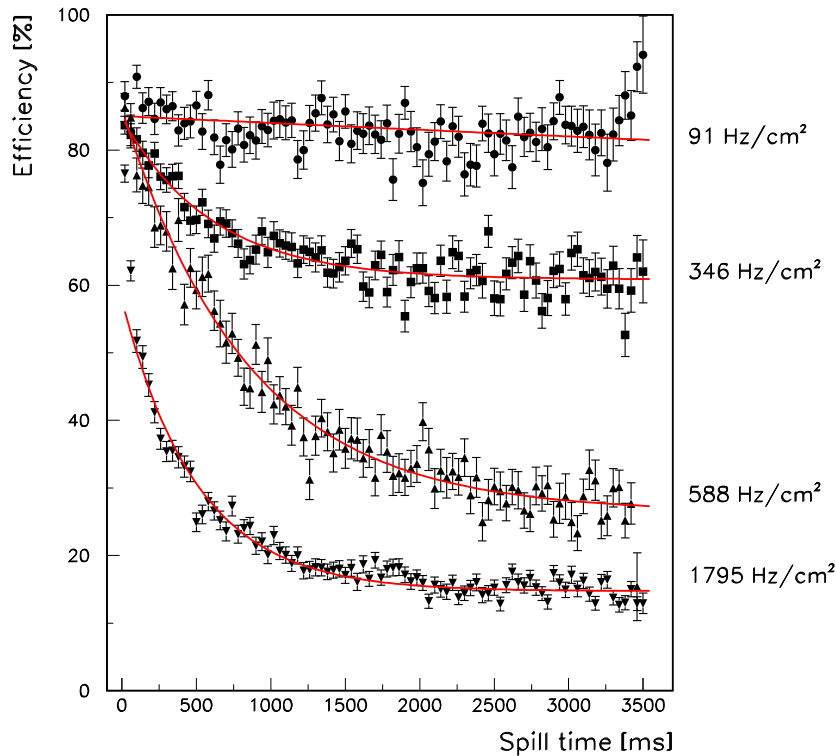


Figure 2.35: MIP detection efficiency as function of time from the start of a spill for different beam intensities.

Timescales

The analysis of the data from the small scale prototype is close to complete. An additional three publications are planned: Response to positrons and pions, Measurement of the rate capability, and Measurement of the Environmental Dependence of the RPC Performance.

The group is currently assembling the large prototype calorimeter to be tested in the Fermilab test beam. Completion of the construction phase is expected sometime during CY 2009, to be followed by tests in the Fermilab test beam. The data analysis will be carried through to 2011.

The projected R&D for the module/technical prototype will initiate in 2010, after the completion of the construction of the large prototype calorimeter. This phase is expected to last 2 – 3 years

2.2.3.3 GEM option

The University of Texas at Arlington (UTA) team and collaborators have been developing a digital hadronic calorimeter (DHCAL)[12] using GEM as the sensitive gap detector technology. GEM can provide flexible configurations which allow small anode pads for high granularity. It is robust and fast with only a few nano-second rise time, and has a short recovery time which allows a higher rate capability than other detectors. It operates at a relatively low voltage across the amplification layer, and can provide high gain using a simple gas (ArCO₂), which protects the detector from long term degradation issues, and is stable. The ionization signal from charged tracks passing through the drift section of the active layer is amplified using a double GEM layer structure. The amplified charge is collected at the anode layer with pads at zero volts. The GEM design allows a high degree of flexibility with, for instance, possibilities for microstrips for precision tracking layer(s), variable pad sizes and shapes, and optional ganging of pads for finer granularity of future readout, if allowed by cost considerations and demanded by physics requirements. Fig. 2.36 depicts how the double GEM approach can be incorporated into a DHCAL scheme.

Performance of Prototype GEM Chambers

A number of double GEM chambers have been built and tested with cosmic rays sources, and test beam. Initial studies were conducted on signal characteristics and gain from a small prototype GEM detector read out using the QPA02 chip developed by Fermilab for Silicon Strip Detectors. The gain of the chamber, with a 70% Ar/20% CO₂ gas mixture, was determined to be of the order 3,500, consistent with measurements done by the CERN GDD group. The MIP efficiency was measured to be 94.6% for a 40 mV threshold, which agrees with a simulation of chamber performance. The corresponding hit multiplicity for the same threshold was measured to be 1.27, which will be beneficial for track following and cluster definition in a final calorimeter system. A gas mixture of 80% Ar/20% CO₂ was shown to work well and give an increase in gain of a factor of three over the original mixture. A minimum MIP signal size of 10 fC and an average size of 50 fC were observed from the use of this new mixture. The prototype system has proved very stable in operation over many months, even after deliberate disassembly and rebuilding, returning always to the same measured characteristics.

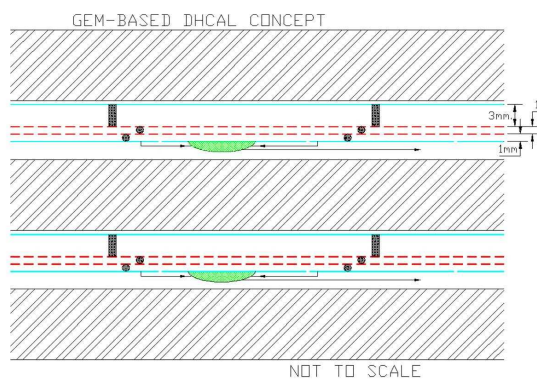


Figure 2.36: Left: GEM DHCAL Concept. Right: A 30cm x 30cm foil from 3M Corporation.

As the first step for the full-size $1\text{m} \times 1\text{m}$ test beam chambers, we developed $30\text{cm} \times 30\text{cm}$ GEM foils together with Micrinterconnect Systems Division of 3M Corporation. The foils are divided into 12 independent HV strips for operational safety. An example of one of these foils is shown in Fig. 2.36. For mechanical assembly, we have developed tools to handle large area foils, maintaining flatness of the foils, and the detector walls that provide gas and HV feed throughs. A modification of this foil design will allow sections of $1\text{m} \times 30\text{cm}$ foils for the unit chamber. We constructed several prototype chambers using these foils and readout pad boards and exposed them in various beams. These chambers were read out using the 32-channel QPA02 chip. Beam tests were conducted at Fermilabs Meson Test Beam Facility (MTBF). Using a 120 GeV proton beam we tested a single multi-channel chamber.

We were able to determine relative efficiency and fractional cross talk ratio. Fig. 2.37 (a) shows the signal without noise subtraction (blue), noise (purple) and noise subtracted signal (red) when the 120 GeV proton beam is incident on the target pad. The noise subtracted signal distribution shows a Landau shape as expected. Fig. 2.37 (c) shows the relative efficiency measured on this pad as a function of threshold, giving an efficiency of 94% at 40mV.

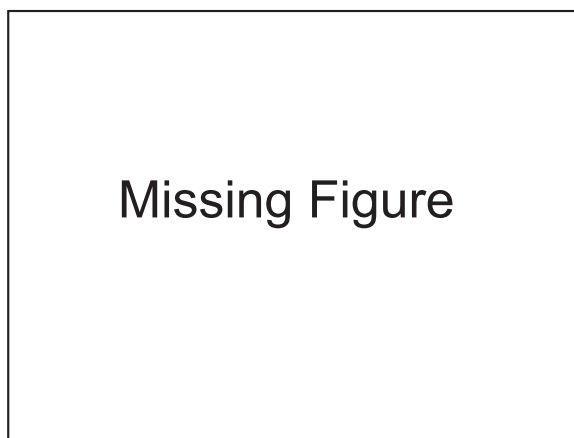


Figure 2.37: (a) Noise subtracted signal, (b) Adjacent pad, (c) Relative efficiency, (d) Cross talk

In order to measure the cross talk rate, we read out the pad immediately next to the pad with the trigger. Fig. 2.37 (b) shows the pulse height distribution of the pad number 7 when beam is incident on the immediate neighboring pad. Blue dotted lines represent the signal before noise subtraction, the purple lines represent noise, and the red line is the noise subtracted signal. From these, we can extract the fractional cross talk rate on a pad, as shown in Fig. 2.37 (d). From these studies, while the probability of the cross talk is small for both the pads, it should be emphasized that given the size of the trigger paddle this distribution includes charge sharing between the neighboring pads and multiple proton events.

Multi-channel Readout using the KPiX chip

As the next phase for multiple channel readout system, we have been working with the high density analog readout system, KPiX, which is being developed at SLAC, and is described in detail in Ref. [13]. We plan to conduct further beam tests using KPiX once we complete integrating the chip with our GEM chambers and fully characterize its behavior in bench tests. The chip has been modified to include a switchable gain to accommodate small signals from a GEM chamber. We have characterized KPiX v.4 in terms of time variations of gains and pedestals. We now have KPiX v.7 and a new anode board with protection on each of the 64 channels. Fig. 2.38 shows the signal distribution from the GEM chamber with the KPiX chip from a channel right under the Sr90 source.

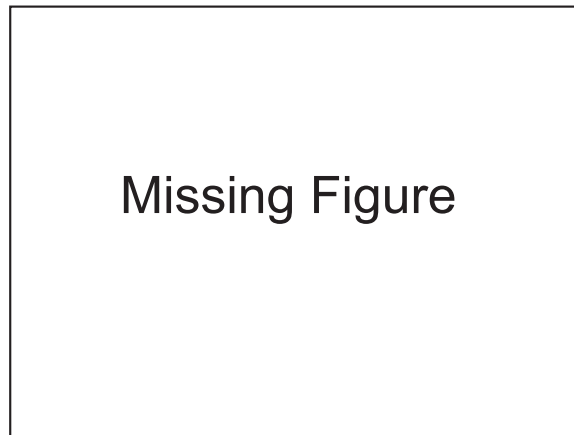


Figure 2.38: Signal from KPiX chip - anode pad under source

The plot does not show the usual Landau peak due to the periodic reset scheme used in KPiX v.7. We have simulated this behavior and have obtained agreement with the observed results.

Future R and D Plans

The next stage of development is to build and test 1m x 33cm chambers. We will use foils from CERN GDD since 3M Corporation is no longer a source of GEM foils. We plan to construct as many unit chambers using 1m x 33cm GEM foils produced by CERN as funds allow. Three of these unit chambers will make up one sensitive layer of size 1m x 1m. The CERN GDD workshop has been working on developing cost effective technology to produce large size GEM foils. We have decided to place an order with CERN to produce 1m x 33cm GEM foils. We will work on development of mechanical structure, the electronic readout board schemes and the schemes for connecting the three unit chambers together to form one 1m x 1m large layer. We plan to construct these unit chambers through 2009. Through the construction stage, we will test these unit chambers with source, cosmic rays

and with beams. We will then put as many of these 1m x 1m chambers as possible into the CALICE cubic-meter stack in early or mid-2010. This phase, however, depends heavily on the availability of funds.

Finally, we have been considering an alternative to the standard GEM foil technology. Tests of Thick-GEMs (TGEM) [14] have shown that a single layer achieves multiplication levels typical of at least a double-GEM device. A TGEM is a printed circuit board, clad with copper on both sides through which holes have been drilled. A typical configuration might be a 0.4 mm thick board with 0.3 mm diameter holes spaced 1 mm apart. It also has been shown that TGEMs can be produced on a large scale. We are collaborating with the Weizmann Institute to work on production and prototyping of GEM chambers using large scale TGEMs. In addition, the recent development of resistive-electrode TGEM (RETGEM) [15] will also be investigated as another alternative solution.

2.2.3.4 MICROMEGAS option

Micromegas - a compact approach

A very interesting alternative for the DHCAL active medium is the Micro Mesh gaseous structure (MicroMegas) [16], a detector based on the micro-pattern detector technology, today widely used by many experiments: COMPASS, CAST, NA48, n-TOF, T2K and the ILC TPC project. First prototypes consist of a commercially available fine mesh which separates the drift gap (3 mm) from the amplification gap (128 μm). This simple structure allows full efficiency for MIPs and thanks to thin pillars, provides a good uniformity over the whole surface. The rate obtained with Micromegas chamber is not constrained, as it is the case for the Glass RPC. Moreover the tiny size of the amplification avalanche, results in fast signals without physical cross talk and leads to low multiplicities. The chosen bulk technology based on industrial PCB processes, offers a robust detector with no working voltages higher than 500 V. MicroMegas are therefore a very appealing possibility to equip a DHCAL optimized for the PFA.

Description of Prototypes

Three different kind of prototypes with 1 cm² pad size were built at LAPP. One type with analog readout for characterization, two types with embedded digital ASICs.

The analog readout is performed with boards from the CEA laboratory equipped with 6 GASSIPLEX chips (96 channels in total), connected to VME ADCs and featuring high resolution charge determination (12 bits, 0.4 fC per ADC Count). The data acquisition is performed by the CENTAURE program from SUBATECH-Nantes [17]. Three MicroMegas with 6x96 pads and one MicroMegas with 12x32 pads (see Fig. 2.39) were designed for this analog readout.

Two mixed-signal ASICs are foreseen for the digital readout, the HARDROC [18] and the DIRAC [19]. The former was chosen for the baseline of the 1 m³ European DHCAL project in order to get rapidly the digital readout of either MicroMegas or Glass RPC. Whereas the latter is a longer term R&D which aims to obtain a low cost ASIC with an easy signal routing implementation on the detector PCB, an easy calibration and a digital readout down to MicroMegas MIP charges.

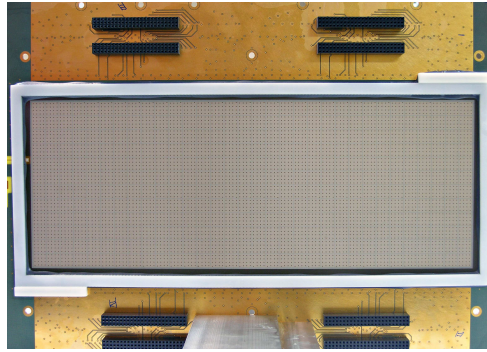


Figure 2.39: MicroMegas 12x32 cm² prototype with 384 pads of 1 cm² and designed for analog readout.

All MicroMegas bulks are realized by lamination of photosensitive foils and a mesh laid on a PCB with different signal routing depending on the readout. By a photolithographic method, the photo resistive material is etched producing the 128 μm pillars. A thin copper foil, glued to the calorimeter absorber medium (2 mm thick plate out of a 2 cm thick absorber), defines the drift cathode. The top of the chamber is therefore not contributing to the active medium thickness. The drift gap is realized with a 3mm thick frame which provides also the gas inlets (see Fig. 2.39 and 2.44).

Analog Readout Prototypes

Using a ^{55}Fe X-ray source, the gain was measured with the analog readout up to 10000 and the energy resolution down to 8.5% corresponding to a FWHM of 19.6% (see Fig. 2.40). The gain and the FWHM were measured as a function of the drift field, amplification field, gas flow and pressure variables. The expected exponential behavior of the gain versus the amplification field was verified and an absolute pressure dependence of -2 fC per mbar was determined.

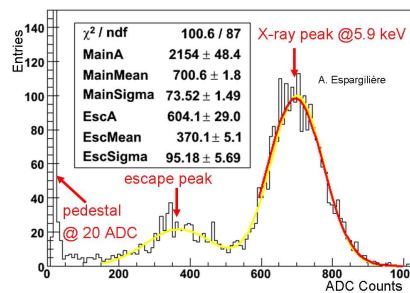


Figure 2.40: MicroMegas analog response to a ^{55}Fe X-ray source with $E_{\text{mesh}} = 35$ kV/cm and $E_{\text{drift}} = 167$ V/cm. The 5.9 keV emission leads to 680 ADC Counts or 277 fC. For a 3 mm drift gap and a gas mixture of 95% argon, 5% isobutane, the gain is 7600.

In summer 2008, four prototypes with analog readout were assembled in a stack and tested at the H2 line of the SPS-CERN. A total acquisition time of 5 days has allowed collection of data with about 200k muons and 200k pions without absorber, plus 250k pions with an upstream 30 cm iron block and 1.8 cm iron absorbers between each prototype.

In the preliminary analysis of the 200k muons at 200 GeV, platinum events were selected by requiring one and only one hit (ADC Counts > 27) in each chamber. The MIP Landau distribution on each pad was obtained with a Most Probable Value (MPV) around 45 fC. The four chamber mapping was performed in terms of pedestal mean and sigma, MIP landau MPV and sigma. The pedestal gaussian fits have shown very good noise conditions with an average sigma of 0.6 fC. The gain is uniform within each prototype with a RMS of 11% for the four prototypes gain dispersion normalized to 100% (see Fig. 2.41). Electronics channel disparity and drift space homogeneity are still to be checked.

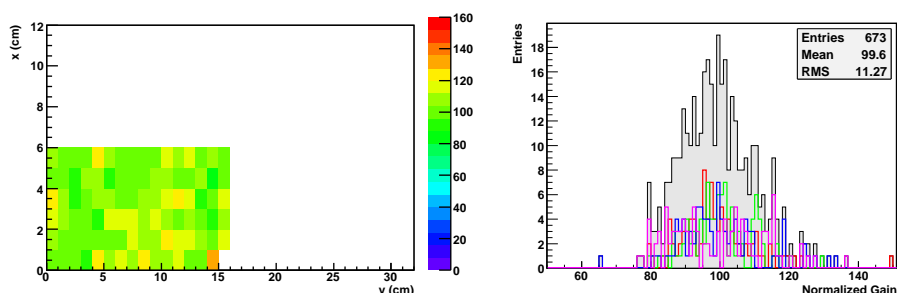


Figure 2.41: Example of a prototype mapping with analog readout: MPV in ADC Counts for golden events selected in a 200 GeV muons sample. Gain dispersion normalized to 100% for the four prototypes with analog readout

With the same muon sample, golden events were selected by requiring one and only one safe hit (ADC Counts > 51) in three of the four prototypes. Using these three hits, a straight line fit is performed. The efficiency of the last prototype is obtained by looking for at least one hit (ADC Counts > 29, charge > 2.8 fC) in a 3x3 pads square, centered around the extrapolated line (see Table 2.8). With the golden events the multiplicity was measured by counting the number of hits in the same square. A multiplicity of about 1.07 was found.

Prototype	Efficiency (charge > 2.8 fC)
0 (96 pads)	$97.05 \pm 0.07\%$
1 (96 pads)	$98.54 \pm 0.05\%$
2 (96 pads)	$92.99 \pm 0.10\%$
3 (384 pads)	$96.17 \pm 0.07\%$

Table 2.8: Efficiencies for the MicroMegas prototypes with analog readout
Digital Readout Prototypes

The DIRAC chip was embedded on an 8x8cm PCB with additional sparks protection (see Fig. 2.42) [19]. For the first time a prototype with a bulk laid on a PCB with embedded electronics reaching a total thickness of 12 mm including 2 mm absorber was operational and exposed to 200 GeV pions at the H2 beam line in summer 2008. Fig. 2.43 shows the beam profile with a threshold above 19 fC. Further tests with a stack of prototypes are compulsory to measure threshold dependence, efficiencies and multiplicities.

Several new 8x32 pads prototypes have been realized with four HARDROC chips em-

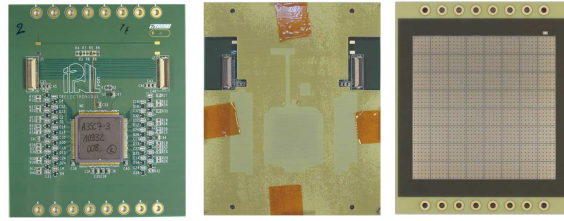


Figure 2.42: Prototype of the MicroMegas with DIRAC digital readout. From left to right: ASIC side, ASIC side with mask for bulk laying and pad side with bulk.

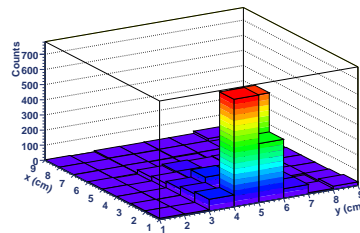


Figure 2.43: Prototype mapping of the MicroMegas with DIRAC digital readout: digital counts in a 200 GeV pion sample.

bedded on one PCB (see Fig. 2.44). The electronics is tested with the Detector InterFace board (DIF) which has been designed at LAPP in the frame of the DHCAL CALICE data acquisition system [20]. These prototypes have been exposed to 7 GeV pions during the November 2008 beam test at the T9 line of the PS-CERN.

The 1 m² Prototype

The 1 m² prototype is an assembly of six bulks with 24 ASICs each in on a single mask. The chamber is closed by two plates of 2 mm thick stainless steel (see Fig. 2.45). This prototype should not exceed a total thickness of 6 mm (without absorber). It is scheduled to build this prototype beginning 2009 in order to test it in the beam with the former smaller prototypes during late summer 2009. The 1 m² design is foreseen for large quantities production in order to build a 1 m³ DHCAL prototype. The funding for the Micromegas DHCAL is from European sources.

2.2.3.5 SCINTILLATOR option

Scintillating Tiles

The CALICE Collaboration has been pursuing the design and prototyping of a fine granularity scintillator-based hadron calorimeter. This option capitalizes on the marriage of proven detection techniques with novel photodetector devices. Absence of fluids/gases and strong electric fields inside the detector aids longevity and operational stability. A scintillator hadron calorimeter will perform much better at traditional calorimetry than most of the other options under consideration. This is important since the performance of PFA's degrades as a function of the energy. Furthermore the flexibility offered by the scintillator response allows one to trade amplitude resolution with granularity to optimize the overall cost and performance.

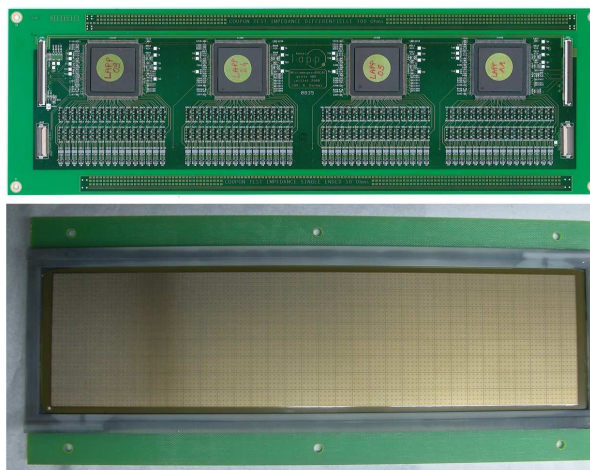


Figure 2.44: Prototype of the MicroMegas with 4 HARDROCs digital readout. From top to bottom: ASIC side and pad side with bulk and drift frame.

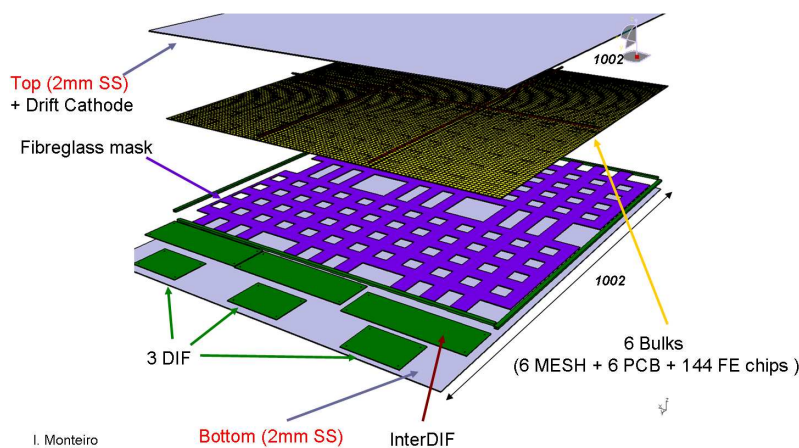


Figure 2.45: Design of the 1 m² MicroMegas Prototype.

The main challenge for a scintillator-based calorimeter is the architecture and cost of converting light, from a large number of channels, to electrical signal. Our studies demonstrate that small tiles interfaced to Silicon Photomultipliers (SiPMs)/Multi Pixel Photon Counter (MPPC) photodetectors [21], [22] offer an elegant solution. SiPM/MPPCs are multi-pixel photo-diodes operating in the limited Geiger mode. They have distinct advantage over conventional photomultipliers due to their small size, low operating voltages and insensitivity to magnetic fields. The *in situ* use of these photodetectors opens the doors to integration of the full readout chain to an extent that makes a high channel count scintillator calorimeter entirely plausible. Also, in large quantities the devices are expected to cost a few dollars per channel making the construction of a full-scale detector instrumented with these photo-diodes financially feasible.

Test Beam Prototype

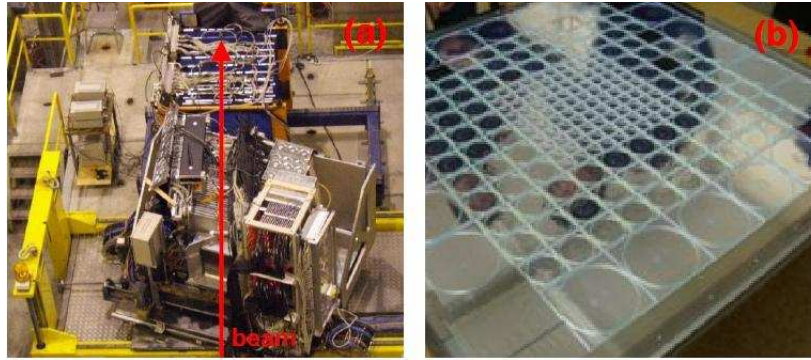


Figure 2.46: CALICE test beam setup at CERN (left) and an active layer of the scintillator-SiPM prototype (right)

A $\approx 1 \text{ m}^3$ scintillator-SiPM prototype has been designed, constructed and exposed to a test beam during the 2006-2008 period at CERN and Fermilab (see Fig. 2.46a). The active layers of the HCAL prototype consist of 5 mm thick scintillator tiles sandwiched between 2 cm thick steel absorber plates. In reality the absorber is split into three parts: 1.6 cm absorber plate and two 0.2 cm thick top and bottom skins of the module which houses the tiles. Each tile comes with its own 1mm diameter WLS fiber mated to a SiPM embedded in it. The faces of the tile are layered with the VM2000 reflector foil while the edges were matted to provide diffuse reflection. The tiles come in three granularities: 3 cm x 3 cm, 6 cm x 6 cm and 12 cm x 12 cm (see Fig. 2.46b). The granularity of the prototype was optimized to achieve the physics goals within a reasonable budget. The SiPMs are connected to 18-channel custom ASICs read out by a VME based data acquisition system.

Over six run periods each approximately 3-4 week long millions of electron, positron, pion and proton events in the 2-180 GeV/c range were collected (see Fig. 2.47a). Also written to disk were a large sample of muons of determined and undetermined momenta. Additionally, for calibration and monitoring purposes pedestal and LED events were taken at regular intervals. These data have provided a detailed picture of the full hadron shower with a granularity not seen before (see Fig. 2.47b). Ongoing analysis of the data has gone a long way in establishing the scintillator-SiPM option as a calorimeter technology, benchmarking hadron shower Monte Carlo's and testing the particle-flow paradigm using hadrons from real data [23].

Current and Planned R&D

A detector consisting of a few million channels requires a high degree of integration. The small size, low bias voltage and magnetic field immunity of the SiPMs has already allowed us to take the first step towards this goal. The photo-conversion occurs right at the tile thus integrating the light transport and conversion functions on the tile itself [24]. The next logical step is to bring an equivalent level of integration to the electrical signal path. While individual cables per tile are feasible for the prototype containing a few thousand channels, they are not a viable option for a device with a few million channels. What is needed is the development of an Integrated Readout Layer (IRL). In general for the IRL, we propose to have a printed circuit board (PCB) inside the detector which will support the scintillator

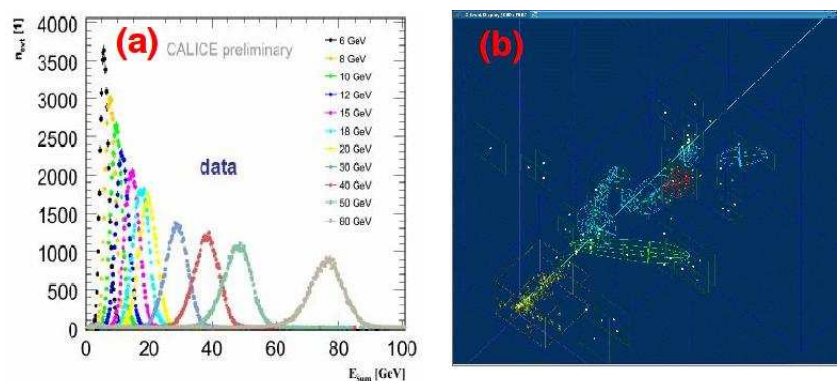


Figure 2.47: Response of charged pions in the scintillator-SiPM HCAL (left) and the imaging qualities of the calorimeter (right).

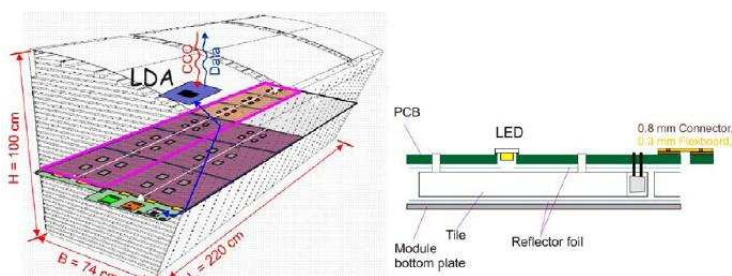


Figure 2.48: Barrel wedge instrumented with IRL planes (left) and conceptual design of an IRL (right).

tiles, connect to the silicon photodetectors and carry the necessary front-end electronics and signal/bias traces (see Fig. 2.48). This can however be achieved in a number of ways and different groups are working on complementary approaches in a coordinated fashion.

Of particular interest in this regard is the potential of direct or fiberless coupling of the silicon photodetector to the scintillator tile. Significant simplification in construction and assembly can ensue if the MPPCs can be coupled directly to the scintillator tiles. Equally importantly, the total absence of fibers would offer greater flexibility in the choice of the transverse segmentation while enhancing the electro-mechanical integrability of the design. Initial studies into this approach have been very encouraging as both adequate response and uniformity can be obtained with directly coupled tiles (see Fig. 2.49).

It is planned that the R&D being carried out on the scintillator-SiPM hadron calorimeter option in America, Asia and Europe will be brought together for a EUDET/CALICE 'technology' prototype in 2010. This 'wedge' will be instrumented with IRL planes. Complementary versions of the IRL planes being pursued by different groups in the collaboration will be tested and compared. All the IRL's will be instrumented with electronics specifically developed with the ILC bunch structure and machine parameters in mind.

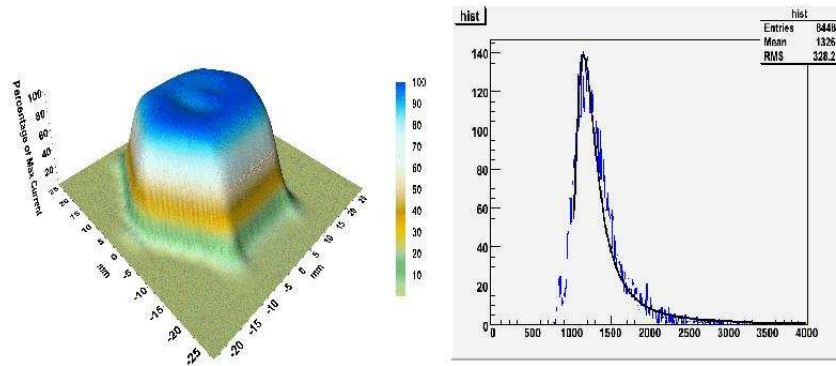


Figure 2.49: Response uniformity of a directly coupled tile (left) and response of a directly coupled tile to cosmic ray muons (right).

2.2.3.6 Dual Readout option

2.3 Homogeneous Dual Readout Option

2.3.1 Principles of Operation: Energy Resolution

The principal limitations of the hadron energy resolution come from two sources:

- The sampling nature of the conventional hadron calorimeters.
- a significant and fluctuating fraction of the incoming hadron energy is converted into non-observable forms of energy (primarily nuclear binding energy).

These effects lead to a significant non-linearity of the response of the detector and to a difference of the response to neutral and charged pions (often referred to as e/π ratio). They are responsible for the dominant contribution to jet energy resolution, as the result of the fluctuations in the jet fragmentation.

Good jet energy resolution requires a calorimeter where both of the above-mentioned factors are eliminated or largely reduced. This can be accomplished with a homogenous, totally active calorimeter with dual readout: scintillation and Cherenkov. Totally active calorimeter eliminates all contributions related to the sampling nature of the device whereas an anti-correlation between the scintillation and Cherenkov light can be used to reduce the fluctuations of the nuclear binding energy loss. Figure 2.50 shows an example of scintillator and Cherenkov energies and their correlation.

A dimensionless anti-correlation function may be derived and is shown in Figure 2.51. Application of an event-by-event correction to a sample of hadron induced showers improves the energy resolution and makes the average hadron response equal to the beam energy

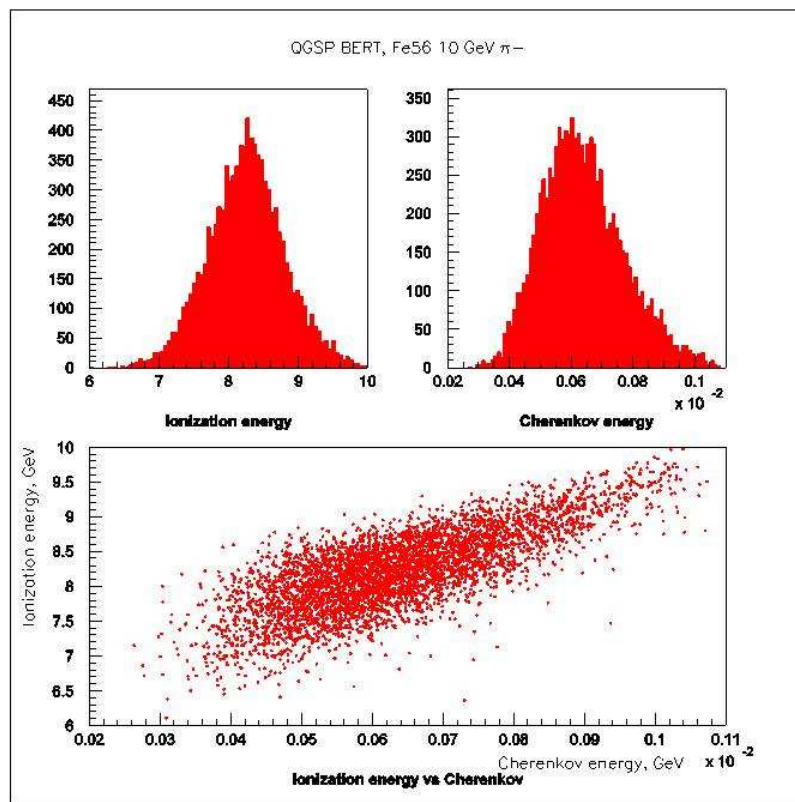


Figure 2.50: Scintillator and Cherenkov signals and their correlation

(hence equal to the response to electrons on neutral pions of the same energy), as shown in Figure 2.51.

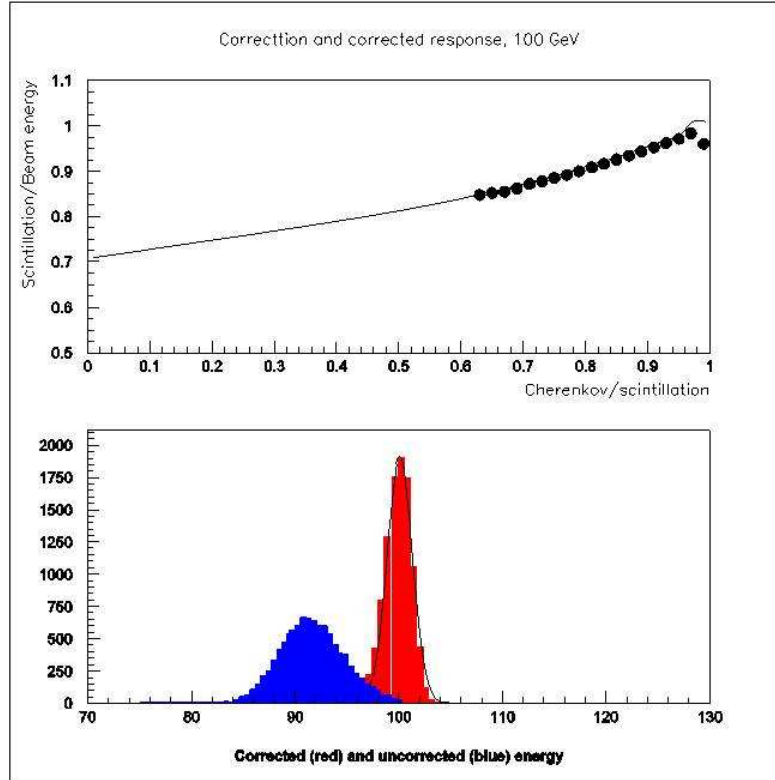


Figure 2.51: (a) (top) The correlation between the average fraction of the beam energy detected via scintillation and the ratio of responses measured with the Cherenkov and the scintillation light. (b) (bottom) A response of the total absorption calorimeter to 100 GeV pion beam (blue) and the same response corrected on the event-by-event basis using the correlation.

A study has shown that, using the correlation, for single hadrons the energy resolution is of the order of $0.15/\sqrt{E}$ whereas for hadronic jets above 100 GeV the energy resolution is better than $0.25/\sqrt{E}$. Figure 2.52 shows results for jets as a function of jet energy.

It should be pointed out that the energy resolution described above is attained without any relation to the detector granularity, only a total amount of scintillation and Cherenkov was used. Such a technique does not, therefore, require any particular segmentation of the calorimeter on one hand, but it does not preclude it other, provided that the adequate cross-calibration of the detector elements is accomplished. The calorimeter segmentation will be determined by a combination of 'other' physics-driven requirements and practical aspects like calibration and engineering aspects. One should expect that additional information available from the spatial distribution of the observed signals may be used to improve further the energy resolution for the hadronic jets.

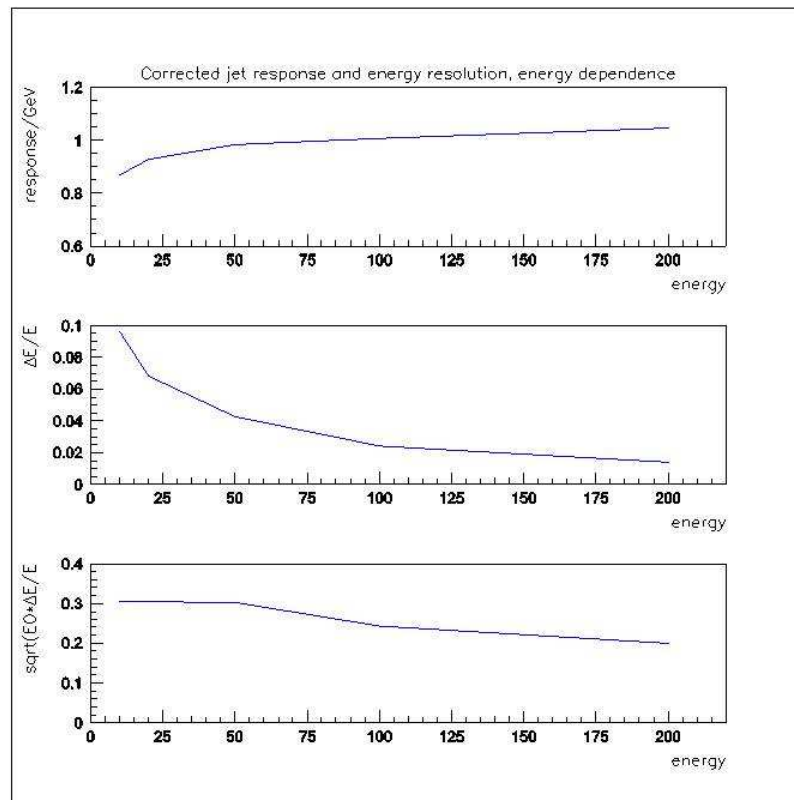


Figure 2.52: Response linearity, energy resolution, and scaled energy resolution for hadronic jets.

2.3.2 Enabling Technological Developments

The concept of the dual readout calorimetry has been around for more than two decades [Paul Mockett]. The required separation of the Cherenkov and scintillation light using the timing information has been demonstrated experimentally in 1984 [IEEE Transaction]. The DREAM Collaboration has recently demonstrated such a separation by using the wavelength separation [Wigmans]. Whereas the principles underlying the possible high resolution hadron calorimetry were known and understood for a very long time, the construction of a practical hadron calorimeter, especially with the hermeticity required in the colliding beam environment, was made possible by several technological breakthroughs:

- development of affordable, high density, scintillating crystals.
- advent of compact, inexpensive silicon-based photodetectors (APD's and SiPM's) capable of operating in a string magnetic field.

The specific requirements of the hadron calorimeter case are quite different from the other applications, hence there are no off-the-shelf solutions to the detector problems but the recent developments allow for an optimistic view that some additional R&D efforts may lead to a successful construction of a hadron calorimeter with unique capabilities of very high energy resolution, good particle identification and very good spatial localization of electromagnetic showers.

2.3.3 Conceptual Design of High Resolution Calorimeter (HRC)

A high resolution calorimeter is designed to fit into the space occupied by the ECAL and HCAL of the baseline design. It is constructed of optical "crystals" equipped with two sets of compact silicon photodetectors at the back. One set, equipped with the low pass optical filter and short integration gate electronics, is used to detect and measure the Cherenkov light. The other set, equipped with high pass filter and long integration gate electronics is used to detect and measure the scintillation component.

The barrel section is composed of four layers of crystals with approximate dimensions of $5 \times 5 \times 5cm^3$, followed by ten layers of larger crystals with approximate dimensions of $10 \times 10 \times 10cm^3$. First four layers of crystals have silicon pixel detectors attached to the front face.

The endcaps are constructed in a very similar fashion, with four layers of $5 \times 5 \times 5cm^3$ crystals followed by sixteen layers of $10 \times 10 \times 10cm^3$ crystals. Assuming crystals of density similar to lead tungstate, with the absorption length of the order of 20 cm this leads to a calorimeter with the thickness of 6λ at 90° and 9λ in a forward direction.

Calorimeter is constructed by assembling the crystals into non-projective modules with the help of structural epoxy and the readout cables transported to the back planes in non-projective slots. Compact nature of the photodetectors and minimal energy consumption of

the photodetectors and the associated readout electronics assures high average density of the calorimeter. The construction may result in mechanical units identical to the ones of the baseline design.

2.3.4 Principal Challenges of the HRC

Fundamental physics principles of the total absorption dual readout hadron calorimetry are relatively well understood. It is, naturally, highly desirable that this understanding is confirmed by a practical demonstration of the performance in the test beam, but for a construction of a practical detector there are several more milestones which need to be reached:

- development of inexpensive optical materials for the dual readout.
- availability of compact photodetectors capable of operation in a strong magnetic field and the corresponding low power dissipation front-end readout electronics.

In addition to these challenges, which must be met by industrial vendors, the realistic design of the detector will require detailed simulation and optimization studies as well as a complete engineering design. A realistic and robust scheme for the relative (channel-to-channel, scintillation-to-Cherenkov) as well as the absolute calibration must be developed as well.

2.3.5 R&D Program

In order to bring the HRC concept to the level necessary for considerations as a possible alternative calorimeter for the SiD detector it is necessary that sufficient progress is achieved along the following directions:

- Task 1: demonstration of good response linearity and energy resolution for hadrons in the test beam. At the same time the capabilities of adequate measurement of the spatial characteristics, in particular two close shower separation, must be established. Although it would be desirable, it is not necessary that these studies must utilize the final crystals and/or photodetectors.
- Task 2: optimization of the detector performance, including the algorithms for local dual readout corrections, jet finding and reconstruction, optimization of the detector granularity
- Task 3: engineering design of the detector and its support structure. In particular the attention must be paid that the inevitable structural members do not degrade the final energy resolution.
- Task 4: development of novel inexpensive optical materials
- Task 5: development of compact photodetection scheme and associated readout electronics

SUBSYSTEMS

References

- [1] Luminosity spectrum ref, eg S. Boogert.
- [2] Graham Wilson, talks.
- [3] Si-W reference(s); KPiX reference.
- [4] MAPS general description - details; appendix?.
- [5] “Various designs have been investigated...”
- [6] CALICE Collaboration.
- [7] Argonne, Boston University, Fermilab, and University of Iowa.
- [8] published muon results
- [9] published pion results
- [10] MIP efficiency results
- [11] RPC environmental
- [12] GEM DHCAL
- [13] KPiX ref.
- [14] Thick GEMs.
- [15] RETGEMs.
- [16] Micromegas
- [17] Subatech.
- [18] HARDROC.
- [19] DIRAC.
- [20] CALICE DAQ.
- [21] B. Dolgoshein et. al, NIM A504:48-52, 2003.

REFERENCES

- [22] Hamamatsu Photonics K. K., Solid-state Division, 1126-1 Ichino-cho, Hamamatsu City, 435-8558, Japan.
- [23] <https://twiki.cern.ch/twiki/bin/view/CALICE/CaliceAnalysisNotes>
- [24] “A high granularity scintillator hadronic-calorimeter with SiPM readout for a linear collider detector.” V. Andreev et al, NIM A540, 2005.

2.4 SiD MAGNET SUBSYSTEM

The magnet subsystem consists of its own following subsystems:

1. a large 5 T superconducting solenoid with a separated iron plate flux return that is integral with the muon tracking system,
2. a power supply, a pressurized water cooled dump resistor, and a conventional mechanical dump switch that move with the detector,
3. a helium liquefier that supplies 4.5 K LHe to both the solenoid and to a pair of 2 K cold boxes for each of the superconducting focusing quadrupoles,
4. oil flooded helium screw compressors with oil removal and helium gas storage all located on the surface,
5. a superconducting Detector Integrated “anti” Dipole (DID), and
6. two superconducting final focus quadrupoles (discussed in a separate section).

2.4.1 Superconducting Solenoid

The superconducting solenoid is an expensive and technically challenging component to procure. Its design is based on the engineering philosophy, experience and details used for the successful 4 T CERN CMS superconducting solenoid, the largest in the world. Thus a direct comparison is warranted with major parameters listed Table 2.9. The now standard high purity aluminum, superconductor stabilization with indirect LHe cooling technique will be used. The CMS individual self supporting winding turn design philosophy is used for SiD, becoming even more important due to the higher 5 T field and the increased radial softness of six layers versus four layers. Figure 2.53 is a cross section of the SiD magnet.

The SiD solenoid has a stored energy per unit cold mass of 12 kJ/kg, which is only slightly larger than the CMS value. This value is close to the upper bound that this type of large aluminum dominated magnet can be operated in a fail safe manner if the quench detection or energy extraction circuit were to fail. This specific energy density yields an average magnet temperature of 130 K. Prudent engineering for the SiD solenoid dictates that the total volume of aluminum stabilizer/structure can not be reduced by much from the present baseline design.

Special field uniformity requiring shims or size graded conductors is not necessary. Fringe field requirements are set at 100 gauss at 1 meter from the iron surface. Two-dimensional and three-dimensional ANSYS magnetic field calculations of the magnet were performed with the resulting field shape in the central region of the detector is seen in Figure 2.54. Eleven 20 cm thick iron plates with 4 cm gaps form both the barrel and end wall portions of the flux return. There is also a 4 cm gap between the barrel and end wall. Magnet field optimization is underway to improve uniformity with the required fringe fields.

REFERENCES

Table 2.9: SiD and CMS Superconducting Solenoid Comparison.

Quantity	SiD	CMS	UNITS
Central Field	5.0	4.0	T
Stored Energy	1.56	2.69	GJ
Stored Energy Per Unit Cold Mass	12	11.6	kJ/kg
Operating Current	17.75	19.2	kA
Inductance	9.9	14.2	H
Fast Discharge Voltage to Ground	300	300	V
Number of Layers	6	4	
Total Number of Turns	1457	2168	
Peak Field on Superconductor	5.75	4.6	T
Number of CMS superconductor strands	36	32	
% of Short Sample		0.33	
Temperature Stability Margin		1.8	K
Total Mass of Solenoid	125	220	Metric ton
Rmin Cryostat	2.591	2.97	m
Rmin Coil	2.731	3.18	m
Rmax Cryostat	3.392	3.78	m
Rmax Coil	3.112	3.49	m
Zmax Cryostat	± 3.033	± 6.5	m
Zmax Coil	± 2.793	± 6.2	m
Operating Temperature	4.5	4.5	K
Cooling Method	Forced flow	Thermosiphon	

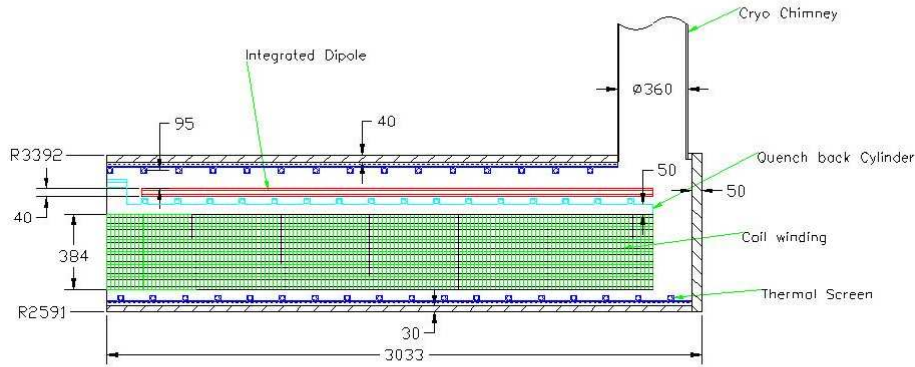


Figure 2.53: SiD Superconducting Magnet: Solenoid with Winding/Quench Back Cylinder/LHe Cooling Tubes, Cryostat, Thermal Shields, and Detector Integrated Dipole.

The CMS conductor was the baseline design and is the fall back position for SiD. All magnet ANSYS finite element stress analysis to date has been with this conductor. However, a more advanced and most likely cheaper conductor is being pursued and is proposed for this LOI. It is based on dilute high purity aluminum alloys such as Al-0.1%Ni that have been studied more extensively since CMS and was used in the ATLAS central solenoid. Figure 2.55 is a photo of the CMS conductor and an advanced SiD conductor design using Al-0.1%Ni and a novel internal high strength stainless steel reinforcement. An ANSYS coupled transient electromagnetic and thermal diffusion model is being used to evaluate conductor stability. Technical Note ?? provides analysis details with the most current set of results. With large size high purity aluminum stabilized superconducting conductors, current is slow to diffuse into the aluminum during a temperature excursion. Thus a higher resistivity, and therefore higher strength, aluminum stabilizer can have stability margins equal to a conductor with lower resistivity aluminum. A stability margin similar to CMS will be used. ANSYS is also being used to evaluate strength and bending stiffness for coil winding. Compared to CMS this advanced conductor has reduced bending stiffness that facilitates winding. Other conductor stabilizer possibilities are also under consideration and study. These include TiB₂ grain refinement, intermetallics creating aluminum matrix composites and cold working via the equal area angle extrusion process. The current state of these studies is referenced in Technical Note ??.

The superconductor will be internally wound into two precision aluminum 5083-H321 mandrels. All CMS winding procedures such as conductor milling to size, cleaning, and taping will be employed. CMS epoxy vacuum impregnation and mandrel joining techniques will be

REFERENCES

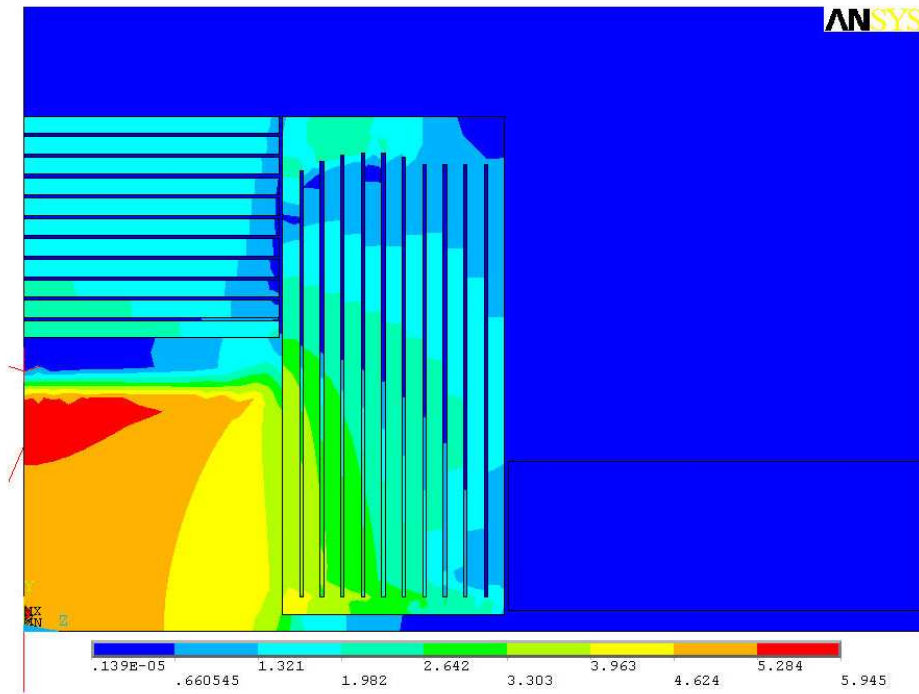


Figure 2.54: SiD central field contours in $|B|$, fields in the iron shown by intensity scale. The iron Pac Man is included and shown in the rectangle in the lower right.

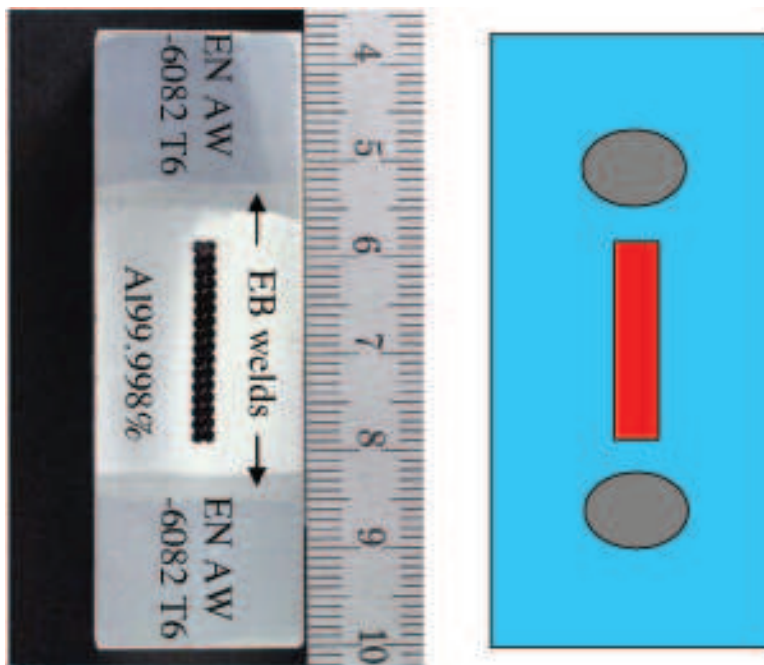


Figure 2.55: Photo CMS conductor and proposed SiD conductor.

used. CMS conductor splicing methods shall also be used. CMS coil winding experience will significantly reduce the SiD time and expense of winding line setup and commissioning. Coil winding and vacuum impregnation will take place at the vendor's facility. Most likely, but to be decided latter, will be a vendor initial assembly, cool down and low current checkout. In any event, the magnet will be shipped as two separate coils and a vacuum shell.

ANSYS studies compared SiD and CMS solenoid stresses, deflections and forces. All stresses are evaluated after cool down and energization. For this comparison the CMS conductor was used in the SiD analysis. Note that all stress and deflections are very similar for the two coils.

Table 2.10: Mechanical Comparison of SiD and CMS Solenoids.

Quantity	SiD	CMS
Von Mises Stress in High Purity Aluminum	22.4 MPa	22 MPa
Von Mises Stress in Structural Aluminum	165 MPa	145 MPa
Von Mises Stress in Rutherford Cable	132 MPa	128 MPa
Maximum Radial Displacement	5.9 mm	~ 5 mm
Maximum Axial Displacement	2.9 mm	~ 3.5 mm
Maximum Shear Stress in Insulation	22.6 MPa	21 MPa
Radial Decentering Force	38 kN/mm	31 kN/m
Axial Decentering Force	230 kN/mm	85 kN/m

The power supply, dump resistor and dump switch are attached on the side of the detector near the top. These three components are arranged to be all in line with the solenoid current leads, thereby minimizing the buswork. Power supply and mechanical dump switch are standard design components procured from outside vendors. A novel compact pressurized water cooled dump resistor will be used instead of a very large air cooled dump resistor such as the type used for CMS and other large superconducting magnets. An ASME coded vessel holding 3100 liter of water will rise to a conservative design value of 150 C at 0.48 MPa assuming the worse case of all 1.56 GJ deposited as sensible heat in the water of the resistor. Correct dimensioning of the stainless steel resistor element ensures that boiling heat transfer is only 1/3 of the peak nucleate boiling flux at the metal/water interface. A 1.50 m diameter \times 3.5 m tall cylindrical tank could be used. This design concept eliminates long runs of 18 kA cable to an air cooled resistor or long vent pipes of boiling water vapor to the surface. Internal connections will provide for both fast dump and normal slow dump modes. A center tap grounding wire is attached to the electrical center of the resistor. Technical Note ?? provides complete design details.

Quench protection safety will less stringent than for the CMS coil due to the lower stored energy and inductance. A conservative 300 V to centered tapped ground is chosen. Experimental tests and computer simulations show that the CMS quench propagation velocity around one complete turn is faster than turn to turn quench propagation through the insulation. Because we have chosen identical CMS conductor size and insulation thickness

REFERENCES

with very similar conductor electrical and thermal properties, peak temperatures will be less than CMS's 80 K with dump resistor but equal to CMS's 130 K with dump breaker failure. Both SiD and CMS safety rely on the winding mandrel serving as a quench back cylinder spreading the quench on the outer layer and absorbing some of the stored energy.

2.4.2 Cryostat and Magnet Iron

The cryostat, ~ 60 K thermal shield, current leads, tie rods, and instrumentation will all be designed using standard cryogenic techniques. Current leads will be very similar to the CMS current leads. Vacuum shells will be built according to the ASME pressure vessel code design rules. Two separate iron penetrations will be used, a $70\text{ cm} \times 40\text{ cm}$ chimney for the current leads and 36 cm diameter chimney for the cryogenic plumbing. Vacuum pump down will take place through both chimneys. Tie rods will be segmented into three different systems based on direction (axial, vertical and radial) just as they were with CMS and BaBar. They will be manufactured from Inconel 718 or Ti-5Al2.5Sn ELI. Radial and vertical loads will be carried to the cryostat outer wall. Axial loads will be carried to the cryostat end plates. In all cases, the tie rod systems are substantially stiffer than the magnetic spring constant.

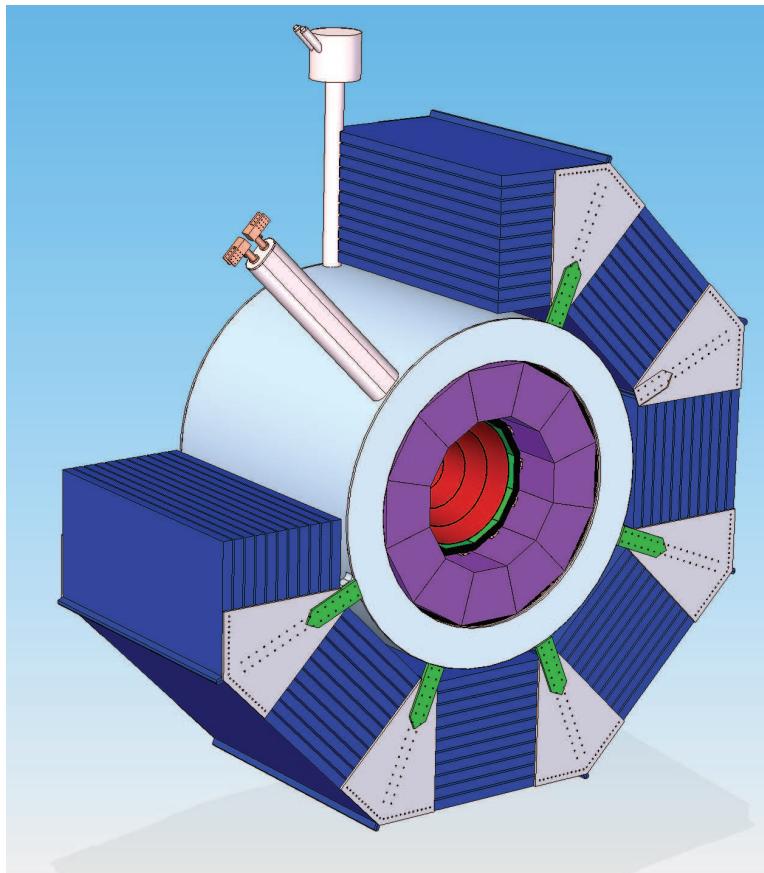


Figure 2.56: Solenoid shown with valve box, current leads and attachments to barrel iron plates..

A helium refrigerator/liquefier of approximately 1 kW of 4.5 K refrigeration is required. Flexible transfer lines connect the liquefier to the detector valve box for push-pull movement with the other detector. In order to minimize the length of the transfer line, the liquefier will be mounted at the same level as the top of the solenoid. The liquefier supplies forced flows of 4.5 K saturated LHe and 40-80 K helium. The latter flow is for the thermal shield and for the thermal intercepts of support rods. The liquefier is a custom built commercial product whose detailed design and construction will be carried out by industry as part of the complete cryo plant procurement. A 5000 LHe storage dewar is stationed next to the refrigerator liquefier and can almost be considered part of the liquefier. It serves as a pressure buffer for forced flow operation and as a LHe supply reservoir during liquefier down times. This technique was used successfully for a decade of running SC solenoid for the BaBar detector.

The detector valve box near the top of the detector is used to minimize flexible connections between detector and refrigerator. It also serves as the distribution point for supply of LHe to the two superconducting QD0 final focusing magnets 2 K cold boxes that are fixed on the detector.

It is expected that both ILC detectors will require similar size cryogenic plants. In order to maintain flexibility, we propose that each detector have its own complete cryogenic system including all the components discussed above. However, the design should allow connections between these plants at both the warm compressor level and at the output of the main cold boxes. These cross connects establish a redundant system for operations and could provide additional refrigeration capacity when cooling one of the magnets from room temperature.

The redundant 1250 kW helium compressors will be oil flooded screw compressors. Compressors and their associated oil removal equipment are commercially available (though typically custom modified). The compressors will be on the surface to minimize vibration and noise as well as providing easier access. Compressors will be connected to the Cold Box by a 14 -16 bar helium supply and a ~ 1.05 bar helium return lines. Necessary LN2 and helium gas buffer/storage tanks will be located near the compressors.

2.4.3 Detector Integrated Dipole (DID)

The 550 kA turn Detector Integrated “anti” Dipole (DID) generates ~ 600 G dipole field from each of the coils. These dipole coils are to be mounted between the end flanges of the outer winding mandrel of the solenoid. They will be placed just above the solenoid LHe cooling pipes. Solenoid conductor splices will be secured in the open spaces of the dipole coils. The most likely method of fabrication is to flat wind the dipole pancakes in an aluminum case, then bend them to the correct radius and vacuum impregnate with a filled epoxy resin. Dozens of bolted connections to the winding mandrel with additional thermal straps will guarantee mechanical restraint and adequate cooling.

The dipole coils are to be wound with co-extrusion of a high purity aluminum and a CMS single superconducting strand. Four layers of 197 turns of $3 \text{ mm} \times 4 \text{ mm}$ superconductor are proposed. There will be 0.5 mm of fiberglass cloth between each turn and each layer. They operate at 700 amps, corresponding to 1/3 of the critical current. Stored energy for an independently powered DID is in the range of 150 kJ. Because the stored energy is so

REFERENCES

small, the volume fraction of high purity aluminum to superconductor needed for safe energy extraction during a quench has been reduced from the CMS 12.4 to a ratio of 10.3. Forces on each of the four coils are rather large in sum but spread somewhat uniformly and manageable (4100 kN radial and 7800 kN axial). Figure 2.57 shows the dipole size, location and magnetic field profile.

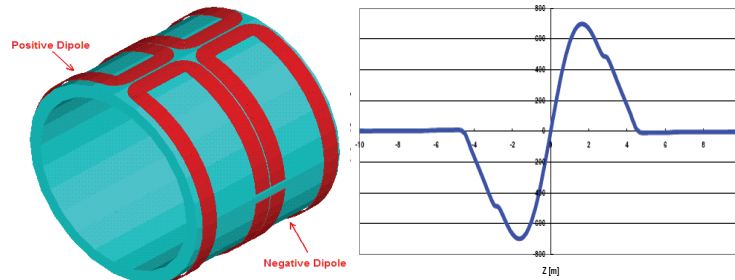


Figure 2.57: 4.5 K Detector Integrated “anti” Dipole with magnetic field profile. Dipole field is horizontal. Gaps in dipole winding are connection points to current leads.

There are no show stoppers for the superconducting solenoid or any other magnet system component. CMS has paved the way, provided many of the difficult to learn techniques and proven that a solenoid of this magnitude and stored energy per unit mass can be built. It remains to correctly implement the CMS construction techniques, examine other possible conductor choice and refine decisions to reduce cost, complexity and improve safety margins.

2.5 Muon System

2.5.1 Overview

The SiD muon system is designed to identify muons from the interaction point with high efficiency and to reject almost all hadrons (primarily pions and kaons). The muon detectors will be installed in the gaps between steel layers of the solenoid flux return. The required position and rate capabilities of the detectors are modest and can be met by several different detector technologies. The baseline design uses double layers of resistive plate chambers(RPC). Also under consideration are extruded scintillator strips read out by silicon photomultipliers (SiPMS). Cost, reliability and physics capabilities should determine the preferred choice.

2.5.2 Design

The muon system will start outside of the highly segmented electromagnetic and hadronic calorimeters and the 5T solenoid cryostat at a radius of 3.40 m. In the baseline design shown in Figure 2.58 a the flux return is divided into eleven layers of 20 cm steel in an octagonal barrel geometry. Endcaps of eleven 20 cm thick steel octagons will cap both ends of the barrel. The muon detectors will be inserted in the 4 cm gaps between the plates. In the barrel a detector layer is also inserted between the solenoid and the first steel plate. The first barrel layer is approximately 2.8 m by 6.0 m and the last layer is ~ 4.8 m by 6.0 m. The total detector area needed in the barrel is ~ 2050 m². As shown in Figure 2.58 b, the endcap detectors will be subdivided into rectangular or trapezoidal modules ~ 2 m by 6m. Each endcap has a total detector area of 1220 m².

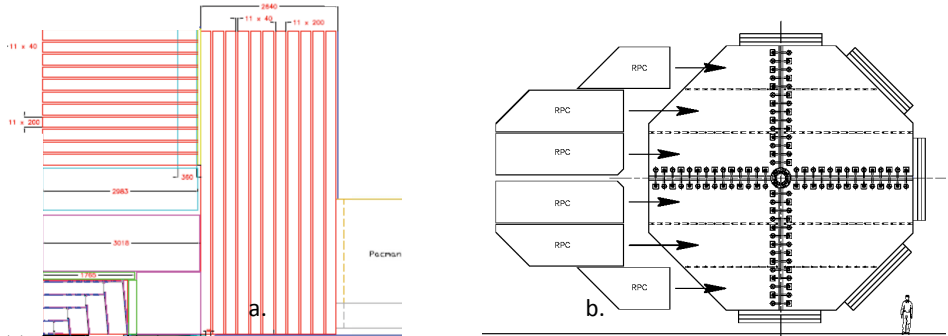


Figure 2.58: Quarter-section of the SiD flux return(a). Sub-division of the endcap into RPC modules.

2.5.3 Function

SiD muon selection will combine information from the central tracker, calorimeter, and muon detectors to construct 3-dimensional tracks through the entire detector for each muon candidate. Candidates will be required to penetrate a number of interaction lengths consistent

REFERENCES

with the muon momentum. In addition, the observed number and position of hits along the fitted track length can be used to further discriminate against hadrons. The first layers of the muon system may also be useful as a tail-catcher for the hadronic calorimeter.

2.5.4 Requirements

To date, physics benchmark/detector studies have been carried out for single muons and pions, Smuon pair production (see Section IV-4 of this report) and b-pair production at 500GeV. The single particle studies were done to develop algorithms to use in determining muon ID efficiency and hadron punch-through probability vs. momentum[1]. The results of these studies show that muon identification efficiency is greater than 96% above a momentum of 4 GeV/c. Muons perpendicular to the e+e- beamline reach the SiD muon system when their momentum exceeds ~ 3 GeV/c.

2.5.5 Detector Design

Muon systems characteristically cover large areas and are difficult to access or replace. Reliability and low cost are major requirements. Over 2.2 meters of steel thickness will be required for the solenoid flux return, providing 13.2 hadron interaction lengths to filter hadrons emerging from the hadron calorimeter and solenoid. Since the central tracker will measure the muon candidate momentum with high precision, the muon system only needs sufficient position resolution to unambiguously match calorimeter tracks with muon tracks. Present studies indicate that a resolution of ~ 1 -2 cm is adequate. This can be achieved by two layers of extruded scintillators or RPC pickup strips of ~ 4 cm width.

Full optimization of the muon system design has not been completed. Although the total steel thickness is set by the solenoid requirements, the optimum number of detector layers is being studied. We have studied the mis-identification rate of pions between 10-50 GeV/c as a function of the depth in the flux return[2] to check that the present design is thick enough. As shown in Figure 2.59, requiring that the track makes hits in some of the outer layers is sufficient to reduce the pion mis-identification rate to 0.25 %, consistent with the expected level of pion to muon decays. Pending further R&D it may be possible to eliminate detector layers without compromising either performance or reliability of the system.

2.5.6 Backgrounds

Backgrounds in the muon system are expected to come primarily from beam losses upstream of the detector. The muon system is shielded from backgrounds generated at the collision point or along the internal beam lines by the calorimeters, which are greater than 5 absorption lengths thick. Therefore only penetrating backgrounds, such as high-energy muons or neutrons, affect the barrel muon detectors. Calculations by N. Mokhov et al[3] of the expected background from muons produced by collimators near the detector hall predict a rate of 0.8 muons/cm² per pulse train (~ 1 ms) without muon spoilers, which is reduced to $3 \cdot 10^{-3}$ /cm²

per pulse train with the addition of muon spoilers. These background rates are significantly higher than the typical RPC noise rate of 1 kHz/m^2 ($10^{-4}/\text{cm}^2$ per pulse train. Physics backgrounds from two-photon processes producing hadrons or muon pairs significantly increase the expected signal rate in the endcap detectors near the beam-line. At a radius of 22 cm the expected rate from hadrons and muons above 2 GeV is < 0.03 is $< 0.? \text{ cm}^2$ per pulse train. The endcap detectors can in addition be hit by electromagnetic shower debris from local beam losses and may require additional shielding around the beam-line.

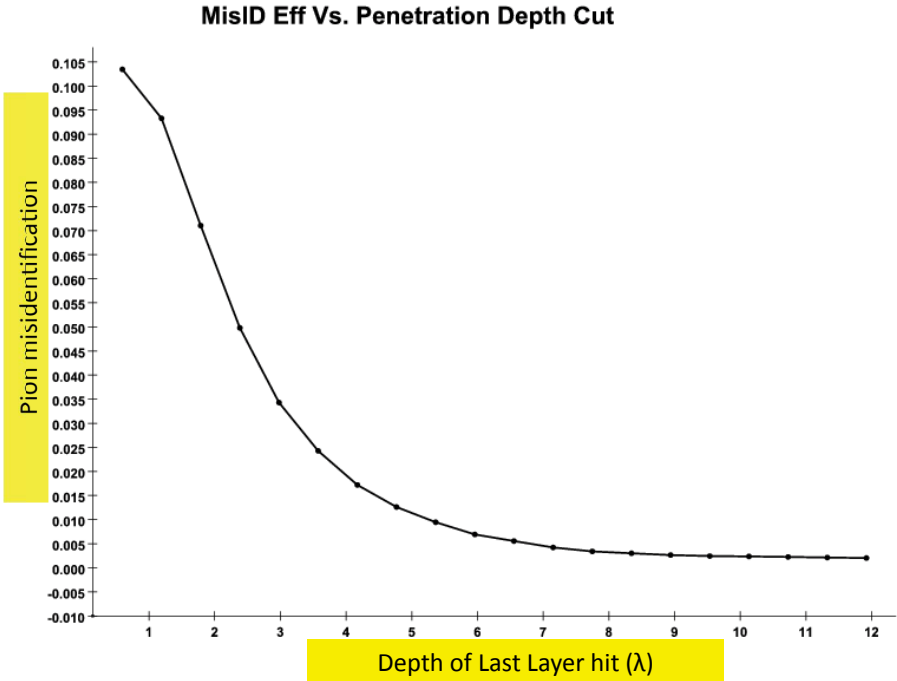


Figure 2.59: Fraction of pions between 1-50GeV/c that produce a hit at a depth x or greater.

2.5.7 Resistive Plate Chambers

RPCs have often been used as muon detectors (BaBar and BELLE) and will be used in both LHC experiments. RPCs are inexpensive to build and can be easily constructed in a variety of shapes and sizes. RPCs use fluorocarbon gases which may be regulated in the future as are greenhouse warming gases and require nontrivial gas delivery systems. The major concern with RPCs are their aging characteristics (BaBar was forced to replace its original RPCs and BELLE had startup problems). However, significant progress has been made in recent years in understanding aging mechanisms. Many of the aging processes are proportional to current passing through the gas gap. LHC detectors will run in avalanche mode which has much lower charge per track. Aging studies of LHC prototypes have shown good stability even at the high background rates expected (100 Hz/cm^2) at the LHC. The 2nd generation BaBar RPCs and the Belle RPCs have performed reliably at low signal rates ($< 0.2 \text{ Hz/cm}^2$). SiD RPCs will run in avalanche mode and be subjected to backgrounds of $< 0.15 \text{ Hz/cm}^2$

REFERENCES

near the beamline and $<0.015 \text{ Hz/cm}^2$ elsewhere.

The baseline RPC detector planes will be made by assembling single gap RPC HV chambers (~ 1 by 2 m) into modules of the required size to fill each slot in the octagonal barrel or endcap. Each barrel layer will be split into three full length modules to allow removal even if the gusset plates holding the steel octants are in place. The supports for the endcap modules will be staggered at different heights to reduce projective dead spaces. If the single gap efficiency is 90%, then an average layer efficiency of 93% can be achieved. Orthogonal pickup strips of a $\sim 3 \text{ cm}$ pitch will cover the sides of each HV module producing two x-y positions per layer. Muon hits will be digitized by a lower channel count (64-128) version of the KPIX chip mounted on a transition board containing circuit protection diodes. The strip area will be limited to $< 300 \text{ cm}^2$ so less than 1 background hit is expected per train under the worst background conditions. Use of the KPIX time information will reduce the expected background occupancy per strip to $< 0.04\%$. Smaller segmentation maybe necessary near the beam-line to keep the occupancy in this region equally low. One KPIX chip will digitize a side of a HV module. One KPIX chip will digitize a side of an HV module. Since the total area of double layer chambers will be $\sim 4500 \text{ m}^2$ and the average HV module is $\sim 2 \text{ m}^2$ about 4500 RPC HV modules and 9000 KPIX chips will be needed. One KPIX concentrator board will collect all of the KPIX data from one layer of each barrel octant or endcap quadrant. High voltage, gas, low voltage, and fiberoptic lines will be routed to the end of the barrel or to the periphery of the endcaps and connected to gas manifolds or trunk lines.

2.5.8 R&D

The primary aim of the muon system R&D is to validate both possible detector choices and to develop cost-effective read-out designs. The RPC R&D effort is focused on adapting the KPIX ADC to digitize RPC signals[4]. Other studies will measure the aging characteristics of IHEP RPCs and search for gas mixtures or cathode materials with better aging properties[5]. The groups involved with the scintillating strip option will evaluate SiPM devices from different manufacturers and develop mounting and calibration designs[6]

2.5.8.1 RPC R&D

Close integration of the RPCs and front-end and digitization electronics is necessary to minimize cabling and costs. It is imperative that low cost, reliable readout schemes for the RPCs be developed since the expected channel counts for the SiD detector are so high (nearly one million for the muon system). One possible low cost solution is to adapt the KPiX chip, presently being developed for use in the SiD electromagnetic calorimeter, for use with RPCs. An RPC/KPiX interface board was designed and built to provide ribbon cable connections to a 64 channel KPiX chip (v7). The RPC strip signal is AC coupled to the KPiX input through a 5 nF blocking capacitor and a 2 stage diode protection network. Each strip is also tied to signal ground via a resistor external to the interface board. Signals induced on the RPC strip have a very fast rise time ($< 10 \text{ nsec}$) and a fall time determined by the RC time constant of the strip capacitance (300 pF) and R, if R is less than the effective resistance

of the Bakelite cathode/anodes. Previous experiments such as BaBar and BELLE used small values of R (50-100 ohm) to make short fast signals (< 100 nsec) suitable for fast timing applications. However, the present KPiX chip samples the signal after > 400 nsec, requiring longer signal widths. Understanding the response of the KPiX device to different values of R and the blocking capacitor is of fundamental importance in adapting the KPiX chip to gas detectors. It is likely that optimizing the performance of the RPC/KPiX will require modification of the KPiX shaping and integration times. Future KPiX versions are planned to have more timing options.

A BaBar test RPC was connected to the interface board by a .5 m cable. The chamber was operated at 9300 V in avalanche mode using a premix gas with composition of 75.5% Freon 134a, 19.4% argon, 4.5% isobutane, and 0.5% SF6. The chamber efficiency had been previously measured to be $>90\%$ using BaBar electronics. The sum of the 13 RPC strips on the HV ground side (positive signal) is shown in Figure 2.60. The sharp spike near zero is due to cosmic ray tracks that either missed the test RPC or to RPC inefficiency. The width of this spike was 29 fC about three times larger than expected based on the noise performance of KPiX, indicating that there may be electronic pickup. The data peak is centered at 3.8 pC with a width of 2.2 pC. The data signal is consistent with, but larger than, avalanche RPC signals measured by other groups (~ 1 pC) which used avalanche gases with no argon component. The BaBar avalanche gas contains 20% argon and should have a higher gas gain. The size and distribution of charge in the RPC pickup strips was studied. The charge of the strip with the maximum charge for each trigger has less than half of the total charge in the event. A strip multiplicity was calculated as a function of the discrimination threshold. With a threshold of 300 fC, about 92% of the cosmic triggers have 1 or more strips hit and the average strip multiplicity is 3.1, more than twice that observed in BaBar. High strip multiplicities are undesirable since they degrade the position resolution and the ability to separate two tracks near each other. Further characterization and optimization of the interface board between the RPC and KPiX chip is needed to understand the larger than expected noise and strip multiplicities that were observed.

Many large RPC systems have been built within the last 10 years and understanding their performance will provide strong guidance for an SiD design. Several types of RPC construction have been used in high energy experiments. RPCs with Bakelite cathodes and anodes were pioneered by Santonico et al[7] and used in BaBar, CMS, ATLAS and a variety of cosmic ray and neutrino experiments. The early failure of many BaBar RPCs stimulated detailed study of RPC aging and led to many significant improvements in construction practices and operation. The linseed oil used to coat the inner HV surfaces has often been a source of concern. The IHEP group and Chinese industry have developed a Bakelite /melamine cathode for use in the BES III and Daya Bay detectors that does not require linseed oil treatment to achieve acceptable noise rates. These RPCs are operated in streamer mode in their present applications. SiD proposes to operate its RPCs in avalanche mode. Tests of IHEP RPCs in avalanche mode will be used to determine the efficiency, current and noise rate as a function of HV and gas composition and to establish their suitability for use in SiD. Longer term tests will also be needed to investigate the aging properties of the IHEP RPCs. All of the working RPC systems utilize Freon as a major gas constituent. Several researchers have found significant levels of HF acid in the exhaust gas indicating the breakdown of the Freon or SF6 during the gas avalanche or streamer. BELLE found that in the presence of water

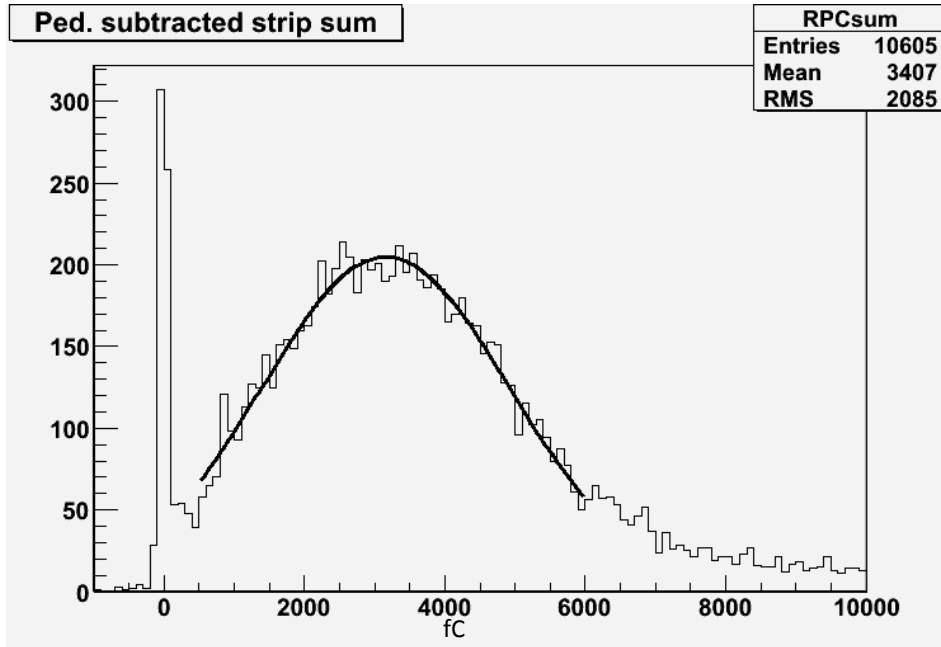


Figure 2.60: Sum of the pulse heights in 13 RPC strips readout by KPIX. The peak position of ~ 3 pC and efficiency of $>90\%$ are consistent with previous studies of avalanche mode RPCs.

vapor that the HF would etch the glass surface, generating sizable noise currents and lowering efficiency. The effect on Bakelite RPCs is less understood, but there is clear evidence that pollutants generated by high rate in the gas can affect both the noise rate and dark current. Groups from the University of Wisconsin and Roma have measured the fluorine levels of the exhaust gas in both streamer and avalanche RPCs at BaBar and correlated these levels with the chamber current, noise rate, and efficiency[8]. Further studies of BaBar RPCs may shed light on the long term effects of HF on the Bakelite surfaces. Longer term goals are to develop RPC gas mixes which either eliminate or substantially reduce the Freon component. A group at Princeton University is also studying the effect of HF on Bakelite surfaces and will extend these studies to the new RPCs developed by IHEP.

2.5.8.2 Extruded Scintillator and Photodetector R&D

In 2000 it was noted that the ILC muon system requirements could be met with a MINOS type scintillator detector design[9] that would give both muon identification and be used to measure the tails of late developing or highly energetic hadron showers. This seems rather appropriate since the depth of the ILC calorimeters is limited because they are inside the superconducting (SC) solenoid. As an example, neutral hadrons that represent $\sim 11\%$ of the final-state energy in Higgs and W-W production, primarily neutrons and K_L 's, prove to be difficult to identify and measure[10]. The physics case for tail catching of showers is based on improvement of jet energy resolution when the energy downstream of the SC solenoid is included in the definition of jet energy[11],[12].

The MINOS experiment has already proved that a strip-scintillator detector works well for identifying muons and for measuring hadronic energy in neutrino interactions. The ILC R&D muon scintillator detector effort is directed at understanding how to deploy such detectors in the ILC environment and to understand possible improvements that could lead to reduced complexity and /or cost, with photon detection based on SiPMS.

A possible layout of quadrant strips for the forward muon scintillator system could have alternate planes of detectors rotated by 90° relative to each other. Each quadrant would contain ~ 158 strips 4.1 cm wide and of variable length. The mean strip length is 5.05 m. Muon scintillator-strip detectors located in the Fe barrel octant gaps could be arranged in planes where the u-v strips are oriented at $\pm 45^\circ$ to a plane's edges or, alternatively, parallel to the edges in x-y fashion.

Earlier strip-scintillator R&D[13] using 4.1cm wide by 1cm thick extruded MINOS style scintillator that was readout with multi-anode photomultiplier tubes (MAPMTs) demonstrated that > 9 photo-electrons were achieved with 1.8m long strips in which the wavelength shifted scintillation light was carried to MAPMTs through a thermally fused clear optical fiber to the MAPMT a few meters away[14]. The measured light transmission was required to be $> 80\%$ for each splice.

We have recently procured Silicon based photon detectors (SiPMS) for tests with our scintillator. Sixty multi-pixel photon counters (MPPCs) have been purchased from Hamamatsu: 20 each of 100, 400 and 1600 pixels in a 1 mm square array. In addition INFN Udine-based collaborators have obtained 100 IRST SiPMS that have approximately 688 pixels inside a 1.2mm dia. circular matrix for muon/tailcatcher R&D.

Recently strips with MPPCs and IRST devices have been assembled and tests with beam have begun. A real advantage of the SiPMS is the ability to see the summed output from the full assembly of pixels and observe in a pulse height spectrum that shows a number of photo-electron peaks. A modest calorimetric disadvantage is that the SiPMs put out spontaneous pulses with no defined input (noise). This disadvantage can be parlayed into an advantage in terms of calibration. With a good oscilloscope one observes bands of 1, 2 and sometimes 3 photo-electrons from which a reasonable calibration is possible. This calibration aspect needs study and engineering, which is part of our proposed R&D program. It should be mentioned that during our test beam studies we accumulated well over a million triggers using a 1.8m long strip and observed 100% efficiency when triggers were formed with independent trigger counters. Figure 2.61 shows an MPPC output spectrum from a test circuit and constant amplitude input LED pulses.

The SiD Muon Studies group consists of physicists from: Fermilab, Indiana U, INFN Udine, Livermore, NIU, U Notre Dame, Rochester, Wayne State and Wisconsin. These groups are testing RPCs, scintillator, SiPMS, prototype planes, frontend electronics and we are using beam test results to understand issues and costs associated with the application of RPCs and strip-scintillator technology to an LC muon system. The tests are an exploration of construction issues, device characteristics such as pulse shaping, readout, amplitude, gain and cross-talk, digitization, packaging, cables, signal collection from many strips and their transport from the detector to signal storage. A list of R&D items with the priorities and personnel is shown in Table 2.11.

REFERENCES

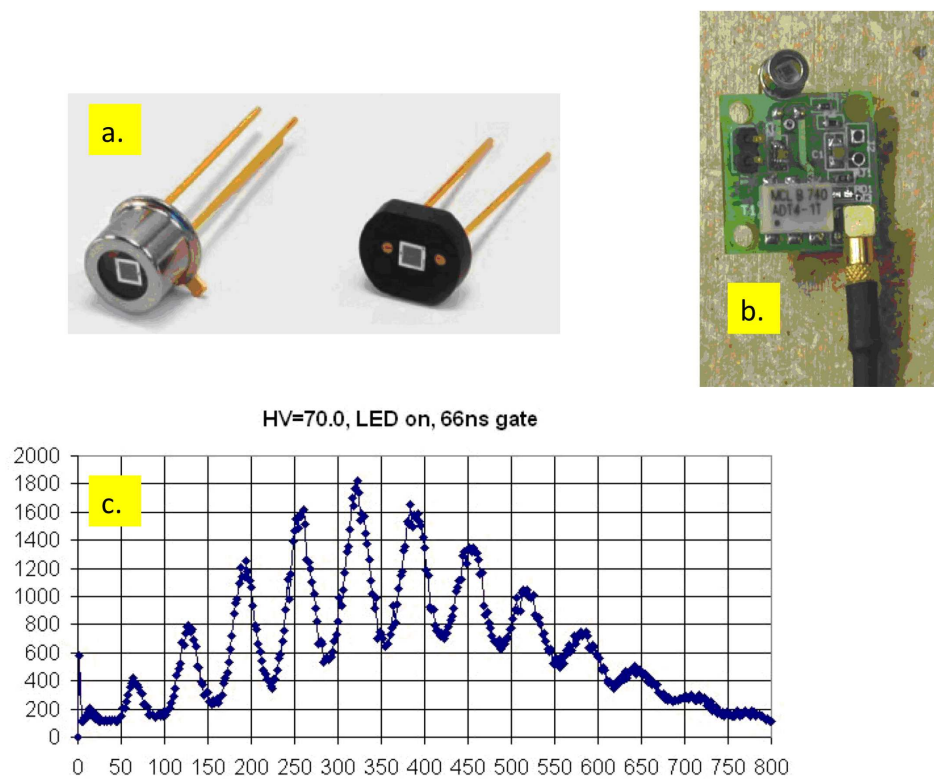


Figure 2.61: SIPM Hamamatsu MPPC and 2cm scale front-end electronics test setup. The output is generated with a pulsed LED providing the input light.

Table 2.11: Muon/Tail Catcher R&D Summary

Rank	R&D Item	Institutions	Personnel	K\$
1	Studies of KPIX/RPC readout with IHEP RPCs Continue tests of KPIX readout for RPCs in avalanche mode. Optimize interface board, test performance & reliability Begin aging tests of IHEP RPCs.	Wisconsin	H. Band & student	45 WIS
1	SiPMs from HPK and IRST - Bench Tests Current vs Bias Voltage to establish operating voltage, gain, noise rate vs. temp., threshold, etc. Test 150 devices from IRST (It.) & HPK (Jp.) LED pulser development.	Fermilab Indiana INFN Udine NIU Notre Dame Wayne State	Si Detector Facility: Para Van Kooten et al Pauletta et al. Hedin, Chakraborty, Dychkant, Zutshi. Wayne, Baumbaugh, McKenna Karchin, Gutierrez, et al.	30 F 21 IU 20 WSU
1	Strip & Fiber Mechanical R&D. Geometry of strip ends + SiPM FE miniature circuit. Prep. of ~30 strips w/WLS fiber. QC checks. Light pulser tests.	Notre Dame Fermilab INFN Udine	McKenna, Wayne Rubinov, Fisk. Pauletta	23 UND 50 F
1	MTest studies of strips and instrumentation. Calibration from photoelectron peaks. Signal/noise vs. trans. & long. position. CAMAC/Minerva electronics.	INFN Udine Fermilab Notre Dame Wayne State	Pauletta et al Rubinov, Fisk Baumbaugh Gutierrez, students	20 F
2	FE electronics devel. AC vs. DC coupling; Temp. compensated gain; Strip signal transport, collection & digitization. Multiplexing scheme.	Fermilab Indiana Wayne State INFN Udine	Rubinov, Fitzpatrick Van Kooten Karchin Pauletta	30 F
2	Tail catcher R&D with CALICE; Gain issues, E Res. vs. # of pixels.	NIU	Chakaraborty, Zutshi	30 NIU
3	Fast timing studies	NIU	Hedin	
3	Simulations. Testbeam software. Analysis software.	Rochester INFN Udine All	Manly Pauletta, et al	
4	Co-extrusion of scintillator and WLS fiber	Fermilab Notre Dame	Fisk Ruchti, Wayne.	

REFERENCES

2.5.9 Milestones

- RPC/KPIX proof of principle -2008-9
- Optimize interface board & protection circuitry design 2009-10
- Cosmic ray tests
- Beam tests – RPC/KPIX
- SiPM proof of principle -2008-9

References

- [1] Milstene, C. , H.E. Fisk, A. Para (Fermilab), “Tests of the Charged Particle Stepper with Muons”, **FERMILAB-TM-2274-E**, Oct 2004. 17pp.
- [2] Band, H. R. and H. E. Fisk, “SiD Muon System,”
http://silicondetector.org/download/attachments/33358377/SiD_Muon_Oxford_hrb.ppt,(unpublished) Apr 2008.
- [3] Mokhov, N. V., A. I. Drozhdin, M. A. Kostin, “*Beam Collimation and Machine Detector Interface at the International Linear Collider*,” PAC 2005 Paper **Fermilab-Conf-05-154-AD** May 2005.
- [4] H. R. Band, “*RPC/KPiX Studies for Use in Linear Collider Detectors*,”
http://silicondetector.org/download/attachments/37323762/RPC_Wisc.pdf
- [5] C. Lu *et al.* “*Aging Study for SiD Hcal and Muon System RPCs*,”
http://silicondetector.org/download/attachments/37323762/RPC_Princeton_k.pdf
- [6] P. Karchin *et al.*, “*Scintillator Based Muon System & Tail-Catcher R&D*”,
http://silicondetector.org/download/attachments/37323762/ILC_Muon_2009_proposal_v2.pdf
- [7] R. Santonico, “*RPC understanding and future perspectives*”. Nucl. Inst. and Meth. **A533**, 1-6(2004).
- [8] H.R. Band et al, “*Study of HF production in BaBar Resistive Plate Chambers*”. Nucl. Inst. and Meth. **A594**, 33-38(2008).
- [9] Para, A. “*Solid Scintillator-based Muon Detector for Linear Collider Experiments*,” Physics and Experiments with Future Linear e^+e^- Colliders, ed. A. Para and H. E. Fisk (2001)pg. 865-869, American Institute of Physics, Melville, New York (Vol. **578**)
- [10] Frey, R. “*Experimental Issues for the Workshop*,” International Conference on Linear Colliders – LCWS 2004, p 29 Eds. H. Videau & J-C. Brient, Editions de l’Ecole Polytechnique, Julliet 2005, 91128 Palaiseau Cedex
- [11] M. J. Charles, “*PFA Performance for SiD*,”
(to be published) proc. of the Linear Collider Work Shop,(2008),
Univ. of Illinois at Chicago,
http://arxiv.org/PS_cache/arxiv/pdf/0901/0901.4670v1.pdf

threshold is read out. For diagnostics and debugging, the DAQ includes the ability to assert calibration strobe and trigger signals, transmitted to the front-ends via the Level-2 and Level-1 Concentrator boards using the fibers shown in Figure 1. The fiber transports encoded command, clock, and synchronization to all the front-ends.

Power Conversion circuits on the Level 2 and Level 1 Concentrator boards supply the power to the front-ends, starting with 48V or higher voltages from off-detector supplies. Alternatively, serial powering architectures are also under consideration. The power supplies are located in several racks on or next to the detector.

Environmental and health monitoring circuits are also included on the concentrator boards. In addition there may be additional monitoring boards in the detector, connected to RCE fiber interfaces. In addition there are crates of monitoring modules mounted in several racks on or next to the detector.

Chapter 2 Section 6: Data Acquisition and Electronics (Not yet I latex format)

SiD has a coherent approach to the electronics architecture that seems to fit all the baseline subsystems. Figure 1 shows the simplified block diagram for the data-acquisition from the front-end electronics to the online-farm and storage system. The subsystems with the exception of the Vertex detector (for which the sensor technology is not yet selected) and the FCAL (which has approximately unit occupancy) are read out by variants of KPiX as the front-end Application-Specific Integrated Circuit (ASIC). KPiX is a multi-channel system-on-chip, for self triggered detection and processing of low level charge signals (“KPiX - An Array of Self Triggered Charge Sensitive Cells Generating Digital Time and Amplitude Information” D. Freytag et al, IEEE NSS Dresden 08).

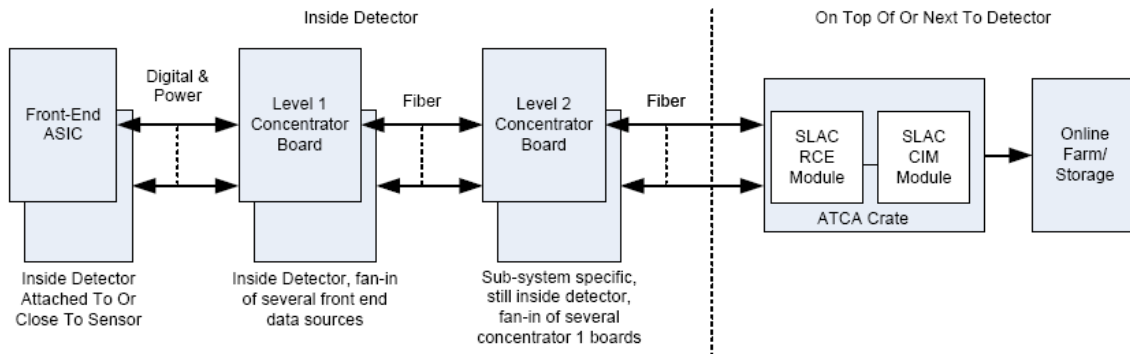


Figure 1: Simplified block-diagram of detector control and readout electronics using the SLAC ATCA RCE and CIM modules.

Figure 2 shows a simplified block diagram of the KPiX, processing signals from 1024 detector channels. The low level charge signal at the input is processed by the charge amplifier in two ranges with automatic range switching controlled by the range threshold discriminator. Calibration is provided covering the full range. Leakage compensation is available for DC-coupled detectors. Internal or external trigger options can be selected.

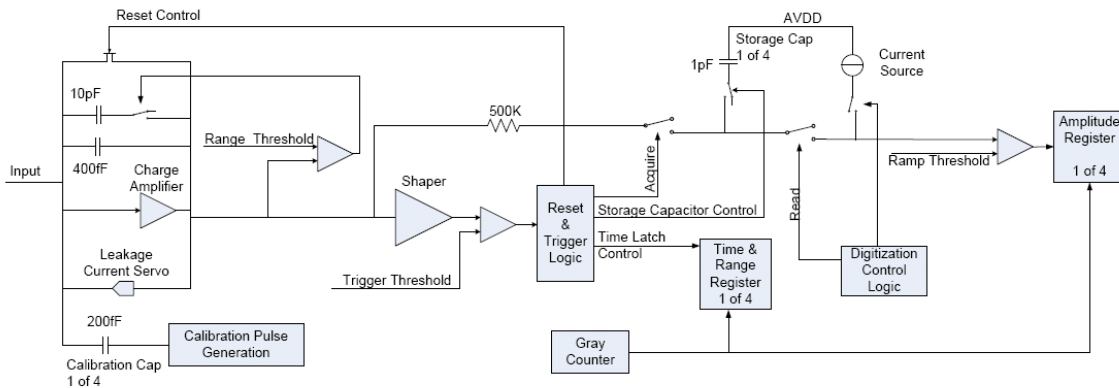


Figure 2: Simplified block-diagram of one channel of the 1024 channel KPiX Application Specific Integrated Circuit.

Up to four sets of signals for each channel can be stored in one acquisition cycle. Time is stored in digital format, the amplitude as a voltage on a capacitor for subsequent digitization in a Wilkinson-type ADC. At the end of the acquisition and digitization cycle nine words of digital information are available for each of the 1024 cells of the KPix chip. The data is read out serially from the ASIC before the next acquisition cycle begins.

Sub-System	KPiX Count	Channels/KPiX
Tracker	22066	1024
EMCAL	99076	1024
HCAL	35412	1024
Muons	8834	64
Total	165388	

Table 1: Count of KPix ASICs for each sub-system.

Table 1 lists the number of KPix ASICs for each sub-system. Tracker, EMCAL, and HCAL use 1024-channel ASICs while the Muon sub-system uses a 64-channel version.

As illustrated in Figure 1, several front-end ASICs (KPix, FCAL or Vertex ASICs) are connected to a Level-1 Concentrator (L1C) board using electrical LVDS. The concentrator board main functions are to fan out upstream signals to the front-end modules, to fan-in data from the front-end modules for transmission to the Level 2 Concentrator (L2C) boards, and to perform zero-suppression and sorting of the event data. Just as an example, for the EMC Barrel a total of 96 1024-channel KPix chips would be connected from 8 front-end cables with 12 KPix's each to one Level-1 Concentrator board. The number of Level 1 concentrator boards in the detector depends on the sub-system, e.g for the EMC Barrel there would be 821 L1C boards and 52 L2C boards (80k KPix, 96 KPix for each L1C board, 16 L1C boards for each L2C board)

Figure 3 shows a block diagram and a prototype of the board.

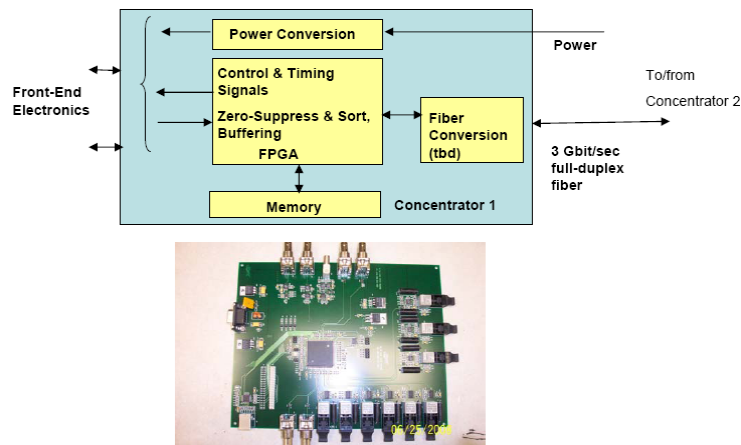


Figure 3 Level 1 Concentrator Board

The Level 1 Concentrator boards are in turn connected via 3-Gbit/sec fibers to the Level-2 Concentrator boards. These are similar to the Level 1 Concentrator boards. They fan out and fan in signals to/from the Level 1 Concentrator boards. In addition the data-streams of sorted event data received from each Level 1 Concentrator board are merged and sorted before transmission to the off-detector processor boards. The Level 2 boards are either located inside the detector or outside, depending on the sub-system. E.g. for the EMC Barrel there are 36 of such boards inside the detector volume.

The Level 2 Concentrator boards are connected via fibers to ATCA crates either on or next to the detector. ATCA stands for “Advanced Telecommunications Computing Architecture” and is the next generation communication equipment used by the telecommunication industry. It incorporates the latest trends in high-speed interconnect, processors and improved Reliability, Availability, and Serviceability (RAS). Essentially instead of parallel bus back-planes, it uses high-speed serial communication and advanced switch technology within and between modules, redundant power, plus monitoring functions. For SiD 10-G Ethernet is used as the serial protocol.

SLAC designed two custom ATCA boards, the Reconfigurable Cluster Element (RCE) Module and the Cluster Interconnect Module (CIM) as shown in Figure 1. Figure 4 shows the RCE which interfaces via eight 3-Gbit/s fiber links to sub-system detector electronics. It provides timing and configuration commands, and reads back configuration and event data. It contains 2 sets of the following: Virtex FPGA with embedded 2 PowerPC processors IP cores, 512 Mbyte low-latency RLDRAM, important 8 Gbytes/sec cpu-data memory interface, 10-G Ethernet event data interface, 1-G Ethernet control interface, RTEMS operating system, up to 512 Gbyte of FLASH memory or 1 TByte/board. The flash memory does not have to be fully loaded, it is implemented in SIMMS plug-in modules. One RCE connects to up to 8 detector cards via 8 3-Gbit/sec fibers connected into the Read Transition Module (RTM)

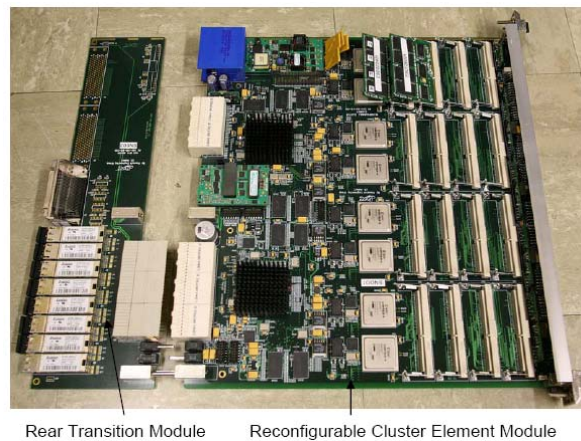


Figure 4: SLAC ATCA Reconfigurable Cluster Element

Figure 5 shows a picture of the SLAC CIM. It is essentially a switch card with two 24-port 10-G Ethernet Fulcrum switch ASICs. The switch ASICs are managed via a Virtex FPGA. The function of the CIM is to provide communication between all the RCE modules in a crate and to destinations external to the crate at 10Gbit/s data rates.

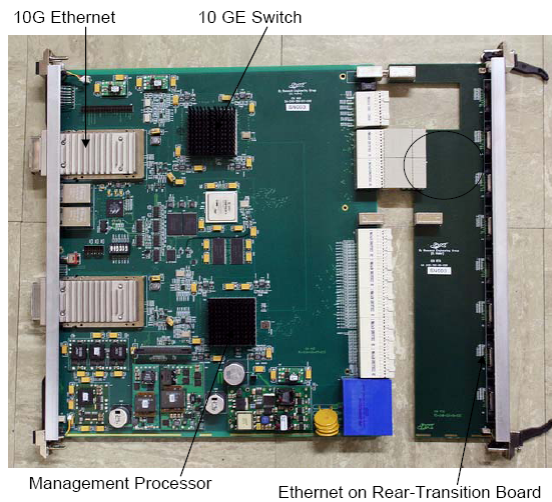


Figure 5: SLAC ATCA Cluster Interconnect Module

One of those network cards serves up to 14 in-crate RCE modules. The data transfer rate is up to 480 Gbit/sec, more than the complete SiD data rate requirement.



Figure 6: ATCA Crate with RCE and CIM

Figure 6 shows an ATCA crate with one RCE and one CIM inserted. A total of 14 RCE's and 2 CIM's can be inserted into one crate providing connections to $8 \times 14 = 112$ 3Gbit/sec fiber links into the detector for a 360 Gbit/sec IO. The estimate for the complete SiD detector is approximately 320 Gbit/sec including a factor of 2 margin, so in principle a single ATCA crate could serve the complete detector. However for partitioning reasons, the ability to run each of the sub-systems completely independently during commissioning is desired, and one crate for each sub-system is planned. The complete SiD DAQ only requires about 4 racks full of Data Acquisition electronics.

The data is further sorted by event in the ATCA system and sent to the online processing system for potential data reduction. Whether further data reduction is required is not determined yet, and the data may directly be forwarded to the offline system.

Note that the event data is zero-suppressed in the sub-systems without the need for a global trigger system. All data produced in the front-ends above a programmable

REFERENCES

- [12] Salcido, P., (CALICE Collab.) LCSW08 Calorimeter & Muons Session: TCMT and combined analysis, Nov. 17,2008 (unpublished)
- [13] P. Karchin, “*A Scintillator-based Muon Detector for the Linear Collider,*” in proceedings of the meeting of the Division of Particles and Fields of the American Physical Society, University of California, Riverside, August, 2004, International Journal of Modern Physics A, World Scientific Publishing Company.
- [14] R. Abrams et al., *LC scintillator-based muon detector tail-catcher R&D.* FERMILAB-CONF-07-589-E, LCWS-2007-CAL14, Nov 2007. 5pp. International Linear Collider Workshop (LCWS07 and ILC07), Hamburg, Germany, 30 May - 3 Jun 2007, SLAC eConf C0705302 Proceedings, S. Riemann (ed.).

2.6 Forward Detector

The forward region is defined as polar angles $|\cos\theta| > 0.99$ ($\theta < 140\text{mrad}$) forward of the SiD Endcap ECAL. The angular coverage is completed by two detectors, the Luminosity Calorimeter (LumiCal) and the Beam Calorimeter (BeamCal). The physics missions in this region are:

- precision measurement of the integrated luminosity using small-angle Bhabha scattering (LumiCal). To measure cross section of an event sample $O(10^6)$ expected for $e^+e^- \rightarrow W^+W^-$ in 5 years with 500fb^{-1} , the goal is to measure the luminosity with an accuracy better than 10^{-3} .
- precise determination of the luminosity spectrum by measuring the acolinearity angle of Bhabha scattering (LumiCal). Due to the beamstrahlung emission the colliding beams lose energies before collision, and the center-of-mass energy is no longer monochromatic. The luminosity spectrum affects mass measurement and threshold scan.
- extend the calorimeter hermeticity into the small angles for physics searches (LumiCal and BeamCal). An excellent hermeticity is essential as many new-physics reactions are accompanied with a large missing energy.
- instantaneous luminosity measurement using beamstrahlung pairs (BeamCal).
- two photon veto for new particle searches (BeamCal).

The detector challenges are good energy resolution, radiation hardness, interfacing with the final focus elements, high occupancy rate requiring special readout, and performing the physics measurements in the presence of the very high background in the forward direction.

2.6.1 Design criteria

2.6.1.1 LumiCal Physics Requirements

The lowest order Bhabha cross-section for t channel one photon exchange is given by:

$$\frac{d\sigma}{d\Omega} = \frac{\alpha^2}{8E^2} \left(\frac{1 + \cos^2\theta/2}{\sin^4\theta/2} \right)$$

We use this simple formula to estimate the polar angle coverage needed, although the complete electro-weak s and t channel cross-section will later be needed in order to do the physics. The number of Bhabha events per bunch crossing for a detector with minimum and maximum polar angle coverage θ_{min} and θ_{max} (in mrad) is:

$$N = 0.5\text{pb} \frac{L}{R} \int_{\theta_{\min}}^{\theta_{\max}} \frac{d\cos\theta}{\sin^4\theta/2} \sim 8 \left(\frac{1}{\theta_{\min}^2} - \frac{1}{\theta_{\max}^2} \right)$$

for $\sqrt{s}=0.5$ TeV, $L=2 \times 10^{34} \text{cm}^{-2}\text{s}^{-1}$, and bunch crossing rate $R=1.4 \times 10^4 \text{s}^{-1}$. Our goal is to measure the luminosity normalization with an accuracy of several 10^{-4} for $\sqrt{s}=0.5$ TeV. To do this one needs $\approx 10^8$ events collected over $\approx 10^7$ s, or about ten events per second. One can then calculate the absolute luminosity with $\approx 10\%$ statistical error every several minutes during the run. With a bunch crossing rate of $1.4 \times 10^4 \text{s}^{-1}$, we need $> 10^{-3}$ events per bunch crossing. To achieve this statistical accuracy, we start the fiducial region for the precision luminosity measurement well away from the beamstrahlung pair edge at $\theta_{\min}=20\text{mrad}$, with a fiducial region beginning at 30mrad , which gives $\approx 10^{-2}$ events per bunch crossing.

2.6.1.2 Luminosity precision and detector alignment

The integrated luminosity, L is measured using the number of Bhabha events N and the Bhabha scattering cross section σ in the detector fiducial region as $L = N/\sigma$. Since the Bhabha cross section is $\sigma \sim 1/\theta^3$, the luminosity precision can be expressed as

$$\frac{\Delta L}{L} = \frac{2\Delta\theta}{\theta_{\min}},$$

where $\Delta\theta$ is a systematic error (bias) in polar angle measurement and θ_{\min} is the minimum polar angle of the fiducial region. Because of the steep angular dependence, the precision of the minimum polar angle measurement determines the luminosity precision. To reach the luminosity precision goal of 10^{-3} , the polar angle must be measured with a precision $\Delta\theta < 0.02$ mrad and the radial positions of the sensors must be controlled within $30 \mu\text{m}$ relative to the IP.

2.6.1.3 Monitoring the Instantaneous Luminosity with BeamCal

The colliding electron and positron bunches at the ILC experience intense electromagnetic fields as they pass each other. These fields generate large Lorentz forces, which cause radiation of gammas called beamstrahlung. A small fraction of the beamstrahlung gammas convert in pairs. Under the ILC Nominal beam parameters at $\sqrt{s} = 0.5$ TeV, approximately $75\text{k } e^+/e^-$ are generated. The BeamCal intercepts $\approx 3 \times 10^4$ beamstrahlung pairs of average energy ≈ 0.7 GeV per bunch crossing when the bunches have maximum overlap. Since the number of pairs is directly proportional to the beam overlap, the instantaneous luminosity can be monitored by detecting pairs in the BeamCal. Our goal is at the ten percent level per beam crossing.

The Detector Integrated Dipole (DID)[2] plays an important role in controlling the beamstrahlung pairs. The DID is a pair of coils wound on the detector solenoid, which creates

sine-like transverse field. In the so-called Anti-DID configuration, the DID field effectively compensates the crossing angle for the outgoing beam and directs the low energy pairs into the extraction aperture, reducing the total pair energy hitting the BeamCal from 20 TeV to 10 TeV.

2.6.1.4 Detector Hermeticity

By hermeticity we mean an accurate measurement of the transverse momentum (P_T) balance in the event, which is achieved by good energy resolution, avoiding cracks, dead areas, and by covering down to small polar angles. The measurement of $e^+e^- \rightarrow \text{slepton pairs}$ in the presence of two photon background has been given as the performance detector design criteria for hermeticity[1]. In the stau production and decay,

$$e^+e^- \rightarrow \bar{\tau}\bar{\tau} \rightarrow \tau^+\chi^0\tau^-\chi^0$$

the χ^0 is the LSP and escapes the detector. Under the SUSY dark matter scenario, the mass difference between stau and the LSP becomes less than 10 GeV, the missing P_T is less and the measurements become more difficult. The main background comes from the two-photon process $e^+e^- \rightarrow e^+e^-X$, where X is ee , $\mu\mu$, or $\tau\tau$ for the slepton search. This background process has no missing P_T ; however, if we miss both electrons then the missing $P_T < 2\theta_{min}E_{beam}$. This is the kinematic limit. Generally one photon is on-shell, so usually the missing $P_T < \theta_{min}E_{beam}$. The search region in the missing P_T is determined by how small angle the two-photon electrons are detected and thereby vetoed. The electron detection must be made in the BeamCal where the beamstrahlung pairs deposit 10 TeV of energy.

2.6.1.5 Dynamic range and mip sensitivity

While minimum ionizing particles (MIP) deposit 93 keV in a 320 μm -thick Si layer, a 250 GeV electron can deposit up to 160 MeV or 1700 MIP equivalents in a single cell near shower maximum. If we want a 100% MIP sensitivity, the S/N ratio for MIP should be greater than 10, and the dynamic range of electronics need to be at least 17,000. This dynamic range can be achieved using 10 bits ADC with two gains.

2.6.1.6 Radiation hardness

The beamstrahlung pairs will hit the BeamCal, depositing 10 TeV of energy every bunch crossing. Sensor electronics could be damaged by the energy deposition, and sensor displacement damage could be caused by neutrons. The radiation dose varies significantly with radius, and a maximum dose of up to 100 MRad/year is expected at near the beampipe. The main source of neutrons is from secondary photons in the energy range 5-30 MeV, which excite the giant nuclear dipole resonance. The number of neutrons produced in one $0.5\text{cm} \times 0.5\text{cm}$ BeamCal detector segment per year is approximately $5 \times 10^{13}\text{n/cm}^2$

2.6.1.7 Occupancy

The issue here is how “deep” we need to make the readout buffer to hold one train of events for the LumiCal. The LumiCal occupancy is studied for the beamstrahlung pairs and two-photon events. The occupancy from the pairs still dominates. In the far LumiCal just outside the pair edge, the number of hits will reach 120 hits per bunch train. The number of hits per bunch train decreases to four at approximately $R \sim 10$ cm in the near LumiCal.

2.6.2 Baseline Design

The layout of the forward region is illustrated in Figure 2.62. The LumiCal covers the polar angles from 40 mrad to 90 mrad, and the BeamCal from 3 mrad to 40 mrad. The conical mask made of 3cm-thick tungsten is located between the LumiCal and BeamCal. When the beamstrahlung pairs hit the BeamCal, low energy secondary particles are generated. The mask shields the SiD central detectors from low energy photons backscattered from the BeamCal. The Low-Z mask made of 13cm-thick Borated-Polyethylene is located in front of the BeamCal. The Low-Z mask reduces the low energy electron and positron albedo from the BeamCal by more than an order of magnitude. Borated-Polyethylene also absorbs low energy neutrons produced in the BeamCal and directed toward the IP.

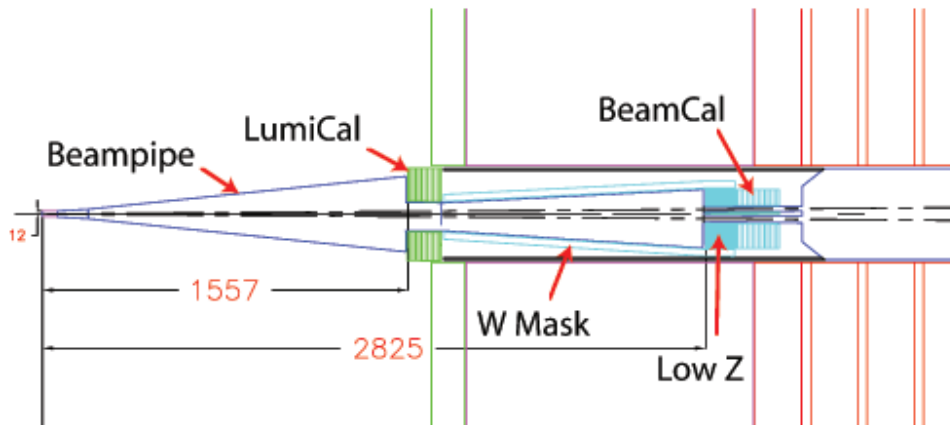


Figure 2.62: Forward region.

The beam pipe at the IP is made of beryllium to minimize multiple scattering. The inner radius is 1.2 cm, and the thickness is $400 \mu\text{m}$. The conical section starts at $R=1.2$ cm, $Z=6.25$ cm, and flares to 103 mrad, which is outside of the LumiCal fiducial region. The flared beam pipe design allows particles to exit the beam pipe at normal incidence before entering the LumiCal. The cylindrical beam pipe inside the LumiCal is 6 cm in radius, and is centered on the extraction beam line to accommodate the 14 mrad crossing angle. The

beam pipe does not intercept the beamstrahlung pairs which are confined within 4 cm radius by the SiD 5 Tesla solenoid.

The entire forward region is supported by the support tube which is cantilevered from the QD0 cryostat. There is a 1 cm gap between the support tube and the endcap door to facilitate the door opening. To minimize the electromagnetic energy loss due to the gap, the LumiCal is 10 cm closer to the IP relative to the ECAL.

The LumiCal consists of two cylindrical C-shaped modules surrounding the beam pipe. The inner radius is 6 cm centered on the extraction beam line with a horizontal offset of $\Delta x = 1.0$ cm (158 cm \times 0.007). The inner radius is dictated by the requirement that no detector intercepts the intense beamstrahlung pairs, which are confined within 4 cm radius by the 5 Tesla solenoid field. The longitudinal structure follows the ECAL design, consisting of 30 alternating layers of tungsten and silicon. The first 20 layers of tungsten each have thickness equivalent to 2.5 mm (or $5/7$ radiation length) of pure tungsten. The last 10 layers have double this thickness, making a total depth of about 29 radiation length. The silicon sensors will be made from 6 inch wafers, and the segmentation is illustrated in Figure 2.63. The sensor is segmented in a $R - \phi$ geometry. A fine radial segmentation with 2.5 mm pitch is used to reach the luminosity precision goal of 10^{-3} . The azimuthal division is 36 with each sensor covering 10 degrees. Table 2.12 summarizes the LumiCal parameters.

z	158 - 173 cm
Inner radius	6 cm
Outer Radius	20 cm
Fiducial	46-86 mrad
Tungsten thickness	2.5 mm (20 layers), 5.0 mm (10 layers)
Silicon sensor thickness	320 μ m
Radial division	2.5 mm pitch
Azimuthal division	36

Table 2.12: LumiCal Parameters

The BeamCal consists of two cylindrical C-shaped modules split in half horizontally to accommodate the incoming beam line. The inner radius is 2 cm centered on the extraction beam line and the outer radius is 13.5 cm. The longitudinal structure consists of 50 alternating layers of tungsten and silicon. The tungsten thickness is 2.5 mm, making a total depth of 36 radiation lengths. The silicon sensor design based on a 6 inch wafer is shown in Figure 2.64. The inner region less than $R < 7.5$ cm is the area where the beamstrahlung pairs would hit. The segmentation in this region is approximately $5\text{mm} \times 5\text{mm}$ with about a half a Molière radius. This segmentation is optimized so that two-photon electron/positron can be detected in the high beamstrahlung pair background. The outer region $R > 7.5$ cm is the far LumiCal and has the same geometrical segmentation as shown in Figure 2.63.

Currently two electronic readout chips are being developed. The KP*X* chip with 1024 channels is designed primarily for the ECAL. The chip has four hits per bunch train to be stored for each channel. The FCAL chip with 64 channels is designed to handle the 100%

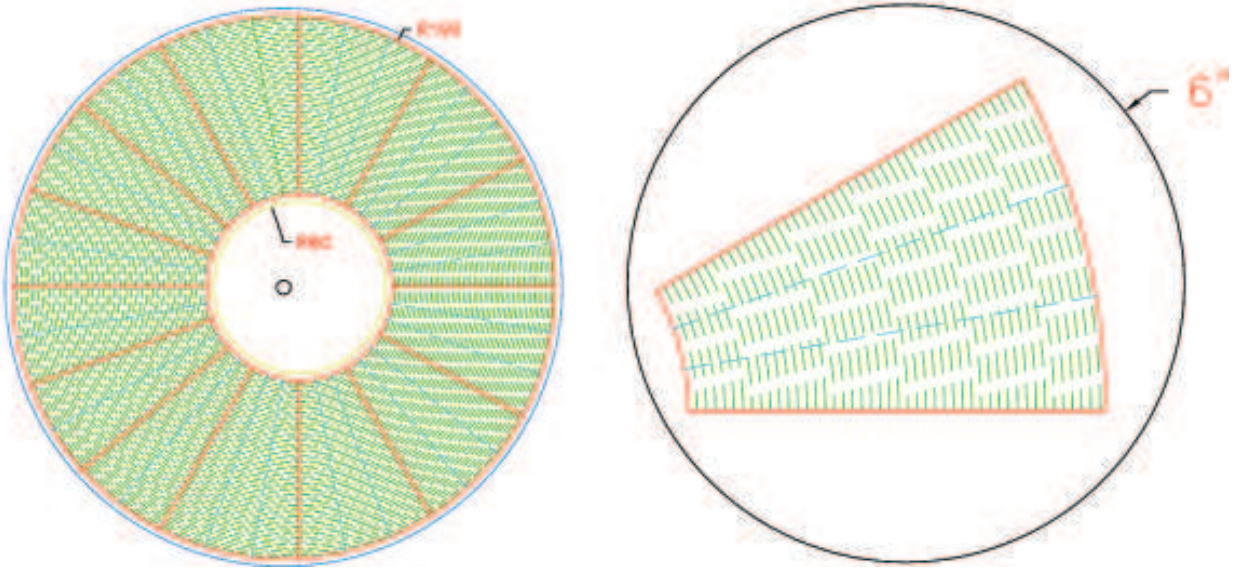


Figure 2.63: LumiCal sensor and segmentation.

occupancy in the BeamCal. The chip has 2820 buffer space so that a complete bunch train can be stored. Although the LumiCal occupancy is not 100%, the LumiCal region smaller than about 10 cm will have more than four hits per bunch train. Therefore, the LumiCal will use the FCAL chip in the inner region and the KPjX chip in the outer region.

2.6.3 Expected Performance

The detector performance has been studied using EGS5 [4], FLUKA [5], and GEANT4 [6] simulation packages. The ILC Nominal beam parameters at $\sqrt{s}=500$ GeV are used. Bhabha scattering is simulated using BHWIDE [7], and beamstrahlung pairs are generated using GUINEA-PIG [8]. The magnetic field map for the SiD 5 Tesla solenoid and the Anti-DID field are used.

2.6.3.1 Energy containment and energy resolution in LumiCal

One of the most important requirements for the LumiCal is the energy containment. If the energy of Bhabha events is not fully contained, some events will be classified as radiative Bhabhas and fail Bhabha event selection criteria, introducing a systematic error. Figure 2.65(a) shows the deposited energy (scaled by the incident energy) distribution as a function of the silicon layer from 1 GeV to 500 GeV electrons. At lower energies, the energy is mostly contained in the front 20 layers. Even at 500 GeV a significant deposition is in the front 20 layers, and the back 10 layers with double tungsten thickness accomplish the energy containment. Figure 2.65(b) shows the energy resolution parameter α in $\Delta E/E = \alpha/\sqrt{E}$ as a function of energy. The energy resolution improves at the lower energies, reaching $15\%/\sqrt{E}$ at 1 GeV, and still maintains $20\%/\sqrt{E}$ at 500 GeV.

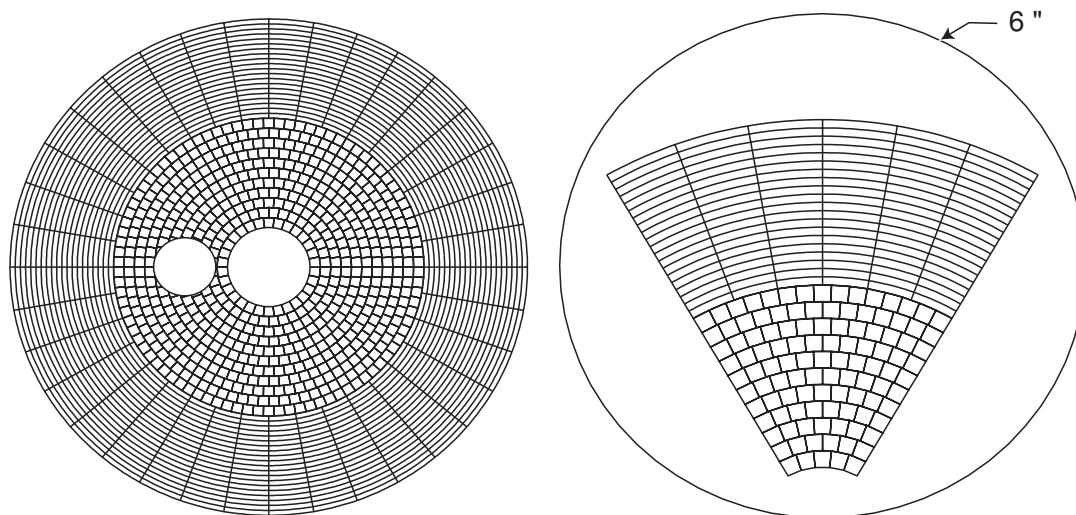


Figure 2.64: BeamCal sensor and segmentation.

2.6.3.2 Luminosity precision and LumiCal segmentation

The polar angle bias ($\Delta\theta$) and achievable luminosity precision have been studied as a function of sensor segmentation. Each silicon layer is segmented equally in the radial and azimuthal directions, and energy depositions in individual cells are calculated. The polar angle is reconstructed by taking a weighted average of the polar angle θ_i of individual cells with a weight W_i as

$$\theta = \frac{\sum_i \theta_i W_i}{\sum_i W_i}.$$

It is well known that the electromagnetic shower development is non-linear and the weight in linear energy introduces a large bias in coordinate measurements[3]. The bias can be reduced by using so-called logarithmic weight,

$$W_i = \max\{0, C + \ln(E_i/E_{total})\},$$

where E_i is energy deposition in each cell, E_{total} total energy deposition, and C is a constant. The constant provides an effective energy threshold, and only cells with a large enough energy deposition are used in the polar angle reconstruction.

The LumiCal is fully simulated using 250 GeV electrons with a $1/\theta^3$ angular distribution. The reconstructed polar angle, θ_{rec} is compared with the generated one θ_{gen} . The polar angle bias $\Delta\theta$ is calculated by an average value of $\theta_{rec} - \theta_{gen}$, and the angular resolution by the rms value. Table 2.13 shows the angular bias, angular resolution and the luminosity precision as a function of the radial segmentation. The azimuthal segmentation

REFERENCES

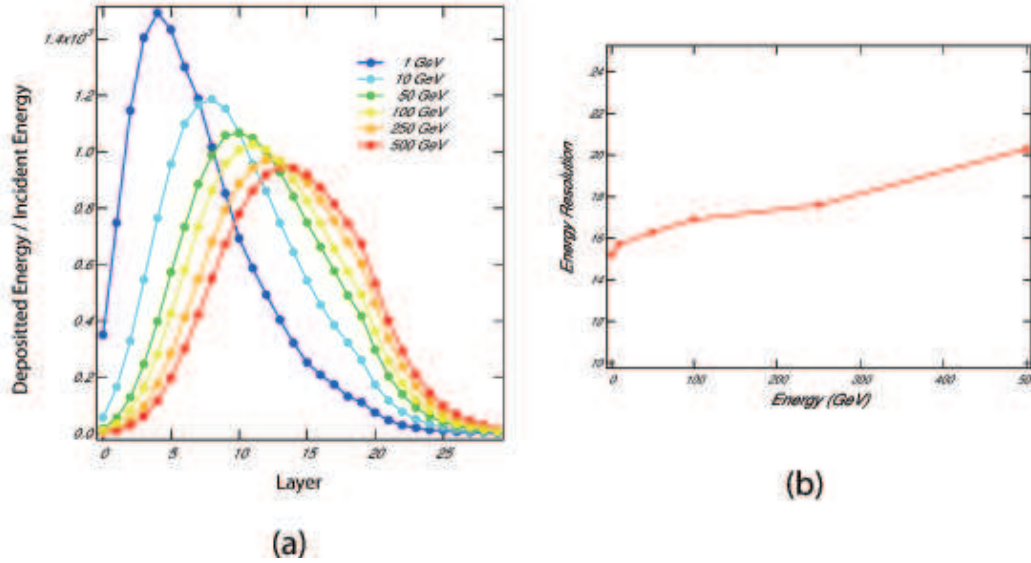


Figure 2.65: (a) Deposited energy in Si layers (b) Energy resolution

is fixed to 32. The luminosity precision improves as the radial segmentation decreases, and the luminosity precision goal of 10^{-3} can be reached when the radial segmentation is smaller than 3 mm. The dependence on the azimuthal segmentation is studied using a fixed 2.5 mm radial segmentation. Table 2.14 shows the result. The luminosity precision improves as the azimuthal segmentation is decreased, but the improvement is small. Finer azimuthal segmentation would be beneficial for cluster separation.

$\Delta r(mm)$	$\Delta\theta(mrad)$	$\sigma(\theta)(mrad)$	$\Delta L/L$
2.0	0.008	0.042	3.3×10^{-4}
2.5	0.017	0.046	7.9×10^{-4}
3.0	0.023	0.050	1.0×10^{-3}
4.0	0.036	0.058	1.7×10^{-3}
5.0	0.049	0.069	2.2×10^{-3}

Table 2.13: Radial segmentation

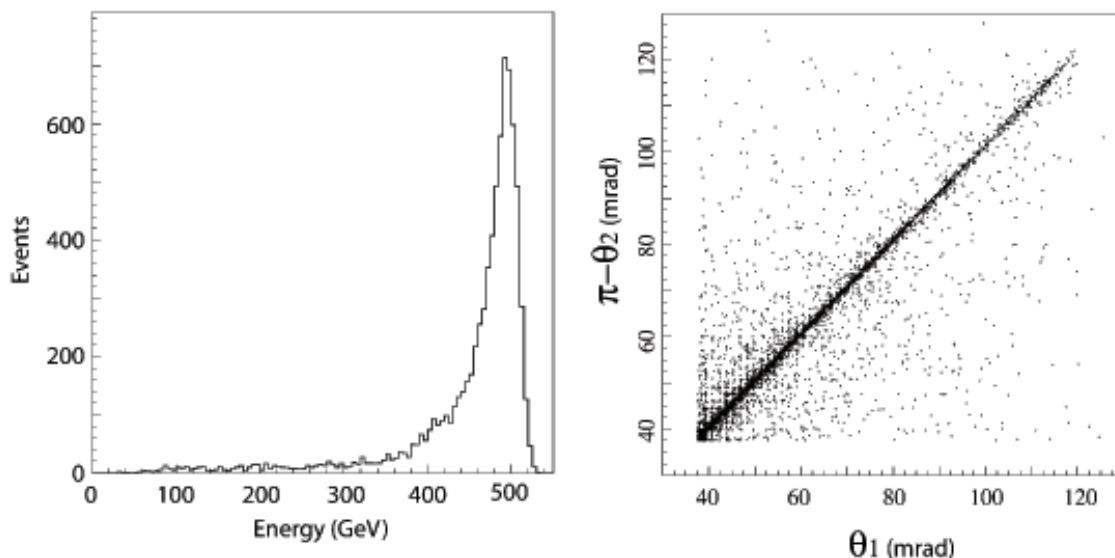
2.6.3.3 Bhabha scattering

The LumiCal performance is studied using Bhabha events at $\sqrt{s}=0.5$ TeV. A sample of 10,000 Bhabha events is generated in the CM system by the BHWIDE event generator[7]. Each event is transferred to the laboratory system with the 14 mrad crossing angle, and then processed through the LumiCal simulation. After energy and angle reconstructions, the event is transferred back to the CM system to understand the characteristics of Bhabha events. Figure 2.66(a) shows the total energy distribution of the reconstructed e^+ and e^- . The distribution has a peak at 500 GeV as expected, and has a long tail of radiative Bhabha

$N\phi$	$\Delta\theta(\text{mrad})$	$\sigma(\theta)(\text{mrad})$	$\Delta L/L$
16	0.017	0.046	7.7×10^{-4}
32	0.017	0.046	7.9×10^{-4}
48	0.017	0.045	7.6×10^{-3}
64	0.014	0.045	6.6×10^{-3}

Table 2.14: Azimuthal segmentation

events. The current cluster finder can reconstruct shower above 25 GeV. Figure 2.66(b) shows the correlation between the reconstructed e^- and e^+ polar angles. The 14 mrad crossing angle has been properly taken care of. The radial segmentation is visible at small angles.

Figure 2.66: (a) Total energy distribution (b) Correlation of e^+ and e^- polar angles

2.6.4 High energy electron detection in BeamCal

We have studied the ability to identify and reconstruct high energy electron in the presence of beamstrahlung pair background in the BeamCal[9]. The analysis consists of three parts:

1. A lookup table which would correlate the energy and position of a shower on the BeamCal to an incident particle energy. This accounts for the θ and ϕ dependence of shower energy introduced by energy loss down the beampipe, and also incorporates the sampling fraction of the detector.
2. A lookup table of average beamstrahlung depositions which would be used to subtract the expected beamstrahlung energy from the shower of interest.

REFERENCES

3. A cluster algorithm which would analyse the total signal on the BeamCal and attempt to isolate the part of the signal that is due to the high energy electron.

BeamCal signals are created by overlaying a high energy electron shower and one bunch crossing of beamstrahlung backgrounds randomly selected from the 10,000 crossings. After subtracting the average beamstrahlung energy, the cluster algorithm reconstructs the high energy electron if the subtracted energy is greater than three sigma of the beamstrahlung energy variation. As the beamstrahlung energy has a strong radial and azimuthal dependence, the detection efficiency is calculated as a function of the distance from the extraction beam axis at three azimuthal angles (0, 90, and 180 degrees). Figure 2.67 shows the detection efficiency as a function of radius in the BeamCal for 50, 100, and 150 GeV electrons. The inefficiency between 30 and 50 mm at $\phi=180^\circ$ is due to the incoming beam hole. Since the beamstrahlung background energy is the highest at $\phi \approx 90^\circ$ (and 270°), the detection efficiency is lower at this angular region. The efficiency to detect more than 150 GeV electrons is almost 100% up to 8 mrad from the beam axis.

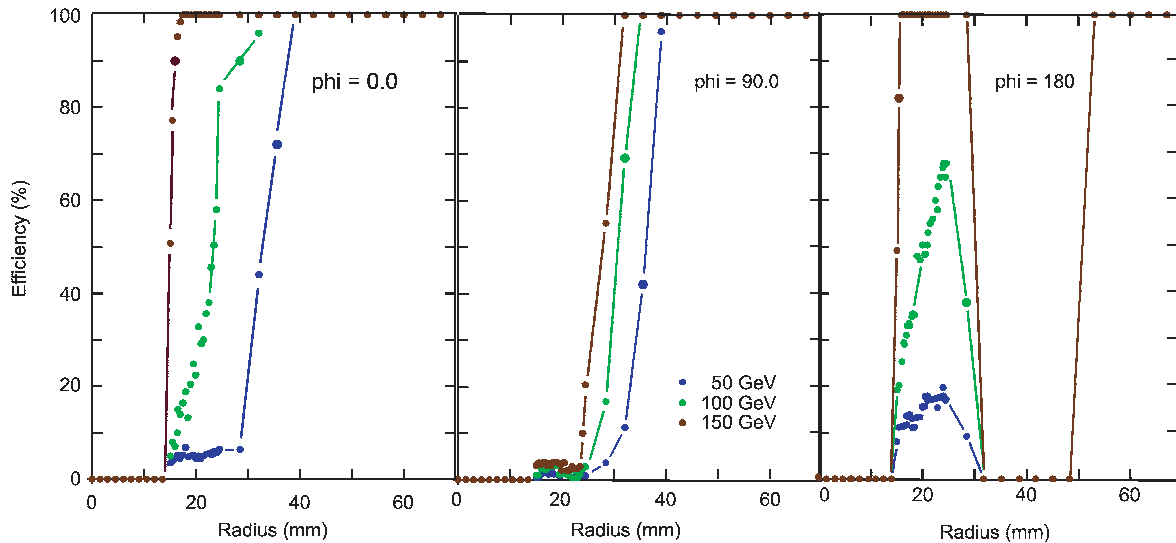


Figure 2.67: Efficiency to reconstruct high energy electrons at three azimuthal angles

2.6.4.1 Calorimeter hermeticity

Calorimeter hermeticity is surveyed using 250 GeV electrons. Figure 2.68 shows the total energy deposition in Silicon layers as a function of $\cos \theta$. The ECAL, LumiCal and BeamCal angular coverages are indicated in the figure. Five sets of simulation are made with different LumiCal Z locations. When the LumiCal is at the same Z location as the ECAL, a significant energy is lost at $\cos \theta \sim 0.993$. To achieve calorimeter hermeticity, the LumiCal is moved 10 cm closer to the IP.

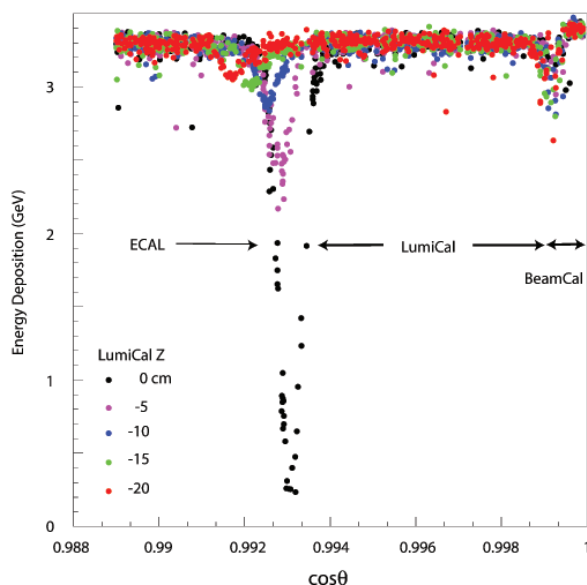


Figure 2.68: Energy deposition in Si layers as a function of $\cos\theta$

2.6.4.2 Tungsten mask

When the beamstrahlung pairs hit the BeamCal, a large number of secondary photons are produced and about 35k photons per bunch crossing are back scattered. The tungsten mask is to shield the central detector from these low energy photons. Figure 2.69 shows the number of photons penetrating the tungsten mask as a function of the mask thickness. To eliminate the photons, a mask thicker than 6 cm is necessary. But such a thick mask takes up the space and significantly increases the weight. The mask thickness of 3 cm is chosen. Although about 1000 photons are penetrating the mask, they are low energy (~ 200 KeV) and are uniformly distributed over the inner surface of Endcap HCAL.

2.6.5 R&D

The radiation level in the forward direction implies that one will need to probably specify specialized Si material. One needs to select the materials and expose them to radiation levels equivalent to what will be seen at the ILC forward region over period of 5 years. Two possible radiation hard materials are oxygenated Float Zone Si wafers and magnetic Czochralski Si wafers.

REFERENCES

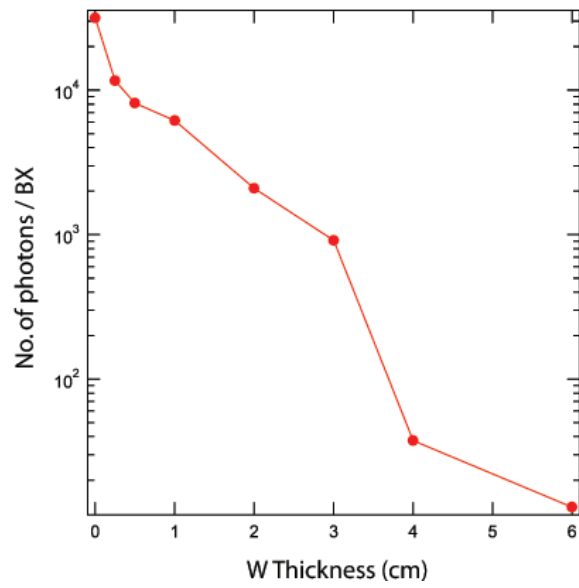


Figure 2.69: Number of photons penetrating the tungsten mask as a function of the mask thickness

References

- [1] “Experimental implications for a linear collider of the SUSY dark matter scenario,” P. Bambade et al., arXiv:hep-ph/0406010v1, june 2004.
- [2] “IR Optimization, DID and Anti-DID,” A. Seryi, T. Maruyama and B. Parker, SLAC-PUB-11662, Jan. 2006.
- [3] “A simple method of shower localization and identification in laterally segmented calorimeters,” Nucl. Instrum. Methods A, vol. 311, 130 (1992).
- [4] “The EGS5 code system,” H. Hirayama, Y. Namito, A.F. Bielajew, S.J. Wilderman and W.R. Nelson, SLAC-R-730 (2005)
- [5] “FLUKA: a multi-particle transport code,” CERN-2005-10 (2005), INFN/TC-05/11, SLAC-R-773.
- [6] “GEANT4 developments and applications,” IEEE Transactions on Nuclear Science, 53, 270 (2006)
- [7] “ $O(\alpha)$ YFS exponentiated monte carlo for Bhabha scattering at wide angles for LEP/SLC and LEP2,” Phys. Lett. B390, 298 (1997)
- [8] “Study of Electromagnetic and Hadronic Background in the Interaction Region of the TESLA Collider,” D. Schulte, Ph.D Thesis, Hamburg University 1996.
- [9] “Electron Identification in the BeamCal of the Silicon Detector at ILC,” G. Oleinik, J. Gill and U. Nauenburg, ILC-SID-TechNote-003. For details, see http://hep-www.colorado.edu/~uriel/Beamstrahl_TwoPhoton-Process/grp_results.html .

REFERENCES

Chapter 3

Machine-Detector Interface and Global Issues

3.1 SiD Assembly

SiD expects the VXD, EMCal, and HCal modules will be built at collaborating labs and universities and transported to the ILC site. The iron will be built in sub modules with a mass suitable for transportation from an industrial site, and bolted together at the ILC. The solenoid would probably have two sections, and will be wound industrially.

The detailed strategy of final assembly must await site selection. A shallow site strategy will likely be different than one for several hundred m underground. The optimal mass for steel modules will depend on transportation modes available between the factory and ILC, and sea, rail, or road limits will lead to different conclusions. (As a baseline, SiD is designing for road transportation and approximately 100 tonne maximum unit weight). The shape of an underground hall and the capacity for underground bridge cranes may depend on the site geology. In addition, an optimal strategy will depend on the ILC construction schedule.

SiD subsystems will have few data and power connections compared to those for the LHC detectors because of the absence of a trigger and the low aggregate data rates. The subsystems will be integrated with their electronics and tested at their assembly points and at staging areas at the ILC site; final connection, integration and test should be relatively simple. The utility needs (electricity, water, LHe, compressed air, data fibers) needs of SiD are modest, and are expected to be flexible connections to the wall.

SiD will assemble the lower sections of the flux return, lower the solenoid into this cradle, and then complete the flux return. The complete barrel assembly weighs approximately 4 Ktonnes, and each door weighs approximately 1.9 Ktonnes. Surface assembly and lowering with a substantial gantry crane is possible, as is assembly on the interaction region floor with a 300 to 400 tonne bridge crane. A possible alternative would be two approximately 200 tonne cranes on the same rails, one nominally for each experiment, with occasional coordinated use of both cranes for the larger lifts. Dedicated tooling is assumed for the insertion of the barrel

detectors into the solenoid.

SiD expects to move on hardened steel rails, grouted and locked to the floor. Rail sets for transverse motion (push pull) and door opening in both the beamline and garage positions will be needed. SiD expects that locations for these rails can be found that either can be shared with the other detector, or not interfere with its system. If ILC is built in a seismic location, provision will be needed for locking SiD down in both the beamline and garage positions.

3.2 Push Pull

Introduction:

SiD strongly supports the notion of two detectors at the ILC, and considers the push-pull interchange of the two detectors on a frequent schedule necessary for a successful project. Consequently, SiD has made technical subsystem choices that support a rapid exchange of position and that will be require minimal alignment and calibration time on beamline. It has also made engineering decisions to optimize these moves.

SiD assumes an interchange frequency of about a month, with a fixed (but adjusted) time allocation to each detector. This is long enough to make the lost data taking time reasonable if the transition time is approximately a day, and short enough to both avoid the possibility of significant data disparity opportunities, and to limit the “improvements” that would require re-commissioning for the detector that was out. We assume that the time a detector takes to clear the beamline after the beginning of a transition will be subtracted from its next time allocation, and that a detector may take as long as it wants to set up on beamline, but that this time is part of its allocation. We assert that with a properly engineered detector and adequate experienced staff, the time from beginning detector exchange to beginning beam-based alignment of the final quadrupoles should be less than one day. We assume that except for unusual machine mishaps, both detectors take their chances with the machine luminosity.

Machine Detector Interface Assumptions:

1. QD0 is located in SiD and moves with it. Supporting it with adequate vibrational stability is a responsibility of SiD. Its transverse position within SiD is remotely adjustable to ± 1 mm.
2. QF1 is a fixed part of the machine, and is shared by the two detectors. Its support system includes a longitudinal anchor that will be used to stabilize the Z position of the QD0 assembly when the SiD door is opened.
3. There is a warm removable spool piece between QD0 and QF1. It has two RF smooth, remotely operated high vacuum valves isolating the spool piece, and there is provision for purging, pumping to high vacuum, and leak checking this assembly (presumably permanently installed RGA's). There is a bellows system that will accommodate ± 1 mm misalignment.

4. SiD will be self shielded. In addition to the SiD calorimeters and iron providing sufficient shielding in the event of an accident to the portion of the beamline approximately inboard of the QD0's, the rest of the beamlines are shielded by a system of portable iron and concrete (Pacmen). In a conceptual sense, each Pacman consists of a section fixed to the tunnel mouth wall, a pair of hinged shields that open to gain access to the beamline connection described above, and a section fixed to the detector door. It is expected that the hinged sections and the piece fixed to the tunnel wall will be common with the other detector, and that dimensional differences between the two detectors will be made up in the third section.
5. The 2K He cryogenic system for QD0 is carried on a support fixed to SiD and supplied from a 4K He system on SiD. All connections to QD0 are undisturbed during a move, and the magnet remains cold.
6. An automatic alignment system with an accuracy of at least ± 1 mm will relate the position of SiD to the beamline coordinates (when SiD is near the beamline).

Detector Assumptions:

1. The superconducting solenoid has all of its services and utilities carried with SiD. The He liquefier is mounted on a hall wall, and supplies He to SiD by a flexible vacuum insulated line. (It is assumed that He compressors are located remotely for vibration isolation.) (It is assumed that each detector has its own liquefier, but that cross connect valves are incorporated in the cold boxes to allow mutual assistance.) SiD will have support platforms, attached above, aside, or adjacent to the detector. These platforms will support the solenoid power supply, dump resistor, quench protection system, and other auxiliaries.
2. The detector will receive utilities of ~ 350 KW 480 VAC 3 phase power from a flexible line that remains connected during a move. Low Conductivity water, chilled water, and compressed air will also be provided by continuously connected flex lines.
3. Data will exit the detector via an optical fiber system continuously connected to the wall. Monitoring and control communications will also be via a fiber system. All detector subsystem power will come from supplies that travel with the detector. No subsystem signal cable will come off the detector.
4. The detector will roll on hardened steel rails using Hilman rollers or equivalent. Sid will carry its doors when moving in Z, and will have rails in both the beam and garage position to open its doors. The drive mechanism will have minimal energy storage, possible a gear drive to a fixed cog rail. It is expected that a velocity between 1 and 5 mm/s is desirable and reasonable.
5. The detector transport system will deliver the detector to its appropriate position on the beamline to a precision of ± 1 mm.
6. The detector is designed so that any stresses caused by the force required to move the detector are not transmitted to the calorimeter supports, and so the precision calorimeter and tracker systems will not be distorted from the moving process.

MACHINE-DETECTOR INTERFACE AND GLOBAL ISSUES

7. The detector will have an internal alignment system, probably based on frequency scanning interferometers that will provide high precision measurements of the relative positions of the barrel components, endcap systems, and beamline components.
8. The Sid beamline is supported by the inboard ends of the QD0's, and moves with them as they are moved to the ILC beamline during beam based alignment. The SiD Vertex Detector (VXD) is mounted to the beamline, and will remain coaxial to the beam during the alignment process.
9. The SiD flux return will limit leakage field to be less than 100 gauss at 1 m from the iron.

The Push Pull Process

SiD envisions the process as a series of rehearsed steps which are described here and in Microsoft Project Gantt chart format in Fig "Push Pull Schedule". The time units are hours, and SiD believes that with suitable experience and engineering, this is a rational schedule. Some of this belief is based on the experience with the 600 ton SLD doors, in which a door could be opened, the detector internals accessed for two hours, the door closed, and beam based alignment begun – in 8 hours.

1. Secure ILC Beams: This is the first step of the detector exchange process, and involves ensuring that ILC can not deliver a beam to the hall, and releasing the necessary keys (physical or otherwise) to permit opening of the shielding. This step would be very similar to that before a detector could open a door. (1 time unit)
2. De-energize magnets: At this time, it is not obvious whether the QD0's and solenoid should be (partly) de-energized. We assume here that the QD0's and solenoid will be run down, and that the time will be approximately equal to the charging time for the solenoid, which is 3 hours. If the ILC is built in a region with seismic requirements, this time can also be used to release seismic restraints.
3. Open Beamline Shielding: It is assumed that the beamline shielding is mechanically locked and requires the previously mentioned keys to unlock. The moving parts of the Pacmen are supported by hinges, and are activated by fixed mechanisms so that no crane activity is required. It is assumed that all 4 Pacmen are opened together by coordinated but separate crews. (1 time unit).
4. Disconnect Beamlines: This process involves checking that the isolation valves have properly shut, venting the spool piece with an appropriate purge, and disconnecting the flanges. It is assumed that separate crews work on each end. (2 time units).
5. Check Detector Transport System: The detector transport system should be carefully checked to see that it is ready to move the detector. It is assumed that the transport system is carefully maintained, and so this is a safety step rather than an opportunity for regular maintenance. (2 time units).
6. Transport Detector: The detector is moved in X for 15 to 20 m. The time, including a provision for acceleration and deceleration, would under 5 hours for a top velocity of 1 mm/s (15 m travel) and about 1 hour for 5 mm/s. (2 time units)

MACHINE-DETECTOR INTERFACE AND GLOBAL ISSUES

Chapter 4

Physics Performance and Benchmarking

4.1 Simulation of SiD.

In order to design a detector which is capable of exploiting the full physics discovery potential of the ILC, a fairly sophisticated and mature simulation and reconstruction environment is needed. The Simulation & Reconstruction Working Group has concentrated its efforts on assembling a flexible framework to allow different detector designs to be simulated and multiple reconstruction algorithms to be implemented and used for physics and detector analyses. The code, binary executables, and documentation in the form of Application Programming Interface (API) and tutorials are all available online at <http://lcsim.org>.

Event Generation

A number of different event samples have been generated for detector design studies, ranging from single particles to inclusive Standard Model processes.

Single particle studies are essential for developing reconstruction algorithms and understanding the basic detector response and resolution. Accordingly, the following set of single particles is available:

1. Single particles: $e, \gamma, \mu, \pi, p, K, n, K_L^0$
2. Simple resonances: $\pi^0, K_S^0, \psi \rightarrow \mu^+ \mu^-, \rho$
3. Complicated decays: $\tau, u, d, s, c, b, Z, W$

Samples of $e^+e^- \rightarrow q\bar{q}$ events with no beam- or bremsstrahlung were also generated at various center of mass energies. These samples were primarily intended as a test-bed for evaluating different reconstruction algorithms. By concentrating on the reconstructed event

energy as a figure of merit, complications arising from such things as jet-finding algorithms are minimized.

The following canonical set of benchmark signal processes was generated for the default ILC configuration at 500 GeV:

1. $e^+e^- \rightarrow q\bar{q}, q = u, d, s, c, b, t$
2. $e^+e^- \rightarrow f\bar{f}, f = \mu, \tau$
3. $e^+e^- \rightarrow Z\gamma, ZZ^*, WW, ZZ^*\nu\bar{\nu}, WW\nu\bar{\nu}$
4. $e^+e^- \rightarrow Zh, m_h = 120 \text{ GeV}, 140 \text{ GeV}$

Finally, an almost complete set of Standard Model processes at 500 GeV was generated using the Whizard Monte Carlo program [1]. All 0, 2, 4 and 6 fermion final states, as well as top quark-dominated 8 fermion processes were generated. PYTHIA [2] was used for final state QED and QCD parton showering, fragmentation and decay to provide final-state observable particles. Included in this sample are backgrounds arising from interactions between virtual and beamstrahlung photons. This sample is intended to serve as an unbiased background sample for physics analyses. Samples were generated with electron and positron polarizations of 100%. Arbitrary polarization samples can be generated by properly combining events from the four data samples. For the purposes of the physics benchmark analyses, event samples were created which reflect the expected ILC baseline parameters of 80% electron and 30% positron polarization. Because of the large size of the full dataset, only a fraction of these events have been processed through the full detector simulation, with individual events weighted to reflect the statistical sampling.

Full Detector Simulation

The simulation of the response of the detector to the generated events is based on the Geant4 toolkit, which provides the classes to describe the geometry of the detector, the transport and the interactions of particles with materials and fields. A thin layer of Linear Collider-specific code provides access to the Monte Carlo events, the detector geometry and the output of the detector hits. The geometries are fully described at runtime, so physicists can vary detector parameters without having to rebuild the simulation executable binaries. The output uses the standard LCIO format, so that detectors modeled using other simulation packages could be analyzed, and data generated using this system could be analyzed in other reconstruction and analysis frameworks.

Fast Detector Simulations

Although the main purpose of the SiD simulation and analysis effort is to define the detector performance using full simulations, some analyses still need to be able to quickly simulate the response of the detector in a parameterized fashion. Two packages are available for such fast MC studies. The first is a fully parameterized package which simply smears the resolution of input particles. See the benchmarking section for more details. The other package is *lelaps* (<http://lelaps.freehep.org>). This program propagates particles through the detector using helical propagation through a simple solenoidal magnetic field. It is capable of

handling decays in flight, multiple coulomb scattering and energy loss in tracking detectors. It parameterizes the shower development of particle interactions in the calorimeters using functional forms which have been shown to be very good approximations to electromagnetic showers, and statistically reasonable facsimiles of hadronic showers. It produces hits in detector sensitive elements which can be used in subsequent reconstruction and analysis. It is, therefore, an intermediate between the fast Monte Carlo, which provides Reconstructed-Particle objects which are directly usable in physics analysis, and the full Geant4 simulation which simulates the detector interactions much more realistically.

Detector Variants

The XML format allows variations in detector geometries to be easily set up and studied, e.g. Stainless Steel vs. Tungsten hadronic calorimeter absorber material, RPC vs. scintillator readout, calorimeter layering (radii, number of layers, composition, . . .), readout segmentation (pad size, projective vs. fixed cell size), tracking detector topologies (“wedding cake” vs. Barrel + Cap), magnetic field strength.

In addition to the baseline Silicon Detector (sid02), a number of variants have been developed in order to study the dependence of the performance on detector options.

sid02

For reference, we include here a fairly complete textual description of the baseline detector. Full details can be found at <http://lcsim.org/detectors/#sid02>.

4.1.1 Beampipe:

The beampipe is composed of three sections: a cylindrical central tube and forward and backward conical sections. The central tube has an inner radius of 1.2cm and a z extent of +/- 6.251cm and is made of 0.040cm thick beryllium. The conical sections are .875mm thick beryllium and flare from 1.2cm inner radius at 6.25cm to 8.2cm at the edge of the tracking region. The beam pipe has a titanium inner liner .0025cm thick for the central barrel section and 0.0075cm thick for the conical sections.

4.1.2 Vertex Detector:

The vertex detector is composed of a central barrel system with five layers and forward systems composed of four disks. The barrels are all 12.5cm long and are composed of .0113cm silicon, of which the outer 0.002 is sensitive. The inner radii of the layers are:

1.46, 2.26, 3.54, 4.8, 6.04cm.

There are four forward disks on either end, composed of a total of 0.0113cm of silicon, of which the inner 0.002cm is sensitive. All of the disks extend to a maximum radius of 7.1cm. The z positions and inner radii for the four disks are:

z (cm)	inner radius (cm)
7.18	1.4
9.02	1.6
12.16	1.8
17.0	2.0

The entire vertex detector is enclosed within a double walled carbon fiber support tube. The support tube walls are 0.05cm thick carbon fiber with inner radii of 16.87cm and 18.42cm and a z extent of $z \approx 89.48$ cm. The ends of the support tube are double-walled disks of 0.05cm thick carbon fiber disks.

The mechanical supports for the endcap disks are modeled as carbon fiber rings with a reduced density of 25% to reflect the lightening holes in the real structures. The VXD utility mixture of cooling channels, cables and fibers etc. is represented by layers of G10 and copper at the endplates, extending down to the beampipe and exiting the detector along the beampipe.

4.1.3 Tracker:

The tracker is composed of five cylindrical barrels with four disk-shaped endplanes. The z extent of the barrels increases with radius and the endplane for each extends beyond its cylinder in radius to provide overlap. The sensitive medium is silicon, assembled into carbon-fiber/Rohacell/PEEK modules and read out via a bump-bonded chip and Kapton/copper cables. These modules are supported by carbon-fiber/Rohacell/carbon-fiber barrels or disks. Each barrel cylinder is supported from the next barrel out by an annular carbon fiber-ring. Outside each of these support rings in z , G10/copper printed circuit boards are mounted for power and readout distribution to all silicon modules in a layer.

Barrels: The radii and z extent of the barrel silicon are:

layer	z (cm)	inner radius (cm)
1	55.8	21.8
2	82.5	46.8
3	108.3	71.8
4	134.7	96.8
5	160.6	121.8

For the barrels, the support tubes are composed of 0.05cm carbon fiber, 0.8cm of Rohacell31 (15% coverage) and 0.05cm carbon fiber. The sensor modules for the barrel are single-sided and have 0.03cm of silicon mounted on carbon fiber/Rohacell31 frames that clip into PEEK (Polyetheretherketone) mounts. The average thickness of the carbon fiber,

Rohacell31 (50% coverage) and PEEK in the modules of each barrel layer are 0.016cm, 0.28cm and 0.02cm respectively. The average thicknesses of the readout materials are 0.00048cm of silicon, 0.0064cm of Kapton and 0.00065cm of copper, however, the thickness of the cable material varies by layer.

Endcap: The z positions and radial extents of the endcap silicon are:

layer	inner radius (cm)	outer radius (cm)	z (cm) for u plane	z (cm) for v plane
1	20.7	49.4	85.5	85.9
2	20.7	74.7	111.4	111.8
3	20.7	99.9	137.8	138.2
4	20.7	125.0	163.6	164.0

where each layer is composed of two sensor modules to measure coordinates in two stereo (u-v) views. The forward disk supports are composed of .05cm carbon fiber, 0.63cm Rohacell31 (15% coverage) and 0.05cm of carbon fiber. There are two sensor modules mounted outside of the disks to provide stereo measurements and have 0.03cm of silicon mounted on either side of carbon fiber/Rohacell31 frames that clip into PEEK (Polyetheretherketone) mounts. The average thickness of the carbon fiber, Rohacell31 and PEEK in the modules of each disk double-layer is assumed to be the same as that for the barrel modules.

4.1.4 Calorimeters:

Electromagnetic Calorimeter: This element sets the basic size and aspect ratio for the rest of the detector. The inner radius for the barrel is 127cm. The aspect ratio is set to $\cos(\theta)=0.8$, meaning the inner z of the endcap EM calorimeter is at z of 168cm. The EM calorimeter is a sampling calorimeter composed of 20 layers of

material	thickness (cm)
Tungsten	0.250
Silicon	0.032
Copper	0.005
Kapton	0.030
Air	0.033

This is followed by ten layers of the same readout, but doubled thickness of tungsten. There is a sensitive silicon layer before the first layer of tungsten to provide additional electron/photon discrimination, giving a total of 31 layers of silicon readout. The tungsten alloy being used is TungstenDen24 (93% W, 6.1% Ni, .9% Fe) with a density of 17.8 g/cm³.

The endcap plug sits inside the barrel cylinder, so the barrel z extent is +/- 182cm. The endcap starts at an inner radius of 20cm and extends out to 126.5cm.

PHYSICS PERFORMANCE AND BENCHMARKING

Hadron calorimeter: The hadron calorimeter is a sampling calorimeter composed of 40 layers of

material	thickness (cm)
Steel	2.0
PyrexGlass	0.11
RPCGas	0.12
PyrexGlass	0.11
G10	0.3
Air	0.16

It begins immediately outside of the EM calorimeters, with the endcap plug sitting inside the barrel. The barrel inner radius is 141cm with a z extent of +/- 294cm. The endcap extends from an inner radius of 20cm to an outer radius of 140.75cm, inner z of 182cm.

4.1.5 Solenoid:

The solenoid is modeled as a cylinder with an inner radius of 255cm. This is larger than the outer radius of the hadron calorimeter since we will not be building a cylindrical detector, but a polygonal one (current thinking is dodecagonal). The barrel composition is as follows:

material	thickness (cm)	z (cm)
Steel	6.0	271.0
Air	8.5	271.0
Aluminum	39.3	262.5
Steel	6.0	262.5
Air	20.0	271.0
Steel	3.0	271.0

This is capped with disk endplates of 6cm steel from $r=250\text{cm}$ to 332.8cm . The field is solenoidal, constant 5 Tesla along z up to half the coil thickness and -0.6 outside.

4.1.6 Muon System:

The muon system is composed of 11 layers of 20cm thick iron plates interspersed with double RPC readout. The barrel inner radius is 338.8cm with z extent of +/- 294cm. The endcap sits outside the barrel at an inner z of 303.3cm and radius from 20.0cm to 608.2cm.

4.1.7 Masks and Far Forward Detectors

The far forward region is designed for the 14mr beam crossing solution so has separate incoming (inner radius 1.0cm) and outgoing (inner radius 1.5cm) beampipes. The far forward plug is designed to fit within a radius of 20cm. It starts with an electromagnetic calorimeter (LumiCal) with the same composition as the endcap calorimeter, extending from 6.0cm out to 19.5cm.

The calorimeter is backed up by a conically tapered tungsten mask, inner radius 8.0cm at z of 182cm, tapering to 16cm at z of 313.5cm. The outer radius is constant at 15.5cm.

There is a far forward low- Z shield (12.39cm thick Borated polyethylene) at z of 282cm.

This is followed by a 50 layer silicon-tungsten calorimeter (BeamCal) at z of 295cm.

4.2 Benchmark Reactions

Physics performance studies are needed to quantify the performance of SiD, revisit the performance requirements on the various ILC detector subsystems, and ultimately optimize the SiD design by studying how the performance changes as one varies the basic detector parameters. In a broader context, these studies further the physics case of the ILC.

A list of physics benchmark reactions [3] was presented to the ILC community at Snowmass 2005. This list of about 30 reactions provides comprehensive coverage of ILC physics topics and detector challenges, but is too long to be addressed by detector concept groups at this time. Thus, a reduced list of 6 reactions was specified by the ILCSC Research Director which is more appropriate for studies on the time scale of the LOI:

1. $e^+e^- \rightarrow e^+e^-H, \mu^+\mu^-H, \sqrt{s}=250$ GeV;
2. $e^+e^- \rightarrow ZH, H \rightarrow c\bar{c}, Z \rightarrow \nu\bar{\nu}, q\bar{q}, \sqrt{s}=250$ GeV;
3. $e^+e^- \rightarrow ZH, H \rightarrow \mu^+\mu^-, Z \rightarrow \nu\bar{\nu}, q\bar{q}, \sqrt{s}=250$ GeV;
4. $e^+e^- \rightarrow \tau^+\tau^-, \sqrt{s}=500$ GeV;
5. $e^+e^- \rightarrow t\bar{t}, t \rightarrow bW^+, W^+ \rightarrow q\bar{q}', \sqrt{s}=500$ GeV;
6. $e^+e^- \rightarrow \tilde{\chi}_1^+\tilde{\chi}_1^-/\tilde{\chi}_2^0\tilde{\chi}_2^0, \sqrt{s}=500$ GeV .

In addition to these compulsory LOI benchmark reactions SiD also investigated the following physics processes:

7. $e^+e^- \rightarrow ZHH, H \rightarrow b\bar{b}, \sqrt{s}=500$ GeV;
8. $e^+e^- \rightarrow e^+e^-(\gamma), \mu^+\mu^-(\gamma), \sqrt{s}=500$ GeV .

4.2.1 $e^+e^- \rightarrow e^+e^-H, \mu^+\mu^-H, \sqrt{s}=250 \text{ GeV}$

Studies of the Higgs Boson are expected to be center stage at the ILC. The production of the Higgs through “Higgs-strahlung” in association with a Z, will allow a precision Higgs mass determination, precision studies of the Higgs branching fractions, measurement of the production cross section and accompanying tests of SM couplings, and searches for invisible Higgs decays. When the associated Z decays leptonically, it is possible to reconstruct the mass of the object recoiling against the Z with high precision. The resolution in the recoil mass, which translates into how sharply the Higgs signal rises above the Z Z background, depends on the initial beam energy spread, which at ILC is about 0.1%, and the precision with which the lepton momenta are measured. Assuming the Higgs mass is 120 GeV, $\sqrt{s} = 350 \text{ GeV}$, and the integrated luminosity is 500 fb^{-1} , we find that the Higgs mass can be determined with a precision of 100 MeV in SiD for Z decays to muon pairs.

It is interesting to see how the precision of the mass measurement depends on the momentum resolution of the SiD tracker. Figure 4.1 shows the recoil mass distribution opposite the Z for four different values of tracker momentum resolution, characterized by the parameters a and b. Here the momentum resolution is written $\delta p_t/p_t^2 = a \oplus b/p_t \sin\theta$. Accuracy in the mass measurement improves significantly as the tracker momentum resolution improves, even as it improves beyond the $a = 5 \times 10^{-5}$ level often cited as the goal for tracker resolution at the ILC. The SiD detector has superb momentum resolution, with a $\sim 2 \times 10^{-5}$; the dilepton recoil mass measurement will benefit accordingly.

The 4-jet channel provides a better measurement of the mass of the Standard Model Higgs, but the recoil mass technique will provide the best measurement of the Higgs mass if the Higgs has a substantial invisible branching ratio. Measurements of the ZH cross-section and Higgs branching ratios show little dependence on tracker performance since events outside the peak are used to maximize statistics.

4.2.2 $e^+e^- \rightarrow ZH, H \rightarrow c\bar{c}, Z \rightarrow \nu\bar{\nu}, q\bar{q}, \sqrt{s}=250 \text{ GeV}$

Determination of the Higgs branching ratios is a classical example of a precision measurement at ILC where the absolute Higgs couplings to particles of different masses can be verified. These measurements are also an important test for the Higgs mechanism and discriminating different SM models. The decay modes result in two and four jet final states and exercise the tagging of charm quarks which is particularly sensitive to the vertex detector performance.

4.2.2.1 Data Samples

In the simulation of the measurement of the Higgs boson branching ratio to charm quarks, the Higgs mass is assumed to be 120 GeV at $\sqrt{s} = 250 \text{ GeV}$ with total integrated luminosity of 500 fb^{-1} . The Higgs bosons in the signal process are produced in Higgsstrahlung, $e^+e^- \rightarrow ZH$, with the Higgs decaying to charm quarks. The choice of center-of-mass of energy maximizes the the cross-section value for Higgsstrahlung. Figure 4.2 shows the Higgs boson production cross-section at different center-of-mass of energy. The main backgrounds are

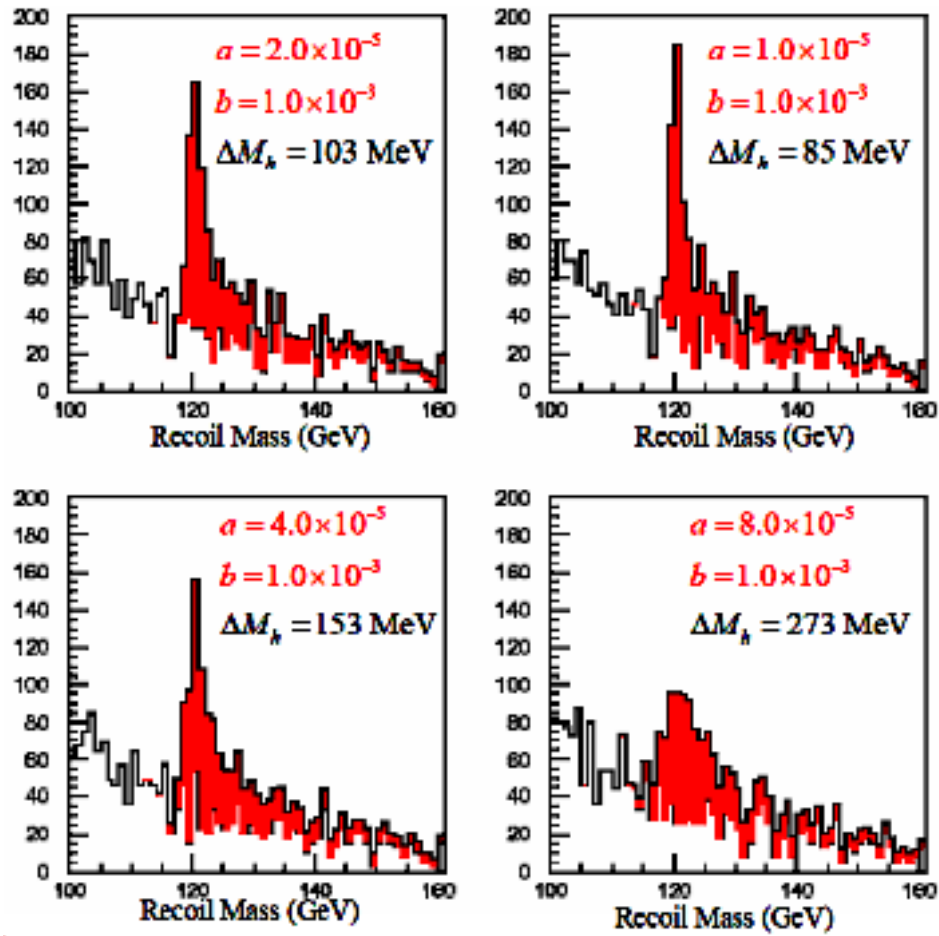


Figure 4.1: Higgs recoil mass spectra for several values of parameters characterizing the tracker momentum resolution.

WW, ZZ and qq pairs. A Standard model sample which includes all processes is used as background. The results assume +80% electron polarization and -30% positron polarization.

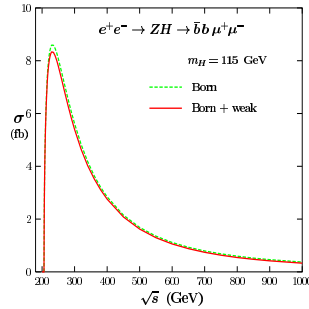


Figure 4.2: SM Higgs production cross-section.

The SM Higgs boson branching ratios calculated with HDECAY are shown in Tab.4.1.

Channel	$m_H=120$ GeV
$b\bar{b}$	68.16
W^+W^-	13.45
gg	6.71
$\tau^+\tau^-$	6.74
$c\bar{c}$	3.04
ZZ	1.5

Table 4.1: Standard Model Higgs Boson branching ratios for 120 GeV mass.

4.2.2.2 Tools

In this study one of the most important parts of the analysis is a proper identification of jets. The jets are reconstructed from particle flow objects, e.g. tracks, with the DURHAM jet algorithm. The LCFI Vertex Package is employed for jet identification and flavour tagging. The software is based on the ZVTOP vertex finder[1]. By default, the flavour tag provided is obtained from the algorithm by R. Hawkings[2] and is based on a neural network approach, combining track and vertex information to distinguish b, c and light jets. This provides measurement of charged particle tracks in the vertex detector, allowing reconstruction of the decay vertices of heavy flavour hadrons. In the hadronic channel, all four primary partons are reconstructed. In order to optimise the Higgs mass resolution, a kinematic fit with 4/5 constraints is applied. The constraints are obtained from energy and momentum conservation and from the requirement that one di-jet mass be similar to that of the Z boson mass. The MarlinKinFit[3] Package is used for this. The fit minimizes a chi-square, which is given as

the difference between fitted and measured parameters of the fit object. The FANN-2.1.0 Package[4] is used for neural network based selection in the analysis.

4.2.2.3 Event Selection

The selection of signal events that are used in the branching ratio calculation is performed in three stages. The first step involves the classification of events into two channels depending on the decay products of the Z boson. Classification of events into the two decay modes is done using number of leptons and the visible energy in the event. Visible energy is given as the total sum of the measured energy of all jets found in each event. Leptons are defined to be any particles whose monte carlo PDG code corresponds to electrons or muons and have minimum momentum of 15 GeV. Figure 4.3(a) shows the distribution of the visible energy and the number of leptons (b) for the Higgs events (dashed) and Standard model background before event classification. The second step is a cut based selection which reduces the background

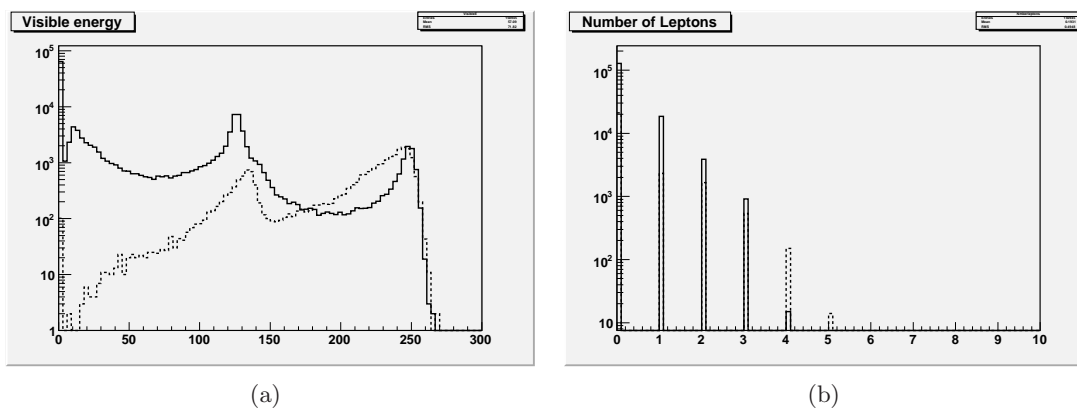


Figure 4.3: Visible energy (a) and the number of leptons per event (b). The distributions are used for channel classification

in the selected channel. Then, a neural network selection is done using the trained signal and background samples. The remaining events after the neural network selection are used for the calculation of the branching ratio.

4.2.2.4 Decay modes

The signature is dependant on the Z boson decay products (leptons, hadrons or neutrinos). The channels studied in this analysis are the neutrino mode (Z decaying to neutrinos) and the hadronic mode (Z decaying to hadrons). The neutrino mode is defined as events with no leptons and with a minimum of 90 GeV and maximum of 160 GeV of visible energy. The hadronic events are defined as events with no leptons and visible energy above 170 GeV.

4.2.2.5 The neutrino channel

In this decay mode events are forced to two jets which for the signal are assumed to come from the Higgs boson recoiling against two neutrinos from the Z boson decay. By looking at kinematic information, the reconstructed invariant mass of the hadronic jets is expected to be consistent with the Higgs mass. Figure 4.4 shows some kinematic distributions of the signal and background after classification but before any selection cuts. The background includes all SM processes but the most important are 2-fermion events, ZZ pairs decaying to neutrinos and hadrons and WW pairs where one W decays hadronically and the other W decays into a neutrino and a lepton which is undetected (due to low angle w.r.t the beam pipe).

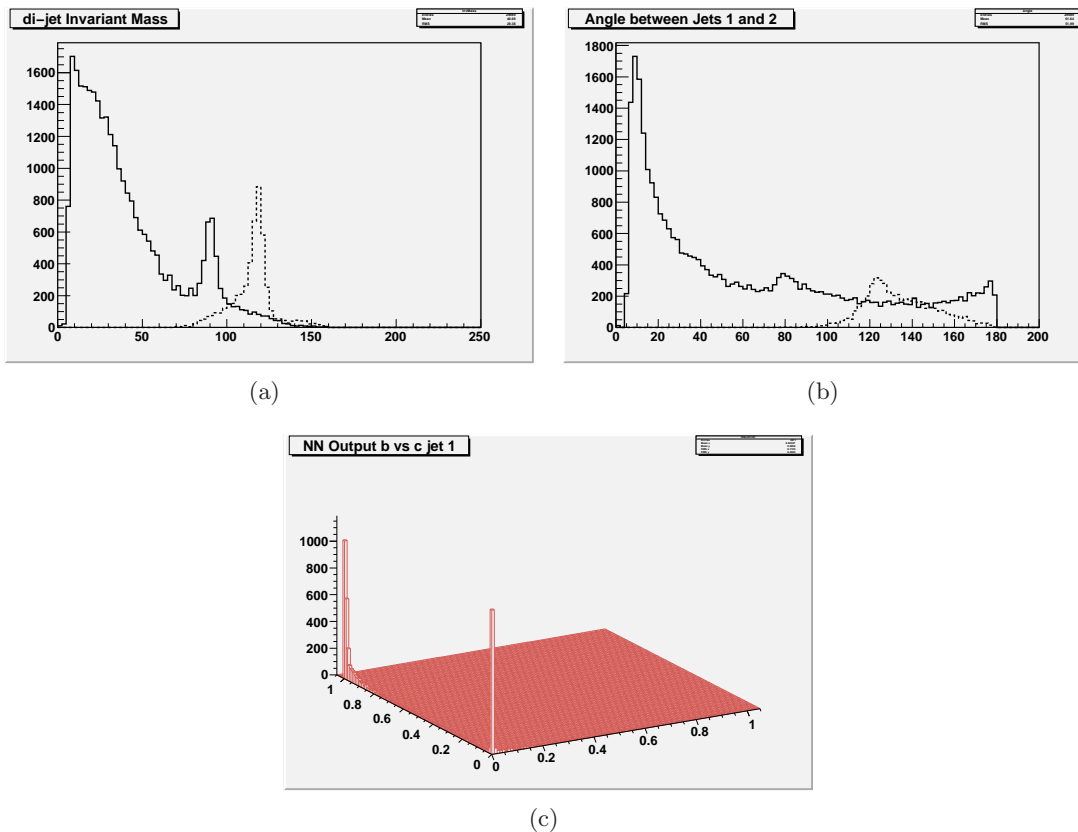


Figure 4.4: kinematic variables: (a) Higgs (dashed) and SM di-jet mass, (b) angle between jets and (c) c quark nn output versus b quark nn output for jet 1

To further reduce the background, the following selection cuts are applied:

1. number of charged tracks > 6
2. $\cos \theta_{\text{thrust}} < 0.9$
3. Thrust > 0.85
4. $100 \text{ GeV} < \text{JetInvMass} < 155 \text{ GeV}$

5. angle between jets $>100^\circ$

The jet invariant mass and angular separation are the most discriminant quantities for this channel. After selection cuts are made, remaining events are undergo a neural network[4] selection. The variables stated above including jet flavour tag neural net outputs are used for the neural network selection. Figure 4.5 shows the distribution of neural network outputs for the signal and background. All events with an NN greater than 0.7 are used in the branching ratio extraction. The signal selection efficiency for this channel is $\sim 40\%$ with more than 95% reduction of background.

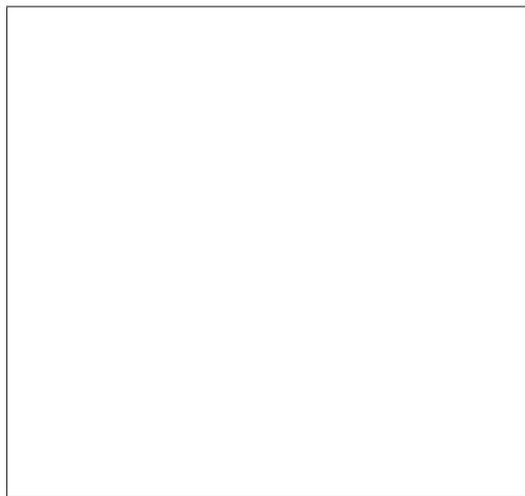


Figure 4.5: Neural Network Selection

4.2.2.6 The hadronic channel

In this channel, events are forced to 4 reconstructed jets. For the signal, two of the jets are assumed to have an invariant mass consistent with the Higgs boson and the other two having mass consistent with the Z boson. The background includes all SM processes of which the most important are 2-fermion events, WW and ZZ pairs where the all the bosons decay to hadrons. Identification of jets belonging to the Higgs boson and those belonging to the Z-boson is performed by a kinematic fitter[3]. Figure 4.6 shows some kinematic distributions of the signal and background after classification and jet combinatorics have been resolved but before any selection cuts.

For further reduction of the background, the following cuts are employed:

1. number of charged tracks > 8
2. $\cos \theta_{\text{thrust}} < 0.9$
3. Thrust > 0.85
4. $\log_{10} y_{34} > -5$

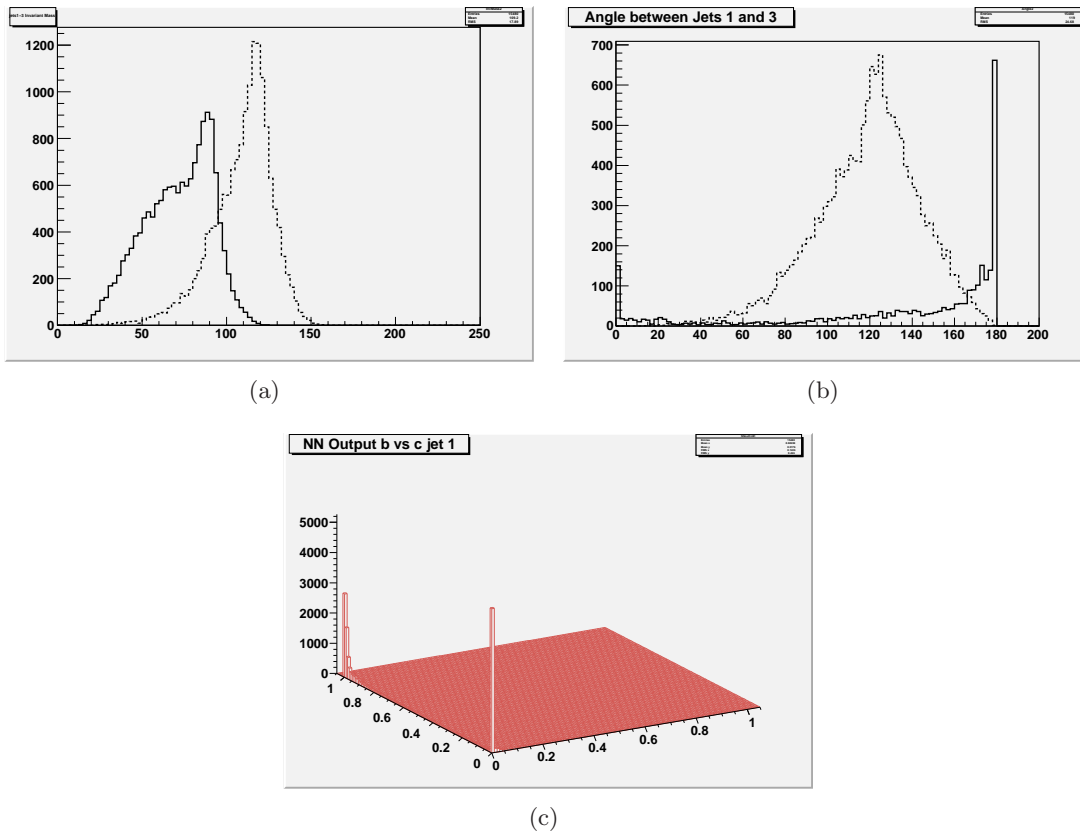


Figure 4.6: Kinematic variables: (a) Higgs (dashed) and Z-boson mass, (b) angle between jets and (c) c quark nn output versus b quark nn output for jet 1

To further reduce the background after the selection cuts, the variables above and others, which include flavour tag outputs, are used in the neural network based selection. Figure 4.7 shows the distribution of neural network outputs for the signal and background. All events with an NN greater than 0.7 are used in the branching ratio extraction. The signal selection efficiency for this channel is, with..... percent of background being cut.

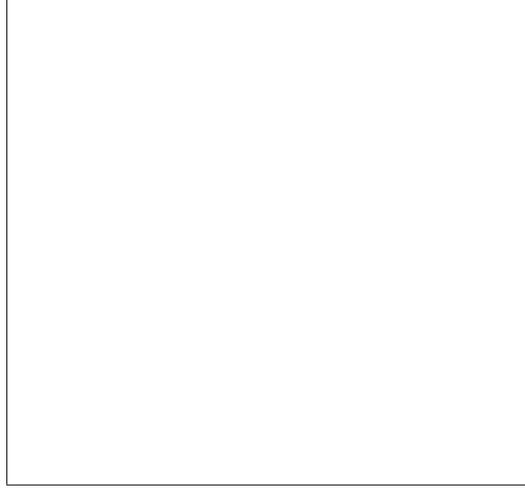


Figure 4.7: Neural Network Selection

4.2.2.7 Calculation of Branching ratio

All events that pass the neural network selection are used for the branching ratio extraction. The calculation is done by using the direct method where the branching ratio is calculated using equation:

$$BR(H \rightarrow c\bar{c}) = \frac{N_I(1 - F_I^{non-H} - F_{non-I}^H)}{N_{sel}(1 - F^{non-H})\varepsilon}$$

where

- N_I is the number of selected signal events in the chosen Higgs decay mode
- F_I^{non-H} is the fraction of non-Higgs background in the chosen mode
- F_{non-I}^H is the fraction of Higgs background coming from Higgs decays other than chosen mode
- F^{non-H} is the fraction of the non-Higgs background in the channel being analysed (neutrino or hadronic)
- N_{sel} is the number of signal events in the channel being analysed (neutrino or hadronic)

- ε is the efficiency of signal selection.

The branching ratio can also be calculated using a binned least squares fit to the flavour tagging probabilities of the Higgs decay to $c\bar{c}$. The fit yields a parameter which helps obtain the branching ratio from the ratio of the measured cross-section to the SM Higgsstrahlung cross-section. This method has not been used as we obtain a good separation between the background and signal and the direct method works well. One key problem, however, is the proper derivation of the error of the branching ratio as the quantities used are interdependent. We can get round this by assuming that the background fractions that end up in the calculation are small enough not to contribute highly to the statistical error. The branching ratio values and the associated errors are summarised in

4.2.3 $e^+e^- \rightarrow ZH, H \rightarrow \mu^+\mu^-, Z \rightarrow \nu\bar{\nu}, q\bar{q}, \sqrt{s}=250 \text{ GeV}$

4.2.3.1 Introduction

The decay of a Higgs boson into muons is one of the rare decay modes of the Higgs Boson in the Standard Model. It is also the only accessible channel besides the $c\bar{c}$ final state that gives access to the Higgs coupling to second generation fermions. The expected branching ratios are on the order of 0.01% and are given in Tab.4.2. A plot showing the mass dependence

Channel	$m_H=120 \text{ GeV}$	$m_H=130 \text{ GeV}$
$b\bar{b}$	67.7	52.5
W^+W^-	13.3	28.9
gg	7.1	6.5
$\tau^+\tau^-$	6.9	5.4
$c\bar{c}$	3.0	2.3
ZZ	1.5	3.9
$Z\gamma$	0.1	0.2
$\gamma\gamma$	0.2	0.2
$\mu^+\mu^-$	0.02	0.02

Table 4.2: Standard Model Higgs Boson branching ratios for different masses calculated using HDECAY.

for some of the rare Higgs decay modes is shown in Fig. 4.8.

This decay channel will allow a precise direct determination of the Higgs mass as it only relies on the performance of the tracking and will also give allow to set an upper limit on the Higgs decay width, which is only limited by the resolution of the tracking system. At the ILC Higgs bosons are produced either using the associated production with a Z boson - the so-called Higgs-Strahlung - or in the WW and ZZ fusion t-channels as shown in Fig. 4.9. At center-of-mass energies close to the threshold, the Higgs-Strahlung process is by far dominating, while the fusion processes become more important at higher energies.

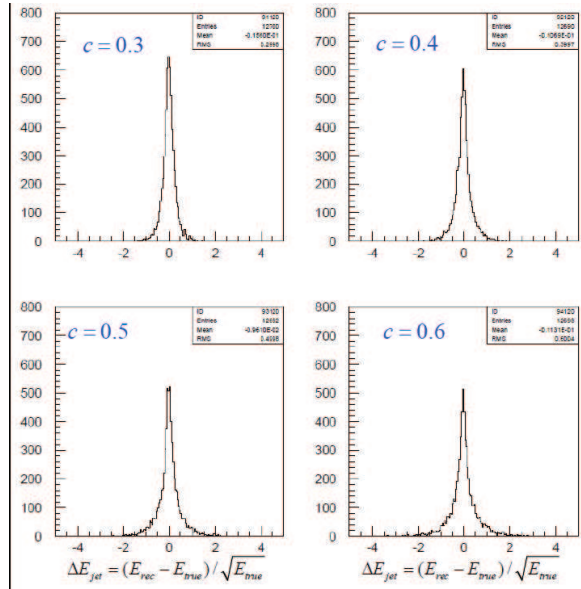


Figure 4.8: The branching ratios of the Higgs boson in the Standard Model depending on the Higgs boson mass.

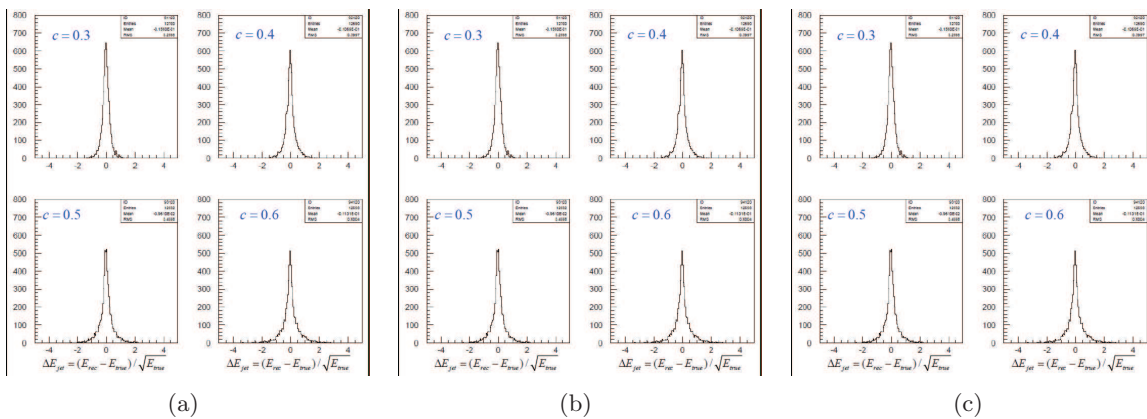


Figure 4.9: Higgs production in the SM: Higgs-Strahlung (a), WW fusion (b) and ZZ fusion (c).

The challenge in this analysis is to extract the signal out of an overwhelming background from two-fermion and four-fermion processes.

For the event simulation, we have been using the 250 GeV sample provided centrally at the SLAC repository. They have been simulated using WHIZARD for the event generation and PYTHIA for the handling of the hadronization. To take into account the polarization effects, we have looked at both 80%-30% and 30%-80% (check) for the electrons and positrons respectively. The 250 GeV samples corresponds to an integrated luminosity of 250 fb^{-1} altogether. (again, check numbers)

4.2.3.2 Search for $H \rightarrow \mu^+ \mu^-$

We using the standard SiD definition of a muon, which is done by associating a reconstructed track to a MIP segment in the calorimeter and a stub in the muon system. For both analyses we require two isolated muons which an energy of at least XXX GeV and a momentum of at least GeV/c...

The signature of this channel consists of two high-energetic muons from the Higgs decay and two jets from the hadronically decaying Z boson. This channel covers $\approx 70\%$ of the branching ratio. For this channel we force the event into two jets excluding the previously identified muons. We then require the mass of the di-jet system to be compatible with the Z boson mass and the total visible momentum to be less than X GeV/c and the visible to be close to center-of-mass energy. We then combine several event shape variable to form a final discriminant between signal and background.

For the fit to the $\mu\mu$ invariant mass spectrum we apply ROOFIT.

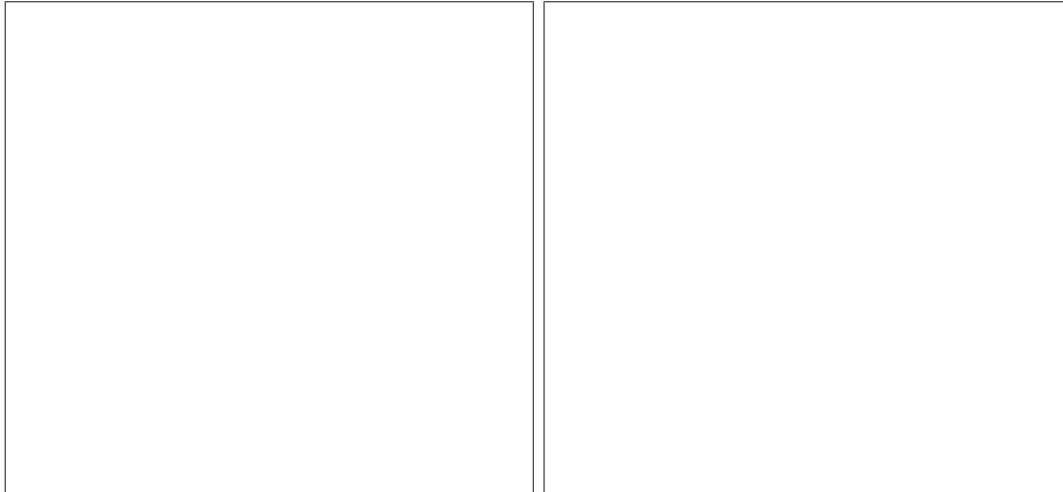


Figure 4.10: The invariant mass of the $\mu\mu$ system and the di-jet system in the hadronic channel

The signature of the missing energy channel consists of two high-energetic muons from the Higgs decay and a missing mass compatible with the Z mass. In this channel there is the

additional complication of the contribution of the WW-fusion channel to this process, which is however small at 250 GeV center-of-mass energy. The missing energy channel covers 21 % of the total branching ratio. We select events with a missing mass compatible with the Z mass and then employ a multivariate discriminant analysis to combine several event shape variables to form a final discriminant variable.

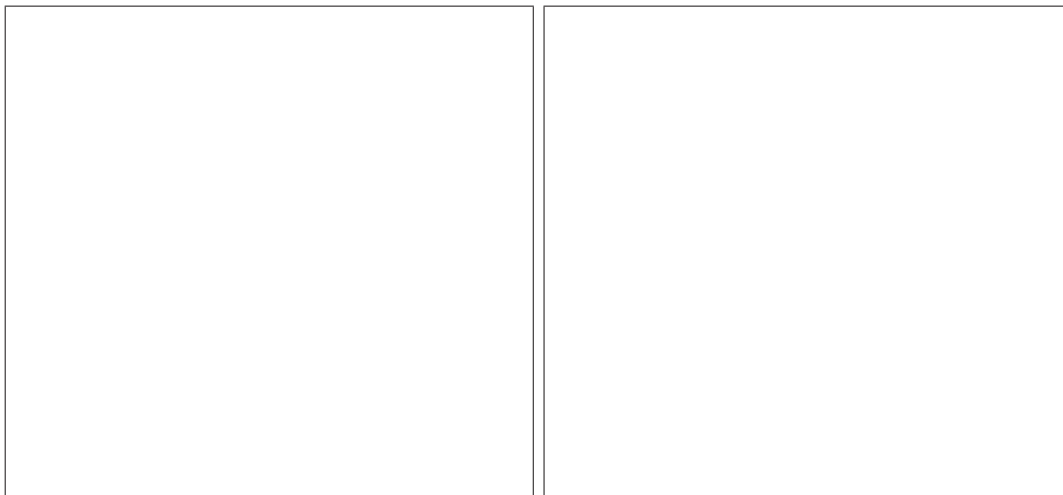


Figure 4.11: The invariant mass of the $\mu\mu$ system and the missing mass in the missing energy channel

For the fit to the $\mu\mu$ invariant mass spectrum we apply ROOFIT.

4.2.3.3 Combined Results

The results are then combined together using, we have been checking the overlap between the two channels and found 0 % overlap between the two channels.

4.2.3.4 Summary

4.2.4 $e^+e^- \rightarrow \tau^+\tau^-$, $\sqrt{s}=500$ GeV

The identification of 250 GeV taus and their decay modes is a challenge for the tracker and calorimeter. Low multiplicity but tightly collimated jets must be reconstructed in terms of the underlying charged hadron and π^0 constituents. Particle flow algorithms designed to measure jet energy may require modification to provide optimal tau mode identification.

Two sets of observables are used to quantify the ability of the SiD detector to reconstruct 250 GeV taus. First, tau decay mode efficiencies and purities are determined, and then the tau polarization is measured. Decay mode efficiencies are determined for the decays $\tau^- \rightarrow e^- \bar{\nu}_e \nu_\tau$, $\mu^- \bar{\nu}_\mu \nu_\tau$, $\pi^- \nu_\tau$, $\rho^- \nu_\tau$, $a_1^- \nu_\tau$. With the exception of $a_1^- \nu_\tau$ the same set of decay modes are used for the measurement of the tau polarization.

4.2.4.1 Tau Decay Mode Efficiencies and Purities

Full energy tau pair events are selected using the following criteria:

The particle flow algorithm was modified as follows:

The decay mode $\tau^- \rightarrow e^- \bar{\nu}_e \nu_\tau$ is identified using the following criteria:

The decay mode $\tau^- \rightarrow \mu^- \bar{\nu}_\mu \nu_\tau$ is identified using the following criteria:

The decay mode $\tau^- \rightarrow \pi^- \nu_\tau$ is identified using the following criteria:

The decay mode $\tau^- \rightarrow \rho^- \nu_\tau$ is identified using the following criteria:

The decay mode $\tau^- \rightarrow a_1^- \nu_\tau \rightarrow \pi^- \pi^+ \pi^- \nu_\tau$ is identified using the following criteria:

The decay mode $\tau^- \rightarrow a_1^- \nu_\tau \rightarrow \pi^- \pi^0 \pi^0 \nu_\tau$ is identified using the following criteria:

The decay mode efficiencies and purities are summarized in Table 4.3.

decay mode	efficiency (%)	purity (%)
$e^- \bar{\nu}_e \nu_\tau$	1.0	1.0
$\mu^- \bar{\nu}_\mu \nu_\tau$	1.0	1.0
$\pi^- \nu_\tau$	1.0	1.0
$\rho^- \nu_\tau$	1.0	1.0
$\pi^- \pi^+ \pi^- \nu_\tau$	1.0	1.0
$\pi^- \pi^0 \pi^0 \nu_\tau$	1.0	1.0

Table 4.3: - Tau decay mode efficiencies and purities.

4.2.4.2 Tau Polarization

The tau polarization $P_\tau(\cos\theta)$ is related to the differential decay width $d\Gamma/d\vec{x}$ via $d\Gamma/d\vec{x} = f(\vec{x}) + P_\tau(\cos\theta)g(\vec{x})$ where \vec{x} represents the kinematic variables for all of the tau decay products. Detector response to the single optimal observable ω defined by $\omega = f(\vec{x})/g(\vec{x})$ can be used in place of the response to the set of variables \vec{x} without loss of sensitivity.

Among the decay product kinematic variables \vec{x} are the momenta of neutrinos. These can be recovered in some situations using energy–momentum conservation constraints applied to the entire event. Vertex detector information can further constrain the neutrino momenta. The process by which this is done is described here.

The distribution for the optimal observable ω for the decay $\rho^- \nu_\tau$ is show in Figure 4.12

The measured tau polarization is show in Figure 4.13

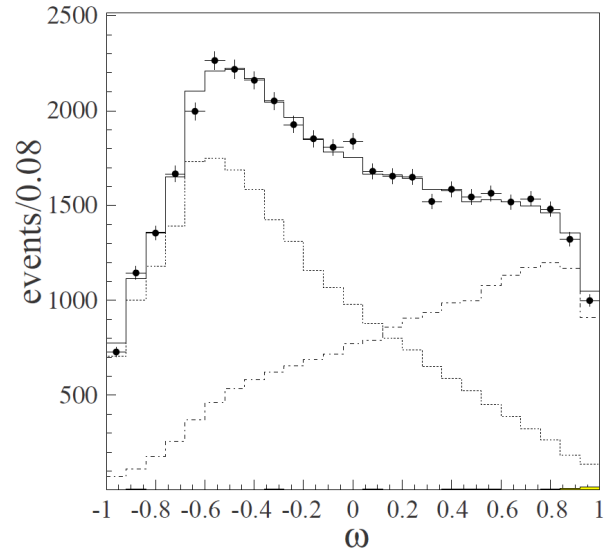


Figure 4.12: Optimal observable ω for the decay $\rho^- \nu_\tau$.

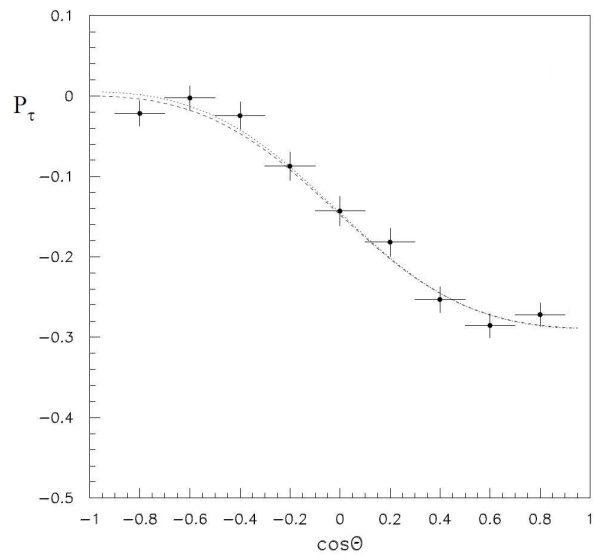


Figure 4.13: Tau polarization versus $\cos \Theta$

4.2.5 $e^+e^- \rightarrow t\bar{t}$, $t \rightarrow bW^+$, $W^+ \rightarrow q\bar{q}'$, $\sqrt{s}=500$ GeV

The top quark is substantially more massive than the rest of the observed quarks. It is therefore important to search for the physical mechanism that introduces the mass difference and at the same time use the top as a probe into new physics, which often couples to mass. In order to investigate such mechanisms it is essential to determine precisely the mass of the top and to characterize the top quark couplings to the standard model bosons.

It is therefore the aim of the LoI to measure the total top cross-section of the channel $e^+e^- \rightarrow t\bar{t}$, $t \rightarrow bW$, $W \rightarrow qq$, the mass of the quark and the forward backward asymmetry of the top quark and of the bottom quark derived from the top quark decay.

The sample used in the analysis is a weighted all inclusive standard model sample. The tops are then identified from the quark content at the MC level. All events that satisfy the condition of deriving from two b quarks and 4 differently flavoured quarks are classified as fully hadronically decayed t-tbar events and hence as our signal. All the events have been reconstructed and the lepton identification, jet clustering and Flavour tagging algorithms have been performed. In particular we are using the Durham ycut algorithm with the jet number fixed to 6 for jet clustering and the LCFIVertex algorithm for Vertexing and Flavour tagging. The first step of the analysis is therefore to identify the hadronically decaying top quarks and to reject most of the non-top SM background, the leptonic (both W-bosons produced from the top quark decay leptonically) and semi-leptonic (one of the W-bosons produced from the top quark decays leptonically) decay channels as well as the hadronic events which are not well reconstructed. For this purpose a simple but powerful preselection cut is applied. All events that hold a jet composed of only a reconstructed electron or muon are discarded. A list of further cuts used in the analysis can be found in Table 1. Most of the cuts essentially insure that the event, which has been previously forced into six jets, is physically and hence topologically also a six jet event. Indirectly these cuts result to be also quality of reconstruction cuts. For example in a case where two physical jets overlap each other in the detector. These jets will be merged by the jet clustering algorithm, however due to the forcing of the event into six jets another physical jet of the event will have been separated into two reconstructed jets. This will result in the substantial decrease of the $ycut_{min}$ value and in the event being cut. Similarly events with jets going down the beam-pipe appear as having substantial missing energy and will hence be cut as well. Once it has been insured that events are topological six jet events all that remains to be done is to tag the bquarks. This further reduces the background by eliminating most of the non top six jets events and also substantially reduce the backgrounds and also the combinatorics of jets in the top quark events Figure 4.14(a).

Selection cuts

$E_{total} > 450$ GeV
 $\log(y_{cut_{min}}) > -8$ GeV
 btag-most b-like jet > 0.7
 btag-2nd most b-like jet > 0.5
 Btag-sum of all jets > 1.5
 Number of Particles in event > 65 GeV
 Number of tracks in event > 95 GeV
 Table 1: Selection cuts applied to sample.

Constrains (kinematic fitter)

$mass(top1) = mass(top2)$
 $mass(W1) = 80.4$ GeV
 $mass(W2) = 80.4$ GeV
 $E_{total} = 500$ GeV
 $P_x = 0$
 $p_y = 0$
 $p_z = 0$
 Table 2: Kinematic fitting constrains.

The performed selections are found to be 99.99% efficient in eliminating leptonic decay channels and 95.9% efficient in eliminating semi-leptonic modes. These cuts also reduce the remaining Standard Model Background to approximately 2000 events from an original value of more than 10^{10} (equivalent to an integrated luminosity of 75 fb^{-1}). However they also eliminate 48% of the hadronic sample. The efficiency of the procedure is hence 52% and the final purity is 83.8%, where purity is defined as number of events passing all cuts that originated from two b quarks and four other quarks at parton generator level divided by all events that pass the cuts. (Figure 4.14).

By using these values it is then possible to calculate precision obtainable at SiD on the top-topbar total cross-section in the hadronic channel: (NEEDVALUE)

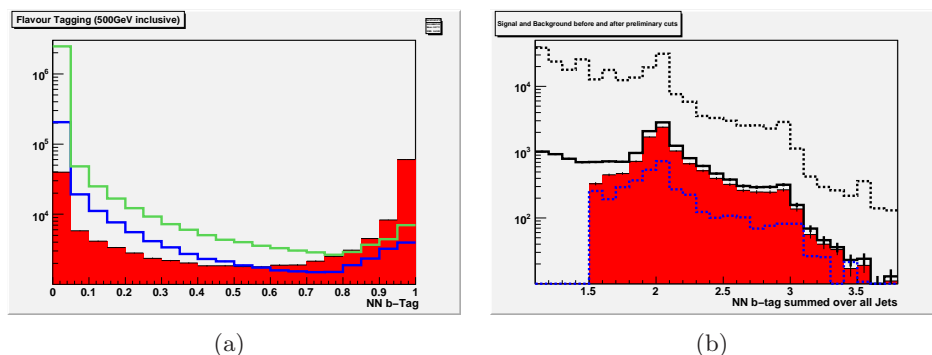
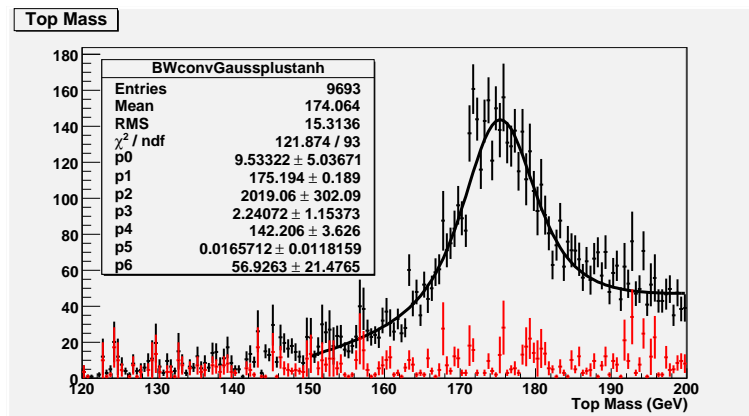


Figure 4.14: Btag of all jets for b quarks(red) c quarks(blue) and uds quarks(green) (a) and (b) Btag sum over all jets for all signal(full line,area) and background(dashed line) events before and after preliminary cuts.

The next step of the analysis is the calculation of the top mass. Given the combinatorial possibilities of a six-jet environment and given the availability of many constrains a kinematic fitter needs to be used. The list of constrains can be found in Table 2. It must be noted that before using the kinematic fitter the b-tagging is performed and the two most b-like jets are considered to be bottom quark and treated as such in the fitter. All the events that do not meet the constrains set to the fitter are rejected. Effectively corresponding to a probability cut of 1% on the kinematic fit. Clearly such cut is extremely dependent on the energy resolution and on the momentum resolution of the jets. By using this method we are rejecting events with top quarks that are not well reconstructed. Given the complexity of a six jet environment this are not very rare occurrences. Additionally this

method further rejects the background. After these selections the reconstruction efficiency is 44.8% and the purity of the sample is 85.6%. It is now possible to perform a simple fit and derive the mass of the top as well as an error on the mass. The function used in the fit is a Gaussian convoluted with a Breit-Wigner. To this a function that models combinatorial background is added. Experimentally it has been found that a suitable function is the hyperbolic tangent. By using this method the top mass resolution that is obtainable at SiD with 500 fb^{-1} has been calculated. This resolution for the hadronic channel only is 71 MeV. (Figure 4.15(b) presents a similar study performed with approximately 75 fb^{-1}). (TO BE STUDIED FURTHER, NOW USING MORE OR LESS DEFAULTS).



(a)

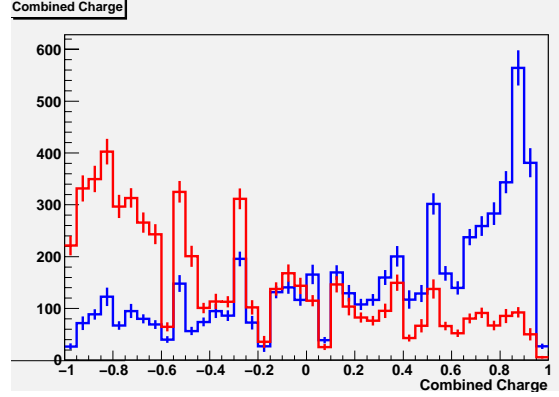
Figure 4.15: Top Mass after Kinematic fitting(, black signal+ background, red background only).

Finally it is possible to characterize the top couplings. In particular by analyzing the forward backwards asymmetry of the top quark and of the b quark (from the top decay) one can set a limit on the anomalous couplings of $Z \rightarrow t\bar{t}$ and $t \rightarrow Wb$ respectively. For this purpose one must be able to discriminate between b quarks and b anti-quarks. This can be done by using the Momentum Weighted Vertex Charge and the Momentum Weighted Jet Charge variables. The first variable effectively uses the reconstructed secondary vertices and calculates the total charge of all the secondary vertices present in the jet. Clearly this has good discriminating power first when the mesons producing the jets are charged (although because of momentum weighting it also has some discriminating power otherwise) and can only be used when secondary vertex can be found. The momentum weighted jet charge instead uses all the tracks present in the jet to determine the total charge of the jet. This performs better in all the remaining, more problematic, cases. In this analysis the variables are recombined by using a technique based on the PDFs at Monte Carlo level and a single variable is used; see Figure 4.16(a).

By using this method the resulting b quark forward-backwards asymmetry in a 75 fb^{-1} sample is: 0.28 ± 0.06 . See Figure 4.16(b). The t quark forward-backwards asymmetry is instead calculated to be: 0.38 ± 0.05 . (VALUE AND ERROR STILL A ROUGH CALCULATION, but method clearly proven!)

The efficiency of this reconstruction is substantially lower than the one previously presented

for the rop mass. There are two main reasons behind this. Firstly a cut is applied and only top quarks reconstructed with a mass between 160 and 190 GeV are used. Secondly the cut on the combined charge is intrinsically also a topological cut. This rejects a large sample of the B^0 mesons and of events in which a secondary vertex has not been reconstructed in both b-tagged jets. Additionally there is also a chance of interpreting a b as a bbar. Once all this facts are take in account th the efficiency of the reconstruction is 6.4%. The purity of the events is 70.2%



(a)

Figure 4.16: (a) Combined charge for b and bbar quarks. (b) Events used in calculation of A_{fb} for the b quark - black signal plus background, blue SM backgrounds, red mistagging background.

4.2.6 $e^+e^- \rightarrow \tilde{\chi}_1^+ \tilde{\chi}_1^- / \tilde{\chi}_2^0 \tilde{\chi}_2^0$, $\sqrt{s}=500$ GeV

Short motivation and a Feynman diagram go here..

The masses of charginos and neutralinos are important parameters in supersymmetry which can be measured in ILC with high precision. In the chosen SUSY scenario the charginos and neutralinos decay into a $\tilde{\chi}_1^0$ and a W/Z gauge boson:

$$\begin{aligned} e^+e^- &\rightarrow \tilde{\chi}_1^+ \tilde{\chi}_1^- \rightarrow \tilde{\chi}_1^0 \tilde{\chi}_1^0 W^+ W^- \\ e^+e^- &\rightarrow \tilde{\chi}_2^0 \tilde{\chi}_2^0 \rightarrow \tilde{\chi}_1^0 \tilde{\chi}_1^0 Z^0 Z^0 \end{aligned}$$

If we consider the all-hadronic decay of the gauge bosons in the final states, the above processes will both be identified with the signature of four jets with large missing energy. Once the W or Z bosons are successfully reconstructed their energy distribution will provide information on the chargino or neutralino masses. The value of masses can be measured using template fitting.

A Monte-Carlo sample with \sqrt{s} of 500 GeV and integrated luminosity of 500 fb^{-1} was used for this study. It consists of the chargino/neutralino signals and SUSY backgrounds such as $e^+e^- \rightarrow \tilde{\chi}_1^0 \tilde{\chi}_2^0$ and slepton pair production. Apart from this sample, three more samples

with the same statistics are generated in order to estimate the error of these mass measurement, each with one SUSY mass shifted by 0.5 GeV (Table 4.4). A Standard Model background sample at $\sqrt{s} = 500\text{GeV}$ was generated separately.

sample	$m_{\tilde{\chi}_1^0}$ (GeV)	$m_{\tilde{\chi}_1^\pm}$ (GeV)	$m_{\tilde{\chi}_2^0}$ (GeV)
Reference	115.7	216.7	216.5
$m_{\tilde{\chi}_1^0} + 0.5$	117.2	216.7	216.5
$m_{\tilde{\chi}_1^\pm} + 0.5$	115.7	217.2	216.5
$m_{\tilde{\chi}_2^0} + 0.5$	115.7	216.7	217.0

Table 4.4: MC sample parameters.

First we select the all-hadronic channel events by forcing four jets at jet finding and applying a series of cuts on jet angles, lepton ID and energy (Table 4.5).

cut	value
Jet number	= 4
$\theta(1, 2)$	> 60°
$\theta(1, 3), \theta(1, 4), \theta(1, 3)$	> 60°
$\theta(2, 4), \theta(3, 4)$	> 60°
E(jet 4)	> 10 GeV
E(photon in jet i)/E(jet i)	< 80%

Table 4.5: Pre-selection cuts. $\theta(i, j)$ defines the angle between the i th and j th jet. The jets are ordered in energy, e.g. jet 1 is the most energetic jet.

To reconstruct the two gauge bosons from the four jets we have to determine the jet pairing corresponding to the correct combinations. It is done by minimizing the quantity of $(m(j_1, j_2) - m_{W/Z})^2 + (m(j_3, j_4) - m_{W/Z})^2$, where $m(j_1, j_2)$ is the invariant mass of the jets j_1 and j_2 . W mass will be used when selecting $\tilde{\chi}_1^+ \tilde{\chi}_1^-$ events, and Z mass for $\tilde{\chi}_2^0 \tilde{\chi}_2^0$ events. The scatter plot of the two reconstructed boson masses is shown in Figure 4.17. The reconstructed boson masses will occupy different regions in the histogram for chargino and neutralino events, and their separation can be achieved by a cut indicated by the thick line in Figure 4.17. Events on the lower left part are classified as $\tilde{\chi}_1^+ \tilde{\chi}_1^-$ events and upper right $\tilde{\chi}_2^0 \tilde{\chi}_2^0$ events. For chargino events selection we also add a cut to remove the events on the most lower left corner of 2D mass histogram, which are most likely due to the remaining leptonic or semi-leptonic decay of the bosons.

After these cuts the reconstructed boson mass and energy distribution for chargino and neutralino events are shown in Figure 4.18.

In the rest frame of $\tilde{\chi}_1^\pm/\tilde{\chi}_2^0$, W^\pm/Z bosons are monochromatic and their energy is determined by $m_{\tilde{\chi}_1^\pm}/m_{\tilde{\chi}_2^0}$, m_{W^\pm}/m_Z and $m_{\tilde{\chi}_1^0}$. For a boosted parent $\tilde{\chi}_1^\pm/\tilde{\chi}_2^0$, the boson

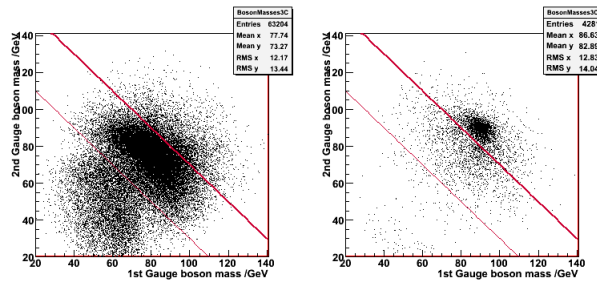


Figure 4.17: The reconstructed boson masses from the four jets, selecting chargino events. left: pure chargino; right: pure neutralino

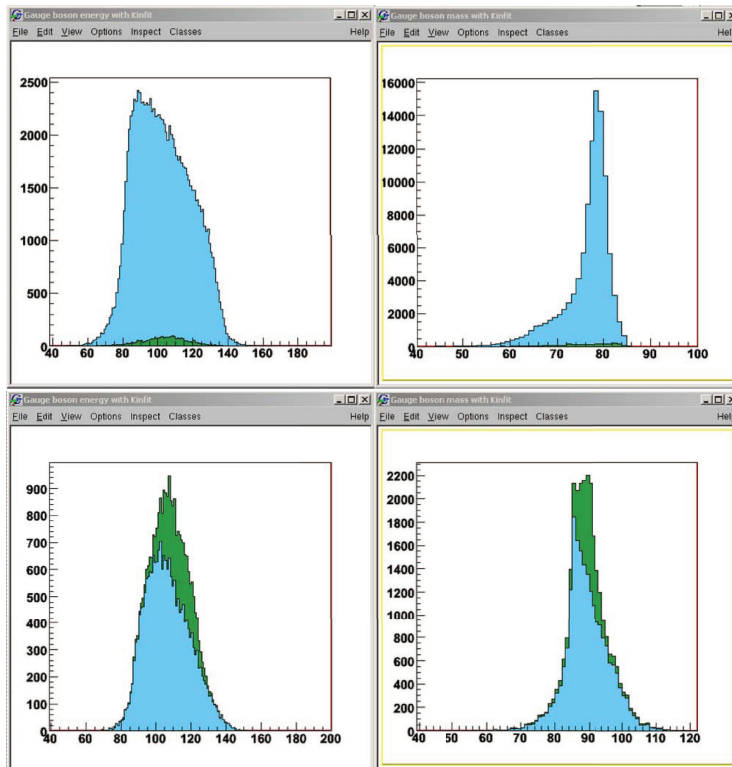


Figure 4.18: Upper: The reconstructed W energy (left) and mass (right) for chargino event selection; Lower: The reconstructed Z energy (left) and mass (right) for neutralino event selection. Blue is the true chargino events and green the neutralino events.

energy distribution depends on the SUSY particle masses which will determine the edges of the energy spectrum. Our approach to obtain these masses is to compare the energy spectrum with a reference MC sample (Table 4.4), therefore best possible energy resolution is important for high-precision mass measurement. Using the fact that the two bosons reconstructed from the four jets have the same mass in both $\tilde{\chi}_1^+ \tilde{\chi}_1^-$ and $\tilde{\chi}_2^0 \tilde{\chi}_2^0$ cases, kinematic fitting with one constraint ($m_{boson1} = m_{boson2}$) can be used for improving the energy distribution assuming that the detector resolution is known. Kinfit in Marlinreco package is used for the fitting. (Figure 4.19)

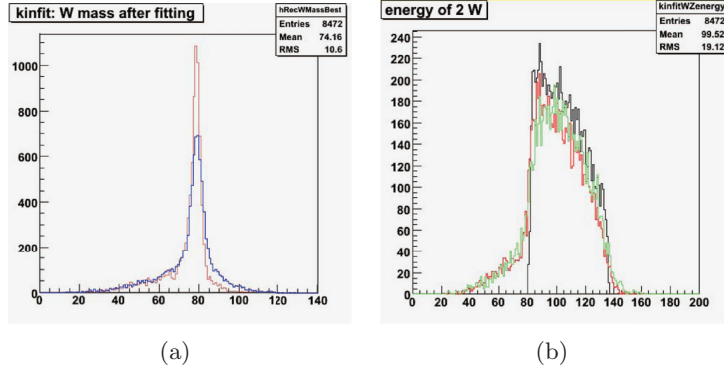


Figure 4.19: (a) Mass distribution of reconstructed bosons before (blue) and after (red) kinematic fitting; (b) Energy distribution of reconstructed bosons. Black is MC information, Green and Red lines are before and after kinematic fitting.

The determination of SUSY particle mass is explained using the example of $\tilde{\chi}_1^+ \tilde{\chi}_1^-$ process. To the first order approximation the change in the content of each bin with respect to the template sample is proportional to the change in $m_{\tilde{\chi}_1^\pm}$ and $m_{\tilde{\chi}_1^0}$:

$$\Delta y_i = \left(\frac{\partial y}{\partial m_{\tilde{\chi}_1^\pm}} \right)_i \Delta m_{\tilde{\chi}_1^\pm} + \left(\frac{\partial y}{\partial m_{\tilde{\chi}_1^0}} \right)_i \Delta m_{\tilde{\chi}_1^0} \quad (4.1)$$

where Δy_i is the difference of the i th bin content with respect to the template. The derivatives $(\partial y / \partial m_{\tilde{\chi}_1^\pm})_i$ and $(\partial y / \partial m_{\tilde{\chi}_1^0})_i$ can be calculated using the samples in Table 4.4 with $\tilde{\chi}_1^\pm$ or $\tilde{\chi}_1^0$ mass shifted by 0.5 GeV. (Figure 4.20) For the real data we can calculate each Δy_i and do a two-dimensional linear-least-square fit to obtain the parameter $\Delta m_{\tilde{\chi}_1^\pm}$ and $\Delta m_{\tilde{\chi}_1^0}$. It is similar with $\tilde{\chi}_2^0 \tilde{\chi}_2^0$ if $m_{\tilde{\chi}_1^\pm}$ is replaced by $m_{\tilde{\chi}_2^0}$. From the theory of linear-least-square fit it is easy to show that the error on $\Delta m_{\tilde{\chi}_1^\pm}$ can be obtained from error on each bin, which gives ... (the final result for error on the three should be given.)

4.2.7 $e^+e^- \rightarrow ZHH$, $H \rightarrow b\bar{b}$, $\sqrt{s}=500$ GeV

The most promising way to measure the Higgs self-coupling is via the processes with two Higgs bosons in the final state, see Figure 4.21. The cross section is relatively large – about

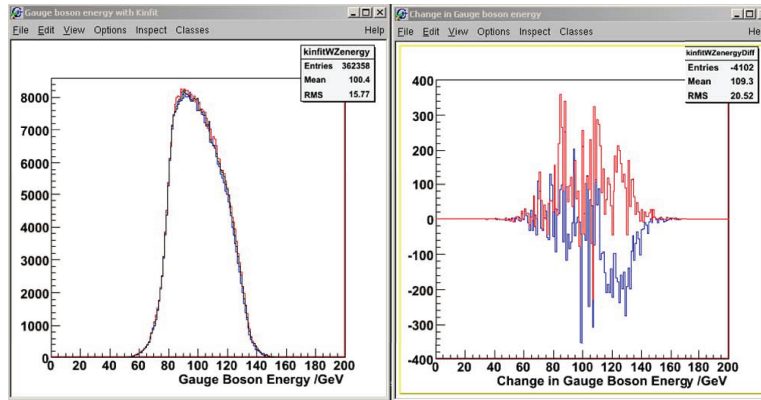


Figure 4.20: The boson energy distribution for $m_{\tilde{\chi}_1^0} = \dots$ and \dots

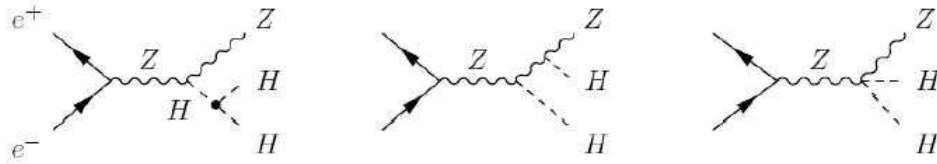


Figure 4.21: Feynman diagrams describing $e^+e^- \rightarrow ZHH$ process. Higgs self-interaction vertex contributes to the first diagram.

0.158fb for unpolarised beams and the centre of mass energy of 500GeV. Furthermore, the final states can be identified without large missing momentum.

A signal sample consisting of approximately 145k events was generated with two beam polarisations, i.e. $e^-(80\%L) e^+(30\%R)$ and $e^-(80\%R) e^+(30\%L)$. In the same manner dominant background samples were produced for the most relevant Standard Model backgrounds, see Table 1 for details. The final state gluon radiation is considered. The samples were processed by FastMC and by the LCFI jet tagging package.

sample	# events 1	# events 2	Unpolarised cross-section /fb
Zhh	72519	72486	0.1584
tbW	85517	84546	558
Zh	115983	115888	68.63
ZZ	148445	148891	445.2
ZZh	83998	83968	0.5177
ZZZ	100089	99968	0.9982

Pre-selection of events is based on a set of cuts summarised in Table 4.6. Samples are consequently split into two halves. One is used to train Neural Network and the other half for analysis itself. The Neural Network consists of 26 inputs, 26 neurons in one hidden layer and one output. It is trained with 50% of generated events accounting for event weight,

which are calculated based on cross section of a particular sample and a reference luminosity. The reference luminosity used to normalise all samples is 2000 fb^{-1} .

Selection cuts	
$ \cos(\theta_{thrust}) $	< 0.95
thrust	< 0.85
$ P_{tot}(z) $	< 50
$M_{thrust_hemisphere}$	$> 110\text{GeV}$ - for at least one hemisphere
$N_{isolated_leptons}$	$= 0$
$N_{charged_tracks}$	> 25
$E_{jet}(\text{photons})/E_{jet}(\text{total})$	< 0.8 - for all jets

Table 4.6: - Selection cuts used to preselect events for both Neural Network training and the cross section measurement analysis.

The neural net inputs are listed below:

1. The b tagging results for six jets;
2. Invariant mass for variant jet combinatorics (and the difference with respect to gauge bosons, e.g $Jet12H = (m_{jet1,jet2} - m_H)^2$). All the inputs used are: $Jet12H$, $Jet13H$, $Jet14H$, $Jet23H$, $Jet24H$, $Jet34H$, $Jet56H$, $Jet56Z$, $Jet34W$, $Jet56W$, $Jet25W$, $Jet26W$, $Jet35W$, $Jet36W$, $Jet45W$ and $Jet46W$;
3. The variable representing the mass difference of reconstructed particles with respect to the signal/background final states. For example:
 $ch2_zhh = \min\{(m_{j1,j2} - m_H)^2 + (m_{j3,j4} - m_H)^2\}$, where $\{j1, j2, j3, j4\}$ are all possible permutations for the first four jets (ordered by b tag value), assuming the two least b-like jets are assumed from Z. Similarly defined such variables are:
 $ch2_tt = \min\{(m_{j1,j2} - m_W)^2 + (m_{j3,j4} - m_W)^2\}$ (where the two most b-like jets are assumed to be b jets), $ch2_zzh = \min\{(m_{j1,j2} - m_Z)^2 + (m_{j3,j4} - m_H)^2\}$, and
 $ch2_zzz = \min\{(m_{j1,j2} - m_Z)^2 + (m_{j3,j4} - m_Z)^2\}$.

Resulting Neural Network output is shown in Figure 4.22(a). Filled histogram corresponds to signal events while various backgrounds are plotted separately. The most contributing background is tbW, which is eventually difficult to separate from the signal. It can be seen that generated statistics for tbW is not sufficient and thus its increase could improve the result. Cross section measurement statistical error is plotted in Figure 4.22(b) as a function of number of signal events selected according to a particular sliding cut on the Neural Network Output. The lowest error value is at around 50-60 signal events and it amounts to 35%. The corresponding error on the Higgs self-coupling measurement is 63%.

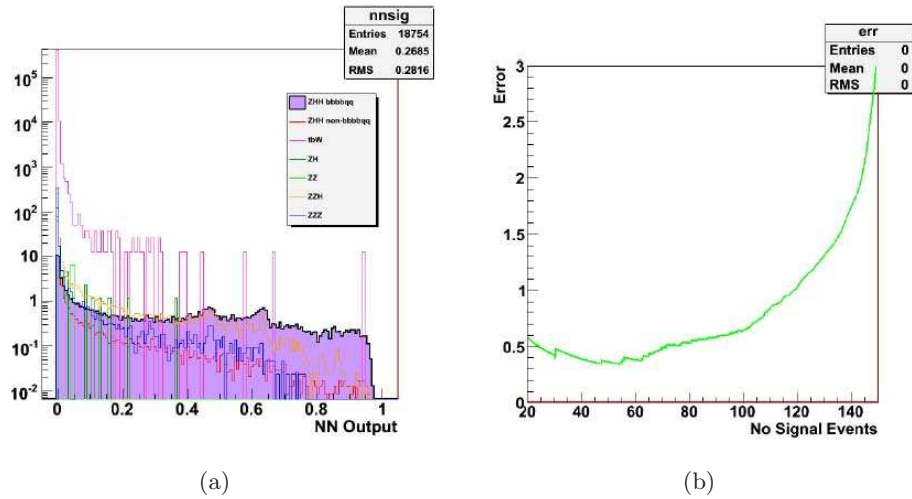


Figure 4.22: (a):Neural Network output for signal (filled histogram) and background. (b): Cross section measurement statistical error as a function of a number of selected signal events.

4.2.8 Sbottom Quark Production: $e^+e^- \rightarrow \tilde{b}\tilde{b}^*$, $\tilde{b} \rightarrow b\tilde{\chi}_1^0$

Recent comparisons of WMAP measurements [4] of the neutralino relic density with minimal supergravity (mSUGRA) model predictions are suggesting preferred regions of the model parameter space. The Linear Collider has a potential to cover a large fraction of this dark matter allowed area. Such a measurement is challenging due to a very low energy of jets and eventually small cross sections. Very low jet energies, below 20-30 GeV, test the event reconstruction as well as jet tagging algorithms thus pushing them to their limits. An example of the jet flavour tagging efficiency as a function of the jet momentum is shown in Figure 4.23 for an arbitrary cut on jet tagging Neural Net output. While above around 60 GeV the efficiency is about constant it is falling down steeply at low jet energies.

4.2.8.1 Tools

In this study CalcHEP event generator [5] is employed to generate SUSY signal events. This package allows event generation based on numerical calculation of Feynman diagrams directly from Lagrangian of a particular model. Generated events are converted to Les Houches format and passed to Pythia for their fragmentation and particle decays. The jets, reconstructed from particle flow objects, are tagged using the LCFI Vertex Package. Event classification is partially based on Neural Networks classifier. For this purpose Fast Artificial Neural Network (FANN) [6] package is introduced into the analysis chain. It provides fast and reliable framework written in C programming language called from within a C++ wrapper. FANN was partially modified in order to account for event weights during Neural Network training.

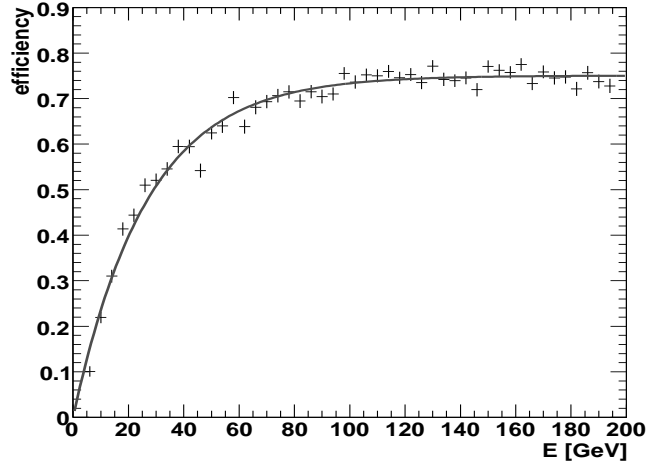


Figure 4.23: Jet flavour tagging efficiency as a function of the jet momentum for b-jets. The gray line corresponds to a fitted Gompertz-like curve.

4.2.8.2 Data Samples

Four points in EWSB SUSY model parameter space were chosen close to kinematic acceptance limits in order to investigate Linear Collider potential. These points correspond to various masses of the sbottom quark and the neutralino and to different parameters in the model, for details see Table 4.7 and Figure 4.24. For each point in model parameter space 200k events were generated accounting for ISR, FSR and beamstrahlung.

$m_{\tilde{b}}$ [GeV]	$m_{\tilde{\chi}_1^0}$ [GeV]	M_{G1}	M_{D3}
230	210	241.2	242.7
240	210	241.2	251.5
230	220	262.7	242.7
240	220	262.7	251.5

Table 4.7: Selected parameters of the EWSB SUSY model corresponding to various masses of sbottom quark \tilde{b} and neutralino $\tilde{\chi}_1^0$.

The mass of sbottom quark $m_{\tilde{b}}$ essentially governs the cross section of the process. While samples with $m_{\tilde{b}} = 230$ GeV have the production cross section 1.3×10^{-3} pb for $m_{\tilde{b}} = 240$ GeV the cross section is almost $3.5 \times$ larger, 0.37×10^{-3} pb. The mass difference between $m_{\tilde{b}}$ and $m_{\tilde{\chi}_1^0}$, on the other hand, determines the hardness of b-jets. The smaller it is the more challenging is the event reconstruction and the jet tagging efficiency.

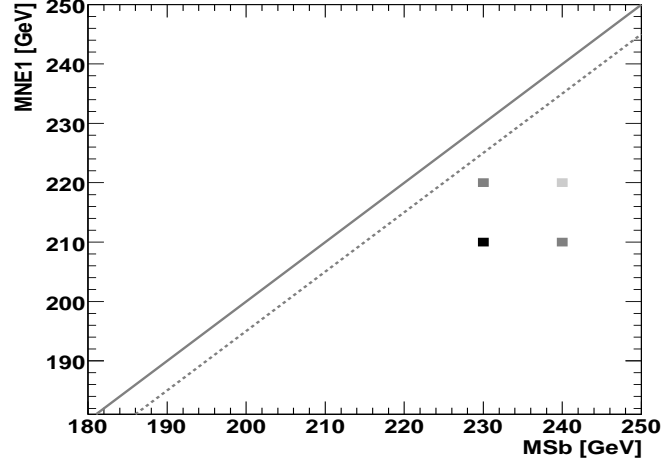


Figure 4.24: Selected points in SUSY model space. Color coding corresponds to an estimated difficulty of the measurement (lighter is more challenging). Full line shows a kinematic limit corresponding to $m_{\tilde{b}} > m_{\tilde{\chi}_1^0}$ while dashed line to a limit $m_{\tilde{b}} > m_{\tilde{\chi}_1^0} + \Delta M$, where $\Delta M = 5$ GeV.

4.2.8.3 Event Reconstruction and Selection

Jets are reconstructed by employing Durham k_T algorithm with $k_T^{min} = 10$ GeV and limiting the maximum number of jets to two. Majority of Standard Model background is suppressed by $E_{visible} < 80$ GeV cut. To further suppress $e^+e^- \rightarrow b\bar{b}$ background $max(|\eta_1|, |\eta_2|) < 0.6$ is required, where η_1 and η_2 are jet pseudorapidities. Signal events are misbalanced due to neutralinos while dominant two-photon and $e^+e^- \rightarrow b\bar{b}$ backgrounds produce jets in back-to-back topology. This feature leads to $\Delta R_{\eta\phi} < 2.0$ cut. Finally, due to kinematics of signal events, acoplanarity A is required to be above 0.6 since b-quarks and beamline are generally not planar. Figure 4.25 shows respective distributions for $m_{\tilde{b}} = 230$ GeV and $m_{\tilde{\chi}_1^0} = 210$ GeV. It can be seen that the signal is a number of orders of magnitude smaller than dominant backgrounds.

For the final event selection Artificial Neural Network is trained on a half of both signal and background events - so called training sample. The resulting NN output for testing samples is shown in Figure 4.25 bottom-right. Note the logarithmic scale of y-axis.

4.2.8.4 Sbottom Cross Section Measurement

The measurement is interpreted in terms of confidence level calculated as $S/\sqrt{S+B}$, where S is the number of selected signal events and B the number of selected background events. The event numbers are normalised to an accumulated luminosity of 2000 fb^{-1} and the splitting of the samples into training and testing subsamples is accounted for. Figure 4.26 shows a distribution of $S/\sqrt{S+B}$ as a function of a number of selected signal events. Thus each bin corresponds to a particular selection of a final cut on NN classifier output.

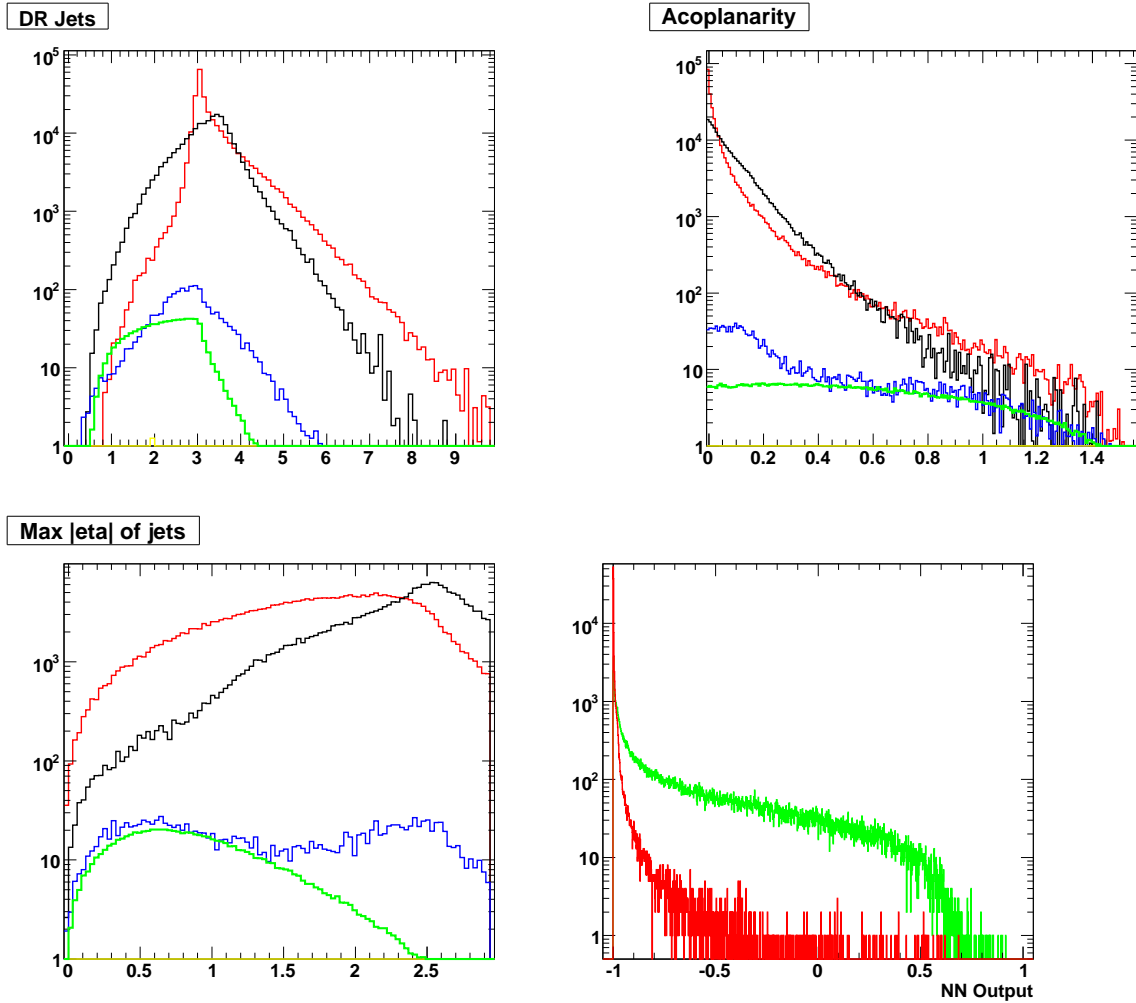


Figure 4.25: The main selection variables, from top left: Distance of jets in $\eta - \phi$ plane, acoplanarity and maximum pseudorapidity of jets. Signal (green) is shown together with major backgrounds: two photon background (red), $e^+e^- \rightarrow b\bar{b}$ (black), $e^+e^- \rightarrow b\bar{b}\nu\nu$ (blue) and $e^+e^- \rightarrow t\bar{t}$ (yellow). Neural Network output (bottom right) is shown for events which passed the basic selection cuts (see text for details) for signal (green) and backgrounds (red). All histograms are normalised to luminosity.

Conclusions - it is not clear what to conclude yet - the final data are not ready.

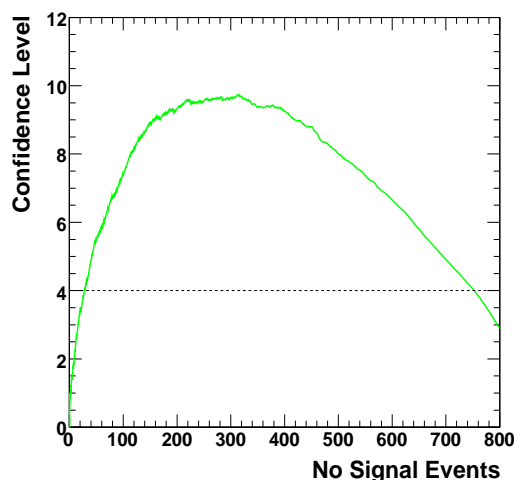


Figure 4.26: Confidence level plotted as a function of a number of selected signal events, depending on a particular Neural Net output cut used for signal event selection. Dashed line shows a limit of four standard deviations.

4.2.9 $e^+e^- \rightarrow e^+e^-(\gamma), \mu^+\mu^-(\gamma), \sqrt{s}=500$ GeV

Accurately determining the center of mass energy at the ILC is prerequisite for many physics studies, and major efforts are being devoted to measuring the beam energy before and after the interaction. Because the E_{cm} measured upstream and downstream of the interaction point can differ from the luminosity-weighted E_{cm} by as much as 250 ppm, it is important to be able to compare such measurements with a direct detector measurement of the center-of-mass energy based on physics events. The latter measurement directly measures the luminosity-weighted center-of-mass energy. As we show below, the high performance of the SiD tracker is particularly advantageous in this measurement, which can be done by studying muon pair production, and radiative returns to the Z, where the Z subsequently decays to muon pairs.

E_{cm} measurements at LEP using $e^+e^- \rightarrow \mu^+\mu^-\gamma$ relied solely on lepton angle measurements because little additional information could be gleaned from a direct muon momentum measurement. The resolution was inadequate. However, with the tracker being considered for SiD, the momentum measurement can significantly improve the E_{cm} measurement over what can be achieved with angles alone. $\diamond\diamond$ Figure 4.27 shows the accuracy with which E_{cm} can be determined with a data sample of 100 fb^{-1} by utilizing radiative returns ($Z\gamma$) or full energy muon pairs ($\mu\mu$) as a function of the parameters which describe the momentum resolution. For comparison, the accuracy obtained by using an angles-only measurement is also shown. For full energy mu pair production there is a strong dependence on curvature error, and for both methods there is a strong dependence on multiple-scattering because so many of the events are in the forward region. In any case, utilizing these reactions will

PHYSICS PERFORMANCE AND BENCHMARKING

improve the determination of E_{cm} to about 20 MeV. The superb resolution of the SiD tracker will impact these measurements.

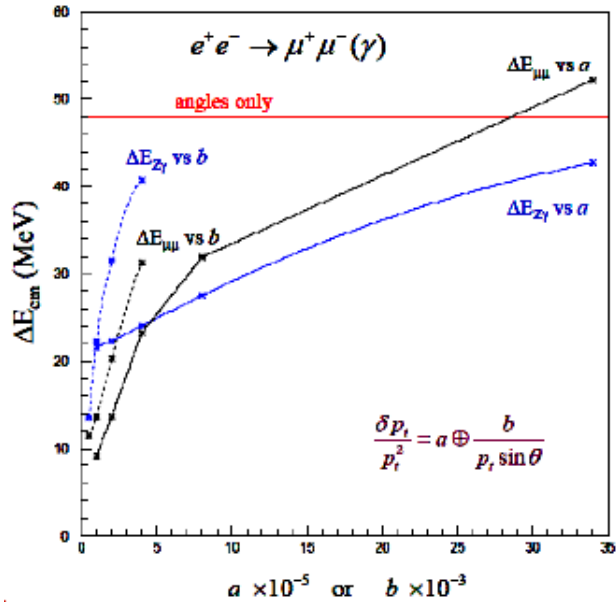


Figure 4.27: Error in E_{cm} as a function of the parameters describing the tracker momentum resolution coming from several possible measurements.

References

- [1] W. Kilian, T. Ohl and J. Reuter, “WHIZARD: Simulating Multi-Particle Processes at LHC and ILC,” arXiv:0708.4233 [hep-ph].
- [2] T. Sjostrand, S. Mrenna and P. Skands, “PYTHIA 6.4 physics and manual,” JHEP **0605**, 026 (2006) [arXiv:hep-ph/0603175].
- [3] M. Battaglia, T. Barklow, M. E. Peskin, Y. Okada, S. Yamashita and P. M. Zerwas, “Physics benchmarks for the ILC detectors,” *In the Proceedings of 2005 International Linear Collider Workshop (LCWS 2005), Stanford, California, 18-22 Mar 2005, pp 1602* [arXiv:hep-ex/0603010].
- [4] WMAP
- [5] CalcHEP
- [6] FANN package

REFERENCES

Chapter 5

Cost Estimate

The SiD design process has continuously monitored costs using a parametric cost model. This tool has been essential for the ongoing detector optimization process. At various stages, detector parameters (e.g. dimensions or masses) have been transferred to a Work Breakdown Structure where it is more convenient to describe a subsystem to arbitrary levels of detail. Here we describe the LOI version of SiD as such a point design.

The parametric model of the detector is a large set of Excel spreadsheets that first maintain a self consistent model of SiD. It is straightforward to vary parameters ranging from the most basic, such as the tracker radius and aspect ratio, to parameters such as the number of tracking layers, the number and thickness of HCal layers, and calorimeter radiator material. The tracking layers and disks are adjusted to fit the allocated space. The calorimeters are adjusted to nest properly with the tracker. The solenoid model is adjusted for its radius and field, and the flux return is adjusted to roughly contain the return flux. For each system, the cost driving component count, such as tungsten plate, silicon detectors, and readout chips for the EMCal, are calculated. The model has tables for material costs and estimates both M&S and labor costs that are associated with the actual scale of SiD. Costs that are approximately fixed, for example, engineering, fixturing, or solenoid He plants, are imported from the separate Work Breakdown Structure program. Finally, a set of macros calculate the costs of SiD as parameters are varied.

The cost process also develops a Work Breakdown Structure using the SLAC program WBS. WBS facilitates the description of the costs as a hierarchical breakdown with increasing levels of detail. Separate tables describe cost estimates for purchased M&S and labor. These tables include contingencies for each item, and these contingencies are propagated by WBS. The M&S costs are estimated in 2008 US \$. Labor is estimated in man-hours or man-years as convenient. The WBS had about 50 labor types, but they are condensed to engineering, technical, and clerical for this estimate. The statement of base M&S and labor in man-years by the three categories results in a cost which we believe is comparable to that used by the ILC machine, and is referred to here as the ILC cost. ¹

¹ To expand this to U.S. DOE style costs, the following steps are made:

Contingencies are assigned to M&S and Labor. The purpose of the contingency is primarily to make funding available to hold a schedule in the face of unforeseen problems; to fund items that were forgotten in

COST ESTIMATE

The philosophy of contingency is interesting. While it may not be used in the ILC value system, it does give some idea of the uncertainties in the costs of the detector components. Items which are close to commodities, such as detector iron, have had costs swinging wildly over the last few years. It is also difficult to estimate silicon detector costs for such large quantities.

There are a substantial set of interfaces in the interaction region hall. For the purpose of this estimate, the following has been assumed:

- The hall itself, with finished surfaces, lighting, and HVAC are provided by the machine.
- Utilities, including 480 VAC power, LCW, compressed air, and internet connections are provided on the hall wall.
- An external He compressor system with piping to the hall is provided. The refrigeration and associated piping is an SiD cost.
- Any surface buildings, gantry cranes, and hall cranes are provided by the machine.
- Data storage systems and offline computing are provided by others.
- Detector motion rails (push-pull and opening in the beamline and garage positions) are installed by SiD in suitably prepared areas in the concrete floor.

The subsystem level summary is shown in Figure 5.1, the M&S costs are plotted in Figure 5.2, and the labor costs are shown in Figure 5.3. The costs are dominated by the Magnet and the EMCal. The magnet has roughly equal costs for the superconducting coil and the iron. The EMCal is dominated by the silicon detectors.

Figure 5.4 through Figure 5.7 show simple examples of the parametric costs of SiD. In all cases, the non varied parameters are the SiD baseline: $R_{trkr} = 1.25$ m, $\text{Cos}(\theta)_{trkr} = 0.8$, $B = 5$ T, and Hcal thickness = 4.5λ . The parametric model is used with an analytic expression for the PFA resolution in terms of the tracker radius, B field, and HCal thickness to optimize SiD for a fixed PFA resolution. Finally, physics performance versus PFA resolution is used to study physics performance versus SiD cost. This is discussed in more detail elsewhere in this document.

The cost estimate has several important “commodity” items whose costs have recently been fluctuating significantly. For SiD, these include most metals and processed Si detectors. Table 5.1 illustrated the cost sensitivity to these prices by indicating the unit cost used in the estimate and the effect on the SiD cost of doubling the unit cost.

the estimate; and to provide some relief from underestimates.

Labor is transformed to a dollar value by using SLAC salaries that include benefits but not overhead.

Indirects are computed as a fraction of the M&S and Labor. SLAC large project values are used.

Escalation is computed assuming a start date, a 6 year construction cycle, and an inflation rate. For this study, a start date of 2016 and an inflation rate of 3.5%/year is assumed. The escalation is both quite substantial and uncertain.

		M&S Base (M\$)	M&S Contingency (M\$)	Engineering (MY)	Technical (MY)	Administrative (MY)
1.1.1	Beamline Systems	\$ 3.68	\$ 1.42	4.0	10.0	0.0
1.1.2	VXD	\$ 2.10	\$ 2.00	6.5	10.9	0.0
1.1.3	Tracker	\$ 14.83	\$ 5.46	20.0	76.6	0.0
1.1.4	EMCal	\$ 66.93	\$ 26.38	13.0	264.8	0.0
1.1.5	Hcal	\$ 14.76	\$ 7.88	12.0	78.7	0.0
1.1.6	Muon Sys	\$ 3.67	\$ 1.44	4.0	27.6	0.0
1.1.7	Electronics	\$ 3.91	\$ 1.30	75.0	63.0	0.0
1.1.8	Magnet	\$ 116.49	\$ 39.94	29.2	25.0	0.0
1.1.9	Installation	\$ 2.62	\$ 0.52	5.0	51.0	0.0
1.1.10	Management	\$ 0.92	\$ 0.17	37.0	5.0	25.0
Totals		\$ 230	\$ 87	206	613	25

Figure 5.1: Subsystem Summary of Costs

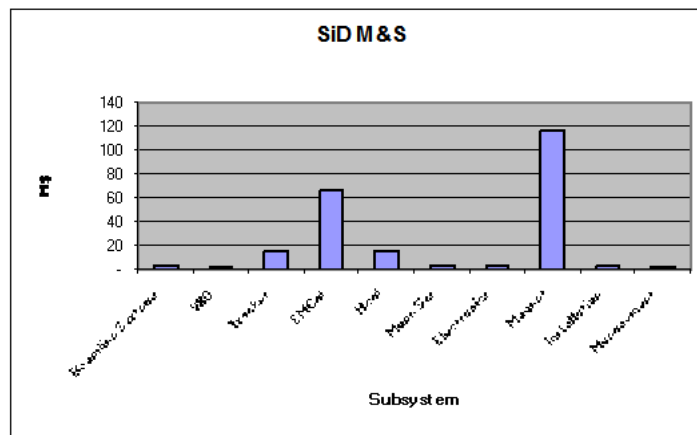


Figure 5.2: Subsystem M&S Costs

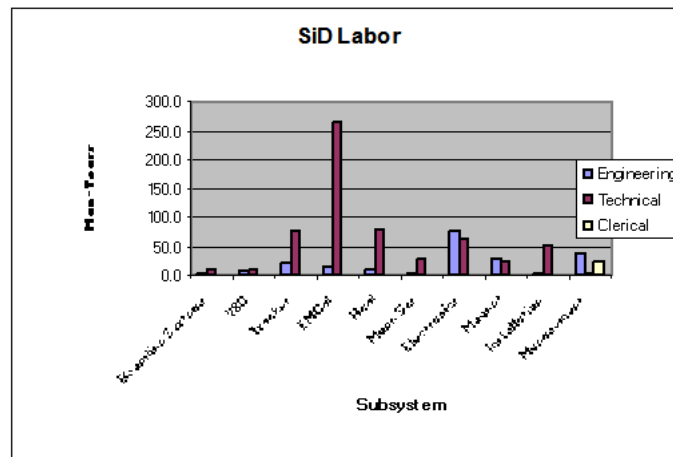


Figure 5.3: Subsystem Labor

COST ESTIMATE

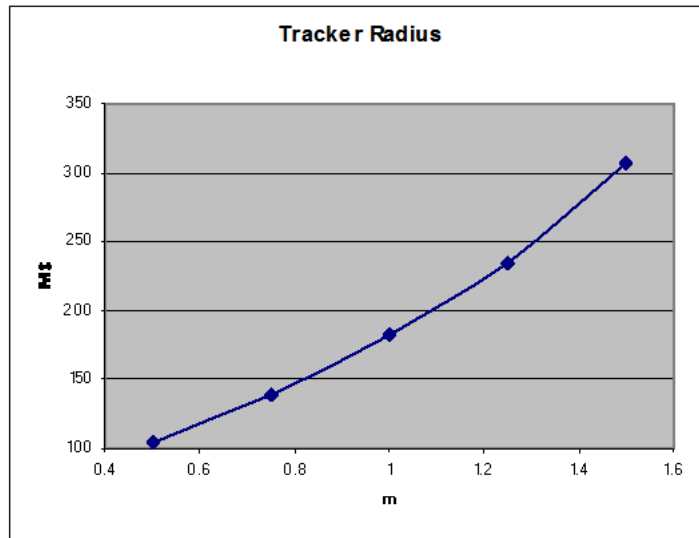


Figure 5.4: SiD Base M&S Cost vs Tracker Radius

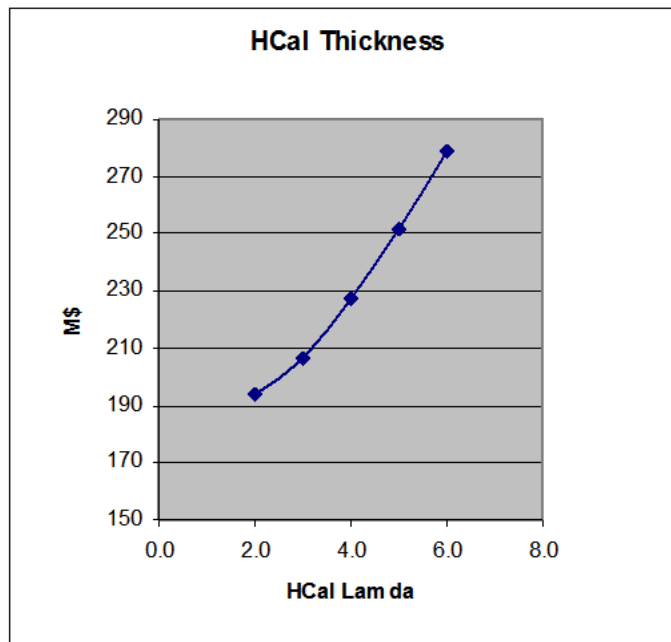


Figure 5.5: SiD Base M&S Cost vs Hadronic Calorimeter Thickness

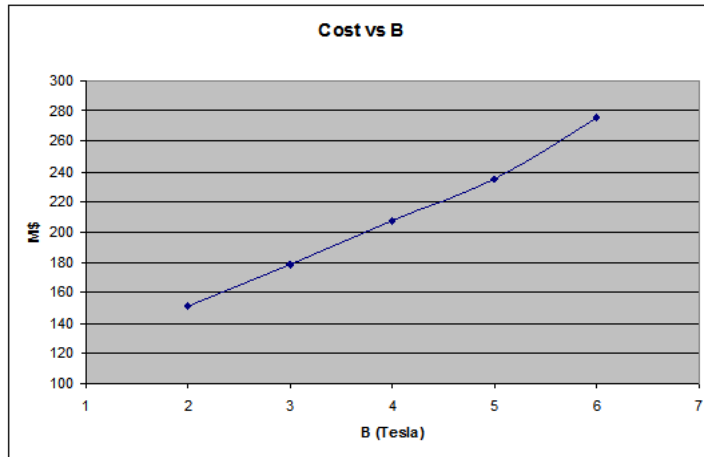


Figure 5.6: SiD Base Cost vs B

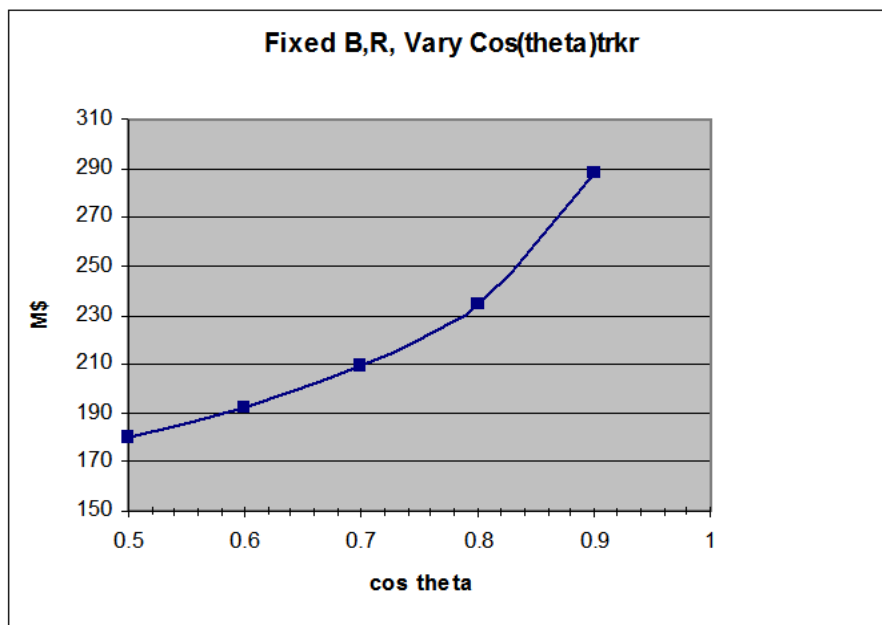


Figure 5.7: SiD Base Cost vs Tracker Aspect Ratio

Item	Nominal Unit Cost	Δ SiD Base M&S Cost (M\$)
Magnet Iron (finished and delivered)	\$7/Kg	56
Tungsten (powder alloy) plate	\$88/Kg	6
Si Detector	\$3/cm ²	38
HCal Detector	\$2000/m ²	7

Table 5.1: Cost Sensitivity to selected unit costs

COST ESTIMATE

The superconducting coil cost is difficult to estimate, because there is little data and experience with coils of this size and field. An attempt was made to extract the CMS coil cost, and it is believed to be ~\$48M\$ for cold mass and vacuum tank. A Japanese industrial estimate for the SiD coil was obtained, and it was approximately the same as CMS, but for a coil with roughly half the stored energy. Cost functions linear in the stored energy and with a 0.66 exponential dependence have been studied. SiD has taken a conservative approach and for the parametric study has used a linear model fit to the Babar coil at the low end and the industrial estimate at the high end. The result for the current SiD design is \$55M, higher than the CMS cost, but inflation and currency exchange variations have been ignored. SiD is doing R&D on advanced conductor design, and there is some reason to expect the coil cost estimate to decrease.

The WBS cost tables have been reviewed by the subsystem groups. The quality of the estimate is considered roughly appropriate for a Letter of Intent; it would not be defensible for a construction readiness review. A sample of the WBS for the tracker is shown in Figure 5.8.

The SiD cost in ILC value units is \$238M\$ for M&S, 206 MY engineering, 613 MY technical, and 25 MY administrative labor. The estimated M&S contingency, reflecting uncertainty in unit costs and some estimate of the maturity of this study, is \$88M. The cost in US accounting, assuming a construction start in 2016 and 3.5% per year inflation and US National Laboratory labor rates, is \$700M. For the SiD Detector Outline Document in 2006, the base M&S cost estimate was \$203M, to be compared with the \$238 present value. About \$20M of the difference is in the approach to estimating the superconducting solenoid.

WBS ID	Description	Unit	Quantity	Rate	Amount	CF	Amount	Amount	Amount	Amount
1.1.3	Tracker	1 each			15,446,950	@CF=Tracker	5,869,383	11,473,252	4,015,638	36,805,223
1.1.3.1	Tracker ED&I	1 each			0		0	7,761,320	2,716,462	10,477,782
1.1.3.1.1	Mechanical Engineer	20 man year			0		0	140,000	49,000	3,780,000
1.1.3.1.2	Mechanical Designer	10 man year			0		0	91,520	32,032	1,235,520
1.1.3.1.3	Mechanical Tech	40 man year			0	WAG	0	101,153	35,404	5,462,262
1.1.3.2	Tracker Mechanics	1 each			2,900,000		1,375,000	1,200,325	420,114	5,895,439
1.1.3.2.1	Tracker Space Frame, Barrel	1 lot			1,250,000		625,000	0	0	1,875,000
1.1.3.2.2	Outer Endcap Frame[0]	2 lot			250,000		125,000	0	0	750,000
1.1.3.2.3	Tracker Cooling	1 lot			150,000		150,000	0	0	300,000
1.1.3.2.4	Tracker Alignment System	1 each			1,000,000		350,000	0	0	1,350,000
1.1.3.2.5	Mechanical Engineer	3 man year			0		0	140,000	49,000	567,000
1.1.3.2.6	Mechanical Designer	3 man year			0		0	91,520	32,032	370,656
1.1.3.2.7	Mechanical Tech	5 man year			0		0	101,153	35,404	662,783
1.1.3.3	Tracker Silicon Detectors	1 each			11,546,950		4,244,383	2,511,607	879,063	19,182,003
1.1.3.3.1	Barrel	1 each			6,340,450		2,341,108	1,531,015	535,855	10,748,428
1.1.3.3.1.1	Tracker Barrel Module	8,130 each			665	Parametric	248	188	66	9,487,528
1.1.3.3.1.1.1	Tracker Silicon	0.01 Sq.m.			30,000		10,500	0	0	405
1.1.3.3.1.1.2	Tracker Module Mechanics Barrel	1 each			65		23	0	0	88
1.1.3.3.1.1.3	Tracker KPX	2 each			100		35	0	0	270
1.1.3.3.1.1.4	Tracker Cable	1 each			100		50	0	0	150
1.1.3.3.1.1.5	Mechanical Tech	2 man hour			0		0	54	19	145
1.1.3.3.1.1.6	Procurement Officer	1.5 man hour			0		0	54	19	109
1.1.3.3.1.2	Level 1 Concentrator, Tracker	467 each			2,000		700	0	0	1,260,900
1.1.3.3.1.3	Level 2 Concentrator, Tracker	1 each			0		0	0	0	0
1.1.3.3.2	Endcaps	2 each			2,603,250		951,638	490,296	171,604	8,433,575
1.1.3.4	Tracker Integration	1 lot			1,000,000		250,000	0	0	1,250,000

Figure 5.8: Example of WBS

COST ESTIMATE

Chapter 6

Research and Development Issues

Dummy text.

